ISTITUTO NAZIONALE DI FISICA NUCLEARE
Laboratori Nazionali di Frascati

FRASCATI PHYSICS SERIES

VULCANO 2018

Frontier Objects in Astrophysics and Particle Physics

Editors:

R. Fusco Femiano, G. Mannocchi, A. Morselli, G.C. Trinchero

FRASCATI PHYSICS SERIES

Series Editor
Paola Gianotti

Technical Editor
Lia Sabatini

Cover by Claudio Federici

Volume LXVI

Istituto Nazionale di Fisica Nucleare – Laboratori Nazionali di Frascati
Divisione Ricerca
Ufficio Biblioteca e Pubblicazioni
P.O. Box 13, I-00044 Frascati Roma Italy
email: library@lists.lnf.infn.it

ISBN 978-88-86409-67-4

VULCANO Workshop
Frontier Objects in Astrophysics and Particle Physics
2018

Foreword

The seventeenth edition of the Vulcano workshop: Frontier objects in Astrophysics and Particle Physics was organized jointly by the National Institute for Nuclear Physics (INFN) and the National Institute for Astrophysics (INAF). The workshop was held in the Conference Room of the Therasia Resort (Vulcano Island, Sicily, Italy) from May 22th to May 28th and was attended by more than 80 scientists world wide. This workshop is certainly one of the first that since 1986 has the aim to gather people from High Energy Astrophysics and Particle Physics to discuss the most recent highlights in these fields. It is well known that at the beginning of the 80's the Universe was considered the greatest particle accelerator of the world to test the Grand Unified Theories ideas. Of course a machine hard to use because all the experiments happened only once, a long time ago. Today, gigantic underground accelerators and space crafts probe everyday this connection. As never before, these two fields of knowledge complement and integrate each other. The discovery of new particles may unveil some cosmic mysteries, conversely, astrophysical observations may give new information on the infinitely small. The programme of the Vulcano workshop was organized in several sessions where many topics have been discussed. In particular, some of these sessions regarded the state of the art of the possible answers to the three fundamental questions provided by Cosmology, namely: what is Dark Energy ? What is Dark Matter ? And why in the Universe we have matter and not antimatter ? One of these sessions was dedicated to the spectacular detection of gravitational waves in August 2017 by Neutron Stars coalescence accompained for the first time by electromagnetic detections. These observations may be considered the act of birth of a new era for astrophysics. In this session we have discussed not only the results of these observations but also the possibilities given by this new powerful tool to deepen our knowledge on the birth and evolution of the universe and we think that this new season for physics and astrophysics will bring us to many discoveries that we can not imagine now, as it happens in the cases where we can really expand the horizon of our knowledge. The workshop has been opened by a recollection by Prof. Giorgio Parisi of our dear colleague and friend Dr. Aurelio Grillo that has been member of the SOC of this workshop since the first edition. Besides, we have remembered Giovanni Nicoletti that has been staff member of this workshop since 1986, giving a fundamental contribution to the succes of the workhops thanks to his expertise in the computer science. The final scientific program was selected by the Scientific Organizing Committee chaired by Roberto Fusco-Femiano (INAF) and Giampaolo Mannocchi (INFN) and composed by: Antonella Antonelli (INFN), Simone Dell'Agnello (INFN), Pino Di Sciascio (INFN), Nicola Menci (INAF), Aldo Morselli (INFN), Luigi Piro (INAF), Marco Ricci (INFN), Gian Carlo Trinchero (INAF), and Francesco Vissani (INFN). The Local Organizing Committee was composed by Maria Cristina D'Amato (INFN), Roberto Fusco-Femiano, Giampaolo Mannocchi, and Lia Sabatini (INFN) with the precious help of Alessio Gorgi (INAF). A special thank to Maria Cristina D'Amato and Lia Sabatini for their fundamental work not only in the preparatory phase but also during and after the conclusion of the workshop.

Roberto Fusco-Femiano and Giampaolo Mannocchi

Conference Program

G. Parisi	Scientific and personal Recollections of Aurelio Grillo

Gravitational Waves and Multimessenger Astronomy

M.A. Papa	Introduction to Gravitational Waves and Gravity
V. Fafone	The dawn of Gravitational Waves Astromomy
M. Branchesi	Multimessenger Astrophysics: The new era of Gravitational Waves
A. Chieffi	Formation of stellar Black Holes and origin of binary sistems
C. Kopper	Neutrinos in the multimessenger era
C. Fryer	Origin of heavy elements from Gravitational Waves events
H. Van Eeerten	Theory of off-axis GRBs and Gravitational Waves events
G. Prodi	Emission of Gravitational Waves from the BH coalescence
A. Corsi	Radio counterparts from Gravitational Waves events
E. Troja	Discovery of the X-ray counterpart and the GW - GRBs connection

Astrophysics and Cosmology

O. Straniero	Stellar Nucleosyntesis
E. Brocato	Kilonovae observations
R. Dolesi	GW with LISA-Pathfinder and e-LISA
C. Gustavino	BBN, Neutrinos and Nuclear Astrophysic
M. Burgay	Detection and origin of Fast Radio Bursts
F. Nicastro	Missing baryons and cosmological filaments from X-rays
P. Klimov	Recent results from the TUS/LOMONOSOV Space Mission
E.S. Battistelli	CMB observations: implications for inflation and early Universe
L. Piro	The hot energetic universe with Athena

Cosmic Rays, Neutrino and Gamma Rays

J. Goodman	Photons in the multimessenger era
G. Morlino	Cosmic rays in the multimessenger era
F. Aharonian	The connection between Gamma Rays and Cosmic Rays
A. Lamastra	AGN outflows as accelerator of Cosmic Rays and neutrinos
B. Dingus	Recent results from HAWC
M. Vecchi	Review on direct measurements of Cosmic Rays
F. Longo	Gamma-ray Physics in the Fermi era
C. Pittori	Highlights from AGILE
P.S. Marrocchesi	CALET: Calorimetric Electron Telescope
V. De Sousa	Recent results from AUGER
M. Bertaina	Search for UHE Cosmic Rays from space: the JEM-EUSO program
A. Capone	Observations of HE Neutrino in the multimessenger Prospects
S. Buson	Flaring blazar and high-energy neutrinos
M. Circella	ANTARES and KM3NeT experiments: status and future developments
R. Iuppa	Antimatter in Cosmic Rays
Z.G. Yao	Status of the LHAASO experiment

A. Petrukhin	Nucleus-Nucleus interactions at LHC and in cosmic rays
E. Bissaldi	Fermi-GBM and Gravitational Waves
A. Morselli	The Cherenkov Telescope Array Project: current status and science goals
P. Desiati	Cosmic Ray anisotropy
J.P. Daz Vlez	Anisotropy with HAWC and IceCube
L. Natalucci	Integral discovery of GRB from Neutron Stars coalescence
L. Natalucci	AHEAD, High Energy Astrophysics H2020 infrastructure

Dark Matter and Dark Energy

A. Nierenberg	Hints on the nature of DM from gravitational lensing
M. Castellano	Constraints on the nature of DM from the abundance of extremely distant galaxies
A.D. Ferella	Dark Matter Direct Detection Experiments
E. Aprile	The XENON1T Dark Matter Search at LNGS: Results and Prospects
G. Bertone	New strategies in the quest for dark matter

Neutrino

L. Di Noto	Low energy solar neutrinos with Borexino
S. Dell'Oro	A review on neutrinoless double beta decay
M. Messina	PTOLEMY:Relic Neutrino Detection

Gravity

L. Iess	Testing gravity with the BepiColombo mission
S. Capozziello	Beyond Einstein's Gravity
F. Fiore	Quantum gravity constraints from electromagnetic domain
S. Dell'Agnello	Tests of gravity in the solar system
M. Crosta	Testing gravity with GAIA

Particle Physics

M. Borsato	Search for dark matter at LHC
B. Dobrich	Search for dark matter at fixed target, status and prospects
M. Incagli	The Muon g-2 experiment at Fermilab
M. Pospelov	Dark sector in accelerators
M. Raggi	The PADME experiment
M.D. Moulson	Results and future projects on $K_L \to \pi^0 \nu\bar{\nu}$
G. Ruggiero	NA62 first result on $K^+ \to \pi^+ \nu\bar{\nu}$
L. Pontecorvo	Highlights on Atlas and CMS
V.M. Vagnoni	Highlights on LHCb

Future Projects

L. Linssen	Future projects at CERN
R.C. Shellard	LATTES project
C. Signorini	Overview of ESA science missions

E. Cavazzuti	ASI programs for HE Astrophysics
A. Olinto	The space mission POEMMA: Probe of Extreme Multi-Messenger Astrophysics
N. Pastrone	The Muon Collider
M. Ferrario	LNF new projects
U. Kose	he Research Activities within CERN Neutrino Platform

Slides are available at:
https://agenda.infn.it/event/14775/timetable/?view=nicecompact

Frontier Objects in Astrophysics and Particle Physics
Conference Proceedings

Frascati Physics Series Vol. 66 (2018)
Frontier Objects in Astrophysics and Particle Physics
May 20-26, 2018

Personal and scientific recolletions of Aurelio Grillo

Giorgio Parisi
Dipartimento di Fisica, Università di Roma La Sapienza
Nanotec-CNR, UOS Rome, INFN-Sezione di Roma 1,
Piazzale A. Moro 2, I-00185, Rome, Italy

Abstract

In this talk I will present some personal and scientific recollections of my dear friend Aurelio Grillo. These recollations will be mainly devoted to his early part of his career, because at that time we had frequent scientific exchanges and we were working on similar field (often together).

1 Introduction

Aurelio was born in 1945: he was three years older than me. We did not see each other too much while he was studying at the university. However we started to see each other very frequently after he left the university: we had a very good common friend, Massimo Testa. When I got a fellowship at the National Frascati Laboratories (January 1971), he had already a permanent position there.

At the Frascati Laboratories there was the largest e^+e^- colliding beam in the world: it was constructed under the scientific leadership of Bruno Touschek. Unfortunately, the project-energy was 1.5+1.5 Gev, not 1.6 Gev+1.6 Gev, so Frascati was unable to discover the ψ[1].

When arrived at Frascati I found a small, but wonderful, theory group: beyond Aurelio there where Gianni de Franceschi, Paolo di Vecchia, Antonino Drago, Etim Etim, Sergio Ferrara, and Mario Greco. We were working at a few meters one from the others and we were going to eat together at the excellent cantine of the laboratories. At lunch time we were discussing everything, maybe the most popular arguments were connected to the experiments that were done in Frascati at that particular moment.

Indeed it was an exciting time. The first results from the experiments were coming out and they presented evidence for a completed unexpected production of many pions with a quite high cross section. This was in variance with the most fashionable theories that predicted that there should be only two or three mesons production and that the total cross section for hadron production should be much smaller than the observed one. An explanation was in the parton model, but this interpretation of the data was not so compelling as it is nowadays. We were very interested to understand how sound were the experimental results, we were pondering the information that was coming out from informal discussions with the experimentalist and we were trying to figure out which was the best interpretation of the data.

People would hardly visually recognize Aurelio: at that time he had not his beard we are accustomed now. We were part of a company of very good friends: we met very frequently outside working time, eating and drinking beer in Roman pubs, playing poker, etc. Aurelio had a strange luck at poker. I remember that once in 8 consecutive deals he had 7 very good deals: one quad, one flush, three full houses, two straights. It was a very impressive sequence: I cannot remember anything similar. Unfortunately for him and fortunately for us, he lost all the deals.

[1]The ψ was observed by increasing the electron and positron energy to a value that was of about %3 higher that the project-energy. Fortunately it turned out that this increase was within the tolerance of the magnets and everything was fine.

2 Aurelio, the conformist

Aurelio started to work (with di Vecchia and Drago in Frascati and other people from outside) on the modifications of the Veneziano model produced by the effect of unitarity [1, 2]. It was a very hot problem at that time, that faded with time with the introduction of the systematic loop expansion and with the awareness that the Veneziano model could not be a viable starting point for strong interactions.

His scientific interest changed when Raul Gatto came to Rome (1971). He strongly pushed Aurelio and Sergio Ferrara to work on the conformal group. He was already working on this field while in Padova and he wanted to continue his investigations in Rome. The collaboration was extremely successful and 15 papers were produced: most of them were written between 1971 and 1974 [3, 4, 5, 6, 7, 8]. I joined the group 1972 and I cosigned 5 of them [9, 10].

If a quantum field theory is scaling invariant, the trace of the energy-momentum tensor must be zero, and usually, the theory is also conformal invariant (at least for gauge invariant quantities). Conformal invariance is thus a natural extension of scale invariance. Indeed the four-dimensional conformal group (i.e. $O(4,2)$) is an extension of the direct product of Lorenz group and of dilatations.

Why at the time people were deeply interested in studying the conformal group? Bjorken scaling was suggesting that the strong interaction theory was scaling invariant at high energies. Extending scaling invariance to conformal invariance could give some extra clues to understanding the physics of the (at that time) mysterious scaling invariance.

In a very nice review [11] Aurelio explains very clearly the motivations for these studies: *It is an important idea, due to Wilson, that the renormalization procedure of any sensible field theory could eventually give an anomalous part to the dimensions fo the fields: this comes from the infinite strength renormalization and it is a parameter which is determined by the interaction and in some sense characterizes the dynamics. (...) Since the discovery of scaling behavior in deep inelastic electroproduction, many theoretical investigations have been devoted to the study of the origin of this phenomenon.*

Various models, such as the parton model, have been invented, that give a partially satisfactory (or unsatisfactory) explanation of experimental results, but the most important achievement which emerges is the emphasis that has

been put on fundamental properties of field theory such as dilatation and conformal invariance.

At that time, in the relatively small circles of people that believed that strong interactions should be understood via a renormalizable quantum field theory, the standard folklore was:

- At high energy (more precisely at short distances) strong interactions were supposed to be a strongly coupled theory: indeed in all the known theories, the interaction was increasing with the energy (decreasing the distance).

- Renormalization group equations could be written and the scaling invariance of the theory implied that the physical coupling constant g at large energy is a fixed point of the renormalization group, i.e. $\beta(g) = 0$.

- Asymptotic free theories were not known: moreover they would be considered to be not natural. For example, in QCD there are two scales of masses: Λ_{QCD} and the quark masses. The following scenario would be more elegant: strong interaction theory are a perfectly scaling invariant at high energies where the scaling invariance is broken only by a mass term. However as suggested by Einstein in the preface of his 1916 book Relativity we should *adhere to the precept of that brilliant theoretical physicist L. Boltzmann, according to whom matter of elegance should be left to the tailor and to the cobbler.*

- The strong interaction theory was not known at that time. As far as the renormalization group fixed point was supposed to be in the strong coupling regime, perturbative techniques were useless. The only hopes were based on the possibility of using symmetry arguments (like the conformal group) in order to get predictions in*terra incognita*.

Let me summarize some of the most important Aurelio's results in this period.

- The construction of a manifestly conformal covariant operator-product expansion [3]. This paper was the mathematical and physical base of the following papers on the conformal group. The group theoretical aspects were deepened in a subsequent paper on the tensor representations of

conformal algebra and on their contributions to conformally covariant operator product expansion [7].

- A crucial problem was the computation of the contribution of terms arising from the covariant operator-product expansion to the conformal four-point function (the so-called conformal blocks). This was done mainly in two papers [9, 10] where we introduced the shadow operator formalism for operator-product expansion and we applied it to the computation of vacuum expectation values, mainly for the four-point function.

- In a remarkable paper Aurelio studied deeply the conformal algebra in two space-time dimensions and it applies the insight he obtains to the Thirring model, that is a non-trivial interacting model with many interesting features [5]. This paper is very interesting as far the two-dimensional conformal group is much larger: it is an infinite dimensional Lie group, strongly related to the Virasoro algebra.

- In a short but deep paper Aurelio showed that the constraint of positivity (i.e. the Hilbert space of physical states should have a positive norm) gave strong restrictions on the values of anomalous dimensions. [8]

The collaboration faded around in 1973-1974 for many reasons. Logistic difficulties were important: Sergio Ferrara moved away to CERN and I moved to Columbia University. However scientific reasons were the most important. Asymptotic freedom for strong interactions was discovered and it was becoming increasingly popular in our community. At the end of the day, the scaling invariant strong interaction theory was free-field theory and it could be understood in a naive way. The only delicate point was the computation of scaling corrections: they can be evaluated in perturbation theory.

The conformal group turned out to be useless in high energy physics and the interest of conformal theories for strong interactions disappeared for some time and it resurrected much later in string theory.

3 The conformal bootstrap

It is well known that second-order phase transitions in two and tree Euclidean dimensions provide non-trivial strongly coupled scaling invariant theories in the

infrared region when the correlation length goes to infinity[2]. Critical exponents (that are measured both in experiments and in numerical simulations) are related to anomalous dimensions.

The computation of the critical exponents was an evident field of application of the conformal group. This lead to the proposal by Ferrara, Gatto, and Grillo of the conformal bootstrap idea. The attempt to implement this project was my main motivation to start the very complex computations of [9, 10].

The idea at the basis of the conformal bootstrap is quite simple. Conformal invariant Wilson expansion gives:

$$\langle\phi(x)\phi(y)\phi(z)\phi(t)\rangle = \sum_{\mathcal{O}} \int dw \langle\phi(x)\phi(y)\mathcal{O}(w)\rangle\langle\tilde{\mathcal{O}}(w)\phi(z)\phi(t)\rangle\,, \qquad (1)$$

where the sum is done over the primary conformal fields $\mathcal{O}$, i.e. those fields that transform a simple way under the action of the conformal group and $\tilde{\mathcal{O}}$ is the shadow operator corresponding to the operator $\mathcal{O}$. This is essentially a s-channel decomposition in conformal partial waves.

Each term is not symmetric (exchange x with z). The hope was that imposing this symmetry we should get the dimensions of the operators ϕ and $\mathcal{O}$'s. In other terms, we were asking that the sum of s-channel poles should be equal to the sum of t-channel poles. Obviously, there are no simple solutions with a few terms. We needed an infinite number of terms and we did not find a simple way to deal with the problem. It was a natural generalization of the duality arguments that lead to the Veneziano formula.

We abandoned the problem because we were stuck. However, as we learned much later, we were on the right track!

We have already seen that the $D = 2$ conformal group is contained in a much larger group. Each representation of the larger conformal group contains an infinite number of representations of the smaller conformal group (i.e. a Virasoro tower).

In 1984 Belavin, Polyakov and Zamolodchikov [12] computed the $2D$ equivalent of equation (1) using the invariance under the larger conformal group (the one that was studied in [5]). Only for a discrete set of values, one could get

[2]In Euclidean field theory the correlation length is the inverse of the inverse of the relativistic mass and it goes to zero at the critical point.

perfect symmetry with only a few terms. This magnificent computation leads to the exact evaluation of the critical exponents in $D = 2$ for many different models. It provides an invaluable tool for studing two-dimensional physics.

I always regret that we never tried to do the simplest attempt to compute the $2D$ equivalent of equation (1). I do not know why: maybe the effort to compute one term in $D = 3$ was so high that we believed that the $D = 2$ computation with an infinite number of terms was too difficult (ironically the computation was much simpler).

In $D = 3$ the story was quite different. In 2012 appeared an other magnificent paper [13], where the conformal bootstrap program was used to put a strict bound on the value of the critical exponents for the three dimensional Ising model. Further developments of these techniques allow a high precision computation of the critical exponents. The paper is based on clever new ideas: moreover one can consider the contributions of more than 100 terms: I firmly believe that such a computation could not be done with the computers of 45 years ago. A side effect of these computations is that the citations of Aurelio's old work on the conformal invariance nearly doubled in these recent years.

4 Looking around

In 1974 Aurelio started to look around for other fields and he started to study new topics.

He started to perform some computations that were useful to interpret the experimental data coming from the colliding beam experiments: for example, he analyzed the radiative asymmetry in $e^+e^- \to \mu^+\mu^-$ near a narrow resonance in the case where the beams were polarized [14].

He moved later to study other problems of astrophysical relevance as the production of cosmological black holes in the framework of grand unified theories [15] and the production of Fermions during monopole-antimonopole annihilation [16].

At the end of the eighties, he started a very interesting program of investigations of lattice quantum electrodynamics, trying to arrive to clear-cut results and to a deep understanding of the problems: these achievements were possible given the simplicity of QED with respect to QCD. Some of the most interesting results were:

- The study of the stability of quantum vortices on the lattice in the case of the quantum electrodynamics ($U(1)$ gauge group) in the presence of a charged Higgs-like field in the phase where the Higgs field were breaking the $U(1)$ symmetry, as in the standard model [17].

- In the framework of compact pure gauge lattice QED a careful study of the phase transition that separates the confined phase from the unconfined phases. The delicate point of the order of the phase transition was successfully addressed [18].

- In long series of papers Aurelio addressed the problem of introducing dynamical Fermions in lattice gauge theory and analyzed many of theoretical aspects mainly in the case of QED. In one of these very interesting papers, he introduced a new method for simulating lattice gauge theories with dynamical Fermions based on microcanonical Fermionic average [19]. Many of his later papers are based on the results he obtained with this method.

5 Transforming himself into a refined experimentalist

A complete change of interests happens in Aurelio when he startsdthe MACRO adventure and he became a refined experimentalist. Everything started with the proposal of MACRO: the title was *Proposal for a large area detector dedicated to monopole search, astrophysics, and cosmic ray physics at the Gran Sasso Lab*: it was signed by 73 physicists, among them Aurelio, who used his deep theoretical knowledge of many areas of physics to give a great contribution to the planning of future experiments, especially in understanding the physical relevance of the future results.

MACRO was located underground Gran Sasso Laboratories and it started the data taking with a part of the apparatus in 1989; it has completed in early 1995 and was running in its final configuration until the end of 2000. It was large of the order of $10^4 m^3$: it produced 50 scientific papers that were signed also by Aurelio, who was a crucial part of the collaboration.

It would be difficult for me to summarize MACRO's results: the interested reader can look at the very nice review [20]. I will only mention a selection some of Aurelio's papers just to stress the diversity of his activities:

- An analysis of the performance of the MACRO streamer tube system that was used in the search for magnetic monopoles [21]. Magnetic monopoles were indeed one of his recurrent theoretical interest. Moreover, the magnetic monopoles search was a very important goal of MACRO.

- A theoretical analysis where the high-energy neutrino emission from binary X-ray sources was estimated using the data for very high energy γ rays. The implications of these findings for the future MACRO experiments were clearly spelled out [22].

- An analysis of the multiple muons event in MACRO: it was possible to extract from these data very interesting information on the ultrahigh-energy primary-cosmic-ray composition [23]: the data exhibited a preference towards the light composition model.

- In another paper, he analyzes the atmospheric neutrino interactions using the data on the induced upgoing muon flux [24].

With the turn of the millennium, he started a new adventure: the Pierre Auger Observatory. The Pierre Auger Observatory has some similarities with MACRO, however, the scaling of the involved energies of the primaries and the physical extensions of the experiments are quite different: it was a great leap forward.

Aurelio was a crucial component of the team from the beginning in of the project: he wrote a paper on the properties and performance of the prototype instrument for the Pierre Auger Observator [25]: this study was a crucial analysis that played an important role for the success of the project.

He was involved in technical papers concerning the crucial study of the composition of the atmosphere above the experimental area: as an example, I would like to recall the two papers on the study of the performance of the LIDAR system [26] and of the related measurement of aerosols [27].

He also gave crucial contributions to the much more interesting papers where the main experimental results were presented. I will recall only two the so many papers

- The measurement of the energy spectrum of cosmic rays above 10^{18} eV. This was one of the main motivation for the construction of the Pierre

Auger Observatory [28]: the results are really impressive and they have very deep theoretical implications.

- The high-resolution studies of the anisotropy of ultrahigh-energy cosmic rays. These studies give us information that is crucial to identify the source of these ultrahigh-energy particles [29] and to understand the physical mechanism that that produces them.

6 Conclusions

Aurelio suddenly died on the February of 2017: we all lost a wonderful colleague and a dear friend. At the moment that this paper is written, it is was one and half years ago. It is difficult to convince oneself that we shall not see again, that we will not able to follow his deep advice that he was able to give in his characteristic outspoken way. The only relief may come from the consideration that Aurelio managed to dedicate his life to his two great passions, to music (in this helped by his beloved daughter Stefania) and to physics. I remember that when we were both in Frascati he used to tell to me "Being a physicist is a hard job, but it's always better than working".

References

1. D. Atkinson, L.A.P. Balazs, F. Calogero, P. Di Vecchia, A. Grillo, and M. Lusignoli. Phys. Lett. B **29** 423 (1969).
2. F. Drago, and A.F. Grillo. Nuovo Cimento A **65**, 695 (1970).
3. S. Ferrara, A.F. Grillo, and R. Gatto. **2**, 1363 (1971) .
4. S. Ferrara, R. Gatto, and A.F. Grillo, Nucl. Phys. B **34**, 349 (1971) .
5. S. Ferrara, A.F. Grillo, and R. Gatto, Nuovo Cimento A**12,** 959 (1972).
6. S. Ferrara, R. Gatto, and A.F. Grillo, *Springer Tracts in Modern Physics* **67**, 1 (1973).
7. S. Ferrara, A.F. Grillo, and R. Gatto, Ann. Phys.**76** 161 (1973).
8. S. Ferrara, R. Gatto, and A. Grillo, Phys. Rev. D 9, 3564 (1974).

9. S. Ferrara, A.F. Grillo, G. Parisi, and R. Gatto, Lett. Nuovo Cimento **4** 115 (1972).

10. S. Ferrara, A.F. Grillo, G. Parisi, and R. Gatto, Nucl. Phys. B **49** 77 (1972).

11. A.F. Grillo, Riv. Nuovo Cimento **3**, 146 (1973).

12. A.A. Belavin, A.M. Polyakov, and A.B. Zamolodchikov. Nucl. Phys. B **241**, 333 (1984).

13. S. El-Showk, M.F. Paulos, D. Poland, S. Rychkov, D. Simmons-Duffin, and A. Vichi, Phys. Rev. D **86**, 025022 (2012) .

14. M. Greco and A.F. Grillo. Lett. Nuovo Cimento **6**, 174 (1976).

15. A.F. Grillo and Y. Srivastava. Nucl. Phys. B **187**, 271 (1981).

16. A.F. Grillo A.F. and Y. Srivastava. Lett. Nuovo Cimento **36**, 579 (1983).

17. V. Azcoiti 1, J.L. Cortes, A. Tarancon, G. Di Carlo, A.F. Grillo, Z. Phys. C **47**, 247(1990).

18. V. Azcoiti, G. Di Carlo, and A.F. Grillo. Phys. Lett. B **238**, 355 (1990).

19. V. Azcoiti, V. Laliena, X.Q. Luo, C.E. Piedrafita, G. Di Carlo, A. Galante, A.F. Grillo, L.A. Fernandez, and A. Vladikas, Phys. Rev. D **48**, 402(1993).

20. G. Giacomelli and A. Margiotta, arXiv:0707.1691(2007).

21. M. Ambrosio, et al. Astroparticle Physics **4**, 33 (1995).

22. Auriemma, G., H. Bilokon, and A.F. Grillo. Il Nuovo Cimento C **9**, 451 (1986).

23. S. Ahlen et al. Phys. Rev. D **46**, 895 (1992).

24. M. Ambrosio et al. Phys. Lett. B **434**, 451 (1998).

25. J.M. Abraham et al. Nucl. Instr. and Meth. A,**523**, 50 (2004).

26. S.Y. BenZvi et al. Nucl. Instr. and Meth. A, **574**, 171 (2007).

27. S.Y. BenZvi et al. arXiv preprint arXiv:0706.3236 (2007).

28. A. Aab et al. J. Cosm. Astro. Phys., **4**, 9 (2017).

29. A. Aab et al. J. Cosm. Astro. Phys., **6**, 26 (2017).

Frascati Physics Series Vol. 66 (2018)
Frontier Objects in Astrophysics and Particle Physics
May 20-26, 2018

GRAVITY AND GRAVITATIONAL WAVES

M. Alessandra Papa
Max Planck Institut f. Gravitationsphysik, Callinstrasse 38, 30167 Hannover, Germany
U. of Wisconsin, Milwaukee, USA

Abstract

The first gravitational wave detections have opened a new window on the Universe. Full of excitement and curiosity we are now taking the first baby-steps in this new field.

1 Newton and Einstein

The opening talk on gravity at a meeting like this one cannot but begin by mentioning Newton and his Philosophiae Naturalis Principia Mathematica, where the universal law of gravitation first appeared: two masses M and m at a distance R experience a mutually attractive force equal to $\frac{GMm}{R^2}$. Newton recognised that this is the force that is responsible for objects falling to the ground as well as for the moon orbiting around the Earth, and the Earth around the Sun.

Newton's law implies an action taking place instantaneously at all distances between the masses. Newton rejected this criticism in the second edition of the Principia (1713) by arguing his famous "hypotheses non fingo" , i.e. that his law well described certain physical phenomena but was never intended to make any reference to how/why those happen the way that his law predicts.

The next paradigm shift came nearly 230 years later, with the General Theory of Relativity. The new theory describes gravity in terms of the geometry of space-time, influenced by the masses in it and at the same time determining their motion. No information can travel faster than the speed of light, the theory postulates, so even the information on changes in the gravitational field brought about by a changing mass distribution have to propagate. In Newtonian gravity the masses carry around the gravitational field rigidly with them, in every point of space, even very far away. In Einstein's theory gravity is not an instantaneous condition, it propagates. For this reason gravitational waves are an essential prediction of general relativity.

The gravitational field equations, in their covariant form, are deceiptfuly simple:

$$G_{\mu\nu} = \frac{8\pi G}{c^4} T_{\mu\nu}. \tag{1}$$

On the left hand side is the gravitational field, described by $G_{\mu\nu}$ which is a function of the space-time metric, and on the right hand side the mass-energy tensor $T_{\mu\nu}$, which contains the information about the sources of gravitational field. The equations 1 are actually complex, because they are non-linear differential equations in the metric and exact solutions can be found only in particular cases. Furthermore, in order to extract predictions on physical quantities these equations have to be projected in the appropriate observers' reference frame and coordinate system, and a number of degrees of freedom have to be set with suitable choices of gauge.

2 Gravitational Waves

Gravitational waves are solutions of the linearised field equations. They are transverse and described by two polarisations, typically denoted as "+" and "x" because of the relative orientations of the deformation patterns, as shown in Fig. 1.

Even though Einstein published a paper predicting gravitational waves

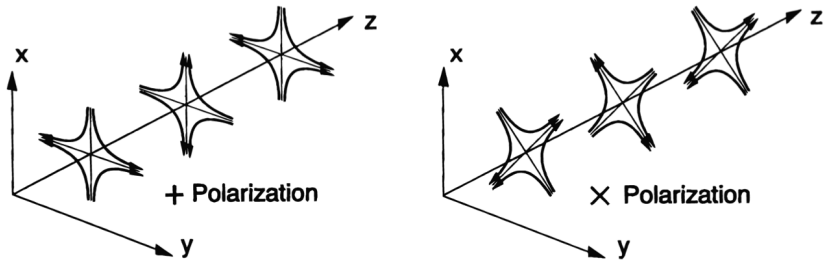

Figure 1: *Deformation patterns induced by the two gravitational wave polarisations, for waves propagating in the z-direction.*

a few months after original presentation of the Theory of General Relativity[1], in the years, he himself became unconvinced that these were actually a real physical phenomenon. The discussion on this topic lasted over 30 years and involved some of the most eminent scientists of those times. In fact, in the 1920s Einstein, Rosen and Eddington, in conversations with Bohr and Schwarzschild, convinced themselves that gravitational waves were not real. In 1936 Einstein and Rosen submitted a paper to Physical Review where they stated that gravitational waves did not exist. The paper was withdrawn when the editor asked Einstein and Rosen to address the comments of the referee (Robertson) who had raised doubts on the correctness of the main result. About a decade later, thanks to the "intellectual mediation" of Infeld, Einstein reconsidered the issue and concluded that Robertson was indeed right [1)]. In 1956 Pirani also reached the same conclusion. But it was only in 1957 that the controversy was settled for good.

In 1957 a conference took place at Chapel Hill, which turned out to be of pivotal importance for gravitational waves. The occasion was the foundation of a new institute, the Institute of Field Physics , thanks to the donation of Mr. Babson. Mr. Babson was a very wealthy business man, who held unorthodox views about how markets worked. Apparently he was convinced that his success was due to having applied to the markets the concept of "what

[1]The correct version however followed two years later, in 1918.

goes up must come down", from Newton's law of gravity, and hence felt that he owed "gravity" his good fortune and was eager to pay back. At the same time, probably due to a family tragedy, the drowning of his sister at a young age, he was obsessed with trying to control gravity and wanted to support research in this direction. For these reasons he had founded the "Gravity Research Foundation" and held an annual research-essay contest with the title "finding ways to control the force of gravity". In 1953 Bryce DeWitt won the essay competition. In his essay he pointed out that the field was not striving and, in order to make progress, young scientists should be encouraged to devote themselves to the study of gravity. Babson was enthusiastic about the proposal and deiced to create an institute solely devoted to the study of gravity, with DeWitt directing it.

During the Chapel Hill conference the inaugural ceremony for such institute was held. In order to attract attention and give credibility to this new endevour, the greatest names in physics at the time were invited. Feynman was among the participants and he presented the conclusive argument supporting the physical reality of gravitational waves. The heart of the "sticky bead argument", as his argument is commonly referred to, shows how a passing gravitational wave can release energy in an external system, for example by heating it, hence proving that gravitational waves do indeed carry energy [3]. A first version on this argument had been previously made by Pirani and a detailed case followed by Bondi and Weber and Wheeler [4].

3 The dawn of gravitational wave experiments

The pioneer of gravitational wave detection experiments is Joe Weber who build the first gravitational wave detectors at the University of Maryland in the 1960s (Fig. 3). His detectors were large metal cylinders, whose fundamental longitudinal mode would be excited by the energy deposited by an impinging gravitational wave. The oscillations of the mode were recorded in these first bars by piezoelectric ceramics. The bars were sensitive in a narrow frequency band, of order of a Hz, around the resonant modes of the coupled system bar + transducer, typically a about 900 Hz. Many groups followed in Weber's steps, in America (New Jersey, Yorktown Heights, Stanford, Louisiana and Rochester in the USA and Regina in Canada), in Europe (Bristol, Glasgow and Reading-Rutherford Lab in the UK, Rome/CERN, Legnaro in Italy, Munich in Germany,

Figure 2: *Weber and his resonant bar detector (credit: Special Collections and University Archives, University of Maryland Libraries)*

Meudon in France), in Russia (Moskow), in Japan (Tokyo), China (Guangzhou and Beijing) and in Australia (U. Western Australia).

Later versions of Weber's bar operating in the 90s were significantly more sensitive than the first ones and operated as a network combining the results of their analyses, but they were not able to corroborate any of the detection claims made by Weber [5, 6]. However the field was kept alive and virtually all of the bar-detector groups active twenty-five or thirty years ago are now deeply involved in the current gravitational wave detection efforts. Interestingly it was a former PhD student of Weber's, Robert Forward, who built the first interferometric antenna [7].

Failure to detect gravitational waves with bars already in the 1970s inspired visionary scientists, among whom Brillet and Weiss [9], to pursue alternative routes. The principle of operation of gravitational wave interferometric detectors is simple: laser light is split in two orthogonal beams and it is reflected back after having traveled a few kilometers. When it is recombined, the two beams interfere destructively unless a gravitational wave has altered the path traveled by the two beams. The idea dates back to Pirani and was proposed independently by several.

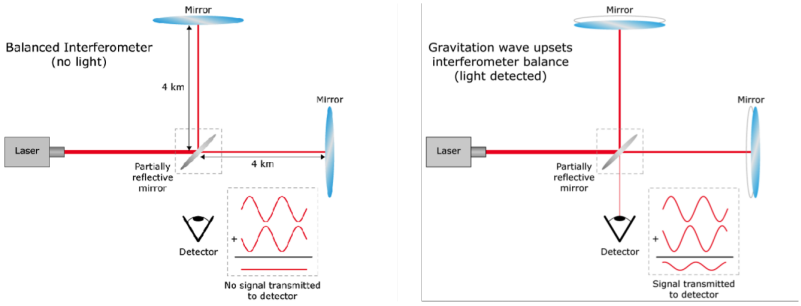

Figure 3: *Principle of detection for a gravitational wave interferometer. Credit: M. Goldman/M.Gerhardt, SITNBoston, Harvard U.* [8].

1974 is an important year because Hulse and Taylor discovered the J1913+16 binary pulsar system (J1913+16-1975). In 1979 their paper demonstrated that the observed spin-down of the orbital period of this system was consistent the loss of energy due to gravitational wave emission [11].

In 1975 Rai Weiss and Kip Thorne, both attending a NSA meeting, find themselves sharing a hotel room in Washington. They spend the night talking about prospects for gravitational wave detection, and emerge convinced that the times are ripe for setting up a large interferometric detector. Shortly after, an experimental effort begun at Caltech.

In 1989 Caltech and MIT put forward a proposal to the National Science Foundation for the construction, operation and supporting research and development of a laser gravitational wave observatory [13].

The pivotal meeting for the Virgo detector happened in 1985, and it was between Giazotto and Brillet during a Marcel Grossmann meeting in Rome. Giazotto had presented his proposal to use super-attenuators to reduce seismic noise in a gravitational wave detector, while Vinet (a colleague of Brillet) showed how Drever's power recycling technique could be utilised to decrease the laser power needed by instruments. In 1989 a proposal for construction and operation of Virgo was put forward to the French CNRS and the Italian INFN. The joint approval process, by two completely independent national funding agencies, was longer compared to that of LIGO, but it came through in 1993/1994. In 2000 the European Gravitational Observatory (EGO) was

created to manage this joint facility.

4 The first generation LIGO and Virgo

The high sensitivity bandwidth of these detectors extends between a few tens of Hz to about 1500 Hz. Emission mechanisms that give rise to signals with significant energy content in this frequency range involve ms to tenths of seconds time scales. These timescales typically involve very compact objects moving very fast: neutron stars and black holes are the prime targets of interferometric gravitational wave detectors. Signals are expected from the inspiral and merger of such systems, from supernova collapse to neutron star or black hole, from rapidly spinning non axi-symmetric neutron stars and also from the superposition of many individually unresolvable signals giving rise to a stochastic background.

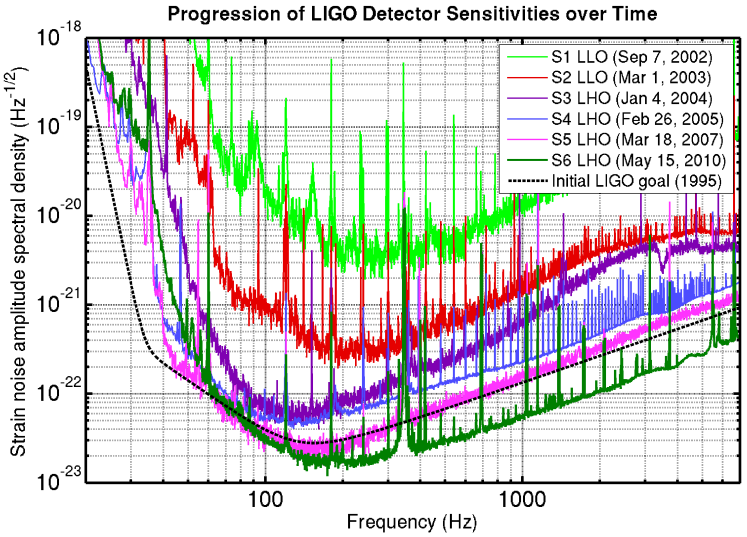

Figure 4: *Detector noise as a function of frequency for the various science runs (indicated as S1, S2, ... S6) of the 1st generation LIGO. Credit: (credit: LIGO Lab [14]).)*

Searches for all these signals have been carried out systematically throughout the operations of the LIGO and Virgo interferometric detectors, as a joint network. The first generation of these comprised six science runs between 2001 and 2010, with progressive sensitivity improvements of over two orders of magnitude (in Fig 4 for illustration I show the sensitivity improvements of LIGO). In spite of these impressive results no gravitational wave detection was made. Albeit still consistent with the standard stellar evolution scenarios, the pressure was mounting and in Fall 2010 the gravitational wave community entered the dark ages: a period of ~ 4 and a half years with no new data, during which the detectors would undergo a major upgrade and come back online, after periods of commissioning, in the *final advanced detector configuration* with a factor of ~ 10 higher sensitivity.

5 GW150914

September 14th 2015 15:0 UTC was the time chosen for the start of the 1st observing run of the LIGO advanced detectors (O1). As it is customary, each observing run is preceded by a series of engineering runs. For O1 the last engineering run had started in late August. With still a number of details to be ironed out, on September 11th the start of the run was postponed to September 18th and E8 was extended. With a stable and reliable calibration by September 12th, the detectors were hence kept operational as the remaining preparations were finalised. These included real-time data stream production and distribution, fake-signal hardware injections, low-latency data analyses, gravitational wave alerts and rapid-response procedures and environmental noise coupling studies.

On September 14th at 9:50 UTC a very loud gravitational wave signal hit the LIGO detectors and was very clearly detected by both. Over three years later, as I write this, I still get goose bumps. 9:50 UTC was 11:50 am in central Europe, 5:50 am on the US East coast and 2:50 am on the US West coast. In Hannover Germany, at my institute, the scientists on duty from the cWB (coherent waveburst pipeline) were watching the triggers produced by their online pipeline and they immediately recognised the interesting event. Within an hour emails had been sent to various LIGO mailing lists asking for cross-checks and confirmation that the recorded event was a fake signal injected during the preparations of the injection system. It was not. What they had

seen was the very first gravitational wave event ever detected.

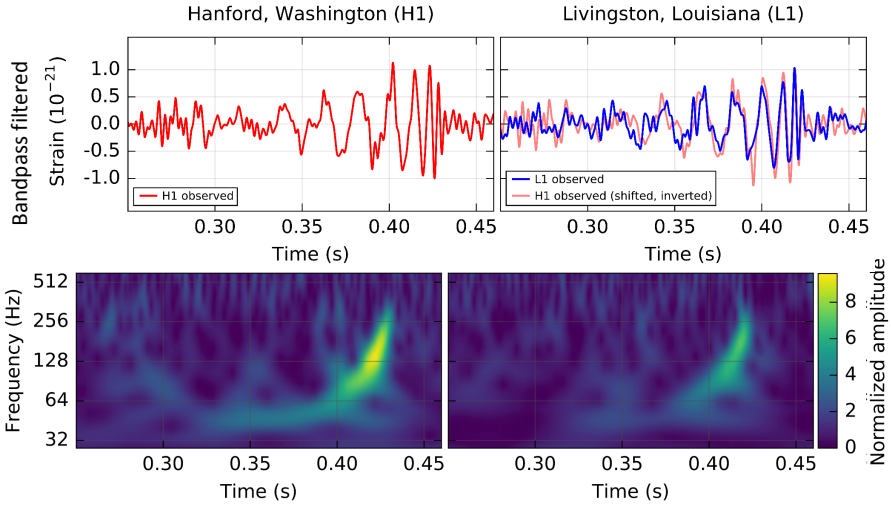

Figure 5: *Both these plots are taken from* [15]. *The top row shows the signal in the Hanford and Livingston LIGO detectors as a function of time. On the right-hand-side plot we see the two signals superimposed on each over, having shifted the Hanford one by about 6.9 ms, the light-travel time between the two detectors for the position of the gravitational wave source. The bottom row shows the energy content as a function of time and frequency in the detectors around the arrival time of GW150914. The signal chirp is clearly visible in both instruments. The noise level of the detectors at the time of GW150914 around 150 Hz was about* $8 \times 10^{-24}\ 1/\sqrt{Hz}$, *about a factor of 2 lower than the best sensitivity previously reached.*

The first gravitational wave detection was not only a milestone because it was the first direct observation of a gravitational wave, but also because it was the first direct observation of a binary black hole merger and because it proved the existence of stellar-mass black hole systems. The masses of the two black holes were 29 $M_\odot$ and 36 $M_\odot$, respectively. The distance of the system was estimated to be about 400 Mpc and the chance probability of the event lower than 1 in $\sim$ 200 000 years.

GW150914, as it was immediately named, was everything and more than the gravitational wave community could have hoped for, as a first detection: the detectors were well-behaved, there was no environmental disturbance, the signal was so strong that one could see it by eye in the raw data 5 and it beautifully matched the expected waveform. It took 4.5 months of crazy work, while the actual run was ongoing, to do all the possible conceivable checks to verify GW150914 and to write the historic paper [15]. I was one of the six scientists who had the honour of being the editors of such paper for the Collaborations. We set up a ticketing system and evaded over a thousand different tickets, reflecting the contributions of hundreds of LIGO/Virgo Collaboration members.

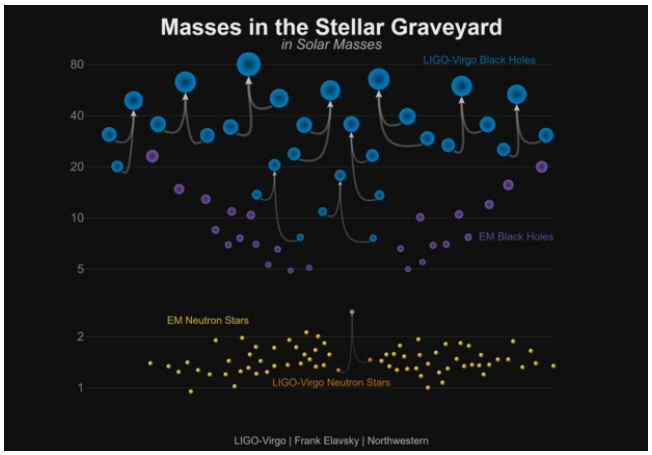

Figure 6: *Masses of observed black holes and binary neutron stars. Credit: LIGO/VIrgo/Northwestern Univ./Frank Elavsky.*

At the time of writing (end of 2018), ten binary black hole mergers have in all been observed [16], confirming the existence of a population of black

holes with masses between 10 $M_\odot$ and 70 $M_\odot$, see Fig. 6. All observations so far are consistent with the predictions of General Relativity, albeit the probing depth of the observations is still somewhat limited. With a factor $\gtrsim 10$ more detections it is likely that it will be possible to discern between different binary black hole formation and evolution scenarios. These measurements rely on estimates of the spins of the objects. Currently the observations slightly favour either small spin magnitudes or large misalignments between the spins and the orbital angular momentum, hence formation in globular clusters.

6 A new window on the Universe

23 months after GW150914, on the 14th of August 2017, the LIGO-Virgo network detected the merger of two neutron stars and was able to pin-point its location to within 28 deg^2 [17]. The independent detection of the gamma ray burst GRB170817A [18] in temporal coincidence with the gravitational wave event immediately flagged the event as very interesting. The slew of observations across the electro magnetic that followed, both in the immediate vicinity of GW170817 (see Fig. 7 and [19]) and on much longer time scales, confirmed the initial observations and propelled us all in the field of multi-messenger gravitational wave astronomy. The richness of these joint observations is evident and the number talks at this meeting on the topic is a testimony to this – I refer you to the contributions by M. Branchesi, A. Chieffi, C. Kopper, E. Troja, C. Fryer, H. Van Eerten, O Straniero, C. Gustavino, A. Corsi, P. Ubertini/L.Natalucci, G. Prodi and A. Chieffi.

Thanks to GW170817 it was possible to establish that neutron star mergers are responsible for short GRBs and that the processes that take place are well described by the kilonova model. In such model the emitted radiation is due to the radioactive decay of heavy r-process nuclei that are produced and ejected during the merger process. Observations on the longer time scale are useful to study the afterglow emission and understand the structure of the outflows, and hence the jet and the ejecta [20].

Neutron stars are objects whose interior we can only probe through gravitational wave observations. Different equations of state for the neutron star matter give rise to different tidal deformabilities. A larger tidal deformability translates into a larger deformation, an increased gravitational wave emission and a faster inspiral phase, so, broadly speaking, the tidal deformability is

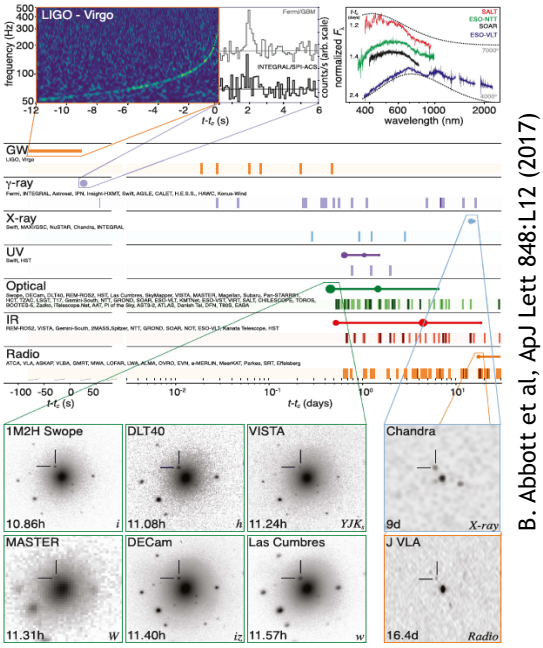

Figure 7: *This figure is taken from* [19] *and illustrates the rapid-response observations for the GW170817 event across the electro magnetic spectrum.*

a parameter that is directly encoded in the gravitational wave form from a neutron star inspiral. GW170817 set constraints on the tidal deformability of $\Lambda < 800$ or $\lesssim 500$, depending on the assumption on whether the neutron stars are assumed to have the same equation of state or not [21, 22].

7 The yet-to-be seen

A **stochastic background** of gravitational waves is expected both due to the superposition of astrophysical compact binary merger signals and to gravitational waves of primordial origin. The most recent search, encompassing not only the standard tensorial modes but also vector and scalar ones, sets 95% credibile upper limits, marginalized over spectral index, on the gravitational wave energy-density at the level of $\Omega_0^T = 5.6 \times 10^{-8}$, $\Omega_0^V = 6.4 \times 10^{-8}$ and

$\Omega_0^S = 1.1 \times 10^{-7}$ for the three modes respectively, at 25 Hz [24].

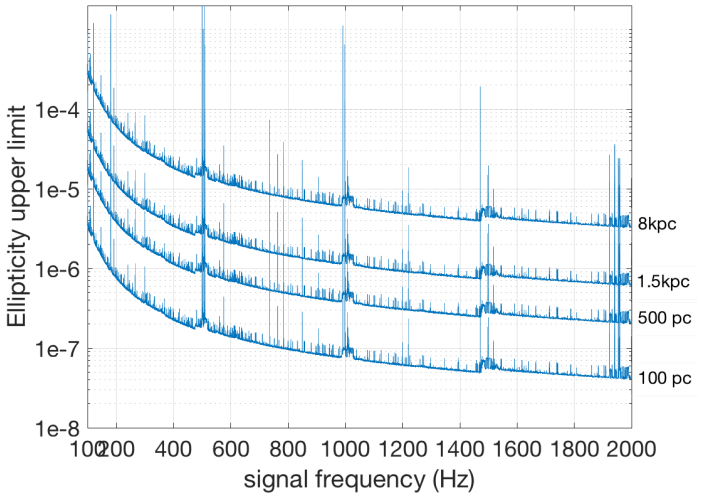

Figure 8: *Population-averaged upper limits on the source ellipticity from the Powerflux search of* [27]*, for sources at different distances.*

Non-tensorial polarizations could also be identified in the detection of **continuous gravitational waves** by rotating neutron stars. A search carried out on a sample of 200 known pulsars at twice the objects' rotating frequency did not reveal any non-tensorial emission [25]. A null result was also obtained while searching for tensorial gravitational waves at twice the spin frequency from a set of known pulsars [26]. The resulting gravitational wave amplitude upper limits constrain the ellipticity (relative deformation) to values as low as 1.3×10^{-8} for J0636+5129, at 200 pc and spinning at 607.12 Hz. Surveys for continuous gravitational waves from unknown neutron stars cannot detect signals as low as this: the number of waveforms that these surveys sample is very high – order 10^{17} – so the smallest signal amplitude that can be confidently detected is increased due to the trials factor by a factor of about 10. However these surveys probe a much larger population of sources (orders of magnitude more) compared to the known-pulsar searches, and potentially could reveal a

population of objects only accessible through their gravitational wave emission. The current most constraining wide-band gravitationa, wave amplitude upper limits are given in [27] and in Fig. 8 I show the corresponding 95% confidence upper limit ellipticity values.

8 The future

A gain factor of 10 in sensitivity, and the extension of the high sensitivity band to even lower frequency, is the goal for the next generation of detectors. With arm lengths of about 10 km, the next generation of detectors might be cryogenic and require underground facilities.

The next generation of detectors promises to tackle fundamental questions pertaining extreme gravity, the nature of compact objects and cosmology. A committee of international experts under the aegis of GWIC (Gravitational wave International Committee) is taking the first steps towards making the third-generation detectors that will "expand the reach of gravitational wave astronomy to the edge of the Universe" [28], a reality.

On a just slightly longer time scale we expect the space-based detector LISA to come online and open a window on the low-frequency gravitational wave sky. LISA science is about massive black holes, tracing their evolution, exploring stellar population and dynamics in active galactic nuclei, mapping extreme space-times with unprecedented accuracy, understanding the population of ultra-compact binaries in our Galaxy, and integrating all the observations in a coherent picture of the Universe and its evolution. The incredible success of the LISA Path Finder mission in February 2017 [29] that exceeded even the LISA science requirements goals, makes this ambitious plan seem closer than ever (see Dolesi's contribution at this workshop).

References

1. A. Einstein and N. Rosen, J. Frank. Inst. , **223**, 43-54, (1937).
2. https://www.gravityresearchfoundation.org
3. R.P Feynmann, (1961), not published but available in a letter to Weisskopf http://www.oac.cdlib.org/findaid/ark:/13030/kt5n39p6k0/dsc/?query=letter to Weisskopf 1961

4. H. Bondi, Nature, **179**, 1072-1073, (1957).

5. P. Astone *et al*, Phys. Rev. D. **68**, 022001 (2003).

6. P. Astone *et al*, Phys. Rev. D. **76**, 102001 (2007).

7. G. E. Moss, L. R. Miller and R.L. Forward, Appl. Opt, **10**, 2495 (1971).

8. `http://sitn.hms.harvard.edu/flash/2016/quest-gravitational-waves-pushes-boundaries-quantum-optics/`

9. R. Weiss, MIT Research Lab of Electronics Quarterly Progress Report, **105**, (1972).

10. R.A. Hulse and J.H. Taylor, Astrophys. J. Lett. **195**, L51-L53, (1975)

11. J.H. Taylor *et al*, Nature **277**, 437-440, (1979).

12. J.H. Taylor and J.M. Weinberg, Astrophys. J. **253**, 908 (1982).

13. R. E. Vogt, R.W.P. Drever, K.S. Thorne, F.J. Raab and R. Weiss (Caltech and MIT), "Construction, operation, and supporting research and development of a Laser Interferometer Gravitational-wave Observatory", proposal to NSF, (1989).

14. `https://labcit.ligo.caltech.edu/ jzweizig/distribution/LSC_Data/`

15. B.P. Abbott *et al*, Phys. Rev. Lett. **116** (6), 061102 (2016).

16. B.P. Abbott *et al*, arXiv:1811.12907

17. B.P. Abbott *et al*, Phys. Rev. Lett. **119**, 161101 (2017).

18. B.P. Abbott *et al*, Astrophys. J. **848**, (2), L12, (2017).

19. B.P. Abbott *et al*, Astrophys. J. **848**, (2), L13, (2017).

20. G.P. Lamb *et al*, arxiv:1811.11491 (2018).

21. B.P. Abbott *et al*, Phys. Rev. Lett. **121**, 16, 161101 (2018).

22. S.De *et al*, Phys. Rev. Lett. **121**, 16, 091102 (2018).

23. B.P. Abbott *et al*, Phys. Rev. Lett. **120**, 9, 091101 (2018).

24. B.P. Abbott *et al*, Phys. Rev. Lett. **120**, 20, 201102 (2018).

25. B.P. Abbott *et al*, Phys. Rev. Lett. **120**, 3, 031104 (2018).

26. B.P. Abbott *et al*, Astrophys. J. **839**, (1), 12, (2017).

27. B.P. Abbott *et al*, Phys. Rev. Lett. **97**, 10, 102003 (2018).

28. https://gwic.ligo.org/3Gsubcomm/

29. M. Armano*et al*, Phys. Rev. Lett. **116**, 231101 (2016).

30. A.H. Nitz *et al*, arXiv:1811.01921

Frascati Physics Series Vol. 66 (2018)
Frontier Objects in Astrophysics and Particle Physics
May 20-26, 2018

THE DAWN (and perspectives) of GRAVITATIONAL WAVE ASTRONOMY

V. Fafone
University of Rome Tor Vergata and INFN Roma Tor Vergata unit

Abstract

The first direct detection of gravitational waves by the LIGO and Virgo Collaborations on September 14^{th}, 2015, opened a new window to explore the Universe. Because of their extremely weak interaction with matter, gravitational waves can in fact bring us information from the innermost regions of compact objects and, after travelling cosmological distances without relevant interactions, can reveal features of their sources unaccessible to electromagnetic radiation or neutrinos. In the following, I'll give an overview of the state of the art of gravitational wave science and of its perspectives in the forthcoming years.

1 Introduction

Efforts to detect gravitational waves (GWs) made a decisive step with the construction of second generation interferometric detectors, the advanced versions

of the km baseline ground-based instruments. At the same time, progress in relativistic astrophysics and numerical relativity have improved our understanding of expected amplitudes and rates of a number of classes of GW signals.

The upgrades of LIGO and Virgo to their advanced configurations started in 2008 and 2011 respectively, with the goal of improving the sensitivity by a factor of 10 in the Hz-kHz frequency band with respect to initial detectors, thus increasing the volume of observable Universe and the rate of detectable sources by a factor of a thousand.

This requirement was motivated by the extremely small effect to be measured: the GWs from a stellar mass binary black hole (BBH) coalescence produces a fractional length change in the arm of a km-scale interferometer of less than 10^{-21} by the time it reaches Earth.

The path to the construction of the Advanced LIGO [1)] and Advanced Virgo [2)] GW detectors is indeed the story of decades of effort by hundreds of scientists and engineers, developing the technology required to measure space-time strains of 10^{-21}. This achievement has been possible thanks to a challenging R&D program planned to mitigate the noise sources affecting the detector at different frequency ranges, from about 10 Hz up to a few kHz. The design performances will be reached through a number of incremental steps characterised by increasing sensitivity (and increasing instrumental complexity).

The first observing run (O1) of Advanced LIGO, took place from September 12^{th}, 2015 until January 19^{th}, 2016 and, with the contribution of the worldwide LIGO Scientific Collaboration and the Virgo Collaboration, marked the first detections of GWs from stellar-mass (BBHs) [3, 4, 5, 6)]. The second observing run (O2) started on November 30^{th}, 2016 after an upgrade and commissioning period of the Advanced LIGO detectors. On August 1^{st}, 2017 Advanced Virgo joined the observing run, thus enabling the first three-detector observations of GWs. The three interferometers collected about 15 days of triple coincidence data till the end of O2 on August 25^{th}, 2017. At present the three detectors are undergoing a commissioning phase to further increase their sensitivity with respect to the O2 performances and are expected to restart data taking in April 2019.

2 GW150914: the first detection and its scientific outcomes

The Advanced LIGO detectors, on September 14$^{\text{th}}$ 2015 at 09:50:45 UTC, reported the coincident observation of a signal, initially detected by a low-latency search for generic GW transients [7]. The signal reached first Livingston and, after about 6.9 ms, arrived at Hanford. The signal was then analysed with a matched-filter, constructed from relativistic models of compact binary objects [5] and found to be the most significant event in each detector in the first part of the observing run, with a combined signal-to-noise ratio (SNR) of 24 [8]. The time evolution of GW150914 suggested that this signal has been produced by the coalescence of a BBH system: the inspiral and merger, and subsequent final black hole ringdown. In about eigth cycles, lasting 0.2 seconds, the frequency increases from 35 to 150 Hz, where also the amplitude is maximum. The evolution of two inspiralling masses, m_1 and m_2, is characterized by the chirp mass [9]:

$$M_c = \frac{(m_1 m_2)^{3/5}}{(m_1 + m_2)^{1/5}} = \frac{c^3}{G}\left[\frac{5}{96}\pi^{-8/3} f^{-11/3}\dot{f}\right]^{3/5} \quad (1)$$

where G and c are the gravitational constant and the speed of light; f and $\dot{f}$ are the observed frequency and its time derivative and can be both estimated from the data. This gives a result of $M_c \simeq 30$ M$_\odot$, which implies that, in the detector frame, the total mass $M = m_1 + m_2$ is larger than 70 M$_\odot$.

To evaluate the source parameters, general relativity-based models have been used [10, 11, 12, 13], in some cases including also spin precession, and,

Table 1: Source parameters for GW150914, given in the source frame; to convert to the detector frame multiply by $(1+z)$ [18] . The evaluation of the source redshift assumes standard cosmology [19].

Primary black hole mass	36^{+5}_{-4} M$_\odot$
Secondary black hole mass	29^{+4}_{-4} M$_\odot$
Final black hole mass	62^{+4}_{-4} M$_\odot$
Final black hole spin	$0.67^{+0.05}_{-0.07}$
Luminosity distance	410^{+160}_{-180} Mpc
Source redshift z	$0.09^{+0.03}_{-0.04}$

for each model, a coherent Bayesian analysis has been performed to derive the distributions of the source parameters [14], discussed in detail in [15] in the source frame. The uncertainties include statistical and systematic errors deriving from the average of the results of different waveform models. Using the fits to numerical simulations of BBH mergers provided in [16, 17], the mass and spin of the final black hole, the total energy radiated in GWs, and the peak GW luminosity [15] have been computed. The total energy estimated to be radiated in gravitational waves is $3.0^{+0.5}_{-0.5}$ $M_\odot c^2$, and the peak gravitational-wave luminosity has been $3.6^{+0.5}_{-0.4} \times 10^{56}$ erg/s, equivalent to 200^{+30}_{-20} $M_\odot c^2$/s.

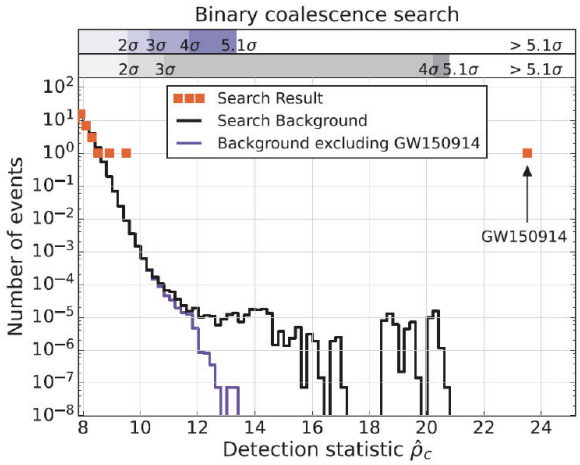

Figure 1: Search results from the binary coalescence search. Figure from [3].

Sixteen days of coincident observations between the two LIGO detectors, from September 12$^{\text{th}}$ to October 20$^{\text{th}}$, 2015, have been analysed to assess the statistical significance of GW150914.

The background for the search class of GW150914 is shown in Figure 1. The histogram shows the number of candidate events (orange markers) and the mean number of background events (black lines) in the search class where GW150914 was found. The scales on the top give the significance of an event in Gaussian standard deviations based on the corresponding noise back-

ground. The tail in the black-line background is due to random coincidences of GW150914 in one detector with noise in the other detector. The purple curve is the background excluding those coincidences.

2.0.1 Tests of General Relativity

The detection of GW150914 provided an unprecedented opportunity to study the motion of a compact binary system in the large velocity, highly nonlinear regime, and to observe the final merger of the binary and the excitation of relativistic modes of the gravitational field. Several investigations have been carried on to determine whether GW150914 is consistent with the merger of a BBH system in general relativity [20].

The first consistency check performed concerns the mass and spin of the final black hole. In the general relativity framework, the product of a BBH coalescence is a Kerr black hole, completely described by its mass and spin. For this family of inspirals, these quantities can be evaluated with Einstein's equations and are a function of the masses and spins of the progenitor black holes. Using the relations between the initial black holes and final black hole masses and spins evaluated through numerical relativity simulations [16], the estimates of the final mass and spin obtained from the low-frequency part of the waveform have been compared to those retrieved from the high-frequency component of the waveform. The test of the inspiral-merger-ringdown consistency showed no evidence of discrepancies with the predictions of general relativity.

Within the post-Newtonian formalism, the phase of the gravitational signal during the inspiral can be expressed as a power series in $f^{1/3}$. The values of these coefficients can also be computed in general relativity. Thus, a test of consistency with general relativity [21, 22] can be performed. The coefficients have been made to deviate from the nominal values and it has been checked whether the resulting waveform was consistent with the data. Thus, empirical bounds on several high-order post-Newtonian coefficients have been determined in the dynamical regime [20].

Finally, the data from GW150914 have been used to constrain the Compton wavelength of the graviton, λ_g. General relativity assumes massless gravitons that travel at the speed of light $v_g = c$. On the contrary, if the graviton has a (small) mass, the dispersion relation becomes $E^2 = p^2c^2 + m_g^2c^4$, where E is the energy, p the momentum, and m_g is the graviton rest mass related to its

Compton wavelength as $\lambda_g = h/(m_g c)$, where h is the Planck constant. Thus, the ratio v_g^2/c^2 becomes equal to $c^2p^2/E^2 = 1 - h^2c^2/(\lambda_g^2 E^2)$, and a massive graviton would propagate at a speed dependent on energy (or frequency). Or, in other words, the lower frequencies propagate slower compared to higher frequencies. This dispersion can be included in the phase of the GW signal from a coalescing binary as $\Phi_{MG} = -(\pi D c)/[\lambda_g^2(1+z)f]$, where z is the redshift and D a cosmological distance defined in [23]. The signal from GW150914 shows no evidence for dispersion, thus it has been possible to constrain the Compton wavelength of the graviton to be $\lambda_g > 10^{13}$ km, which is equivalent to a bound on the graviton mass $m_g < 1.2 \times 10^{-22}$ eV/c^2 at 90% confidence level. This observation improves the Solar System bound [24] by a small factor and that from binary pulsar observations [25] by a factor of a thousand.

To summarize, all these tests are consistent with general relativity in the strong-field regime.

2.0.2 Astrophysics with GW150914

This observation provided the first robust confirmation of several theoretical predictions: "heavy" black holes do exist, binary black hole systems form in nature and merge within the age of the Universe at a detectable rate [26]. Two main types of formation models, involving isolated binaries in galactic fields [27] or dynamical interactions in young and old dense stellar environments [28], predict such mergers. The progenitor black holes of the GW150914 coalescence are more massive than those in known XRBs with reliably measured masses: this discovery provided the most robust evidence for the existence of "heavy" ($\geq$25 $M_\odot$) stellar-mass black holes. It also implies relatively weak massive-star winds and thus the formation of GW150914 in a low-metallicity environment [29]: below $\simeq 1/2$ $Z_\odot$ and possibly below $\simeq 1/4$ $Z_\odot$. The rate of BBH mergers inferred from this observation is consistent with the higher end of rate predictions ($\geq$1 Gpc^{-3} yr^{-1}) from both types of formation models. The low measured redshift ($z \simeq 0.1$) and the low inferred metallicity of the stellar progenitors imply two different scenarios for the formation of BBH systems:

- in a low-mass galaxy in the local Universe and a prompt merger;
- at high redshift with a time delay between formation and merger of the order of several Gyr.

3 GW170814: the first triple black hole binary detection

During the second observing run O2, on August 14^{th}, 2017, GWs from the coalescence of two black holes at a luminosity distance of 540^{+130}_{-210} Mpc, with masses of $30.5^{+5.7}_{-3.0}$ $M_\odot$ and $25.3^{+2.8}_{-4.2}$ $M_\odot$, were observed in the LIGO and Virgo detectors [30].

Until Advanced Virgo became operational, typical GW position estimates were highly uncertain compared to the fields of view of most telescopes. The baseline formed by the two LIGO detectors allowed a localization of mergers events to roughly annular regions spanning hundreds to about a thousand square degrees at the 90% credible level [31, 32]. Virgo adds additional independent baselines, which in cases such as GW170814 can reduce the positional uncertainty by an order of magnitude or more [33]. In fact, with a network of three detectors, sky position can be inferred by triangulation employing the time differences [34, 35], phase differences, and amplitude ratios on arrival at the sites [36].

An initial rapid localization was performed by coherent triangulation of the matched-filter estimates of the times, amplitudes, and phases on arrival [37]. The localization was then progressively refined by full coherent Bayesian parameter estimation [14], using more sophisticated wave-form models and treatment of calibration systematics.

The localization of GW170814 is shown in Figure 2. For the rapid localization from Hanford and Livingston, the 90% credible area on the sky is 1160 deg^2 and shrinks to 100 deg^2 when including Virgo data. The full parameter estimation further constrains the position to a 90% credible area of 60 deg^2 centered at the maximum a posteriori position of right ascension RA=$03^{\text{h}}11^{\text{m}}$ and declination dec=-44°57^{m} (J2000). The shift between the rapid localization and the full parameter estimation is partly due to the noise removal and final detector calibration, that was applied for the full parameter estimation but not for the rapid localization. Incorporating Virgo data also reduces the luminosity distance uncertainty from 570^{+300}_{-230} Mpc (rapid localization) to 540^{+130}_{-210} Mpc (full parameter estimation). The three-dimensional credible volume and number of possible host galaxies also decreases by an order of magnitude [38, 39], from 71×10^6 Mpc^3, to 3.4×10^6 Mpc^3, to 2.1×10^6 Mpc^3.

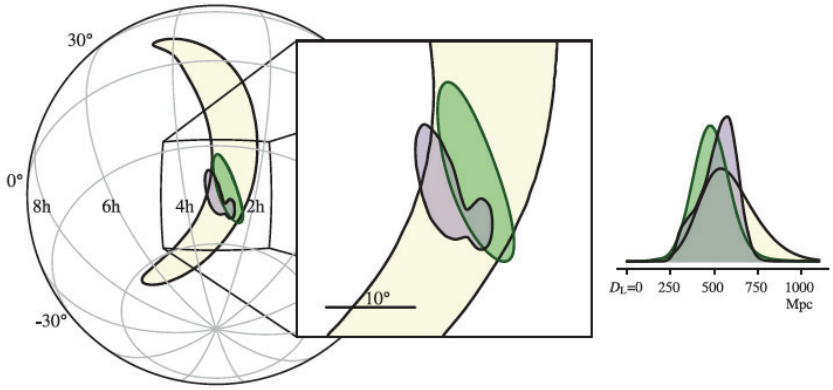

Figure 2: Localization of GW170814. Yellow region: rapid localization using data from the two LIGO sites. Green: localization with the inclusion of data from Virgo. Purple: full Bayesian localization. The contours represent the 90% credible regions. The inset on the right shows the posterior probability distribution for the luminosity distance, marginalized over the whole sky. Figure from [30].

In addition to previous General Relativity tests, the presence of Virgo allowed to probe the polarization content of the signal: a pure tensor polarization of the GWs was found to be favoured over pure vector or pure scalar polarization by a Bayes' factor of more than 200 and 1000, respectively [30].

4 GW170817: the binary neutron star detection and the birth of multimessenger astronomy

Three days after the detection of GW signal from the coalescence of binary black holes, on August 17$^{\text{th}}$, 2017 the LIGO-Virgo network witnessed a signal generated by the merger of two neutron stars [40]. Merely 1.7 seconds after the merger, NASA's Fermi satellite observed a Short Gamma Ray Burst called GRG170817A, an electromagnetic counterpart to the binary neutron star (BNS) merger [41]. This initiated a huge observational campaign which represents the first ever joint observation of gravitational and electromagnetic signals and marks the dawn of multimessenger astronomy [42]. The signal was clearly visible in the spectrograph of LIGO Livingston and Hanford. It lasted

for around 100 seconds unlike the previous BBH cases where signals lasted for around a second or less. The reason being that the masses of neutron stars are around one order of magnitude smaller that the black holes. Thus the merger occurs at higher frequencies and the signal evolves for a longer time in the sensitive bandwidth with a larger number of visible cycles. When the signal reaches frequencies visible in the LIGO detectors, neutron stars are around 100 km apart and orbit around each other around 12 times a second. As they spiral in due to the emission of GWs, both the frequency and amplitude of gravitational wave goes on increasing. The signal was absent Virgo because the arrival direction fell in one of the blind spots of the detector, which in turn played an important role in localizing the source in the sky and observing the electromagnetic counterpart.

The strength and shape of the signal which appears in the detector is dependent on many parameters associated with the source such as component masses of two colliding objects, stiffness of the matter they are made up of, luminosity distance and so on. Thus GW observations allows us to constrain those parameters. The masses of the two objects were determined to be about 1.17 and 1.6 solar masses. This is consistent with the masses of the neutron stars observed in our galaxy, while the masses of the black holes observed till date using both electromagnetic and gravitational wave observations are considerably larger. The distance to the source was calculated to be around 40 Mpc based on the GW signal, indicating the GRB occurred in nearby universe, around hundred times closer than the typical GRB. The GRB was found to be hundred to million times dimmer if compared with previous GRB observations. The possible reason for appearing sub-luminous might be explained with the viewing angle: since GRB‘s are beamed and not uniformly bright throughout the whole beam, with a brightness much lower towards the edge, viewing the GRB off-axis can account for its sub-luminous nature.

4.1 The observational campaign and the kilonova model investigation

Short duration GRBs were expected to be produced by the merger of two neutron stars, differently from long duration GRBs connected with the core collapse of massive rotating stars. The joint observation of GW17817 and GRG170817A provided the smoking gun confirmation that short GRB‘s are indeed associated with the collision of neutron stars.

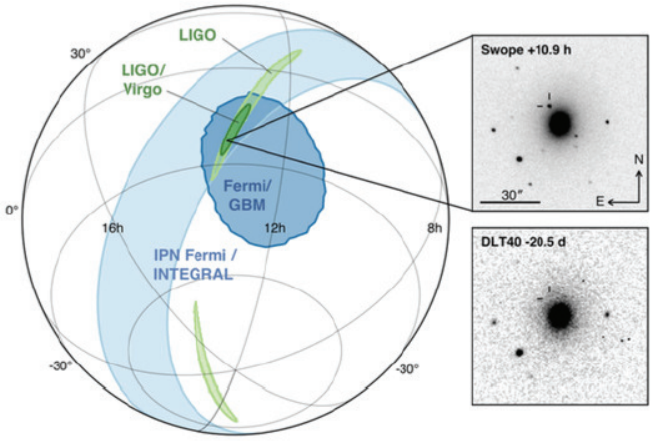

Figure 3: Localization of the gravitational-wave, gamma-ray, and optical signals. Right panels: discovery image taken 11 hours after the merger (top right) located in the host galaxy NGC 4993 and an image taken 20:5 days prior to merger (bottom right). Figure from [42].

Figure 3 shows the sky localization of the GW source by LIGO-Virgo and the localization of the GRB by Fermi and INTEGRAL. The light green patch shows the localization by LIGO, whereas the green patch shows the improved localization including the information provided by Virgo. The source is localized within an area of about 28 square degrees. Pale blue region shows the localization of the GRB by Fermi and INTEGRAL. There is a clear overlap between the two.The computed probability that the GW signal and the GRB are uncorrelated, while coinciding in space and time, is 1 over 20 millions.

In the three dimensional volume identified by Virgo and LIGO, around 49 galaxies can be listed, based on the galaxy catalogue of the local Universe. These galaxies were scanned one by one and optical transient dubbed as SSS17a was located in the galaxy NGC 4993 by the Swope telescope in Chile 10.9 hours after the merger. The optical counterpart shown in Figure 3 in the upper panel on the right is instead clearly absent in the image taken 20 days before (lower panel). A worldwide campaign was initiated to follow up this event spanning the entire electromagnetic spectrum, in UV, optical, IR, X and radio, with the

contribution of 70 ground-based and 7 space-based telescope facilities.

The first X-ray image was taken by NASA Chandra X-ray observatory 9 days later and the first radio image was taken by the Jansky Very Large Array 16 days after the merger. In the meanwhile, observations were made in UV, optical and IR, which monitored the spectral energy distribution and revealed the exceptional electromagnetic counterpart known as Kilonova, the expanding debris formed by the radioactive decay of the heavy elements synthesized in the neutron star collision.

The observation of the electromagnetic spectrum in the optical counterpart indeed provides signature of production of heavy elements such an gold, platinum and uranium. The amount of heavy elements produced during the neutron star merger is estimated to be around sixteen thousand times the mass of the Earth which, given a reasonable assumption on rate of mergers, could account for the heavy elements abundance.

4.2 Neutron star composition

Neutron stars are made up of cold super-dense matter at super-nuclear densities thus representing laboratories to test physics under such extreme conditions. Behaviour of matter is characterised by so called equation of state which is the relationship between various thermodynamic quantities such as density and pressure. Observations allow us to nail down the correct equation of state among those theoretically proposed. During the final stage of the inspiral, when the two objects are sufficiently close, neutron stars get distorted due to the strong gravitational field and produce a quadrupole moment which is proportional to the gradient of the gravitational field of companion star. The proportionality constant is referred to as tidal deformability which depends on the equation of state of the neutron star. The deformation of the neutron stars gets imprinted on the GW signal at the late inspiral stage. For this reason, studying the emitted GW can tell us about tidal deformability and allows to infer the equation of state of super-dense nuclear matter. GW170817 put interesting constraints on the tidal deformability, thus ruling out some of the previously proposed equations of state [40].

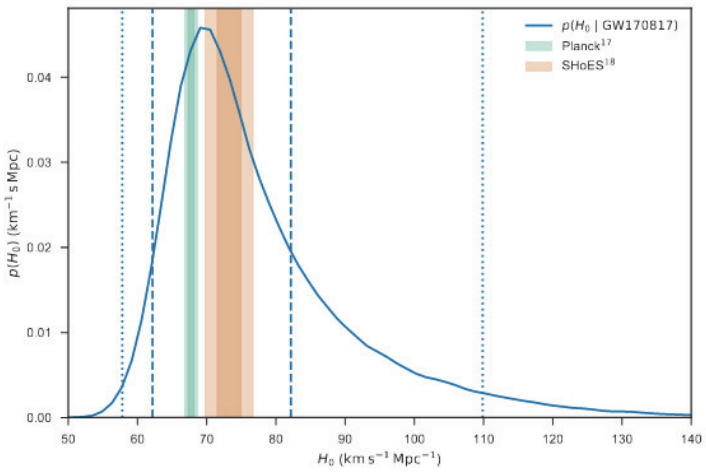

Figure 4: The error in the measurement occurs because the distance to the source as measured from the GW signal is degenerate with the inclination angle of the orbital plane of the neutron stars. The value of the Hubble constant inferred from GW170817 with relatively large error bars is consistent both with the standard candle and CMB measurements. Figure from [44].

4.3 Measurement of the Hubble parameter

Another good example of the implications of the first multimessenger observations in diverse areas of astrophysics is the independent estimate of the Hubble constant (H_0) which is enabled by identification of a counterpart and estimation of its redshift. GW sources are in fact standard sirens, i.e. they have a luminosity tied only to their distance and the intrinsic properties of the source, so that the luminosity distance can be measured from the emitted GWs alone [43]. Combined with a redshift measurement, this enables a novel measurement of H_0 [44]. Till GW170817 two independent approaches were used to measure the Hubble constant. One includes cosmic distance ladders wherein nearby distance indicators are used to calibrate the astronomical objects which can be in turn used to measure distances further into the Universe. The other makes use of the cosmic microwave background radiation. The two methods yield values of the Hubble parameter which differ by about 8%. This can be

seen in Figure 4 where the measurement of the Hubble parameter made with GW170817 is also shown. This tension could be solved in the future thanks to the very peculiar nature of GWs emitted by binary systems. Although with a single observation the measurement is still imprecise, it shows the potential for further developments as more sources are detected in the coming years [45].

The coincident observation of the GWs and the GRB emitted by the binary neutron star system also allowed to put constraints on the fundamental physics of gravity: speed of gravity, Lorentz invariance, tests of the equivalence principle through the Shapiro time delay and alternative theories of gravity which predict that GWs travel at a speed different from the speed of light [41].

5 Further O1 and O2 results

At the time of writing this report, all data collected in the two observing runs, O1 and O2, have been deeply reanalyzed with improved search algorithms in order to reevaluate the significance of previously identified GW events and to potentially discover new ones [46]. The searches identified a total of ten BBH mergers and one BNS signal. The GW events are identified as follows: GW150914, GW151012, GW151226, GW170104, GW170608, GW170729, GW170809, GW170814, GW170817, GW170818 and GW170823. The reanalysis of the O1 data did not result in the discovery of any new GW events, but GW151012 is now detected with increased significance. The analysis of the O2 data put in evidence four more events (GW170729, GW170809, GW170818 and GW170823) besides those already published.

In particular, the total mass of GW170729 has been estimated to be $85.1^{+15.6}_{-10.9} M_{\odot}$, making it the highest-mass BBH observed to date. GW170818 is the second BBH observed in triple-coincidence between the two LIGO observatories and Virgo after GW170814. As the sky location is primarily determined by the differences in the times of arrival of the GW signal at the different detector sites, LIGO-Virgo coincident events have a vastly improved sky localization, which is crucial for electromagnetic follow-up campaigns.

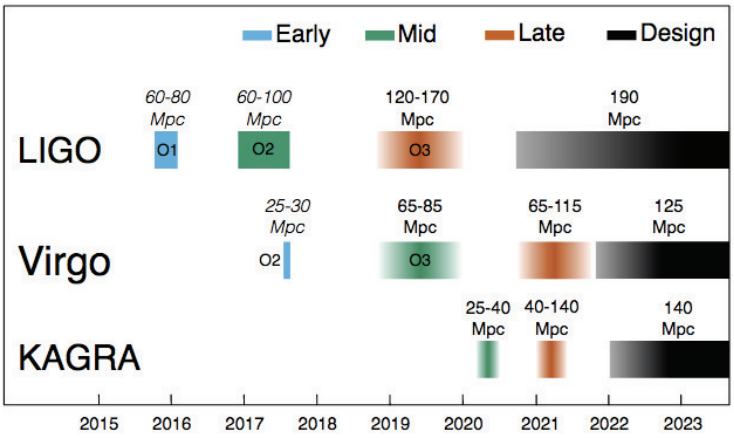

Figure 5: Planned sensitivity evolution and observing runs of Advanced LIGO, Advanced Virgo and KAGRA over the coming years. The colored bars show the observing runs, with the expected sensitivities for BNS detections. There is significant uncertainty in the start and end times of the planned observing runs, especially for those further in the future, and these could move forward or backwards relative to what is shown above. Figure from [48].

6 Future perspectives

The sensitivity of the advanced interferometers achieved during the first two runs has granted the detection of signals generated by the coalescence of binary systems. In addition to this category of GW source, others are expected to be investigated with this generation of detectors: stellar collapses and continuous emitters as asymmetric pulsars are potential new discoveries. In order to improve the performance of the present instruments, upgrades are already foreseen in the middle and longer terms. The "plus" versions of Advanced Virgo and Advanced LIGO will exploit at best the present infrastructures, by implementing solutions to decrease the most offending noise sources: thermal noise in the mirrors, quantum noise, newtonian noise. In the near future, also the Japanese interferometer KAGRA [47] will join data taking, thus strengthening the international network. In Figure 5, the planned sensitivity evolution for Advanced LIGO, Advanced Virgo and KAGRA is shown [48].

A further increase of the sensitivity of the ground-based interferometers requires changes in the infrastructures pushing toward a third generation detectors.

Einstein Telescope (ET) is one of the proposed 3G ground-based GW interferometers: it is currently under study by several scientific institutions in the European Union [49]. The key idea is to realize a new research infrastructure for the GW astronomy. The main features envisaged for ET are: arms longer than 10 km, built underground to limit the effect of the seismic noise and with mirrors cooled at low temperature to directly reduce the thermal vibration of the test masses.

In the US a group of researchers at MIT proposed the simplest approach to improve the sensitivity: building a new detector (LIGO 3G) [50] with increased arms' length, from 4 km of the existing detectors to 40 km. Other more sophisticated ideas are being studied.

All these proposals aim to allow the detection of GWs emitted by sources at cosmological distances and will provide facilities where even more sensitive detectors can be installed in the future by incorporating advanced technologies.

References

1. LIGO Scientific Collaboration, Class. Quantum Grav., **32**(7):074001 (2015).

2. Virgo Collaboration, Class. Quantum Grav., **32**(2):024001 (2015).

3. B. P. Abbott *et al* (LIGO Scientific Collaboration, Virgo Collaboration), Phys. Rev. Lett. **116**, 061102 (2016).

4. B. P. Abbott *et al* (LIGO Scientific Collaboration, Virgo Collaboration), Phys. Rev. Lett. **116**, 241103 (2016).

5. B. P. Abbott *et al* (LIGO Scientific Collaboration, Virgo Collaboration), Phys. Rev. D **93**, 122003 (2016).

6. B. P. Abbott *et al* (LIGO Scientific Collaboration, Virgo Collaboration), Phys. Rev. X **6**, 041015 (2016).

7. B. P. Abbott *et al*, Phys. Rev. D **93**, 122004 (2016).

8. S. A. Usman *et al*, Class. Quantum Grav. **33**, 215004 (2016).
9. L. Blanchet *et al*, Phys. Rev. Lett. **74**, 3515 (1995).
10. A. Taracchini *et al*, Phys. Rev. D **89**, 061502 (2014).
11. M. Purrer, Class. Quantum Grav. **31**, 195010 (2014).
12. M. Hannam *et al*, Phys. Rev. Lett. **113**, 151101 (2014).
13. S. Khan *et al*, Phys. Rev. D **93**, 044007 (2016).
14. J. Veitch *et al*, Phys. Rev. D **91**, 042003 (2015).
15. B. P. Abbott *et al*, Phys. Rev. Lett. **116**, 241102 (2016).
16. J. Healy *et al*, Phys. Rev. D **90**, 104004 (2014).
17. S. Husa *et al*, Phys. Rev. D **93**, 044006 (2016).
18. A. Krolak and B. F. Schutz, Gen. Relativ. Gravit. **19**, 1163 (1987).
19. P. A. R. Ade *et al*, Astron. Astrophys. **594**, A13 (2016).
20. B. P. Abbott *et al*, Phys. Rev. Lett. **116**, 221101 (2016).
21. C. K. Mishra *et al*, Phys. Rev. D **82**, 064010 (2010).
22. T. G. F. Li *et al*, Phys. Rev. D **85**, 082003 (2012).
23. C. M. Will, Phys. Rev. D **57**, 2061 (1998).
24. C. Talmadge *et al*, Phys. Rev. Lett. **61**, 1159 (1988).
25. L. S. Finn and P. J. Sutton, Phys. Rev. D **65**, 044022 (2002).
26. B. P. Abbott *et al*, ApJ Lett. **818**, L22 (2016).
27. V. Kalogera *et al*, Physics Reports **442**, 75-108 (2007).
28. S. F. Portegies Zwart and S. L. W. McMillan, ApJ Lett. **528**, L17 (2000).
29. K. Belczynski *et al*, Astrophysical Journal **714**, 1217 (2010).
30. B. P. Abbott *et al* (LIGO Scientific Collaboration, Virgo Collaboration), Phys. Rev. Lett. **119**, 141101 (2017).

31. M. M. Kasliwal and S. Nissanke, Astrophys. J. **789**, L5 (2014).

32. C.P.L. Berry *et al*, Astrophys. J. **804**, 114 (2015).

33. L. P. Singer *et al*, Astrophys. J. **795**, 105 (2014).

34. S. Fairhurst, New J. Phys. **11**, 123006 (2009); 13, 069602(E) (2011).

35. S. Fairhurst, Class. Quantum Grav. **28**, 105021 (2011).

36. P. Ajith and S. Bose, Phys. Rev. D **79**, 084032 (2009).

37. L. P. Singer and L. R. Price, Phys. Rev. D **93**, 024013 (2016).

38. L. P. Singer et al., Astrophys. J. 829, L15 (2016).

39. L. P. Singer et al., Astrophys. J. Suppl. Ser. 226, 10 (2016).

40. B. P. Abbott *et al* (LIGO Scientific Collaboration, Virgo Collaboration), Phys. Rev. Lett. **119**, 161101 (2017).

41. B. P. Abbott et al. (LIGO Scientific Collaboration and Virgo Collaboration), Astrophys. J. Lett. **848**, L13 (2017).

42. B. P. Abbott *et al*, ApJ Lett. **848**: L12 (2017).

43. Bernard F. Schutz, Nature **323**:310-311 (1986).

44. B. P. Abbott *et al*, Nature **551**:85-88 (2017).

45. Hsin-Yu Chen *et al*, Nature **562**, 545-547 (2018).

46. B. P. Abbott *et al* (LIGO Scientific Collaboration, Virgo Collaboration), arXiv:1811.12907 (2018).

47. Y. Aso *et al* (KAGRA Collaboration), Phys. Rev. D **88**(4):043007 (2013).

48. B.P. Abbott *et al* (KAGRA Collaboration, LIGO Scientific Collaboration and Virgo Collaboration), Living Rev. Relativ. **21**:3 (2018).

49. M. Punturo *et al*, Class. Quantum Grav. **27**, 194002 (2010).

50. S. E. Dwyer*et al*, Phys. Rev. D **91**, 082001 (2015).

Frascati Physics Series Vol. 66 (2018)
Frontier Objects in Astrophysics and Particle Physics
May 20-26, 2018

THE INITIAL MASS - REMNANT MASS RELATION AS A FUNCTION OF THE INITIAL MASS, METALLICITY AND ROTATION VELOCITY

Alessandro Chieffi
Istituto di Astrofisica e Planetologia Spaziali
via del fosso del cavaliere 100, 00133 Roma, Italy

Marco Limongi
Osservatorio Astronomico di Roma
via Frascati 33, 00078 Monte Porzio Catone (Roma), Italy

Abstract

We briefly discuss the competing phenomena that control which fraction of a massive star collapses in the remnant and which fraction is ejected in the interstellar medium. In particular we firstly remind the key evolutionary properties that determine the final Mass-Radius relation and then we discuss our current calibration of the explosion. Eventually we present our current predictions for the masses of the remnants as a function of the initial mass, metallicity and initial rotation velocity.

1 Introduction

Massive stars end their life with an explosion whose energy is provided, broadly speaking, by the gravitational energy released by the collapse of the innermost part of the star down to nuclear densities. A reliable determination of the

relation between the initial mass of a star and the mass of the remnant is of vital importance because it allows to establish the connection between a given population of massive stars and the variegate zoo of systems that involve compact remnants, like, e.g., pulsars, low and high mass X-ray binaries, magnetars ecc. Moreover, many nuclear species are synthesized in the very deep interior of a massive star so that an uncertainty in the mass of the remnant mass directly reflects on the prediction of the yields produced in the deepest part of a massive star. Unfortunately we cannot currently predict the masses of the remnants because we cannot reliably, and routinely, follow the explosion of a star from first principles. Therefore we are forced to rely on calibrations that obviously require at fit to some observational data. The most used ones are the kinetic energy of the ejecta or the amount of ^{56}Ni ejected. In the following we will briefly describe our current predictions for the initial mass-remnant mass relation and we will show that masses of black holes as larger as $35M_{\odot}$ (as detected by the gravitational observatories LIGO-Virgo for GW 150914) [1)] may be easily obtained in metal poor environments provided that the stars do not rotate significantly.

2 Discussion

The determination of the mass location that separates the remnant from the ejecta depends on the competition between the binding energy of the star and the outward moving shock wave generated by the collapse of the inner core. The run of the binding energy with the mass coordinate is the result of the hydrostatic evolution of the star that sculpts the final mass-radius (M-R) relation up to the onset of the collapse while the amount of energy gained by the shock wave depends on the fraction of neutrinos that return their energy to the star after having exited the neutrinosphere.

The final M-R relation (i.e. the binding energy) depends only on the hydrostatic evolution of the star and the main phenomena that contribute to sculpt this relation are the *instabilities*, thermal and/or rotation driven, plus mass loss. The first responsible for the final compactness of a star is the convective core in H burning because it basically determines the size of the key parameter that will drive all the following evolution, i.e. the He core mass. There are several phenomena that may affect the mass size of the convective core, the main ones being the efficiencies of a) the overshooting, b) the rotation

induced mixing and c) mass loss. A more effective overshooting and/or rotation induced mixing increase the He core mass while a more efficient mass loss reduces the size of the convective core (because it scales directly with the current mass of the star) and therefore the He core mass.

The second important instability that controls the final M-R relation is the extension and temporal evolution of the convective core in He burning. Also in this case the presence of some overshooting and/or induced mixing has the same effects already mentioned for the H burning, but now there is an additional product of the He burning that significantly affects the final M-R relation: the amount of ^{12}C left by the He burning in the Carbon Oxygen core. This is very important because it determines the efficiency of the C burning and its ability in advancing in mass. In fact, the lower the ^{12}C concentration at the central He exhaustion, the faster the advancing - in mass - of the C burning shell (because the shell has less fuel to burn in its way out but also because the formation of convective shell(s) is disfavored). Since an efficient active burning shell prevents the contraction of the overlying layers because its energy may sustain the outer layers, the more external the C burning shell is at the onset of the collapse, the more massive and compact the O-Ne core will be. Unfortunately there are a number of uncertainties that do not allow a reliable prediction of the amount of ^{12}C left by the He burning. In fact, it is well know that its final concentration depends not only on the competition among 3α, $^{12}C(\alpha,\gamma)^{16}O$ and mixing but also on the possible occurrence of the so called "Breathing Pulses" (BP), convective instabilities that occur towards the end of the He burning and that may largely affect the final concentration of ^{12}C (we refer the reader to the paper by Castellani et.al (1985) [2] for a deep discussion about the growth of these instabilities). While on average the BP reduce in number and efficiency as the initial mass increases, they may occur or not quasi erratically for even minor variations of the initial mass in the range of the massive stars. Such an occurrence could be responsible for the "chaotic" dependence of the final compactness of the stars as a function of the initial mass found recently [3] [4]. We just started to address in detail such a problem and we will publish our findings shortly. Additional mixing phenomena occur during the more advanced burning phases (Ne, O and Si burnings) but in these cases the evolution is so fast that the rotation driven instabilities do not have time to develop efficiently and the mixing is just controlled by the thermal

instabilities, i.e. by the "standard" convection.

Though the detailed degree of compactness of a star is fully described by the M-R relation, it has been proposed [5] the adoption of a single parameter, ξ, to describe in a concise way the degree of compactness of a star. ξ is the ratio between the Mass and the Radius computed at the mass coordinate of $2.5M_{\odot}$ at the onset of the core collapse:

$$\xi = M(M_{\odot})/R(10^3 km)_{(M=2.5)}$$

The choice of this parameter is based on the comparison between a set of 1D explosions computed for a variety of masses and their ξ parameter. The authors [5] found that ξ, computed at a mass coordinate $M=2.5M_{\odot}$, discriminates well between models that fully collapse in a remnant and those that produce a successful explosion. In particular they found that a successful explosion is obtained for ξ values smaller than 0.45. More recently it has been questioned [3] [4] the possibility of determine the final fate of a star on the basis of this simple parameter and the use of a double parameter has been proposed to determine the final fate of a massive star. For sake of simplicity in our paper [6] we decided to adopt the simplest scenario [5] to discriminate between stars that fully collapse and stars that explode successfully. Our grid of models of massive stars ranges between 13 and $120M_{\odot}$ in mass, between [Fe/H]=-3 and 0 in Fe abundance. In addition to the non rotating models, two initial rotation velocities have been considered: 150 and 300 km/s. A detailed description of the input physics and the assumptions adopted in these computations are discussed in our paper [6]. Figure 21 in that paper summarizes the ξ values that we obtain for our grid as a function of the initial mass. The grey area marks the region that corresponds to the models that fully collapse in the remnant. According to the ξ parameter, only models less massive than $\sim 40M_{\odot}$ should produce a successful explosion. But there is another constraint the models must satisfy in order to represent *real* explosions. From the analysis of the available data about the kinetic energies of the Type II Plateau supernovae detected, it has been discovered [7] that there are no observed Type II Plateau supernovae with kinetic energies of the ejecta in excess of 3 FOEs. If we take into account also this constraint, our models more massive that $25M_{\odot}$ should fully collapse in the remnant.

The net result of this analysis is shown in Figure 36 of our paper, where

the masses of the remnants for the various masses, metallicities and initial rotation velocities are shown. The Figure shows that in order to get black hole masses in excess of $30M_{\odot}$ or so it is necessary to have both a low initial metallicity (so to minimize the efficiency of the mass loss) and a low initial rotation velocity (otherwise the stars would largely overcome their Eddington luminosity and would lose a large amount of mass even at very low metallicities). The interested reader will find all the details about our latest extended grid of models in our paper [6].

References

1 . B. P. Abbott *et al.*, ApJL, **818**, L22 (2016).

2 . V. Castellani *et al.*, ApJ, **296**, 204 (1985).

3 . T. Sukhbold *et al.*, ApJ, **821**, 38 (2016).

4 . T. Ertl *et al.*, ApJ, **818**, 124 (2016).

5 . E. O'Connor *et al.*, ApJ, **730**, 70 (2011).

6 . M. Limongi *et al*, ApJ **13**, 138 (2018).

7 . O. Pejcha *et al*, ApJ **806**, 225 (2015).

Frascati Physics Series Vol. 66 (2018)
Frontier Objects in Astrophysics and Particle Physics
May 20-26, 2018

Understanding the Origin of r-Process in the Era of Gravitational-Wave Astronomy

Chris L. Fryer
CCS-2, Los Alamos National Laboratory, Los Alamos, NM 87545 USA
Jonas Lippuner
CCS-2, Los Alamos National Laboratory, Los Alamos, NM 87545 USA
Benoit Côté
Konkoly Observatory, Research Centre for Astronomy and Earth Sciences
Hungarian Academy of Sciences
Konkoly Thege Miklos ut 15-17, H-1121 Budapest, Hungary
National Superconducting Cyclotron Laboratory
Michigan State University, East Lansing, MI 48824, USA

Abstract

Although nuclear astrophysicists have known for over 60 years that many of the heaviest elements in the universe are produced through rapid neutron capture (r-process), the site or sites of r-process production has remained a matter of contention. A range of proposed sites exist associated with the energetic explosions in the universe: supernovae and gamma-ray bursts. Here we review the different sites, the details of r-process calculations, and the new understanding gained from the first gravitational wave detection of a short-duration gamma-ray burst produced by the merger of two neutron stars. This observation helps to cement some of the ideas behind r-process production but also brings a host of new questions. With prospects of further detections, it is likely that our understanding of r-process nucleosynthesis will rapidly increase over the next 5-10 years.

1 Proposed Sites of the r-Process

Nuclear astrophysicists have long known that the heaviest elements in the universe were likely produced through the capture of neutrons onto ions [1, 2]. Scientists identified two extremes in neutron capture: slow or "s-"process and rapid or "r-"process where the neutron capture rate is much longer (s-process) or much shorter (r-process) than the beta decay rate [1]. These two processes study extreme conditions and it is not surprising that it is also possible that heavy element production can occur in conditions where the capture rate is on par with the beta decay rate. This intermediate or "i-" process has been studied in more detail over the past few years [3, 6, 4].

With both the fast and slow neutron capture processes identified as the source of heavy elements, astronomers began to identify and study sites where such processes could occur. Because of the longer timescales, the s-process was assumed to be produced in stellar burning shells [1] and it is now believed that the bulk of the s-process is produced in asymptotic giant branch stars with a leading site being the thermal-pulse phase of these stars (for a recent review, see [5]). The i-process can occur both in stellar burning shels and stellar collapse and much more work is required to determine its relative importance. The obvious site for the r-process is in the formation of a neutron star during the collapse of a massive star where neutron rich conditions are possible and the timescales are short [1]. Determining how this r-process site will work has been an active area of research for 6 decades.

Rapid neutron capture requires a large source of neutrons and the first well-studied site focused on the newly formed neutron star in core-collapse supernovae [7]. The proto-neutron star is formed in the collapse of a massive star's iron core. The collapse occurs when electron capture reduces the electron degeneracy pressure that supports the core. As the core contracts, the electron capture rate increases, increasing the rate at which the electron degeneracy pressure is removed, ultimately producing a runaway collapse (infalling at free-fall velocities). The collapse continues until the core reaches nuclear densities where neutron degeneracy pressure and nuclear forces halt the collapse and form the proto-neutron star. The core becomes increasingly neutron rich until the neutrinos become trapped in the dense core. At the edge of the core, neutrinos continue to escape and this "neutrino-sphere" region can become quite neutron rich. The neutrino-driven winds blown off this neutrinosphere

could potentially provide the conditions for the r-process.

At the neutrinosphere, electron capture ($e^- + p \rightarrow n + \nu_e$) increases the neutron fraction. But above this region, electron and anti-electron neutrinos streaming out of the core reset the electron fraction[1] ($\nu_e + n \rightarrow e^- + p, \bar{\nu}_e + n \rightarrow p + e^-$, reducing the free neutron fraction, making it more difficult to produce the r-process elements. Because the ejecta is driven by momentum deposition from neutrinos, it is difficult to avoid resetting the electron fraction. But the exact value of the electron fraction will depend upon the spectra of the outflowing neutrinos. A number of modifications have been proposed to fix this particular r-process site: neutrino physics and neutrino oscillations [8, 9, 10] as well as a series of alternate driving mechanisms that alter the flow of the ejecta. For example, magnetic fields can delay drive the ejection of matter in either an excretion disk [11] or a jet [12]. More explosive matter ejections, like those seen in supernova fallback mass ejecta [3], can also alter the flow, making it easier to produce r-process elements. These alternate models would work only in a subset of all supernovae.

A number of opportunities for r-process production exist also in the engines behind gamma-ray bursts. Long-duration gamma-ray bursts are believed to be produced in the collapse of a massive, spinning star [16, 17]. The angular momentum in the star is sufficient to prevent the material from immediately accreting onto the collapsed core (either a black hole or proto-neutron star). Instead, it forms a disk around the compact remnant and the accretion of this disk provides the engine behind gamma-ray bursts [16, 17]. Winds from the disk [13, 14, 15] and relativistic jets driven by magnetic fields [12] have also been proposed as r-process sites.

Short duration bursts are not believed to be produced in the collapse of a massive star, but through the merger of two compact objects. The merger produces a central compact object surrounded by an accretion disk, again producing a gamma-ray burst engine [16, 17]. Scientists predicted that supernova kicks would cause these binary systems to travel well beyond their formation site and, in some cases, beyond their host galaxy, prior to merger [16, 18]. This prediction was finally confirmed by observations [19], cementing neutron star mergers as the leading model for short-duration gamma-ray bursts. These

[1]The electron fraction, or Y_e is the average number of protons in the matter divided by the average number of neutrons plus protons

compact objects are already neutronized, and the material flung out during the merger is extremely neutron-rich, providing ideal conditions to produce r-process. The only concern with this particular r-process source was its unknown rate that was believed to be low. The detection of GW170817 coupled with its corresponding electromagnetic radiation demonstrated that the merger rate and ejecta might indeed be sufficiently high to explain most of the r-process elements [20].

In this review, we discuss many of the assumptions in r-process yield calculations (Section 2). Despite these assumptions, it is useful to understand basic trends in the r-process production. To build this intuition, we mine the simulation results from Lippuner & Roberts [21] to discuss trends in r-process production (Section 3). We conclude with a discussion of the implications from the first advanced LIGO detection of a neutron star merger.

2 Basics Behind r-Process Studies

Although all of these sites have been studied independently, the assumptions in these studies have often been very similar. By understanding these assumptions, we can better compare the different results in the literature as well as the limitations of these assumptions. The early systematic study by Qian and Woosley [7] of r-process from neutron star winds outlined a simple evolution that has been used, with modifications, by nearly every group studying r-process from a wide variety of sources from neutron star winds to neutron star mergers and collapsar jets.

r-Process nucleosynthesis depends sensitively on the conditions, and evolution of the conditions, of matter. Nuclear burning occurs when the temperatures are high and atoms are moving sufficiently high to overcome the energy barrier of electrostatic forces. The number of collisions is proportional to the density of neutrons and ions. If we consider ion and neutron fractions, the reaction rates depend on the density squared. How long the matter stays at a given temperature dictates exactly what is produced in these reactions. Because of this, scientists have focused on the temperature and density evolution, or trajectories, of the ejected matter. The trajectories used in these r-process studies typically use an exponential evolution [22]:

$$T(t) = T_0 e^{-t/\tau} \tag{1}$$

where $T(t)$ is the temperature at time t, T_0 is the peak temperature of the material and τ is the decay time. The entropy of a radiation dominated gas is:

$$S = S_0 T^3/\rho \tag{2}$$

where $S_0 = 1.4 \times 10^{-11} \mathrm{k_B}$ nucleon^{-1} and ρ is the density. If we assume entropy is conserved, the density evolution is simply:

$$\rho(t) = \rho_0 e^{-t/3\tau} \tag{3}$$

where ρ_0 is the density at peak temperature. Although this may be appropriate for some mass ejection scenarios, for many explosions, a power law profile is more appropriate (see [23] for a review). For example:

$$T(t) = T_0/(2t+1). \tag{4}$$

If we again assume entropy conservation, the corresponding density evolution for this power-law profile is:

$$\rho(t) = \rho_0/(2t+1)^3. \tag{5}$$

For this paper, we use the results from Lippuner & Roberts [21] who employed a two-componet approach:

$$\begin{aligned} \rho(t) &= \rho_0 e^{-t/\tau} \text{ if t} < 3\tau \\ &= \rho_0 (3\tau/et)^3 \text{ if t} > 3\tau \end{aligned} \tag{6}$$

where e is Euler's number. This study also allowed the entropy to increase through nuclear decay. The temperature is then set by this time dependent entropy:

$$T(t) = (S(t)/\rho(t))^{1/3}. \tag{7}$$

Figure 1 shows the entropy versus time for 6 models in Lippuner & Roberts [21] varying both the electron fraction and the evolutionary timescale. The entropy can change dramatically over time. Figure 2 shows the resultant change in temperature with this heating. This entropy variation will change the temperature, but the largest modifications occur after the material has cooled below a few billion Kelvin and expanded to low densities where the neutron capture rate is relatively low. Even so, the entropy evolution can affect the nuclear yields,

especially for lower electron fractions. The study did not follow the heating in a full hydrodynamic calculation and it is possible that it will accelerate the ejecta, altering the timescale and minimizing the raise in temperature. Effects such as heating ultimately must be studied in hydrodynamic calculations.

The timescale (τ) for the evolution determines the time available for neutron capture, altering the yields. But the ejecta evolution does not follow either a power-law or exponential evolution profile and it may be that, ultimately, detailed yields require detailed calculations of the ejecta evolution. For jet models [12] and fallback ejecta [3] both found that the ejecta can have a complex ejecta path where the material can expand and compress multiple times before ejecting, an evolutionary path that is not well approximated by power-law or exponential solutions.

Finally, nuclear and neutrino physics uncertainties can dramatically alter the yields. One effect is that the neutrino capture can alter the electron fraction. For neutrino-driven outflows, the neutrinos strongly alter the electron fraction of the ejecta, and hence the r-process yields. Especially in these scenarios, neutrino physics (including neutrino oscillations) can play an important role in modifying the yields [26, 27, 24, 25, 28]. Even in accretion disk scenarios (e.g. the disk formed in neutron star mergers), neutrinos often dictate the electron fraction [13, 14, 15]. In addition, nuclear physics uncertainties, including fission rates, can dramatically change the yields (for a review, see [29]).

3 Rapid Neutron Capture and Heavy Element Production

Despite these uncertainties, we can gain considerable intuition from models with a fixed set of nuclear physics and a specific trajectory assumptions. For this study, we use the models from Lippuner & Roberts [21]. These models use the density evolution set by equation 6 and include direct nuclear heating to evolve the temperature (as in Figure 2). Lippuner & Roberts varied the electron fraction, entropy, and expansion timescale. Figure 3 shows the production of heavy r-process elements ($119 < A < 250$). It has been argued that the success of making the r-process is determined by the value of the product of the entropy cubed divided by the electron fraction cubed and the expansion timescale: $S^3/(Y_e^3\tau)$ [11]. This formula was based on the results of Hoffman et al [30]. Although this might be true for entropies above $100 k_B$ per nucleon, for lower entropies, it appears that the electron fraction is the dominant factor

in determining the amount of r-process element production. For these models, electron fractions below about ~ 0.3 produce large fractions of r-process elements. Note, however, that there are some interesting features in the production rate: e.g., very neutron rich material at high entropy does not effectively produce the heavy r-process.

To produce the very heavy r-process elements ($A > 249$), the electron fraction must be even lower, $Y_e < 0.25$ (Figure 4). But the exact conditions needed to produce these very heavy elements does not have a linear dependence on the entropy or the evolution timescale. For long evolution timescales, high entropies are required to produce very heavy isotopes. But at faster evolution timescales, low entropies produce more very heavy isotopes than high entropies. The production rate of these isotopes is also sensitive to the nuclear physics and a number of results recently have found wide variation in the yields of the heaviest r-process elements with respect to uncertainties in the nuclear physics [31].

Figure 5 shows the Lanthanide production our range of explosion conditions. Lanthanides can dominante the important opacities shaping the light-curves from neutron star mergers known as kilonova. If heavy (isotopes at the 2nd peak and beyond) r-process elements are produced, we expect a sizable fraction of Lanthanides. Because the Lanthanide opacities are strong in the optical and near-infrared, the r-process-rich kilonova ejecta is believed to peak, for the most part, in the infra-red. The production of Lanthanides is similar to the total r-process production but with some similarities to the heavy r-process production. For long timescales, the production is reduced at low entropies. At short timescales, the production is slightly decreased for the lowest electron fractions and highest entropies.

4 The Gravitational Wave Era

A number of potential kilonova observations existed in the late-time emission of short-duration gamma-ray bursts (for a review, see [32]). But it wasn't until the joint gravitational-/electromagnetic-wave detection of a neutron star merger (GW170817) that we had a definitive detection of the emission from the r-process ejecta from neutron star mergers [20]. This detection fit well the existing models for these events assuming a sizable amount ($\sim 0.01\,M_\odot$) of r-process element [33, 34]. The bright infra-red spectrum at late times in

GW170817 is suggestive of heavy r-process production with strong Lanthanide lines. Unfortunately, the forest of lines of Lanthanide elements [35] blend in the ejecta and it is difficult to prove (e.g. by detecting a line of a heavy r-process element) that the heavy r-process was produced in this explosion. Indeed, scientists were able to fit the data with a range of ejecta compositions [36] and we can not prove without any doubt that heavy r-process elements were produced in GW170817.

However, standard models do predict roughly $0.01\,M_{\odot}$ of r-process ejecta and, if we take the standard-model yields (e.g. [37, 38]) and the rates inferred from the gravitational-wave detection, we find that neutron star mergers can dominate the r-process production in the universe [39, 40, 36]. This has led some scientists to claim that the problem of the r-process site is solved. This oversimplifies the problem. We are still understanding the exact conditions that make the r-process. Detailed models and an understanding of the nuclear physics uncertainties is critical. In addition, there is already a set of data that using neutron star mergers as the sole source for r-process does not seem to be able to explain (Cote et al., in preparation). As advanced LIGO helps us increase the number of neutron star merger detections, we will be able to better understand the role of neutron star mergers and, ultimately, the sources of the heavy r-process elements.

5 Acknowledgements

A portion of this work was also carried out under the auspices of the National Nuclear Security Administration of the U.S. Department of Energy at Los Alamos National Laboratory under Contract No. DE-AC52-06NA25396.

References

1. Burbidge, E. M., Burbidge, G. R., Fowler, W. A., & Hoyle, F. 1957, Reviews of Modern Physics, 29, 547

2. Cameron, A. G. W. 1957, Astronomy Journal, 62, 9

3. Fryer, C. L., Herwig, F., Hungerford, A., & Timmes, F. X. 2006, ApJ Letters, 646, L131

4. Roederer, I. U., Karakas, A. I., Pignatari, M., & Herwig, F. 2016, ApJ, 821, 37

5. Prantzos, N., Abia, C., Limongi, M., Chieffi, A., & Cristallo, S. 2018, MNRAS, 476, 3432

6. Cowan, J. J., & Rose, W. K. 1977, ApJ, 212, 149

7. Qian, Y.-Z., & Woosley, S. E. 1996, ApJ, 471, 331

8. Fuller G. M., Meyer B. S., 1995, ApJ, 453, 792

9. Qian Y.-Z., Fuller G. M., 1995, PhRvD, 52, 656

10. McLaughlin G. C., Fuller G. M., 1996, ApJ, 464, L143

11. Thompson T. A., ud-Doula A., 2018, MNRAS, 476, 5502

12. Nishimura N., Takiwaki T., Thielemann F.-K., 2015, ApJ, 810, 109

13. Surman R., McLaughlin G. C., 2005, ApJ, 618, 397

14. Surman R., McLaughlin G. C., Ruffert M., Janka H.-T., Hix W. R., 2008, ApJ, 679, L117

15. Caballero O. L., McLaughlin G. C., Surman R., 2012, ApJ, 745, 170

16. Fryer C. L., Woosley S. E., Hartmann D. H., 1999, ApJ, 526, 152

17. Popham R., Woosley S. E., Fryer C., 1999, ApJ, 518, 356

18. Bloom J. S., Sigurdsson S., Pols O. R., 1999, MNRAS, 305, 763

19. Fong W., Berger E., 2013, ApJ, 776, 18

20. Abbott B. P., et al., 2017, ApJ, 848, L12

21. Lippuner J., Roberts L. F., 2015, ApJ, 815, 82

22. Hoyle, F., Fowler, W. A., Burbidge, G. R., & Burbidge, E. M. 1964, ApJ, 139, 909

23. Fryer C. L., Andrews S., Even W., Heger A., Safi-Harb S., 2018, ApJ, 856, 63

24. Meyer B. S., McLaughlin G. C., Fuller G. M., 1998, PhRvC, 58, 3696

25. McLaughlin G. C., Fetter J. M., Balantekin A. B., Fuller G. M., 1999, PhRvC, 59, 2873

26. Cardall C. Y., Fuller G. M., 1997, ApJ, 486, L111

27. McLaughlin G. C., Fuller G. M., 1997, ApJ, 489, 766

28. Duan H., Friedland A., McLaughlin G. C., Surman R., 2011, JPhG, 38, 035201

29. Horowitz C. J., et al., 2018, arXiv, arXiv:1805.04637

30. Hoffman R. D., Woosley S. E., Qian Y.-Z., 1997, ApJ, 482, 951

31. Vilen M., et al., 2018, PhRvL, 120, 262701

32. Kasliwal M. M., Korobkin O., Lau R. M., Wollaeger R., Fryer C. L., 2017, ApJ, 843, L34

33. Barnes J., Kasen D., 2013, ApJ, 775, 18

34. Wollaeger R. T., et al., 2018, MNRAS, 478, 3298

35. Fontes C. J., Fryer C. L., Hungerford A. L., Wollaeger R. T., Rosswog S., Berger E., 2017, arXiv, arXiv:1702.02990

36. Côté B., et al., 2018, ApJ, 855, 99

37. Troja E., et al., 2017, Natur, 551, 71

38. Tanvir N. R., et al., 2017, ApJ, 848, L27

39. Chornock, R., Berger, E., Kasen, D., et al. 2017, ApJL, 848, L19

40. Cowperthwaite, P. S., Berger, E., Villar, V. A., et al. 2017, ApJL, 848, L17

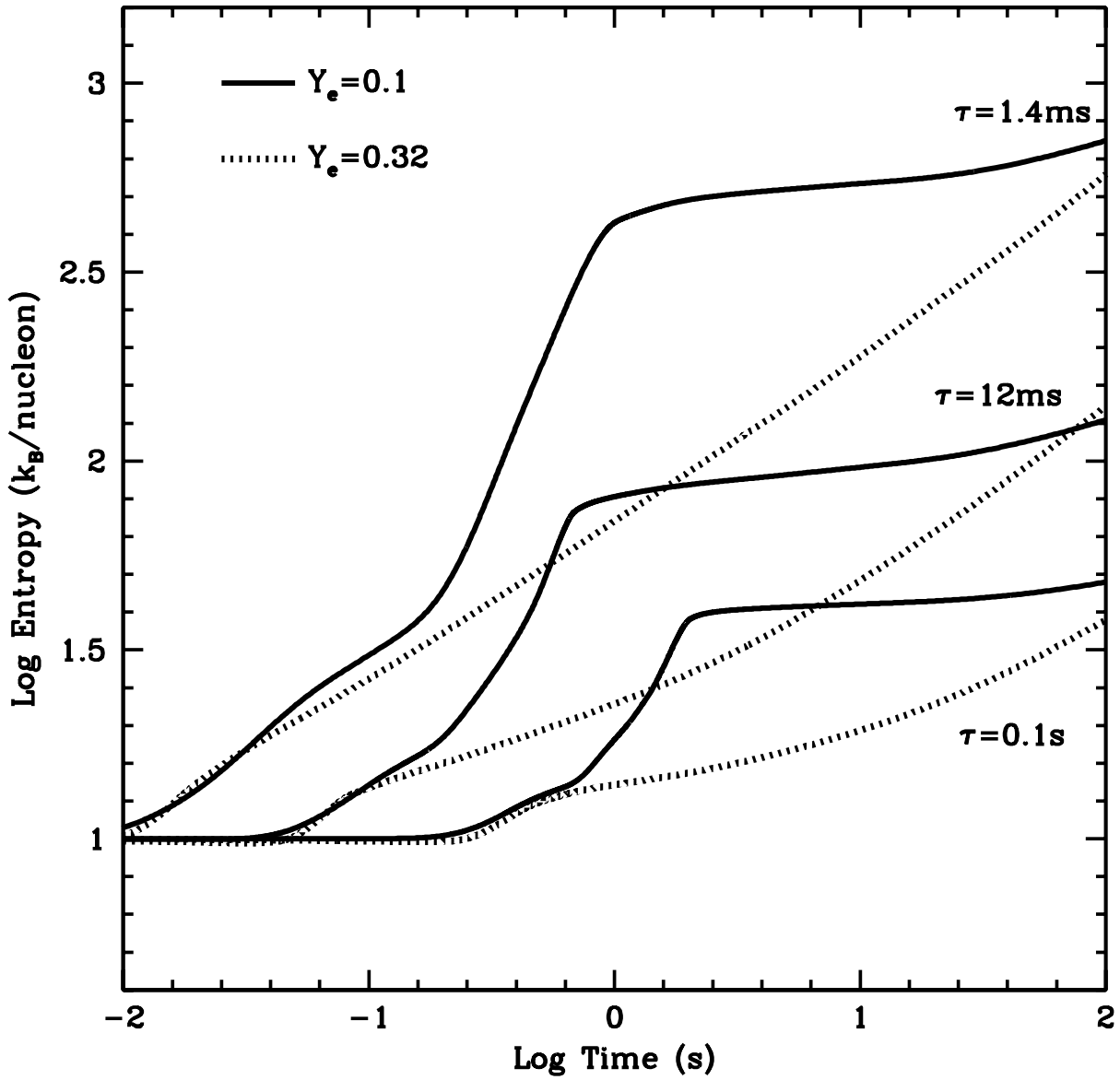

Figure 1: *Entropy versus time for 6 ejecta trajectories assuming two different electron fractions ($Y_e = 0.1, 0.325$) and 3 different expansion timescales ($\tau = 1.4, 12.0, 100.0\,s$). The evolution of the entropy and its total increase is lower for slower trajectories (with higher values of τ).*

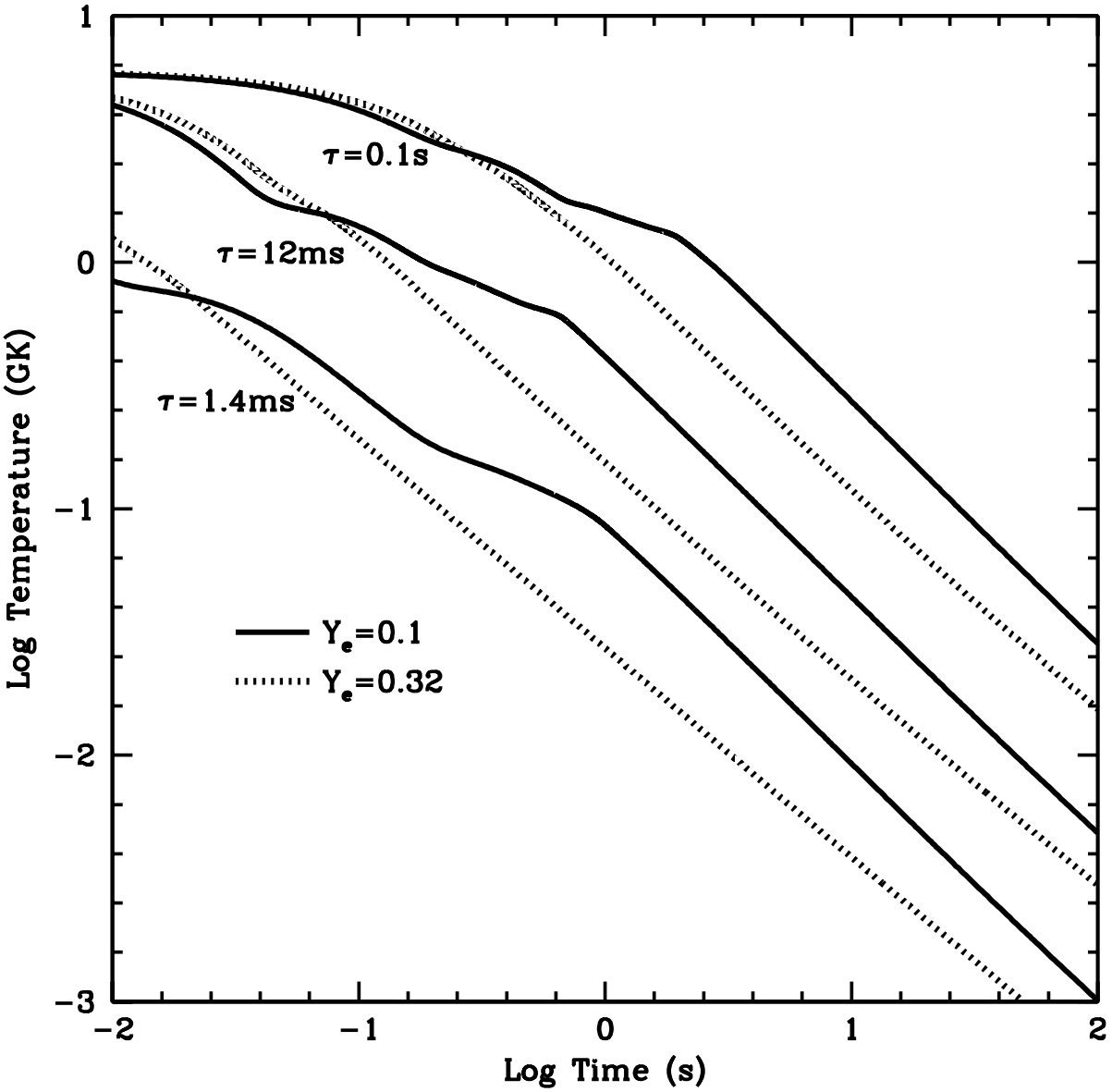

Figure 2: *Temperature versus time for 6 ejecta trajectories assuming two different electron fractions ($Y_e = 0.1, 0.325$) and 3 different expansion timescales ($\tau = 1.4, 12.0, 100.0\,s$). The evolution of the entropy and its total increase is lower for slower trajectories (with higher values of τ).* 62

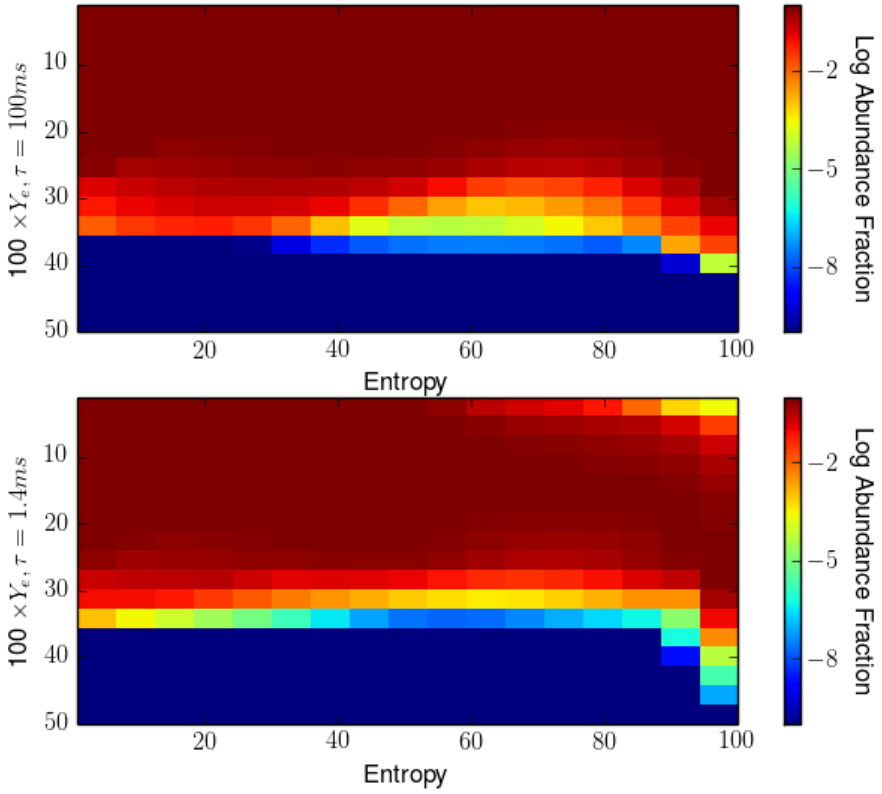

Figure 3: *Production of isotopes with average masses lying between 120 and 249 atomic mass units as a function of entropy (x-axis) and electron fraction (y-axis) for 2 different evolution timescales. For electron fractions below* ~ 0.3*, the production of these heavy r-process elements is high. It is possible to produce heavy r-process at higher electron fractions at high entropies.*

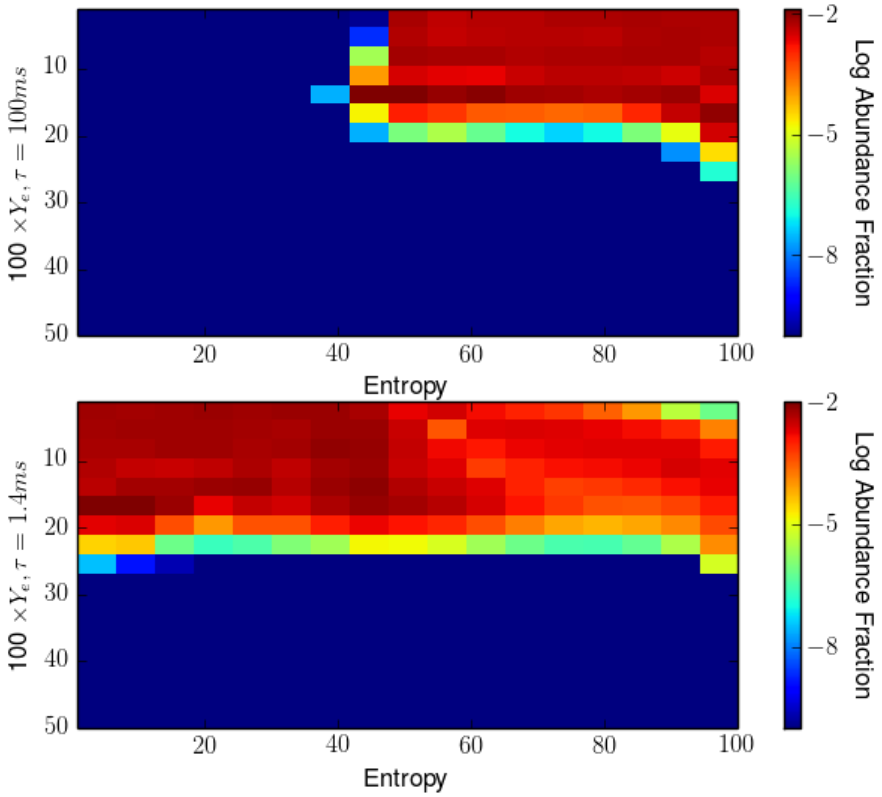

Figure 4: *Production of very heavy elements ($A > 249$) as a function of electron fraction, entropy, and evolution time (same parameters as in Figure 3). Lower electron fractions are needed to make these super-heavy r-process elements: $Y_e < 0.25$. In addition, the production of these heavy elements depends on both the entropy and the timescale. Note that there is not a generic trend in this production: for long evolution timescales, high entropies are needed, for short evolution timescales, lower entropies produce more super-heavy r-process elements.*

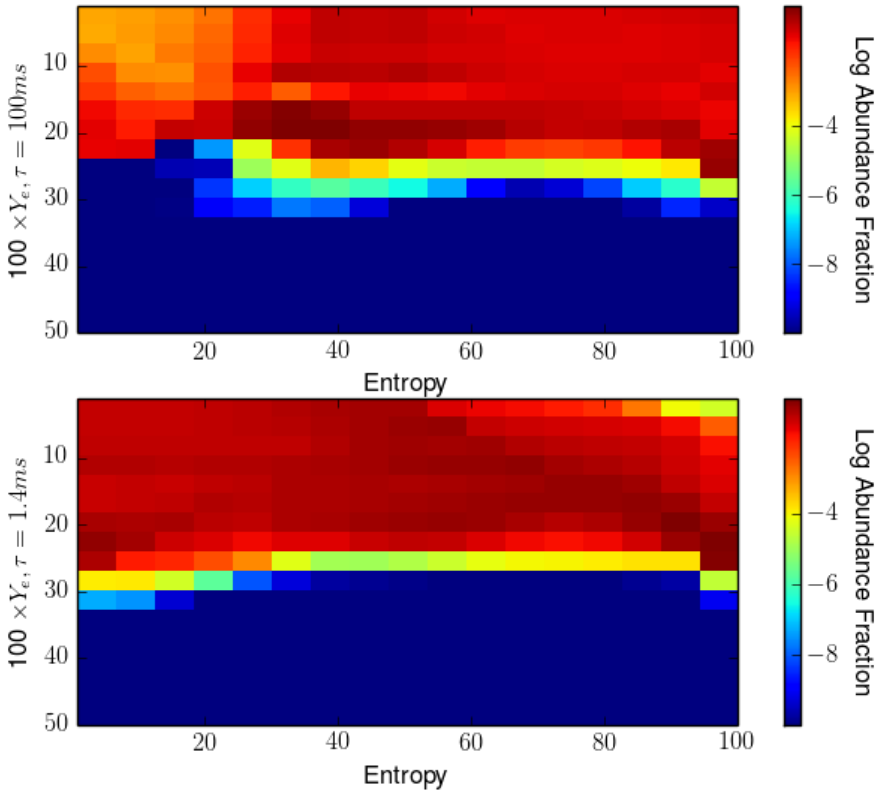

Figure 5: *Production of Lanthanides* ($57 < Z < 72$)*as a function of electron fraction, entropy, and evolution time (same parameters as in Figure 3). Lanthanide production lies somewhere in between very heavy r-process and the total r-process production requiring slightly lower electron fractions than the total r-process production. In addition, the production has additional variation based on both the entropy and the timescale.*

Frascati Physics Series Vol. 66 (2018)
Frontier Objects in Astrophysics and Particle Physics
May 20-26, 2018

THEORY OF OFF-AXIS AND GRAVITATIONAL WAVE EVENTS

H.J. van Eerten
Department of Physics, University of Bath, Claverton Down, Bath BA2 7AY, United Kingdom

Abstract

GW170817 was not merely an absolute breakthrough in gravitational wave astrophysics and a first in multi-messenger astronomy. The quality and diversity of the electro-magnetic counterpart emission is staggering on its own as well, including unprecedented kilonova spectra and a broadband off-axis gamma-ray burst afterglow that has progressed along a trajectory of rise and decay and by now has even been measured using very large baseline interferometry. For these proceedings, I will summarize the points for discussion that I presented during the workshop regarding off-axis short gamma-ray bursts and their (un-)successful jets and their emission. Given that developments are currently moving very fast in the field, I also touch on some results that have appeared in the literature following the Vulcano meeting.

1 Introduction

The recent joint detection [1, 2] of electro-magnetic (EM) and gravitational wave (GW) emission from merging neutron stars (NS) has been one of the biggest scientific achievements of the past decades, revolutionising astrophysical observations and having far-ranging repercussions for transients high-energy astrophysics. Various predictions for a range of potentially detectable EM counterparts had been made prior to the detection of GW170817 / GRB 170817A, but the actual quality and quantity of the data wildly exceeded expectations: kilonovae had largely remained a theoretical construct up to this point, although the first tentative detections were getting published [70, 8], while short gamma-ray bursts (sGRBs) and their subsequent afterglow jets were only expected for a subset of NS mergers due to their collimated nature. GRB 170817A of course provided us not just with a close view of a GW source, but also with a kilonova *and* a GRB *and* a long-lasting broadband afterglow. In these proceedings, I discuss in particular how the detection of the afterglow for this source has forced us to update our models for sGRB jets and afterglows.

2 GW170817 / GRB 170817A prompt emission and gravitational waves

Let us first recap the non-afterglow observations of GW170817 / GRB 170817A that nevertheless have an implication for our understanding of its afterglow. From the GW analysis, the angle θ_ν between the angular momentum vector of the binary neutron has been inferred to be $\theta_\nu \approx 18^\circ \pm 8^\circ$ [3, 41], potentially pointing at an off-axis observation of the prompt and/or afterglow emission, in case the jet collimation angle $\theta_0 < \theta_\nu$. The source was detected in gamma rays, both by INTEGRAL [66] and Fermi-GBM [23], before its gravitational wave signal was identified. The GRB was delayed by 1.7 s relative to the merger time. If the emission is indeed detected off-axis, this delay limits [3, 68, 43] the prompt emission radius R_γ according to $t_{\gamma,\oplus}/(1+z) = t_\gamma - \cos(\theta_\nu - \theta_0)R_\gamma/c$, where t_γ and $t_{\gamma,\oplus}$ the observed time in the burster and observer frame respectively, $z = 0.0098$ the redshift, c the speed of light and $R_\gamma = \int_0^{t_\gamma} \beta_\gamma c \delta t$. For example, an offset $\theta_\nu - \theta_0 \approx 13^\circ$ would limit $R_\gamma \lesssim 2 \times 10^{12}$ cm for $\beta_\gamma \uparrow 1$ (or smaller if the jet launching was delayed or the jet was moving non-relativistically before reaching R_γ). This radius is as expected [53] for

internal shock dissipation, but at odds with Poynting flux dominated models or other models that put the dissipation closer to the deceleration radius.

While labeled 'an ordinary short GRB' [23], GRB 170817A did exhibit some nonstandard features (one other example that comes close to its behavior is GRB 150101B [3, 74, 14]). Its isotropic equivalent prompt energy release $E_{\gamma,iso} \approx 5 \times 10^{46}$ erg, rendering it 2 to 6 orders of magnitude less energetic than other sGRBs. The burst consisted of a brief ($\sim$ 0.5 s) smooth pulse, followed by weak soft emission between 1 and 2 seconds after the GBM trigger time [23, 79]. The gamma-ray spectrum of the initial peak is well described by a power law turning over into an exponential drop (the 'Comptonized function' among the standard fit functions typically used, rather than e.g. the 'Band' function or a smoothly broken power law), peaking at $E_{peak} = 229 \pm 78$ keV. It is noteworthy that this peak value is typical, whereas $E_{\gamma,iso}$ is not, making the burst an outlier in the $E_{peak} - E_{\gamma,iso}$ plane [21]. The later emission is best fit by a blackbody spectrum peaking at $k_B T = 10.3 \pm 1.5$ keV. The smoothness of the initital pulse is consistent with an off-axis observation smoothing out variability relative to an on-axis observation [64]. The minimum variability timescale for the peak, (taken to be the rise time of 0.125 s) yields an upper limit on the size of the emission region of $\delta R \sim 4 \times 10^{13}$ cm [23].

The Lorentz factor Γ at the time of emission can be constrained in a number of ways [32, 71, 43, 79], mostly implying an emission site that is at least mildly relativistic. The low energy of GRB 170817A can be explained by positioning the observer outside of the cone of a collimated outflow, diminishing the observed flux through off-axis relativistic beaming. But the angular dependency of relativistic beaming is extremely steep, so much that a typical flow with $\Gamma \sim 100$ on-axis (as expected for short GRBs [53, 9]), would lead to a predicted energy even lower than what is observed. This issue can be resolved by moving the observer closer to the axis of the jet, lowering the Lorentz factor of the outflow to open up the beaming cone, or both. The limiting cases of this are either placing the observer inside of the sub-energetic wings of a jetted flow, or having only mildly relativistic quasi-spherical flow. However, this is not straightforward either if one wishes to avoid opacity issues due to electron-positron pair-production and Thomson scattering [71, 35]), although not impossible [49]. It is therefore possible that the prompt emission observed for GRB 170817A has been produced by a mechanism different from ordinary

short GRBs.

A discussion of the kilonova emission and properties lies beyond the scope of these notes. Nevertheless, the properties of the merger inferred from the kilonova emission also constrain the physics of the GRB prompt and afterglow. In particular, the are indications for a brief [46] or extended [82] period of energy injection by a magnetar-like remnant. For the latter case of a long-lasting remnant ($\gg 1$ second, which is not a natural fit given that the GW observations constrain internal magnetic fields to not be much lower than $\sim 10^{16}$ G [56]), short GRB afterglow plateaus come to mind, which have been argued to be produced by long-term energy injection from magnetar dipole spin-down. Any plateau stage for GRB 170817A would have been missed by an off-axis observer.

3 GRB 170817A and jet / blast wave toy models

Keeping the constraints from the non-afterglow measurements in mind, we now turn to the afterglow stage of GRB 170817A. The afterglow of GRB 170817A was first detected at radio and X-ray frequencies [30, 71] at around nine days, following a number of non-detections (upper limits) at these wavelengths [18]. At the time when the first reports on this source became public, it was reasonable to interpret the data for these first two weeks as exhibiting signs of a flattening in the light curve, given that the flux levels for the second and third X-ray points were comparable after a rise relative to the first detection, and given that the radio detections were interspersed with another claimed upper limit [5]. The early non-detections made clear that we could not be witnessing an on-axis afterglow, whereas the apparent flattening was consistent with the peak emission from a basic collimated flow model. Here 'basic' refers to the simplicity of the *initial conditions*, a blast wave with an energy, mass and velocity distribution that is independent of angle up to some truncation angle θ_0 (i.e. 'top-hat', the simplest non-spherical starting point). Off-axis observations with observers placed at $\theta_{obs} > \theta_0$ would see a steeply rising light curve as the relativistic beaming cone of the shock-accelerated electrons at the blast wave front come into view. Once the jet is into view completely, the light curve would turn over towards a decaying slope.

However, the explanation of the afterglow light curve observations as revealing the turnover of top-hat jet emission quickly turned out not to be viable when renewed observations showed a continuing rise with $\alpha \approx -0.8$ in $t^{-\alpha}$,

lasting longer than the turnover would have. This compounded issues already identified with the prompt emission in view of off-axis top-hat jet models (i.e. the extremely steep angular dependence of relativistic beaming), that led authors to include structured jet alternatives in the first batch of papers [71, 30]. The latest observations [73], indicate a rising slope of $\alpha \approx -0.9$, a peak time $t_p = 164 \pm 12$ days and finally a steep decay slope $\alpha \approx 2$. To understand the options from here, a brief review of popular jet morphologies in the context of new observations is in order (for an extensive older review on jets, see [27]).

basic top hat jets. The first jetted flow models [58] for long and short GRBs simply assumed a forward shock moving ultra-relativistically and truncated at an angle that would start growing noticeably in the observer frame once the Lorentz factor dropped to $\gamma \approx 1/\theta_0$ (in the observer frame, the sideways velocity is suppressed by this same factor γ; the turning point marks when spreading becomes clear to observers even when including this factor). Once spreading starts, this becomes a runaway effect due to the feedback between the increasing size of the working surface sweeping up external medium and the induced further decay of γ. For reasons of simplicity, this model includes no ininital angular jet structure (with radial structure either neglected in the case of homogeneous shell models, or taken from a self-similar solution [13] before spreading). The evolution of such jets has been numerically simulated in detail, revealing the expected lateral structure of a shock system expanding sideways as well as forwards (see e.g. [44, 84, 76, 80]). Fully numerically resolved simulations [77] confirm that lateral expansion in these systems affects the decay phase slope of the light curve rather than the rising phase slope. For reasonable jet opening angles ($\theta_0 > 0.05$ rad), no runaway stage of expansion occurs in practice because the jet moves into the trans-relativistic stage approximately around the same time full causal contact across all angles is achieved (ultra-relativistic flow and full causal contact are necessary assumptions in runaway spreading models). In conclusion, off-axis top-hat jets remain ruled out by the rising slope, whether simulated numerically or solved (semi-) analytically.

Power-law structured jets. A straightforward extension of the top-hat model is to impose lateral structure on the jet using a discrete number of lateral components or simple functional form such as a power law dependency on angle for the energy, $\epsilon \propto \theta^{-a}$ (e.g. [40, 60]). One of the initial motivations for such models was to shift the observed variation in jet opening angles and

energetics to jet orientation relative to the observer instead [40, 85]. This requires that the lateral drop in energy in energy is not too steep ($a < 2$), but such a shallow slope also has the implication that the afterglow emission must be bright and decaying for off-axis observers still within the wings of the jet. Given the late-time rise of GRB 170817A, this possibility is ruled out as well, and the remaining options for the lateral jet structure are those where the wings have little energy relative to the tip, e.g. through a steep power-law or even exponential dependence of energy on angle.

Gaussian jets. Jets with a steep drop in energy ϵ with angle can also be modeled usings exponentials, i.e. $\epsilon \propto \exp[-\theta^2/2\theta_c^2]$, with θ_c setting the width of the core. On-axis observers and observers at very small angles will observe a light curve that very closely resembles that produced by a top-hat jet (another practical reason why numerical simulations tended to start from top-hats), and observers at $\theta_{obs} \lesssim 4\theta_c$ will see a declining signal from the beginning [61]. However, observers at larger angles will see a smoothly rising signal, as different regions come into view once the beaming cones of their relativistic emission have opened up sufficiently —due to the deceleration of the jet— to encompass the direction to the observer. During the rising stage this behaviour, where the emission is dominated by successively more energetic regions, is equivalent to observing a spherical blast wave with an ongoing injection of energy, and we return to this point below. Another attractive feature of (Gaussian) structured jets is that they manage to capture well the jet morphology produced by detailed numerical simulations of relativistic jet launching [7] and breakout [50, 47, 38, 33, 42]. Once the entire jet has come into view, the effect will be similar to the top-hat jet case, and a steep decay of the light curve is seen comparable to that of a GRB observed on-axis post jet-break [59, 65].

Quasi-spherical blast waves with energy injection. A spherical blast wave model for the afterglow using regular afterglow parameters would show a bright decelerating light curve already at early times. On the other hand, the gamma-rays and afterglow of GRB 170817A might have been produced by a special subclass of GRB, or perhaps by something not normally detected as a GRB at all. One option here would be the (quasi-)spherical release of energy with only moderate velocity, perhaps a cocoon of material (e.g. neutron star merger debris [52]) which has managed to absorb the energy of what would otherwise have been a collimated GRB jet. Initial predictions for quasi-

spherical cocoon models included afterglow peak timescales of days [54, 37], rather than the observed weeks for GRB 170817A. This timescale is set by the deceleration radius of the ejecta. If the peak time is to match that observed for GRB 170817A, the deceleration time needs to be artificially postponed. A natural means to do so, would again be to invoke additional structure in the outflow, this time radial rather than lateral. Indeed, the right peak times can be achieved by assuming a stratification of cocoon outflow velocities behind the front of the shock, effectively acting as a mechanism for the long-term injection of energy [48]. There is ample precedent for models including velocity stratification, both for GRBs [57] and kilonova ejecta [45]. During the rising light curve stage, it is fundamentally not possible to distinguish observationally between radial energy injection and lateral energy 'injection' (i.e. more energetic regions coming into view). However, following the peak, the light curve slope is not expected to be steep [72], and to fall well short of the recently measured value [73].

Of all jet toy models, it turns out that the Gaussian jet plus off-axis observer configuration is the most successful in capturing the observed features of GRB 170817A [72, 73], from initial non-detections to extended shallow rise and turnover to steep decay. Basic cocoon models would have peaked on a timescale comparable to the kilonova. Relativistic jets with extended energetic wings would have been visible too soon. The top-hat jet profile is unable to account for an extended shallow rise. Quasi-spherical (cocoon) models with radial energy injection will ultimately end up decaying according to the non-relativistic Sedov-Taylor solution for a non-relativistic point explosion [20], perhaps slightly steeper on account of lateral spreading, when merely wide-angled rather than quasi-spherical [36]. Either slope will fall short of the observed slope by a large margin, and will only be achieved at larger timescales than currently observed anyway.

3.1 Successful jets, choked jets and cocoons

While a staple of jet modeling of active galactic nuclei and long GRBs for decades, cocoons are a new arrival when it comes to the modeling of short GRBs [51, 52]. Cocoons are produced when (part of) the jet energy gets dissipated in a dense medium before emergence into the more dilute circumburst environment. It is an open question whether enough dense material, for exam-

ple debris from the neutron star merger, is present in the path of the jet to materially effect its evolution. Numerical studies of the ejection of merger debris show that this can be concentrated along the orbital plane [62], but also more isotropic in the case of a soft neutron star matter equation of state [31]. The jet can be choked completely if the combination of jet opening angle and merger debris is sufficiently high (e.g. total quasi-isotropic ejecta mass of $10^{-2} M_{\odot}$, combined with a wide-angled jet injection of $45°$, depending on jet power [52]). In the choked jet case, a quasi-spherical trans-relativistic blast wave is formed.

As stated above, a choked jet scenario appears ruled out by recent observations, but this does not imply the absence of a cocoon entirely. Successful jet breakout with a prominent cocoon component has been simulated by various groups [32, 24, 39, 81]. This leads to a structured jet that can be modeled using the semi-analytical approaches already described. When it comes to the broadband afterglow light curve of GRB 170817A, the data is by this point consistent with a successfully launched jet with significant angular structure that potentially includes a cocoon component.

4 Synchrotron emission from the afterglow

There is little doubt that the predominant emission mechanism during the afterglow phase is synchrotron emission. Afterglow detections covering nine orders of magnitude in frequency (i.e. from radio to X-rays) are fully consistent with a single power law spectrum [71, 29, 72, 42, 6, 63, 73]. Interpreted as being part of the synchrotron spectrum between the *injection break* ν_m (associated with the lower cut-off of the shock-accelerated power-law electron population) and the *cooling break* ν_c (beyond which the impact of the synchrotron energy loss term on the electron population becomes noticeable), the measured spectral slope $\beta = 0.585 \pm 0.005$ implies an electron power law slope $-p = -2.17 \pm 0.01$. The nine orders of magnitude represent a remarkable stretch for a single power law: radio observations (albeit on-axis ones) often fall below ν_m initially, and the cooling break ν_c is often found between optical and X-rays for afterglows [25]. Nevertheless, once the off-axis orientation of the observer is taken into account, the afterglow spectra for GRB 170817A can be fit using otherwise reasonable values for the model parameters [71, 35, 72, 73]. Figure 1 illustrates the broader synchrotron spectrum for variables in this range, including turnover points. A cooling break this high could actually be less rele-

vant to the spectrum than the upper cut-off on the emission resulting from the balance between particle acceleration timescale and synchrotron loss timescale for electrons at very high energies (i.e. the electrons predominantly responsible for high frequency photon emission). Approximations of this timescale are typically based on a comparison between electron gyroradius and characteristic time for synchrotron energy loss [17]. Two further complications to modeling electron cooling are that there can also be additional cooling due to synchrotron self-Compton losses, and that estimates for the cooling break are highly sensitive to the level of detail that is applied to modeling the *local* cooling rate of electrons advected from the shock front [26, 75, 28].

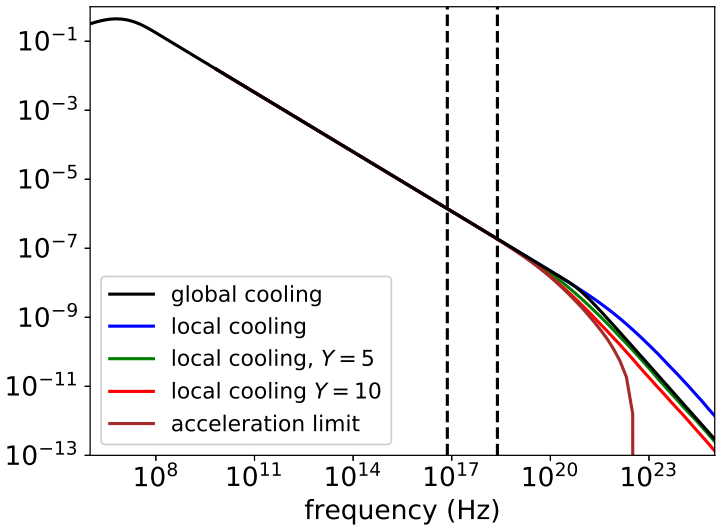

Figure 1: Synthetic spectra for an off-axis structured jet GRB with physics settings comparable to those inferred for GRB 170817A around 150 days, using different approximations to electron cooling. Here Y is the Compton Y-parameter, to account for an additional impact on the electron cooling rate from synchrotron self-Compton losses.

The value $p = 2.17$ lies in between the two typical limiting values for p expected from theoretical considerations. For particle shock-acceleration in non-relativistic blast waves, $p = 2$ is expected [10, 11, 12]. For the case of

ultra-relativistic blast waves, various authors have argued for $p \approx 2.2 - 2.4$, based on particle-in-cell simulations and (semi-)analytical methods [34, 4, 69]. It is therefore tempting to interpret [42] the precise measurement of $p = 2.17 \pm 0.01$ for GRB 170817A directly within this framework as being indicative of a moderately relativistic blast wave Lorentz factor with a Lorentz factor $\Gamma \approx 3 - 10$. However, decades of afterglow modeling (as well as modeling of other synchrotron sources such as blazars), have established an overall observational range and distribution of p values that is at minimum observationally at odds with this direct interpretation. Multiple authors have demonstrated that the distribution of p as measured for various samples of afterglows, is not consistent with a universal value [67, 15, 16], nor does p exhibit a general hardening trend over time when spectral energy distributions are compared over multiple epochs [78] (such a trend which would manifest itself both in a changing spectral slope and in the light curve temporal slope). As a matter of fact, p has even been measured [17, 55, 19, 83] to have values $p < 2$ including measurements using broadband observations covering many orders in magnitude (e.g. $p = 1.73 \pm 0.03$ [78]). It is not (yet) clear whether the view of particle acceleration allowed by an off-axis event such as GRB 170817A is fundamentally more clear than that for the larger sample of shock-accelerating systems.

5 Closing remarks

In all, the long-term evolution of the broadband afterglow light curve of GRB 170817A has been remarkably successful. The late rise was instrumental in ruling out an observer positioned within the opening angle of a relativistic outflow, implying either an observer positioned outside of the jet, or no successful jet and a trans-relativistic quasi-spherical explosion. The continued rise then ruled out off-axis jet models with hard edges and single-shell cocoon models, requiring a structured jet or velocity stratification within a cocoon model. Ultimately, the turn-over to steep decay served to rule-out quasi-spherical models entirely.

In addition, we now even have very large baseline interferometry (VLBI) observations for the same source. The apparent source size at 207.4 days has been constrained to be less than 2 milliarcseconds [22], which is too small to be consistent with an isotropic, mildly relativistic blast wave such as the cocoon-type models described above. Other VLBI observations [49] reveal superluminal

motion consistent with the energetic and narrow core of a structured jet. Taken together, the afterglow evidence is becoming compelling that, like other short GRBs, GRB 170817A came with a collimated relativistic jet, and that the GW170817 / GRB 170817A event has become the smoking gun for the short GRB / neutron star merger connection. Observations of future event will tell whether there is on occasion sufficient material in the path of the outflow to give rise to sub-population of choked jet explosions.

However, even if the afterglow can be reconciled with the 'typical' expected behaviour for short GRBs, the prompt emission does remain puzzling and atypical. Observationally, the energy is very low, but neither off-axis beaming nor low Lorentz factor explanations are a completely satisfactory solution. It remains an open question whether the prompt emission has been produced by the same mechanism as that observed for short GRBs in general. And even in the case the prompt emission was produced differently, it is not clear whether the normal process genuinely did not occur or was merely not detectable at our observational angle.

References

1. LIGO Scientific Collaboration and Virgo Collaboration, Phys. Rev. Lett. **119**, 161101 (2017).
2. B.P. Abbott *et al*, ApJL **848**, L12 (2017).
3. B.P. Abbott *et al*, ApJL **848**, L13 (2017).
4. A. Achterberg *et al*, MNRAS **328**, 393 (2001)..
5. K.D. Alexander *et al*, GCN circular 21851 (2017).
6. K.D. Alexander *et al*, ApJL **863**, L18 (2018).
7. M.A. Aloy, H.T Janka and E. Müller, A&A **436**, 273 (2005).
8. E. Berger, W. Fong and R. Chornock, ApJL **774**, L23, (2013).
9. E. Berger, ARoAA **52**, 43 (2014).
10. A.R. Bell, MNRAS **182**, 147 (1978).
11. R.D. Blandford and J.P. Ostriker, ApJL **221**, L29 (1978).

12. R. Blandford and D. Eichler, PhR **154**, 1 (1987).

13. R.D. Blandford and C.F. McKee, Physics of Fluids **19**, 1130 (1976).

14. E. Burns *et al*, arXiv:1807.02866v1 (2018).

15. P.A. Curran *et al*, MNRAS **395**, 580 (2009).

16. P.A. Curran *et al*, ApJL **716**, L135 (2010).

17. Z.G. Dai and K.S. Cheng, ApJL **558**, L109 (2001).

18. P.A. Evans *et al*, Science **358**, 1565 (2017)

19. R. Filgas *et al*, A&A **535**, A57 (2011).

20. D.A. Frail, E. Waxman and S.R. Kulkarni, ApJ **537**, 191 (2000).

21. G. Ghirlanda *et al*, A&A **496**, 585 (2009).

22. G. Ghirlanda *et al*, arXiv:1808.00469 (2018).

23. A. Goldstein *et al*, ApJL **848**, L14 (2017).

24. O. Gottlieb, E. Nakar and T. Piran, MNRAS **473**, 576 (2018).

25. J. Greiner *et al*, A&A **526**, A30 (2011).

26. J. Granot and R. Sari, ApJ **568**, 820 (2002).

27. J. Granot, RMxAC **27**, 140 (2007).

28. C. Guidorzi *et al.*, MNRAS **438**, 752 (2014).

29. D. Haggard *et al.*, ApJL **848**, L25 (2017).

30. G. Hallinan *et al.*, Science **358**, 1579 (2017).

31. K. Hotokezaka *et al*, PHRvd **87**, 024001 (2013).

32. M.M. Kasliwal *et al*, Science **358**, 6370 (2017).

33. A. Kathirgamaraju, R. Barniol Duran and D. Giannios, MNRAS **473**, L121

34. J.G. Kirk *et al.*, ApJ **542**, 235 (2000).

35. G.P. Lamb and S. Kobayashi, MNRAS **478**, 733 (2018).

36. G.P. Lamb, I. Mandel and L. Resmi, arXiv:1806.03843 (2018).

37. D. Lazzati *etl al.*, MNRAS **471**, 1652 (2017).

38. D. Lazzati *et al.*, ApJL **848**, L6 (2017).

39. D. Lazzati *et al.*, PhRvL **120**, 241103 (2018).

40. V.M. Lipunov, K.A. Postnov and M.E. Prokhorov, Astron. Rep. **45**, 236 (2001).

41. I. Mandel, ApjL **853**, L12 (2018).

42. R. Margutti *et al.*, ApJL **856**, L18 (2018).

43. T. Matsumoto, E. Nakar and T. Piran, ArXiv:1807.04756v1 (2018).

44. Z. Meliani *et al.*, MNRAS **376**, 1189 (2007).

45. B. Metzger, Living Reviews in Relativity **20**, 3 (2017).

46. B.D. Metzger, T.A. Thompson and E. Quataert, ApJ **856**, 101 (2018).

47. .A Mizuta and M.A. Aloy, ApJ **699**, 1261 (2009).

48. K.P. Mooley *et al.*, Nature **554**, 207 (2018).

49. K.P. Mooley *et al.*, arXiv:1806.09693 (2018).

50. B.J. Morsony, D. Lazzati and M.C. Begelman, ApJ **665**, 569 (2007).

51. A. Murguia-Berthier *et al.*, ApJ **788**, L8 (2014).

52. H. Nagakura *et al.*, ApJL **784**, L28 (2014).

53. E. Nakar, Phys Rep **442**, 166 (2007).

54. E. Nakar and T. Piran, ApJ **834**, 28 (2017).

55. A. Panaitescu and P. Kumar, ApJL **560**, L49 (2001).

56. D. Pooley *et al.*, ApJL **859**, L23 (2018).

57. M. Rees and P. Mészáros, ApJ **496**, L1 (1998).

58. J.E. Rhoads, ApJ **487**, L1 (1997).

59. J.E. Rhoads, ApJ **525**, 737 (1999).

60. E. Rossi, D. Lazzati and M.J. Rees, MNRAS **332**, 945 (2002).

61. E. Rossi *et al.*, MNRAS **354**, 86 (2004).

62. S. Rosswog *et al.*, A&A **341**, 499 (1999).

63. J.J Ruan *et al.*, ApJL **853**, L4 (2018).

64. O.S. Salafia *et al*, MNRAS **461**, 3607 (2016).

65. R. Sari, T. Piran and J. Halpern, ApJ **519**, L17 (1999).

66. V. Savchenko *et al*, ApJL **848**, L15 (2017).

67. R. Shen, P. Kumar and E.L. Robinson, MNRAS **371**, 1441 (2006).

68. I.M. Shoemaker and K. Murase, Phys Rev D **97**, 083013 (2018).

69. A. Spitkovsky, ApJL **682**, L5 (2008).

70. N.R. Tanvir *et al*, Nature **500**, 547 (2013).

71. E. Troja *et al*, Nature **551**, 71 (2017).

72. E. Troja *et al*, MNRAS Letters **478**, L18 (2018).

73. E. Troja *et al*, arXiv:1808.06617 (2018).

74. E. Troja *et al*, arXiv:1806.10624 (2018).

75. H. van Eerten, W. Zhang and A. MacFadyen, ApJ **722**, 235 (2010).

76. H. van Eerten *et al.*, MNRAS **410**, 2016 (2011).

77. H. van Eerten and A. MacFadyen, ApJ **767**, 141 (2013).

78. K. Varela *et al*, A&A **589**, A37 (2016).

79. P. Veres *et al*, ArXiv:1802.07328v1 (2018).

80. N. Wygoda, E. Waxman and D. Frail, ApJ **738**, L23 (2011).

81. X. Xie, J. Zrake and A. MacFadyen, ApJ **863**, 58 (2018).

82. Y.W. Yu, L.D. Liu and Z.G. Dai, ApJ **861**, 114 (2018).

83. Q. Zhang, Y.F. Huang and H.S. Zong, ApJ **811**, 83 (2015).

84. W. Zhang and A. MacFadyen, ApJ **698**, 1262 (2009).

85. B. Zhang, P. Mészáros, ApJ **571**, 876 (2002).

Frascati Physics Series Vol. 66 (2018)
Frontier Objects in Astrophysics and Particle Physics
May 20-26, 2018

BIG BANG NUCLEOSYNTHESIS DEEP UNDERGROUND

Carlo Gustavino
INFN-Roma
(for the LUNA collaboration)

Abstract

Big Bang Nucleosinthesis (BBN) theory provides definite predictions for the abundance of light elements produced in the early universe. At BBN energies ($30 \lesssim E_{cm} \lesssim 300$ MeV) the cross section of many BBN nuclear reactions is very low because of the Coulomb repulsion between the interacting nuclei. In order to reduce the cosmic ray induced background it is convenient to perform the measurements deep underground. In this presentation the BBN measurements of LUNA (Laboratory for Underground Nuclear Astrophysics) are reviewed. In particular, It will be shown that the ongoing study of the $D(p,\gamma)^3He$ reaction is of primary importance to derive the baryon density of universe Ω_b. Moreover, this study allows to constrain the existence of the so called "dark radiation", composed by undiscovered relativistic species permeating the universe, such as sterile neutrinos.

1 Introduction

The Big Bang nucleosynthesis (BBN) theory describes the formation of light nuclides during the first minutes of cosmic time, when the Universe was hot, dense and rapidly expanding. Assuming standard physics, the synthesis of light isotopes depends on the nuclear reactions shown in figure 1. The nucleosynthesis begins with the formation of deuterium by p(n,γ)^{2}H reaction. Subsequently, ^{3}H and ^{3}He are produced via the ^{2}H(^{2}H,p)^{3}H, ^{2}H(^{2}H,n)^{3}He and ^{2}H(p,γ)^{3}He processes. The ^{3}H(^{2}H,n)^{4}He and ^{3}He(^{2}H,p)^{4}He reactions produce ^{4}He, in which nearly all the free neutrons end up bound, while the abundances of deuterium, tritium and ^{3}He are relatively small (residual tritium is successively converted into ^{3}He via weak decay). The primordial abundance of heavier isotopes ^{7}Li and ^{6}Li is even smaller (after BBN, the produced ^{7}Be decays into ^{7}Li), because the absence of stable nuclei with mass number 5 impedes nucleosynthesis via ^{4}He + n and ^{4}He + p reactions. Finally, the production of nuclides with A > 8 is negligible, because the lack of stable nuclei with A = 8 prevents nuclear reactions through the ^{4}He + ^{4}He channel to occur.
In standard cosmology, the expansion rate of the universe is governed by the Friedmann equation:

$$H^2 = \frac{8\pi}{3} G\rho, \tag{1}$$

where H is the Hubble parameter, G is the Newton's gravitational constant and ρ is the energy density which, in the early Universe, is dominated by the "radiation", i.e. the contributions from massless or extremely relativistic particles. The only known relativistic particles at the BBN epoch are the photons and the three neutrino families. Therefore, the radiation density can be expressed as follows:

$$\rho = \rho_\gamma \left[1 + \frac{7}{8} \left(\frac{4}{11} \right)^{4/3} N_{eff} \right]. \tag{2}$$

In this formula ρ_γ is the photon density and N_{eff} is the contribution of other relativistic species. Using this formula $N_{eff} = 3.046$ if only the three known neutrino families are considered. Assuming standard physics, the only free parameter in the BBN theory is the baryon density Ω_b or equivalently η, defined as the ratio of baryons with respect to photons.

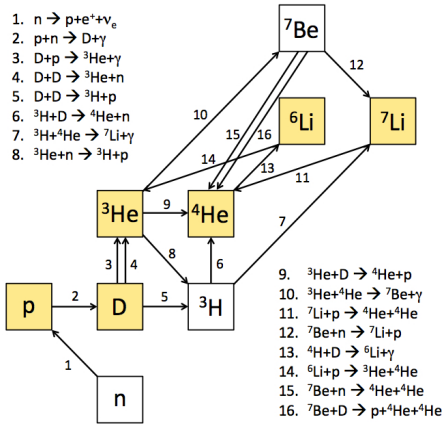

Figure 1: Leading processes of Big Bang Nucleosynthesis. Yellow boxes mark stable isotopes.

Figure 2 shows the calculated abundance of ^4He, D and ^7Li as a function of η (the uncertainty is represented by the red, blue and orange bands, respectively). In this figure are also shown the results of astronomical observations (horizontal bands) and the η value derived from CMB data (vertical band) [1–5]. Table 1 summarises the results of BBN calculations (assuming the ΛCDM model and the η parameter derived from CMB experiments) and the results of direct observations. The computed ^{4}He abundance essentially depends on the amount of free neutrons available, therefore its (very small) uncertainty is almost entirely due to the neutron lifetime error [6]. The primitive abundance of ^{4}He derived from observations is deduced from observations in HII (ionized hydrogen) regions of compact blue galaxies. The uncertainty is mainly due to systematics such as plasma temperature or stellar absorption [2]. Apart from helium, the calculated abundances of all the other nuclides strongly depend on the details of the BBN reaction chain [6]. The abundance of deuterium has been recently derived with good accuracy from the observation of Damped Lyman-Alpha (DLA) systems at high redshift [4]. Note that the error of $(\mathrm{D/H})_{BBN}$ is larger than the $(\mathrm{D/H})_{obs}$ one, mainly because of the paucity of data of the deuterium burning reaction ^{2}H(p,γ)^{3}He [7]. The $(^3\mathrm{He/H})_{BBN}$ value has a quite small error, while the ^{3}He observations in our galaxy are affected by large systematical

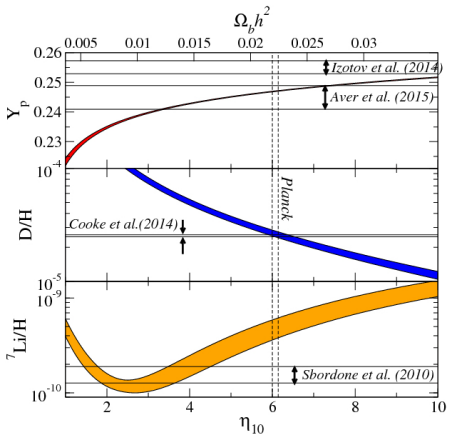

Figure 2: Abundance of light elements produced in standard BBN as a function of η (see text). The vertical region $\Omega_b h^2 = 0.02222 \pm 0.00023$ indicates the constraint from Planck.

uncertainties. In fact, this isotopes is both produced and destroyed in stars so that its primordial amount is quite uncertain [8]. Therefore, up to now ^{3}He does not represent a powerful probe to constrain the ΛCDM model. The abundance of ^7Li is deduced from the strength of its characteristic absorption line at about 680 nm in low metallicity stars in the galactic halo. The observations show that the lithium abundance is almost independent of metallicity ("Spite plateau" [9]). This asymptotic value is interpreted as the primordial ^{7}Li abundance pointing out the tension between observations and theory, referred in literature as the "lithium problem". Finally, a controversial measurement is reported in literature in which the ^{6}Li abundance is obtained from the analysis of metal poor stars absorption spectra [10]. Even though many of the claimed ^{6}Li detections are questionable, for a very few metal-poor stars there still seems to be a significant amount of ^{6}Li ("the second Lithium problem") [11]. The theoretical ^{6}Li abundance has been recently well established by the LUNA collaboration with the first direct measurement of the cross section of the ^{2}H(^{4}He, γ)^{6}Li process at BBN energies.

Although primordial abundances span many orders of magnitude, observations and theory are fairly in agreement, thus confirming the overall validity of BBN

Table 1: Calculated and observed abundances of light isotopes derived from standard BBN and from direct astrophysical observations (see text). In this table, the primordial ^{4}He abundance is given in terms of the baryon mass fraction Y_p i.e. the ratio between helium and baryon densities. The abundance of the other nuclides is expressed by number ratios with respect ^1H.

Isotope	SBBN Theory	Observations
Y_p	0.24771±0.00014[1]	0.254±0.003[2]
D/H	(2.6±0.07)× 10^{-5}[1]	(2.53±0.04)× 10^{-5}[4]
^{3}He/H	(1.00±0.01) × 10^{-5}[14]	(0.9±1.3) × 10^{-5}[8]
^{7}Li/H	(4.68±0.67)×10^{-10}[14]	$(1.23^{+0.68}_{-0.32})\times10^{-10}$[12]
^{6}Li/^{7}Li	(1.5±0.3)×10^{-5}[13]	$\lesssim 10^{-2}$[10]

theory. However, some tension between theory and measurements is apparent, possibly due to the lack of knowledge of astrophysical processes or to physics beyond the Standard Model. As an example, the existence of extra relativistic species beside photons and standard neutrinos increases Y_p and (D/H) [4, 15], while the abundance of lithium isotopes can be affected by new physics, such as the existence of supersymmetric particles at the BBN epoch [16–19]. In this concern, BBN is a powerful tool to constrain particle physics and cosmology, with accuracy depending on astronomical observations and nuclear cross section measurements.

2 Underground Nuclear Astrophysics

BBN started when the temperature of the Universe was low enough to break the equilibrium between deuteron production through p(n,γ)^{2}H ($Q = 2.2\ MeV$) and its photo-dissociation through ^{2}H(γ,n)p ("deuterium bottleneck"). Consequently, BBN processes occur at relatively low energies ($30 \lesssim E_{cm}(keV) \lesssim 300$). In this energy range the cross-section $\sigma(E)$ drops almost exponentially with decreasing energy E, because of the coulomb barrier between the positively charged nuclei. For this reason the cross section is usually factorised as shown in the following formula [20]:

$$\sigma(E) = \frac{S(E)e^{-2\pi\eta^*}}{E} \tag{3}$$

Table 2: *List of the leading reactions and corresponding rate symbols controlling the deuterium abundance after BBN. The last column shows the error on the ratio $(D/H)_{BBN}$ coming from experimental (or theoretical) uncertainties in the cross section of each reaction, for a fixed baryon density $\Omega_b h^2 = 0.02207$ [7].*

Reaction	Rate Symbol	$\sigma_{D/H} \cdot 10^5$
$p(n,\gamma)^2H$	R_1	± 0.002
$d(p,\gamma)^3He$	R_2	± 0.062
$d(d,n)^3He$	R_3	± 0.020
$d(d,p)^3H$	R_4	± 0.0013

$S(E)$ is the astrophysical factor and contains all the nuclear effects. For non-resonant reactions, $S(E)$ is a smoothly varying function of energy. The exponential term takes into account the coulomb barrier. The Sommerfeld parameter η^* is given by $2\pi\eta^* = 31.29 Z_1 Z_2 (\mu/E)^{1/2}$. Z_1 and Z_2 are the nuclear charges of the interacting nuclei, μ is their reduced mass (in units of a.m.u.), and E is the center of mass energy (in units of keV).
At the earth's surface, the low experimental reaction yield makes the measurements severely hampered by the cosmic ray induced background. On the other hand, the cross section extrapolation from high energy data can lead to substantial uncertainties, because the contribution of narrow or subthreshold resonances can partially or completely dominate the reaction rate. To overcome this problem the LUNA collaboration has carried out its measurements underground, at the *"Laboratori Nazionali del Gran Sasso"* (LNGS). Here, the mountain provides a natural shielding which reduces the muon and neutron fluxes by a factor 10^6 and 10^3, respectively. The suppression of the cosmic ray induced background also allows an effective suppression of the γ ray activity by a factor $10^{-2} \div 10^{-5}$, depending on the γ energy.

3 The ^{2}H(p,γ)^{3}He reaction and the primordial deuterium abundance

As shown in table 2, the 3% error of $(D/H)_{BBN}$ is mainly due to the poor knowledge of the $^2H(p,\gamma)^3He$ S-factor (S_{12}) at BBN energies. The experimental data are reported in figure 3. In the relevant energy range only a single

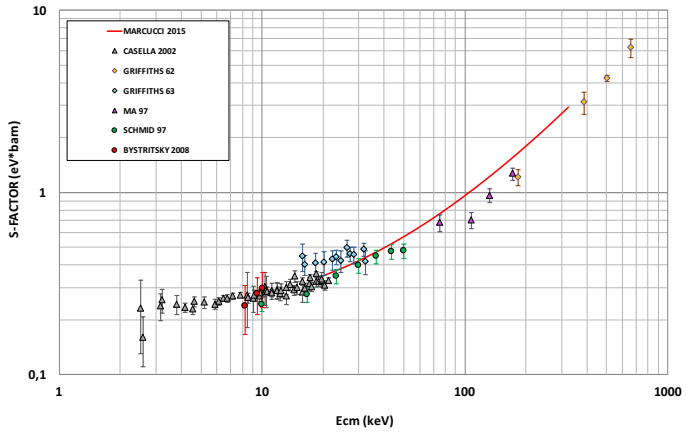

Figure 3: S-factor data for the reaction ${}^2H(p;\gamma)^3He$. the red solid curve shows the prediction of recent ab initio theoretical calculation.

dataset of S_{12} is currently available in [21], in which the authors state a systematic error of 9%. The figure 3 also shows the behaviour of S_{12} as obtained by "*ab initio*" calculations [22]. The concern for ${}^2H(p,\gamma)^3He$ error is made worse by the fact that the theoretical and experimental values of the S_{12} do not agree at the level of 20%. The existing difference between theory and data let some author to adopt the theoretical curve (see for example [15]) or the S_{12} value obtained from measurements [4, 23].
The LUNA collaboration measured the ^{2}H(p,γ)^{3}He reaction in the Solar Gamow peak (2.5 keV $<$ E $<$ 22 keV) in 2002 [24], away from the BBN energy range ($30 \lesssim E_{cm}(keV) \lesssim 300$). However, the LUNA data definitely clarified the situation in the low energy range where previous experimental results differed by more than 50% [25]. Moreover, the inclusion of the new LUNA data increased the accuracy of the S-factor parametrization by a factor 3, when compared to previous analyses [26]. The abundance of deuterium strongly depends on the baryon density (see figure 2). The comparison of observed abundance with the value obtained with standard BBN theory and present literature data provides

the following value for the baryon density [4]:

$$\Omega_{b,0}(BBN) = (2.202 \pm 0.019 \pm 0.041)/h^2 \tag{4}$$

In this equation, $\Omega_{b,0}$ is the present day baryon density of universe and h is the Hubble constant in units of 100 $km\ s^{-1}Mpc^{-1}$. The error terms in eq. (2) reflect the uncertainties in, respectively, observed deuterium abundance and BBN calculation [4]. Therefore, the baryon density accuracy is limited by the the poorly known $d(p,\gamma)^3He$ cross section. The baryon density is derived with similar accuracy from CMB experiments [1]:

$$\Omega_{b,0}(CMB) = (2.22 \pm 0.02)/h^2 \tag{5}$$

It is worth to point out that the baryon density derived from CMB data refers to the recombination epoch (about 380,000 years after Big Bang), while $\Omega_b(BBN)$ is the baryon density during the first minutes of Universe. Hence, the comparison of these two values represents a powerful probe to constrain the ΛCDM model. The deuterium abundance is also sensitive to the expansion rate of Uni-

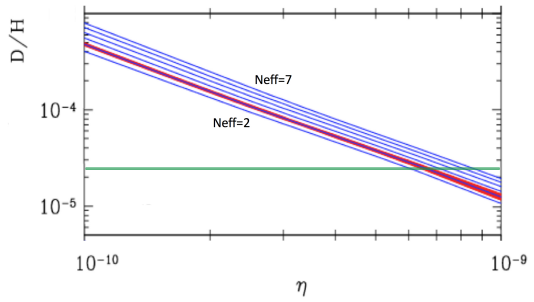

Figure 4: deuterium abundance as function of η. The blue lines indicate yields for a single value (integer plus 0.046) of N_{eff}. The red bands indicates the nuclear uncertainty for $N_{eff} = 3.046$. The horizontal green band indicates observational constraint on D abundance [4].

verse, that depends on the radiation density (see equations 1 and 2). Therefore, it allows to constrain the existence of extra relativistic particles besides photons and the three neutrino species (e.g. sterile neutrinos, hot axions, etc.). Figure 4 shows the calculated abundance of deuterium for several values of N_{eff}.

Again, more than the observed deuterium abundance $(D/H)_{obs}$, the sensitivity to "dark radiation" is limited by $(D/H)_{BBN}$ error, because of the ^{2}H(p,γ)^{3}He cross section uncertainty.
A new study of the $^2H(p,\gamma)^3$He cross section is in progress at LUNA with the 400 kV accelerator [27], with the aim to measure the cross section of the $^2H(p,\gamma)^3$He reaction with an accuracy of $\lesssim 4\%$ and inside the BBN energy range ($30 < E_{cm} < 265$).
The experimental set up for the HPGe-phase consists of a 33 cm long windowless gas target (see figure 5). The target is high purity deuterium (99.9%) circulated at a pressure of 0.3 mbar in the target chamber. The target density has been accurately determined by measuring the pressure and temperature profile. The beam heating effect is of the order of 1% at the typical beam current (about 300 μA), and it has been measured by varying the current intensity from 30 to 400 μA.
A constant temperature gradient calorimeter serves as beam stopper and beam current measuring device. The beam impinges on the hot side of the calorimeter, which is heated up by thermoresistors to a constant temperature of 70 °C provided by a feedback controlled chiller. The cold side is cooled down to 0 °C. The difference between the heating power supply with and without beam is used to calculate the beam current.
Two Germanium detectors are implemented to detect the γ-rays radiating from inside the target chamber. The first detector (main detector, Ge1) is a 130% relative efficiency Germanium detector, faced to the middle of the gas chamber. The second detector (Ge2) has a 120% relative efficiency. It is movable along the beam axis and it is equipped with a lead collimator 50 mm thick, in such a way Ge2 mainly detects photons emitted in front of Ge2 and orthogonal to the beam line. To overcome the problem of measuring the Ge1 efficiency for photons with energy around 5.8 MeV (no source with sufficiently long life time produces photons close to this energy), it has been used a proton beam and a N_2 gas target at 4 mbar, to exploit the $E_R = 259$ keV resonance of the $^{14}N(p,\gamma_1\gamma_2)^{15}O$ reaction. This reaction mainly produces two gamma in cascades with energy 5181+2375 keV (BR=17.1%), or 6172+1384 keV (BR=57.8%) or 6791+765 keV (BR=22.9%). In our working conditions the energy loss of proton beam in the gas target is about 1.32 keV/cm. Therefore, by properly tuning the proton beam energy, it is possible to face the

resonance position in front to the Ge2 detector, (see figure 5). In this way, the detection of the γ_1 photon with Ge1 (e.g. $E_{\gamma_1} = 1384\ keV$) acts as trigger for the coincident γ_2 photon ($E_{\gamma_2} = 6172\ keV$) eventually detected with Ge2. Figure 6 shows the Ge1 efficiency as a function of the position, for all the six energy of photons emitted by the $^{14}N(p,\gamma_1\gamma_2)^{15}O$ reaction. The fine tuning of measured efficiency is obtained by means of a detailed MC simulation, to take into account of the angular correlation between the 2 gammas and to correct other second order effects.
The energy of photons emitted by the $^2H(p,\gamma)^3$He reaction (Q=5.5 MeV) is given by the following relationship (in which c=$\hbar$=1):

$$E_\gamma = \frac{m_p^2 + m_d^2 - m_{He}^2 + 2E_p m_d}{2(E_p + m_d - p_p \cos\theta)} \tag{6}$$

In this formula E_γ is the energy of emitted photon, m_p, m_d, m_{He} are the masses of proton, deuterium and ^3He, respectively. E_p and p_p are the energy and momentum of projectile, and θ is the angle of emitted photon in the laboratory system. This formula shows that the energy of a photon depends on its angle with respect of the beam direction (Doppler effect). Therefore, for a given proton energy, the full detected photons generate a slightly broad peak in the Ge1 energy spectrum, whose shape depends on the angular distribution of emitted photons (see figure 7). The data analysis is presently in progress. Hopefully, the new data will substantially improve the present baryon density determination and will allow to better constrain the existence of "dark radiation". Moreover, the measurement of total and differential cross section represents a solid reference to test theoretical "few body" calculations.

4 The ^{3}He(^{2}H,p)^{4}H reaction and the primordial ^3He abundance

The ^{3}He primordial abundance is mainly determined by the ^{3}He(^{2}H,p)^{4}H process and, to a lower extent, by the D(p,γ)^{3}He reaction. Both reactions were studied at LUNA but outside the energy region of interest for BBN. Differently from the ^{2}H(p,γ)^{3}He case, the LUNA [28, 29] data for the ^{3}He(^{2}H,p)^{4}He reaction did not considerably increase the precision of the ^{3}He primordial abundance estimation. Moreover, it is very difficult to measure the ^{3}He primordial abundance from the astronomical point of view given that this isotope is created and destroyed during the stellar/galactic evolution. This explains why

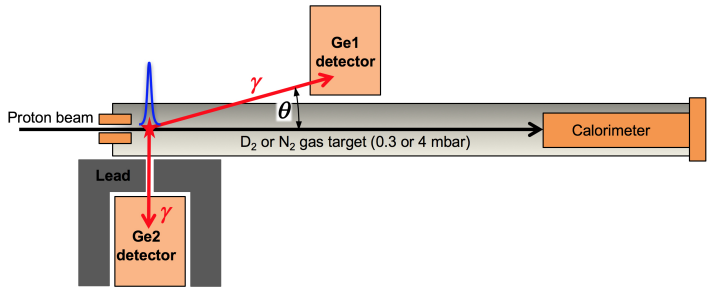

Figure 5: Drawing of the setup used to study the $^2H(p,\gamma)^3$He reaction. The efficiency of Ge1 is measured along the beam axes by exploiting the resonant reaction $^{14}N(p,\gamma_1\gamma_2)^{15}O$ (see text).

^{3}He was never used in the past as a cosmological baryometer due to the huge uncertainty on its observed value.

5 The ^{3}He(α,γ)^{7}Be reaction and the primordial ^7Li abundance

The BBN production of ^{7}Li is dominated by the ^{3}He(α,γ)^{7}Be reaction, with subsequent decay of radioactive ^{7}Be to ^{7}Li. The ^{3}H(α,γ)^{7}Li reaction, on the other hand, plays only a minor role in ^{7}Li production [6]. The ^{3}He(α,γ)^{7}Be reaction was studied at LUNA using two different experimental techniques: First, with the detection of prompt emitted γs by means of a large Ge(Li) detector faced to a windowless target chamber, in which the pressure of ^3He is maintained stable by a differential and recirculating pumping system. Second, the cross section was deduced from the ^7Be activity created in the experiment. Both methods took great advantage of the low radioactivity level of the underground Gran Sasso laboratory [30–32]. For three runs at different beam energies, both methods were used in parallel, allowing to check for possible systematic discrepancies between them. Just such a systematic discrepancy between activation and in-beam γ method had previously been suggested, giving rise to some uncertainty [33]. The LUNA data are shown figure 8), togheter with the results of other experiments. Note that the LUNA data are lower in energy than ever before and well inside the BBN energy region, with an accuracy of about 4%.

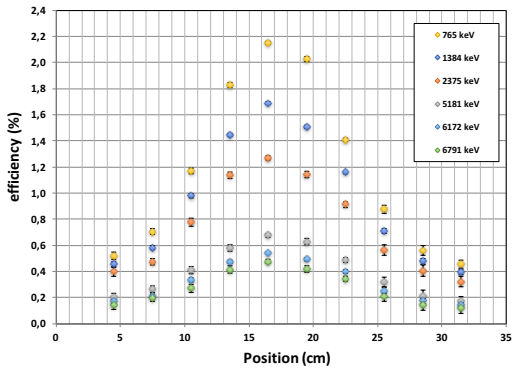

Figure 6: Efficiency of Ge1 detector as a function of the position along the beam line of the emitted photon, for several γ energies (see text).

6 The $^2H(\alpha,\gamma)^6$Li reaction and the primordial ^6Li abundance

If even one of the disputed ^{6}Li/^{7}Li detections, e.g. the one for HD 84937 [39–41], is confirmed, there remains the problem on how to produce ^{6}Li in very primitive stars without at the same time destroying all ^{7}Li. Contrary to the case of ^{7}Li (see previous section), there are no standard physics solutions proposed for the production of ^{6}Li. Standard BBN results in ^{6}Li/^{7}Li = $(2\pm3)\cdot10^{-5}$ [6], much below the detected levels. As possible solution, it has been suggested a catalysis process by long-living particles and non-equilibrium BBN [16–18].
Standard BBN production of ^{6}Li is dominated by just one nuclear reaction, ^{2}H(α,γ)^{6}Li (Q =1.474 MeV) [6]. Before LUNA, only direct measurements far away the BBN energy region were performed [36, 37] and, more recently, an indirect Coulomb dissociation experiments has been done [38]. Finally, for the first time, The ^{2}H(α,γ)^{6}Li cross section was directly measured at BBN energies by LUNA, strongly reducing the error due to extrapolations or theoretical assumptions. The setup used for the LUNA measurement is very similar to the one shown in figure shown in figure 5, but with only the Ge1 detector and an α beam instead of the proton one. The main problem encountered was the very small cross section (about 60 pbarn at E = 133 keV) and the relatively high beam induced background, much higher with respect to the environmental

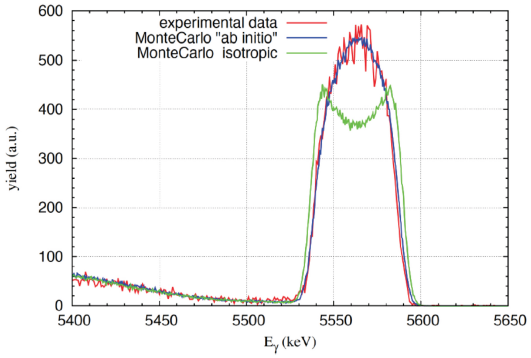

Figure 7: Simulated spectra of the $^2H(p,\gamma)^3He$ reaction, assuming isotropic (green) and ab initio (blue) angular distribution at E_{beam} = 167 keV. The experimental data (red) are also shown. Data have been normalised to remark the close agreement with the ab initio angular distribution.

one but still more than one order of magnitude lower with respect the earth's surface one. The beam induced background is essentially due to deuterons scattered by the incident α beam that interact with other deuterons via the ^{2}H(^{2}H,n)^{3}He reaction, creating a low (about 10 s^{-1}) but steady neutron flux. The neutrons interact with the detector as well as with the setup materials, creating a beam induced background which exceeds the ^{2}H(α,γ)^{6}Li γ signal in the region of interest (1590 keV$<E_\gamma<$1625 keV at E_α = 400 keV) by a factor of more than ten. Hence, a method to subtract the beam induced background has been developed [35].

7 Conclusion

Big Bang Nucleosynthesis is the natural connection between nuclear physics, cosmology and particle physics. The challenge for the next years is the improvement of astronomical observations of D, ^3He, ^6Li, ^7Li and the measurement of BBN cross section with very high accuracy, in order to shed light in many open problems in astrophysics, cosmology, particle physics. In this concern, underground nuclear astrophysics represents a major tool in the "precision era" of cosmology.

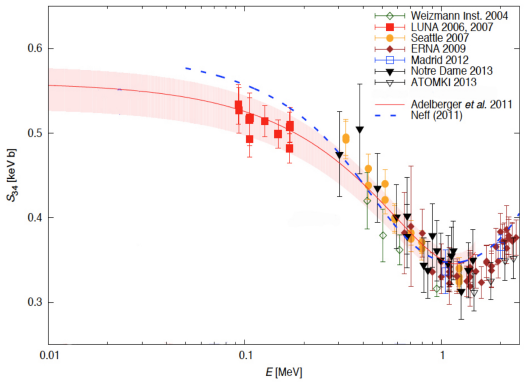

Figure 8: Astrophysical S-factor of the ^{3}He(α,γ)^{7}Be reaction. A theoretical curve rescaled to match the modern data [25], and ab-initio theory [34] are given.

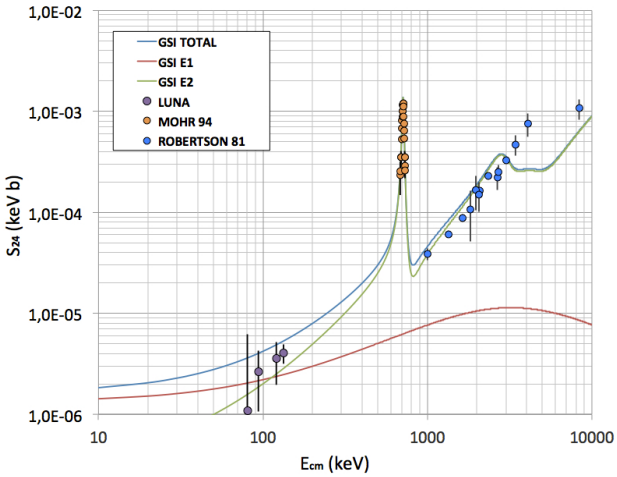

Figure 9: Astrophysical S-factor data of the The $^2H(\alpha,\gamma)^6$Li reaction as a function of the center-of-mass energy. The LUNA data are shown with all the previous direct measurements [35–37] . The continuous lines show the theoretical E1, E2, and total S_{24} factors describing recent Coulomb dissociation data [38].

References

1 . Planck collaboration: AA **594**, A13 (2016)

2 . Y. I. Izotov et al., Astronomy & Astrophysics **558**, (2013) A57.

3 . E. Aver etal., JCAP **1311** (2013) 017.

4 . R. Cooke et al., Astrophys. J. **781** (2014) 31.

5 . L. Sbordone et al., Astron. Astrophys. **522** (2010) A26

6 . P. D. Serpico et al., Journ. of Cosm. and Astrop. Phys. **12**, (2004) 010

7 . E. Di Valentino et al., Physical Review D **90**, (2014) 023543

8 . T. Bania et al., Nature **415**, (2002) 54

9 . M. Spite and F. Spite, Nature **297**, (1982) 483

10 . M. Asplund et al., The Astrophysical Journal **644**, (2006) 229

11 . B. D. Fields, Ann.Rev. of Nucl. and Part. Science **61**, (2011) 47

12 . S. G. Ryan et al., The Astrophysical Journal Letters **530**, (2000) L57

13 . M. Anders et al, Physical Review Letters **113**, (2014) 042501

14 . R. H. Cyburt et al., Rev. Mod. Phys. **88**, (2016) 015004.

15 . K. M. Nollett and G. P. Holder, (2011) arXiv:1112.2683v1

16 . K. Jedamzik and M. Pospelov, New Journ. of Phys. **11** (2009) 105028 (2009)

17 . H. Djapo et al., Physical Review C **85**, (2012) 044602.

18 . M. Pospelov and J. Pradler, Ann. Rev. of Nucl. and Part. Science **60**, (2010) 539

19 . M. Kusakabe et al., Physical Review D **76**, (2007) 121302

20 . C. E. Rolfs, W.S.Rodney, "Cauldrons in the Cosmos", University of Chicago Press, Chicago,1988.

21 . L. Ma et al., Physical Review C **55**, (1997) 588

22 . L. E. Marcucci et al., PRL **116**, 102501 (2016)

23 . PLANCK collaboration: AA **571**, A16 (2014)

24 . C. Casella et al., Nuclear Physics A **706**, (2002) 203

25 . E. G. Adelberger et al., Review of Modern Physics **83**, (2011) 195

26 . R. H. Cyburt, Physical Review D **70**, (2004) 023505

27 . A. Formicola et al: Nucl. Inst. Meth. A **507**, (2003) 609

28 . H. Costantini et al., Physical Letters B **482**, (2000) 43

29 . M. Aliotta et al., Nuclear Physics A **690**, (2001) 790

30 . D. Bemmerer et al., Physical Review Letters **97**, (2006) 122502

31 . Gy. Gyürki et al., Physical Review C **75**, (2007) 035805

32 . F. Confortola et al., Physical Review C **75**, (2007) 065803

33 . E. Adelberger et al., Review of Modern Physics **70**, (1998) 1265

34 . T. Neff, Physical Review Letters **106**, (2011) 042502

35 . D. Trezzi et al., Astroparticle Physics **89** (2017) 57–65

36 . R. G. H. Robertson et al., Physical Review Letters **47**, (1981) 1867

37 . P. Mohr et al., Physical Review C **50**, (1994) 1543

38 . F. Hammache et al., Physical Review C **82**, (2010) 065803

39 . V. V. Smith et al., Astrophysical Journal **408**, (1993) 262

40 . R. Cayrel et al., Astronomy & Astrophysics **343**, (1999) 923

41 . M. Steffen et al., Memorie Societa Astronomica Italiana **22**, (2012) 152

Frascati Physics Series Vol. 66 (2018)
Frontier Objects in Astrophysics and Particle Physics
May 20-26, 2018

AGN outflows as accelerators of CRs and neutrinos

Alessandra Lamastra
INAF - Osservatorio Astronomico di Roma,
via di Frascati 33, 00078 Monte Porzio Catone, Italy
SSDC–ASI, Via del Politecnico, 00133 Roma, Italy

Abstract

Several observations are revealing the widespread occurrence of mildly relativistic wide-angle AGN winds strongly interacting with the gas of their host galaxy. In this scenario strong shocks are expected to form that can accelerate relativistic particles. The interactions of shock-accelerated particles with surrounding interstellar medium and radiation field produce gamma-rays and neutrinos. This is supported by gamma-ray observations of the nearby Seyfert galaxies NGC 1068, NGC 4945, and Circinus with the *Fermi* gamma-ray space telescope. To investigate this hypothesis we study the case of the Seyfert galaxy NGC 1068 that is the brightest of the few non-blazar galaxies detected by *Fermi*, and observations in the sub-millimetre band indicate the presence of a massive molecular AGN-driven outflow. A physical model for the gamma-ray and neutrino emission produced by cosmic rays accelerated by the shocks observed in the central molecular disk of such galaxy is presented. By including this model into a state-of-the-art semi-analytic model of galaxy formation

we derive the contribution to the extragalactic gamma-ray and neutrino backgrounds from AGN winds, and we compare the model predictions with the most recent *Fermi* and IceCube data.

1 Introduction

The discovery that most galaxies host a central supermassive black hole (SMBH), and that the SMBH mass correlates with host galaxies properties, like galaxy stellar mass and velocity dispersion, indicate a link between the formation of SMBH and galaxy evolution [1, 2, 3, 4, 5]. A possible physical origin for this connection is related to AGN feedback. In fact, the energy released during the accretion of matter into a SMBH is about 2 orders of magnitude larger than the binding energy of the host galaxy. Even if a small fraction of this accretion luminosity interacts with the surrounding gas, it can lead to the heating or ejection of the gas, giving rise to the observed scaling relations.

One way of coupling SMBH accretion luminosity to the gas in the host galaxy is through AGN outflows. One form of AGN outflow is jet. Jets are highly collimated outflows of relativistic particles which are present in radio loud AGN, such as blazars. Blazars are AGN in which the jet points towards the Earth, and they represent $\sim 10\%$ of the AGN population. The bulk of the AGN population does not show jet-like structure. The active nucleus of these radio quiet AGN ejects wider-angle winds of lower velocity that are observed in different ionisation states and at different spatial scales (from nuclear to galactic scales) [6].

The possibility that blazars could be sources of cosmic rays (CR) has been discussed in several works, as they are among the brightest gamma-ray emitters in the sky [7]. The detection of nearby Seyfert galaxies NGC 1068, NGC 4945, and Circinus with the *Fermi* gamma-ray space telescope [8, 9] has lead to consider AGN winds as potential CR accelerators. To investigate this possibility we studied the case of the prototypical Seyfert galaxy NGC 1068 that is a nearby Seyfert 2 galaxy that shows both starburst and AGN activities in its central region. This galaxy represents a good test case because it is the brightest of the star forming galaxies detected at by the Large Area Telescope [10] (LAT) on board the *Fermi* telescope , and it shows a massive molecular AGN-driven wind in the central nuclear disk whose properties are

well constrained by observations in the sub-millimetre band [11, 12].

By assuming AGN wind parameters constrained by observations, we derive the gamma-ray and neutrino emission produced by relativistic particles accelerated by the AGN-driven shocks [13], and we compare the model prediction with the *Fermi*-LAT spectrum, and with the gamma-ray spectra corresponding to other models discussed in the literature, like starburst or AGN jet [14, 15, 16].

We also derive the contribution to the extragalactic gamma-ray and neutrino backgrounds from AGN winds, obtained by including the AGN wind model into a state-of-the-art semi-analytic model of galaxy formation, and compare the model predictions with the gamma-ray and neutrino fluxes measured by *Fermi*-LAT and IceCube [17].

2 Gamma-ray and neutrino emission from AGN winds

Similarly to the shocks produced by supernovae explosions, the shocks produced by the interaction of AGN winds with the surrounding interstellar medium (ISM) are expected to accelerate particles to relativistic energies [18, 19, 13]. The wind-ISM interaction is expected to drive a forward shock into the ISM that accelerate the swept-up material, and an inner reverse shock into the nuclear wind decelerating itself, with the two shocks separated by a contact discontinuity [21, 22]. We assume that particles are accelerated by diffusive shock acceleration (DSA) to relativistic energies in the forward shock. The inelastic collisions between shock-accelerated protons and ambient protons produce neutral and charged pions. The decays of neutral pions produce hadronic gamma-ray emission: $\pi^0 \rightarrow \gamma + \gamma$. Leptonic gamma-ray emission is produced by inverse Compton (IC) scattering, and bremsstrahlung radiation of shock-accelerated electrons interacting with the ambient radiation field and ISM. Neutrinos, as well as muons and secondary electrons and positrons, are produced by the decay of charged pions: $\pi^+ \rightarrow \mu^+ + \nu_\mu$ and $\mu^+ \rightarrow e^+ + \nu_e + \overline{\nu}_\mu$; $\pi^- \rightarrow \mu^- + \overline{\nu}_\mu$ and $\mu^- \rightarrow e^- + \overline{\nu}_e + \nu_\mu$.

To calculate the gamma-ray and neutrino spectra produced by these processes we derive the energy distribution of the parent CRs. DSA predicts that the number density per unit volume of accelerated particles can be expressed as a power-law with spectral index $p \simeq 2$ and an exponential high-energy cut-off

23, 24, 25, 26):

$$N(E) = AE^{-p} \exp\left[-\left(\frac{E}{E_{\rm max}}\right)\right]. \quad (1)$$

The normalisation constant A is determined by the total energy supplied to relativistic particles at the shock, and $E_{\rm max}$ is the maximum energy of accelerated particles. As AGN-driven wind is the assumed driver of CR acceleration, the CR particle spectrum must be related to the total energy input from the AGN:

$$\int_{E_{\rm min}}^{E_{\rm max}} N(E) E dE = \eta E_{\rm kin}, \quad (2)$$

where $E_{\rm kin}$ is the wind kinetic energy, η is the fraction of the wind kinetic energy transferred to the particles, and $E_{\rm min}$ is the minimum energy of an accelerated particle which is set to be the particle rest mass. The maximum energy of accelerated particle depends on the age or size of the accelerator, and on the particle energy-loss processes [27].

In this scenario the gamma-ray and neutrino emission from NGC 1068 is determined by the wind dynamics and kinetic energy, and by the magnetic and radiation fields in the shock region. The former are derived from observations in the millimetre band [11, 12]. The observationally derived quantities are the average radial extent of the outflow $R_{\rm out}$ $\simeq$100 pc, the radial outflow velocity $v_{\rm out}$ $\simeq$(100-200) km s^{-1}, and the outflowing gas mass $M_{\rm out}$ $\simeq$1.8$\times$10^7 M$_\odot$, which give a wind kinetic luminosity:

$$L_{\rm kin} = \frac{1}{2} \times \frac{dM_{\rm out}}{dt} \times v_{\rm out}^2 = (0.5 - 1.5) \times 10^{42} ergs^{-1}. \quad (3)$$

For the magnetic field B, we adopt the expression for the volume average ISM magnetic field:

$$B = 6 \times \left(\frac{\Sigma_{\rm gas}}{0.0025 gcm^{-2}}\right)^a \mu G \quad (4)$$

where a $\simeq$(0.4-1), and $\Sigma_{\rm gas}$=(0.01-0.05) g cm^{-2} is the disk gas surface density [28, 29, 30]. The latter corresponds to a gas number density $n_{\rm H}$ =(115-460) cm^{-3} assuming a cylindrical geometry with radius of 350 pc and vertical scale height h $\simeq$10 pc [31]. The gas number density determines the efficiency of hadronic losses and free-free losses. The energy loss of relativistic electrons by IC scattering is determined by the AGN radiation energy density at the

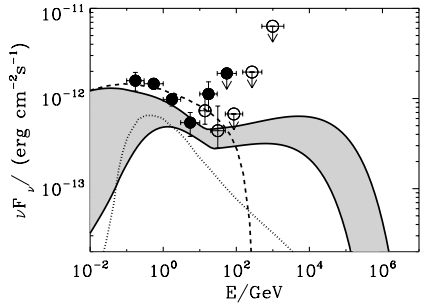

Figure 1: *Gamma-ray spectrum of* NGC 1068 . *The Fermi-LAT points are from* [13] *(filled symbols), and from* [35] *(open symbols). The solid lines show the gamma-ray emission predicted by the AGN wind model* [13]. *The shaded band represents the uncertainty related to the values of particle's acceleration efficiency, ISM density, and magnetic field adopted in the model. The dashed and dotted lines shows the gamma-ray spectrum predicted by the AGN jet model* [16] *and starburst model* [15], *respectively.*

location of the shock $U_{\rm rad} = L_{\rm AGN}/4\pi c R_{\rm out}^2$ where $L_{\rm AGN}$=(0.4-2.1$\times 10^{45}$) erg s^{-1} is the AGN bolometric luminosity [32, 33, 12, 34].

Figure 1 compares the spectrum of NGC 1068 measured by *Fermi*-LAT with the gamma-ray spectrum predicted by the AGN wind model. The latter is calculated through the formulae that relate the CR particle number density with the photon emission from neutral pion decays, IC, and bremmsstrahlung given by [36, 37, 38], respectively. In order to find the model parameters that best reproduce the observed spectrum, the galaxy and AGN parameters were varied within their observational ranges, and both standard particle's acceleration efficiency (η=0.1-0.2 for protons, and η=0.01-0.02 for electrons), and acceleration efficiencies larger than those predicted by the standard acceleration theory were adopted.

Figure 1 also shows the gamma-ray spectra predicted by the starburst model [15] and by the AGN jet model [16]. In the former model the gamma-ray emission is produced by the interactions of CRs accelerated in supernovae-driven winds with the galaxy ISM and radiation field, while in the AGN jet model the gamma-ray emission is produced through IC scattering of infrared

photons from the relativistic electrons accelerated in the misaligned radio jet. The starburst model underestimates the *Fermi*-LAT spectrum, implying a dominant contribution to the gamma-ray emission from the active nucleus. In fact, the observed spectrum at energies < 100 GeV is reproduced reasonably well by both the AGN models. At higher energies, the AGN wind model predict a hard gamma-ray spectrum that extend in the very high energy (VHE) band, which differs significantly from that corresponding to the AGN jet model. Sensitive TeV observations of NGC 1068 with Cherenkov telecopes will allow us to discriminate between the different AGN models. However, the detection of the TeV emission from NGC 1068 is at the limits of the capabilities of currently operating imaging atmospheric Cherenkov telescopes (IACTs). The construction of the Cherenkov Telescope Array (CTA) will afford us a wide (20 GeV-300 TeV) energy range, and will provide an average differential sensitivity a factor 5-20 better with respect to the current IACTs, providing important insight into the physics governing the acceleration of particles in non-relativistic AGN-driven outflows.

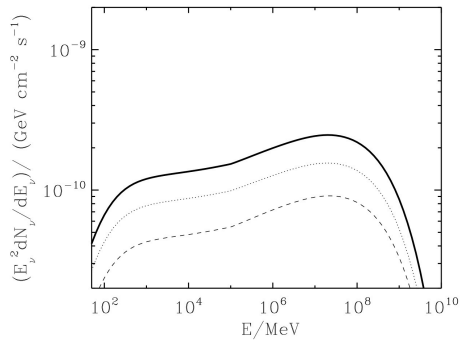

Figure 2: NGC 1068 *neutrino spectrum predicted by the AGN wind model* [13]. *Muon neutrino flux (dotted line), electron neutrino flux (dashed line), total neutrino flux (solid line).*

The hadronic nature of the VHE gamma-ray emission predicted by the AGN wind model implies that NGC 1068 could be a neutrino emitter. Figure 2 shows the neutrino spectrum predicted by the AGN wind model. We combine the neutrino spectrum with the effective area of current and upcoming neutrino detectors to derived the expected number of neutrino events in one year of integration time. The expected number of neutrino events for the ANTARES, IceCube, and KM3NeT detectors are 0.05[1], 0.1, and 0.6 (muon neutrino), respectively. This analysis suggests that in the near future KM3NeT will be able to reveal more effectively the neutrino signal from this kind of source. Moreover, thanks to the angular resolution of the ARCA instrument of $\sim 0.2^\circ$ for neutrino events with energy E>10 TeV (track-like events [39]), KM3NeT will allow us to constrain effectively the position of the possible counterparts of neutrino events, thus providing a possible direct test of the AGN wind model.

3 Extragalactic gamma-ray and neutrino backgrounds from AGN winds

We derive the cumulative gamma-ray and neutrino emission from AGN winds in a cosmological context by including the AGN wind model into a semi-analytic model (SAM) of hierarchical galaxy formation [17]. SAMs connect the formation and evolution of galaxies with the collapse and growth of dark matter (DM) haloes which originate from the gravitational instability of over-dense regions in the primordial DM density field. We use a SAM that includes a physical description of starburst and AGN activities driven by galaxy interaction during their merging histories, and an expanding blast wave model for the mechanism to communicate outwards the energy injected into the interstellar medium by the active nucleus [40]. We assume that all AGN eject winds with kinetic energy that is a fraction ϵ of the AGN bolometric luminosity. The ratio between the wind kinetic power and AGN bolometric luminosity has been observationally determined in a large AGN sample by [6] to be in the range ϵ=0.001-0.1. In our calculation we assume ϵ=0.01 and the maximum efficiency to convert the AGN wind kinetic energy into gamma-rays (calorimetric regime).

[1]this number differs from that reported in Table 2 of [13]. This is the correct number of neutrino events in one year of ANTARES integration time. The low value reported in [13] is due to a bug in the calculation of the ANTARES effective area.

The assumptions adopted in our approach imply that we are maximizing the gamma-ray and neutrino fluxes predicted by the SAM. We find that AGN winds can provide $\sim$35$\pm$15% of the observed extragalactic gamma-ray background in the energy interval E=0.1-1 GeV, $\sim$73$\pm$15% at E=1-10 GeV, and $\sim$60$\pm$20% $E >$10 GeV.

As regards the neutrino emission, we find that the cumulative emission from AGN winds is comparable to the intensity of the neutrino background detected by IceCube, assuming CR spectral index p=2.2. For harder spectral index, the IceCube neutrino flux is overestimated, while for softer spectra AGN winds account for a small fraction of the IceCube signal.

The gamma-ray and neutrino fluxes highly depend on the model parameters and assumptions. For example, neglecting the calorimetric hypothesis, and taking into account the adiabatic cooling of accelerated protons the resulting diffuse gamma-ray and neutrino fluxes are significantly reduced [41]. However, independent of the model details, the intensity and shape of the extragalactic gamma-ray background measured by *Fermi*-LAT already rules out the possibility that the dominant fraction of IceCube neutrinos is accounted for AGN winds for spectral indices p>2.2.

4 Summary and outlook

AGN winds are potential particle accelerators and thus potential gamma-ray and neutrino sources.

The cumulative gamma-ray emission from AGN winds could account from 30% to 80% of the extragalactic gamma-ray background measured by *Fermi*-LAT around 10 GeV.

The contribution to the extragalactic neutrino background from AGN winds strongly depends on the spectral index of the parent CRs.

Further progress in this topic requires better AGN wind and neutrino statistics. In the next future, the improved sensitivity and angular resolution of next generation Cherenkov telescopes and neutrino detectors will allow us to constrain effectively source population models of the extragalctic gamma-ray and neutrino backgrounds.

Acknowledgements

The author thanks Antonio Capone for kindly providing his help in the computation of the ANTARES effective area, and the organizers of the Vulcano workshop for their kind invitation.

References

1. J. Kormendy *et al*, ARA&A **33**, 581 (1995).
2. J. Magorrian *et al*, AJ **115**, 2285 (1998).
3. K. Gebhardt *et al*, ApJ **539**, L13 (2000).
4. L. Ferrarese *et al*, ApJ **539**, L9 (2000).
5. A. Marconi *et al*, ApJ **589**, L21 (2003).
6. F. Fiore *et al*, A&A **601**, A143 (2017).
7. M. Ajello *et al*, ApJ **800**, L27 (2015).
8. M. Ackermann *et al*, ApJ **755**, 164 (2012).
9. M. Hayashida *et al*, ApJ **779**, 131 (2013).
10. W.B. Hatwood *et al*, ApJ **697**, 1071 (2009).
11. M. Krips *et al*, ApJ **736**, 37 (2011).
12. S. Garcia-Burillo *et al*, A&A **567**, A125 (2014).
13. A. Lamastra *et al*, A&A **596**, A68 (2016).
14. T.M. Yoast-Hull *et al*, ApJ **780**, 137 (2014).
15. B. Eichmann *et al*, ApJ **821**, 87 (2016).
16. J.-P. Lenain *et al*, A&A **524**, A72 (2010).
17. A. Lamastra *et al*, A&A **607**, A18 (2017).
18. J. Nims *et al*, MNRAS **447**, 3612 (2015).

19. X. Wang *et al*, Nat. Phys. **12**, 1116 (2016).

20. X. Wang *et al*, JCAP **12**, 012 (2016).

21. C.-A Faucher-Giguere *et al*, MNRAS **425**, 605 (2015).

22. A. King *et al*, ARA&A **53**, 115 (2015).

23. A.R. Bell *et al*, MNRAS **182**, 147 (1978).

24. A.R. Bell *et al*, MNRAS **182**, 443 (1978).

25. R.D. Blandford *et al*, ApJ **221**, L29 (1978).

26. L. Drury *et al*, Space Sci. Rev. **36**, 57 (1983).

27. S.P. Reynolds *et al*, ARA&A **46**, 89 (2008).

28. T. Robishaw *et al*, ApJ **680**, 981 (2008).

29. B.C. Lacki *et al*, ApJ **717**, 1 (2010).

30. J. McBride *et al*, ApJ **780**, 182 (2014).

31. E. Schinnerer *et al*, ApJ **533**, 850 (2000).

32. J.J. Bock *et al*, AJ **120**, 2904 (2000).

33. A. Alonso-Herrero *et al*, ApJ **736**, 82 (2011).

34. A. Marinucci *et al*, MNRAS **456**, L94 (2016).

35. M. Ajello *et al*, ApJS **232**, 18 (2017).

36. S.R. Kelner *et al*, Phys. Rev. D **74**, 034018 (2006).

37. G.R. Blumenthal *et al*, Rev. Mod. Phys. **42**, 237 (1970).

38. F.W. Stecker *et al*, NASA Sp. Publ. **249** (1971).

39. S. Adrian-Martinez *et al*, J. Phys. G: Nuclear Part. Phys. **43** 084001 (2016).

40. N. Menci *et al*, A&A **569** A37 (2014).

41. R.-Y. Liu *et al*, ApJ **858** 9 (2018).

Frascati Physics Series Vol. 66 (2018)
Frontier Objects in Astrophysics and Particle Physics
May 20-26, 2018

SPECTRAL FEATURES IN GALACTIC COSMIC RAYS

Manuela Vecchi
KVI - Center for Advanced Radiation Technology, University of Groningen, The Netherlands and São Carlos Institute of Physics, University of São Paulo, Brasil

Abstract

Recent results by space borne experiments took cosmic ray data to a precision level. These new results are able to challenge the conventional scenario for cosmic ray acceleration and propagation in the Milky Way. In these contributions, written for the XVII Vulcano Workshop, we will give an overview of the latest results of the cosmic ray fluxes, and some possible interpretations will be discussed. These measurements have a common feature, namely the presence of unexpected and still not yet fully understood spectral features.

1 Introduction

We are in a very exciting phase for the field of astroparticle physics: the observation of gravitational waves from the merger of a binary neutron star system [1)] in coincidence with the electromagnetic radiation detected in a broad range of

wavelenghts, in August 2017, marked a milestone for multi-messenger astronomy [2], while the IceCube Collaboration announced, in July 2018, the first evidence for a source of high-energy (TeV) cosmic neutrinos [3]. The BL Lac object TXS 0506+056 is likely to be the first identified source of high energy neutrinos and, consequently, of cosmic rays [4].

More than 100 years after the discovery of V. Hess, the understanding of the origin, the production and propagation mechanisms of cosmic rays (CRs) in the galaxy and beyond is not yet completely understood and cosmic ray physics is still a lively and fascinating field of research.

In the simplified "conventional scenario" [5] to describe the origin and propagation of CRs up to the knee, the primary CRs (e.g. H, He, C) are accelerated in Supernova remnants (SNR) via diffusive shock acceleration up to PeV energies, while their propagation in the interstellar medium (ISM) is described by an homogeneous and energy-dependent diffusion coefficient K. Once primary CRs are released from the sources, they propagate in the interstellar medium (ISM), made mainly by protons and helium nuclei, where they are confined by the magnetic fields for times of the order of a few million years [6]. When primary particles interact with the ISM they produce secondary CRs, like lithium, beryllium, boron as well as antimatter particles such as positrons and antiprotons. This theoretical framework provides featureless and universal (species independent) single power-law energy spectra, and it was supported by experimental results up to one decade ago.

This work aims at providing a concise description of the latest experimental results on direct CR measurements up to the knee, and to provide a quick overview of possible interpretation scenarios. As a further reading, we suggest the review by P. Serpico [7].

2 Spectral features in galactic cosmic ray measurements

The study of spectral features in the fluxes of galactic CRs will provide us with a deeper understanding of the physical processes that occur in the Milky Way.

The "conventional model" was a reasonable option to describe the CR data until the beginning of 2000, when detectors with large acceptance and good resolution were brought to the uppermost layers of the atmosphere or to space: the first hints of deviations from the single power law were provided by the CREAM balloon experiment [9], which suggested an indication for a tran-

sition in the spectral index of CR proton, helium and heavier nuclei. However, the large uncertainties prevented for an unambigous claim. The PAMELA Collaboration published in 2011 precise measurement of proton and helium fluxes [8] between 1 GV to 1.2 TV, showing a clear feature above 200 GeV. The AMS-02 collaboration in 2015 [10] [11] showed that both the proton and helium spectra cannot be described as a single power law (between 1 GV to 1.8 TV), and that a transition in the spectral index takes place above 200 GeV. The top panel of figure 1 shows the flux of CR protons measured by AMS-02 (red dots) as a function of rigidity [1], between 1 GV and 2 TeV. The single power law behaviour, namely $\Phi(R) = CR^{-\gamma}$, is displayed in the dashed line. The transition in the spectral index occurs above 200 GV, and can be described using 5 parameters, as follows:

$$\Phi(R) = CR^{-\gamma}\Big(1 + \frac{R}{R_0}^{\Delta\gamma/s}\Big)^{s} \tag{1}$$

where the parameter s quantifies the smoothness of the transition of the spectral index, from γ to $\gamma + \Delta\gamma$, that occurs at the rigidity R_0. The fit obtained in [10] yelds $\gamma \sim -2.814$ for a transition rigidity value $R_0 \sim 366\ GV$ and $\Delta\gamma \sim 0.133$. The result of the fit to this function is shown in the solid line in the top panel of figure 1. The spectral index as a function of rigidity is shown in the bottom panel of figure 1. The helium flux was also found to show puzzling spectral features. Not only the helium flux cannot be described by a single power law, but the ratio between the proton and the helium flux is rigidity-dependent. This behavior is not expected in the conventional model, and it was also observed in the flux ratio of other species, like C/p, O/p [12]. This can be inferred from figure 2 that shows that helium, carbon and oxygen exibit the same rigidity dependence, with different abundances. The black dots in figure 2 show the CR helium flux as a function of rigidity, while the green and red dots show the flux of heavier CR species: carbon and oxygen. The three species are mainly primary particles.

The AMS-02 recently published precise measurements of lithium, berillium and boron [13], reporting that the three fluxes deviate from a single power law above 200 GV in an identical way. Figure 3 shows the primary and secondary CRs fluxes as a function of rigidity. The magnitude and the rigidity dependence of the Li, Be, and B spectral indices are nearly identical, but

[1] The rigidity is given by the particle momentum over the charge $R = \frac{pc}{Ze}$

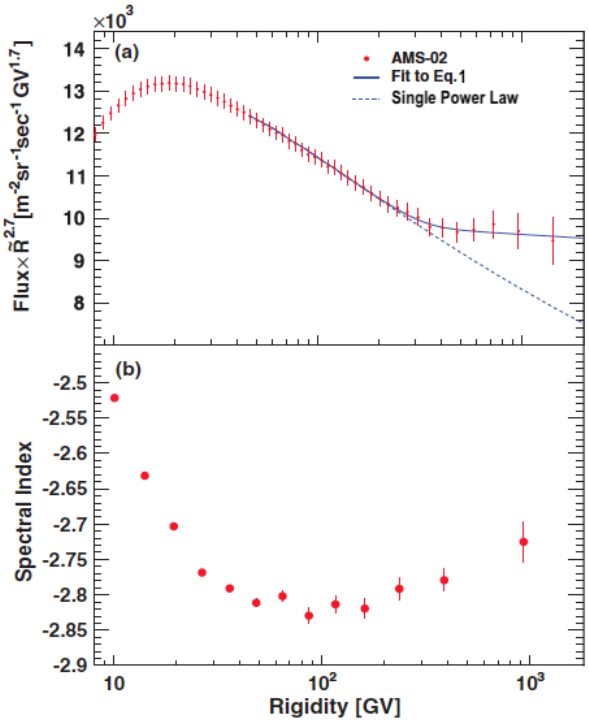

Figure 1: *Top plot:* The AMS proton flux multiplied by $R^{2.7}$ as a function of rigidity. The solid curve indicates the fit of equation 1 to the data. The dashed curve indicates the single power law behavior. *Bottom plot:* The flux spectral index γ as a function of rigidity. Plots adapted from [10].

distinctly different from the rigidity dependence of the He, C, and O spectral indices. It is clear that the flux of CRs in the GeV to TeV range cannot be described by a single power law, moreover the rigidity behavior between primary and secondary species is remarkably different. In particular, above 200 GV, the secondary CRs harden more than the primaries, pointing to the non universality of spectral indices.

Figure 4 shows the spectral index γ for primary (He, C, O) and secondary CR particles (Li,Be,B) as a function of rigidity, between 5 GV and 2 TV. For

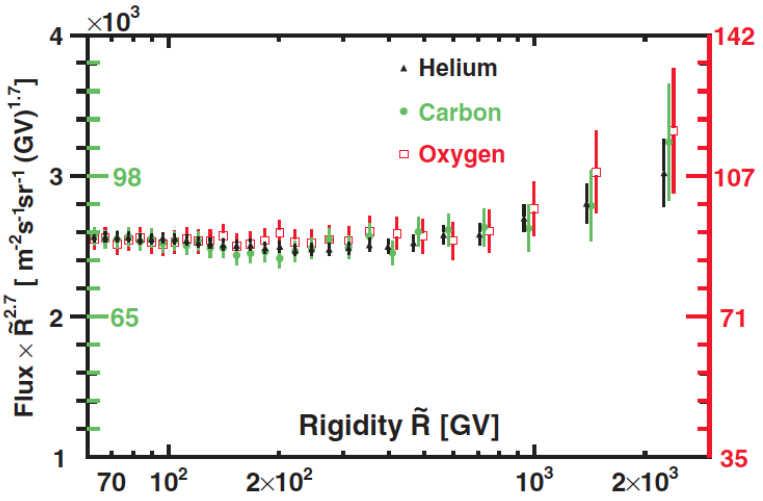

Figure 2: The rigidity dependence of the helium (left black axis), carbon (left green axis), and oxygen (right red axis) fluxes [12]. For clarity, horizontal positions of the helium and oxygen data points above 400 GV are displaced with respect to the carbon.

clarity, the Li, B, He, and O data points are displaced horizontally.

3 Possible scenarios behind the spectral features

The uncertainties on current CR measurements up to the knee are significantly smaller than those of measurements carried out one decade ago. The new observations revealed subtle and unexpected spectral features that require to re-examine or at least improve the theoretical framework used to describe the CR origin and propagation. In order to reproduce the observed transition in the spectral index above 200 GeV, we need the transition to arise either at the source (injection or acceleration) either during the propagation in the Milky Way. A short description of the open scenarios will be given in the following.

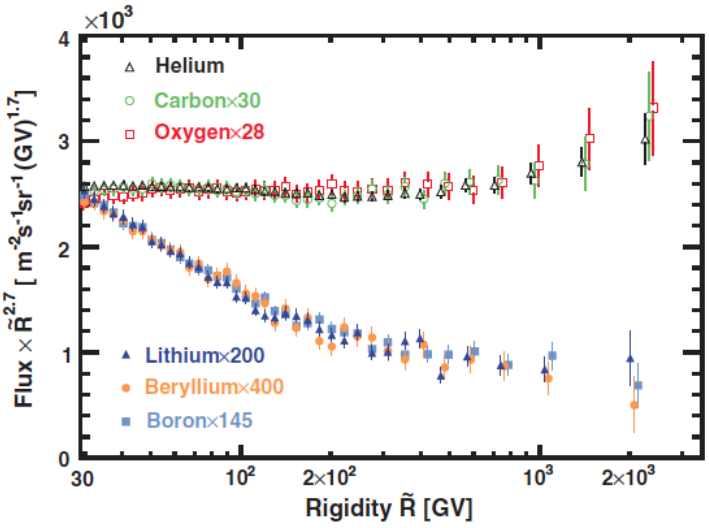

Figure 3: Comparison of the secondary cosmic ray fluxes [13] with the AMS primary cosmic ray fluxes [12] multiplied by $R^{2.7}$ with their total error as a function of rigidity above 30 GV. For display purposes only, the C, O, Li, Be, and B fluxes were rescaled as indicated. For clarity, the He, O, Li, and B data points above 400 GV are displaced horizontally.

3.1 Propagation effects

One class of scenarios connects the observed spectral features with the description of the propagation in the Milky Way. In the conventional "diffusion-convection-reacceleration" scenario [14] the diffusion coefficient is described as a single power law in rigidity, and it is space-independent. A more complex rigidity dependence of the diffusion coefficient is naturally provided by the non-linear effects of propagation presented in [15] and recently rivisited in [16]. Different explainations for the spectral feature include the "two halo model" discussed in [17] , in which CRs are allowed to experience a different type of diffusion when they propagate in the region close to the Galactic disk. In the context of this particular model, recent results of a global Bayesian analysis based on a Markov-Chain Monte-Carlo sampling algorithm are presented in [18].

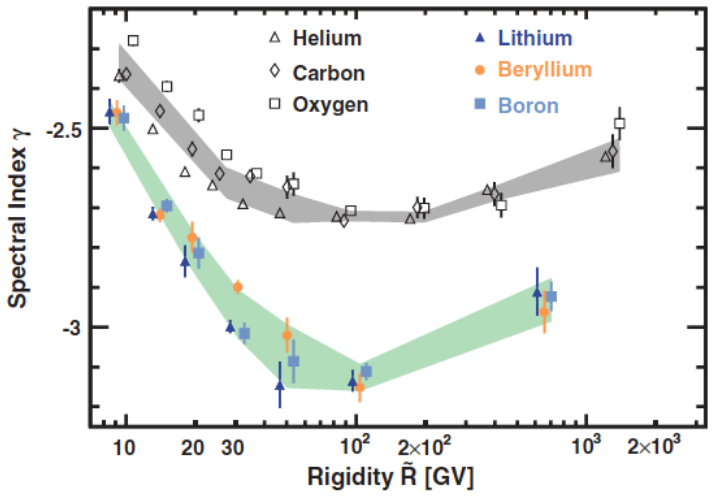

Figure 4: The dependence of the Li, Be, and B spectral indices on rigidity, together with the rigidity dependence of the He, C, and O spectral indices [13].

3.2 Source effect

The space-time discreteness of the galactic sources of CRs, as well as their intrinsic features, such as their age or distance, play an important role in the theoretical description of CR fluxes. It was proposed that spectral features may be caused by the accidental proximity of a source [19]. However, this possibility was estimated to be extremely faint in [20]. In [21] [22] it was argued that these classes of models are often in tension with other complementary observations, namely their predictions on the anisotropy level of the signal is overestimated [22] and they predict a small diffusion effect, that is not in agreement with other measurements, like the boron to carbon flux ratio.

The spectral features in proton and helium fluxes are connected with the rise in the positron fraction in the frame of a two-component SNR scenario in [23]. The low-energy component (below about 500 GeV) in the proton and helium spectrum would be thus a local phenomenon. Nuclei and antiprotons would not show a corresponding rise since dominated by a Galactic ensemble of SNRs, that are on average younger and more efficient to accelerate primary

hadrons at high energies (but unable to accelerate secondaries).

3.3 Re-acceleration effects

The re-acceleration of both primary and secondary CRs in shock fronts, discussed in [24] and recently revised in [25] is another viable option to explain the spectral features in galactic CRs. This model is based on the assumption that the same shocks that are accelerating CR in the sources are also able to re-accelerate the secondary particles and nuclei that happen to be in the vicinity of the acceleration regions where SN explosions take place.

3.4 Secondary to primary ratios as a tool to discriminate between the available scenarios

The most promising tool to discriminate between the different classes of models described above resides in the study of secondary species, like boron or lithium, or alternatively on the secondary-to-primary flux ratios, such as boron to carbon (B/C) and complementary observables, like Li/O. If the transition in the spectral index is already present in the spectra accelerated at the sources, the B/C should appear featureless, since the spectral feature is conveyed from the parent to the daughter nucleus. Conversely, if these features are due to propagation phenomena, a spectral feature should appear visible in a secondary over primary ratio, being roughly twice as pronounced in secondary species. Using cosmic-ray boron to carbon ratio (B/C) data recently released by the AMS-02 experiment [27], the first evidence in favor of a diffusive propagation origin for the broken power-law spectra of protons and helium nuclei was found [28]. Updated results from AMS-02 [13] also including additional flux measurement of other secondary species could consolidate this statement.

4 Conclusions

The new observations from recent space borne CR experiments, like PAMELA and AMS-02, revealed subtle and unexpected spectral features that require to re-examine or at least improve the theoretical framework used to describe the CR origin and propagation. In these proceedings I gave a short overview of the recent results of CR proton, helium and heavier nuclei up to oxygen: these measurements have a common feature, namely the presence of unexpected and

still not yet fully understood spectral features. The main classes of plausible scenarios to interpret the presented results were outlined: the secondary to primary flux ratio, like the B/C, constitute a solid observable to ascertain the origin of galactic CRs. If the contribution from local sources seems disfavoured by the anisotropies and by the measurement of B/C and other secondary-to-primary flux ratios, the competition between the propagation effect and the re-acceleration in the vicinity of the shockwaves is not yet concluded. A conclusive model that coherently describes the numerous and very precise measurements provided by AMS-02 in the past 7 years is eagerly awaited by the scientific community.

5 Acknowledgements

I am grateful to the organizers of the XVII Vulcano Workshop for their kind invitation to talk about such a stimulating topic. I would like to thank Mathieu Boudaud for his constructive comments and suggestions in the final stage of the preparation of this manuscript.

References

1. B. P. Abbott *et al.*, Phys. Rev. Lett. **119**, 161101 (2017).
2. B. P. Abbott *et al.*, Astrophys. J. **848** (2017) no.2, L12
3. M.G. Aartsen *et al.*, Science 361, 147-151 (2018).
4. M. L. Ahnen *et al.*,to appear in Astrophys. J. Lett. arXiv:1807.04300
5. R. Aloisio, P. Blasi, I. De Mitri and S. Petrera, arXiv:1707.06147.
6. P. Blasi, Astron. Astrophys. Rev. **21**, 70 (2013)
7. P. D. Serpico, PoS ICRC **2015**, 009 (2016) `arXiv:1509.04233`
8. O. Adriani *et al.*, Science, vol. 332, pp. 69-72, (2011).
9. H. S. Ahn *et al.*, Astrophys. J. **714**, L89-L93 (2010).
10. M. Aguilar *et al.*, Phys. Rev. Lett. **114**, 171103 (2015).
11. M. Aguilar *et al.*, Phys. Rev. Lett. **115**, no. 21, 211101 (2015).

12. M. Aguilar *et al.*, Phys. Rev. Lett. **119**, no. 25, 251101 (2017).

13. M. Aguilar *et al.*, Phys. Rev. Lett. **120**, no. 2, 021101 (2018).

14. A. W. Strong, I. V. Moskalenko and V. S. Ptuskin, Ann. Rev. Nucl. Part. Sci. **57**, 285 (2007)

15. P. Blasi and E. Amato and P. D. Serpico, Phys. Rev. Lett. **109**, 061101 (2012)

16. C. Evoli, P. Blasi, G. Morlino and R. Aloisio, Phys. Rev. Lett. **121**, no. 2, 021102 (2018)

17. N. Tomassetti, Astrophys. J. **752**, L13 (2012)

18. J. Feng, N. Tomassetti and A. Oliva, Phys. Rev. D **94**, no. 12, 123007 (2016)

19. Thoudam, S. and Hörandel, J. R. 2012, Mon. Not. Roy. Astron. Soc. 421, 1209

20. Y. Genolini, P. Salati, P. Serpico and R. Taillet, Astron. Astrophys. **600**, A68 (2017)

21. P. Blasi and E. Amato, 2012, JCAP, 1, 010

22. P. Blasi and E. Amato, E. 2012, JCAP, 1, 011

23. N. Tomassetti and F. Donato, Astrophys. J. **803**, no. 2, L15 (2015)

24. P. Blasi, G. Morlino, R. Bandiera, E. Amato, & D. Caprioli, Astrophys. J. **755**, 121 (2012)

25. P. Blasi, Mon. Not. Roy. Astron. Soc. **471**, no. 2, 1662 (2017)

26. O. Adriani *et al.*, Astrophys. J. **791**, no. 2, 93 (2014)

27. M. Aguilar *et al.*, Phys. Rev. Lett. **117**, no. 23, 231102 (2016).

28. Y. Genolini *et al.*, Phys. Rev. Lett. **119**, no. 24, 241101 (2017)

Frascati Physics Series Vol. 66 (2018)
Frontier Objects in Astrophysics and Particle Physics
May 20-26, 2018

On overview on Gamma Ray Astrophysics in the *Fermi* era

Francesco Longo
Dipartimento di Fisica, Università degli Studi di Trieste, via Valerio 2, Trieste
Istituto Nazionale di Fisica Nucleare, sezione di Trieste, via Valerio 2, Trieste
on behalf of the *Fermi*-LAT collaboration

Abstract

After 10 years of data taking by the Large Area Telescope (LAT) on board the *Fermi* Gamma-ray Space Telescope, we present an overview of the current status of high-energy gamma-ray astrophysics. Particular emphasis will be given to the broad range of time-domain astrophysics topics studied by the LAT and to the increasingly important multimessenger connections involving gamma-ray sources.

1 Introduction

The second decade of the 2000s will be remembered as the golden era for gamma-ray astrophysic from space. The simultaneous presence in orbit of two satellites, AGILE [1)] and *Fermi* [2)], has made possible the observation in the energy band from 100 MeV to around few TeV with a wealth of information

and details, both in the temporal and in the spectral domain, until now never reached . Gamma astrophysics is also at the crossroads of many other observations concerning, in particular, the connections with the new multimessenger astrophysics, in particular the astrophysics of high-energy neutrinos [3)] and the one related to gravitational wave events [4)].

Both satellites operate in the pair-production regime, typical of photons with an energy greater than 10 MeV. They are both equipped with the same operating configuration, see fig. 1. In this configuration, the gamma-ray detection takes place within a silicon-tungsten converter tracker, equipped with thin layers of high Z material, interspersed with pair of layers covered by Silicon microstrip detectors. The energy of the incident photon is estimated by an electromagnetic calorimeter.

In this contribution only the results obtained by the Fermi Large Area telescope will be discussed.

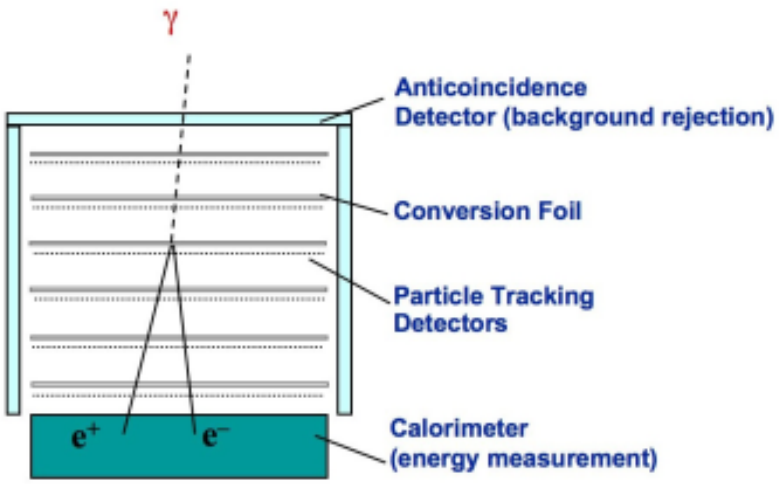

Figure 1: *Typical Gamma-ray Telescope operating configuration.*

2 The Large Area Telescope

The Large Area Telescope (LAT) (see fig. 2) onboard the *Fermi* Gamma-ray Space Telescope (*Fermi*) mission, covers the energy range from below 20 MeV to around few TeV. The LAT is composed of a pair-conversion telescope with 16 modules, containing each a Si-W tracker and an electromagnetic calorimeter, surrounded by a segmented Anticoincidence shield. The LAT has also a versatile trigger and data acquisition system. Each tracker module is made of 16 high-Z (tungsten) converter layers and 18 tracking planes with two orthogonal layers of single-sided silicon micro-strip detectors. Every calorimeter module has 96 CsI(Tl) crystals, arranged again in subsequent orthogonal layers with a total depth of 8.6 radiation lengths. This configuration allows the LAT to obtain a large Field Of View (around ~ 2.5 sr), a very good angular resolution (around 0.1° at 10 GeV), a large effective area and a very good energy resolution (of the order of 10%).More details, particularly, related to data selection and analysis to reject the hugh cosmic ray background to be avoided by gamma-ray space experiments are included in the following publications [2, 5, 6].

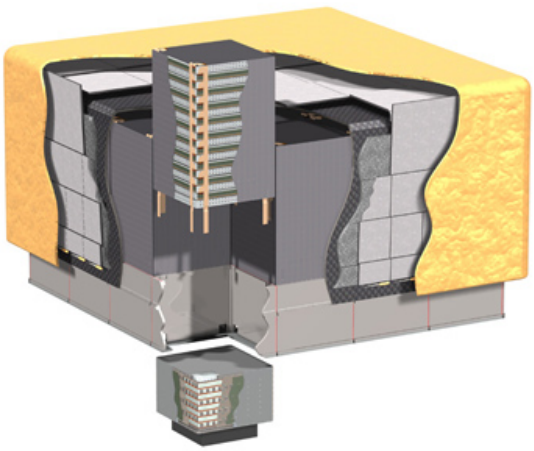

Figure 2: *Schematic view of the Fermi Large Area Telescope. A single tracker and calorimeter module are shown separate from the telescope structure. Also the segmented anticoincidence detector and the thermal blanket can be seen.*

The *Fermi* mission was launched on a Delta Rocket by Cape Canaveral on 11 June 2008. This year its ten years in orbit have been celebrated worldwide and its main results have been discussed at the eighth Fermi Symposium, held in Baltimore, Maryland, in October 2018[1].

The data collected by the LAT instrument were expected to allow the fast notification of high-energy gamma-ray bursts [7)] and transients such as Solar Flares, the regular monitoring of variable sources such as the Active Galactic Nuclei, the realisation of deep catalogs of thousand high-energy sources obtained from a continuous all-sky survey program, the spectral, temporal and spatial studies of point and extended sources, the exploration on different possibilities of the candidate dark matter particles and its distribution on the sky [8)].

3 The traditional topics of Gamma Ray Astrophysics

The typical topics of the Gamma-ray Astrophysics were traditionally grouped around some main themes. Among them the study of the origin and the propagation of cosmic rays, through the analysis of the emission in gamma by the interactions of the same particles and the identification of the nature of the Dark Matter, in the hypothesis that there are some decay or annihilation channels of the candidate dark matter particles into gamma rays. These two issues were in fact among the purposes of the LAT project since the beginning[2], together with the study of pulsars and the analysis of acceleration mechanisms in AGN jets, in addition to high-energy solar physics and the study of the high-energy behaviour of GRBs and of the nature of the unidentified gamma-ray sources. Recently some new issues arised concerning particularly the research of the gamma-ray counterparts of high energy neutrinos and of gravitational wave events.

The main scientific themes concerning celestial sources in the gamma ray band derive, before the launch of *Fermi*, mostly from the observations of the EGRET instrument on board the Compton Gamma ray Observatory [9)]. The wealth of EGRET's observations can be found in the third EGRET catalog (see fig. 3 from [10)]).

[1]Web site: https://fermi.gsfc.nasa.gov/science/mtgs/symposia/2018/

[2]See for example the 1999 GLAST proposal, available at this link: http://www-glast.stanford.edu/pubfiles/proposals/bigprop/

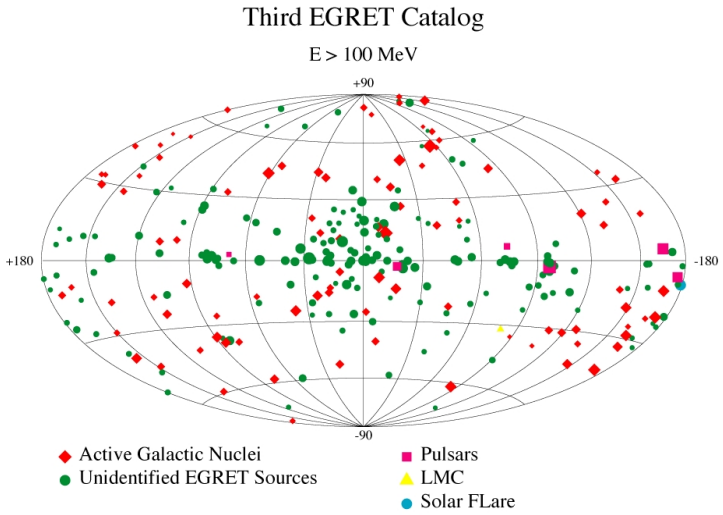

Figure 3: *Location of the sources detected by EGRET in Galactic coordinates and their association as reported in the third EGRET catalog* [10].

On the basis of these observations and thanks to the perspectives opened by *Fermi*-LAT superior capacities, many open questions in gamma astrophysics were expected to be answered by *Fermi*-LAT observations. The questions still open at the time of the *Fermi* launch ranged from the origin of the gamma emission in the solar flarers [11], to the possibility of identifying the signature of the acceleration of protons in the supernova remnants [12], from the understanding of the mechanisms underlying the emission of pulsars in the gamma-ray band [13, 14] and that responsible for the high variability of active galactic nuclei [15] to the nature of the processes underlying the high-energy gamma emission of Gamma Ray Bursts [16]. A possible evidence of an excess of emission in the GeV band around the galactic plane was interpreted as possible evidence of Dark Matter [17]. The design of the LAT instrument and its consequent excellent scientific capabilities have allowed us to solve many of these issues and to open further ones.

4 10 years of Fermi Gamma Ray Astrophysics

Fermi's operations began on August, 4 2008. Since then the instrument has continued to collect data. Currently the FSSC website[3] collects more than $1.15 \cdot 10^9$ photons classified as SOURCE class events [6, 18]. The richness of the gamma sky observed by LAT can be highlighted initially by comparing the whole sky maps observed by EGRET and *Fermi*-LAT. Comparing the two images 4 and 5 you can appreciate the greater wealth of details observed by the latter.

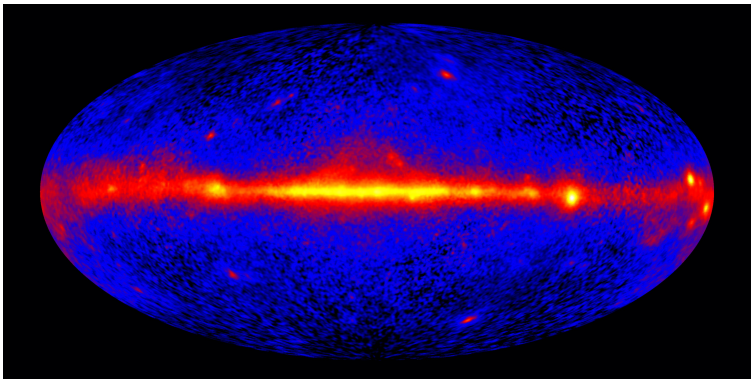

Figure 4: *Image of the Gamma-ray Sky observed by EGRET in Galactic coordinates at energies greater than 100 MeV.*

Starting from the collected data collected, the LAT collaboration has published a series of catalogs [19, 20, 21, 22, 23, 24, 25], in which, thanks to the greater statistics obtained, it was possible to discover a greater number of sources with respect to EGRET. The latest catalog produced in 2015 [22], the so called 3FGL catalog, contains 3033 gamma-ray sources, associated through direct identification or through statistical methods to different categories of sources (see fig.6). The collaboration has then produced several other specialized catalogs over the years (on Pulsars [26, 27], on Supernova Remants [28], on GRBs [29] and on AGNs [30, 31, 32]). Other catalogs are being prepared, e.g. on Solar Flares and on the GRBs detected in 10 years. In order to realize the

[3]Web site: https://fermi.gsfc.nasa.gov/ssc/data/

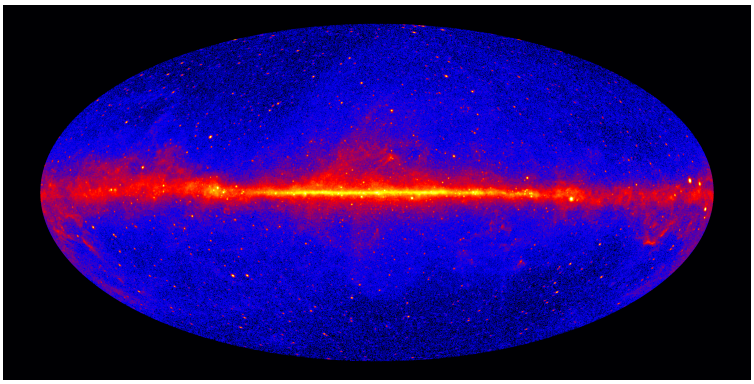

Figure 5: *Image of the Gamma-ray Sky observed by Fermi-LAT in Galactic coordinates at energies greater that 1 GeV. The image is obtained using 10 years of events collected by the LAT and classified as Pass8 Source class events of the PSF3 event type* [18].

catalogs, the Galactic background and the diffuse extragalactic emission had to be studied and modeled, studies by themselves of great value and of great impact [33, 34].Follow-up analysis of catalog work include the recent EBL and Star Formation History measurement [35].

Already these analyses could demonstrate the variety of gamma physics made possible by *Fermi*. Among the various scientific research carried out by the *Fermi* team, it is worth mentioning some that have solved some of the typical problems but are also opening up new frontiers in the traditional fields of gamma-ray astrophysics.

The detection of a typical neutral pion decay spectrum, observed by AGILE [36] and *Fermi*-LAT [37] in the case of middle aged Supernova Remnants IC443 and W44 seems finally to resolve the long debate on the origin of cosmic rays and their acceleration by a diffusive shock between the rest of the Supernova and the interstellar medium. The observation of 3 Behind the Limb Solar Flares [38, 39] has gained an increasing interest in the community of solar astrophysicists because it allows the study of the energy release and of the acceleration mechanisms at work in solar flares and consequent coronal mass ejections. Active galactic nuclei were found to be gamma-ray emitters up to

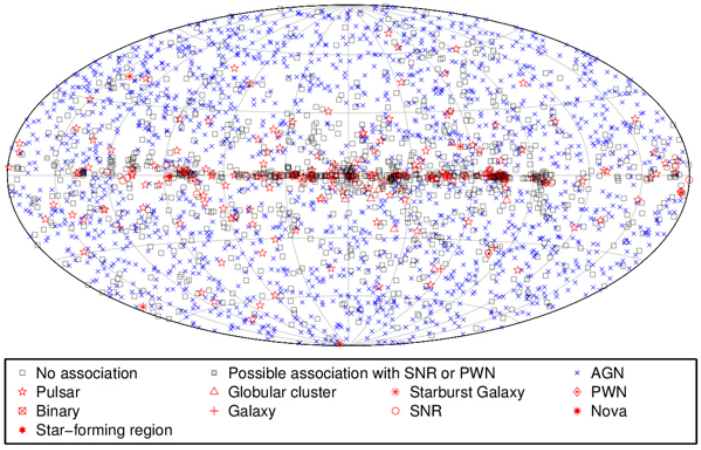

Figure 6: *Location and Associations of the 3FGL gamma-ray sources* [22)]

high redshift [40)]. This could shed light on the formation of Supermassive Black Holes in the Early Universe.

The search for Dark Matter is still continuing [41)], in fact no gamma radiation in the directions of dwarf galaxies [42)] have been found at the time, nor has it been the excess of gamma radiation observed by EGRET [43)], nor a line tentatively reported a few years ago [44, 45)]. An interesting study could however be a possible excess emission in the direction of the galactic center [46)], whose interpretation is still matter for great debate [47, 48)].

Among the study of stationary sources, in my opinion, the discovery of the *Fermi* Bubbles [49, 50)], a large structure (about 50000 thousand light years tall, which extend from the region of the galactic plane perpendicular to it) is of great importance. Their huge dimension and their characteristics of spectral homogeneity make their interpretation difficult (see fig. 7).

5 Time domain astrophysics

One of the current more active developments in multi-wavelenght astrophysics is the so-called "Time Domain Astrophysics", ie the identification of phenomena with particular characteristics with respect to their temporal behaviour. The

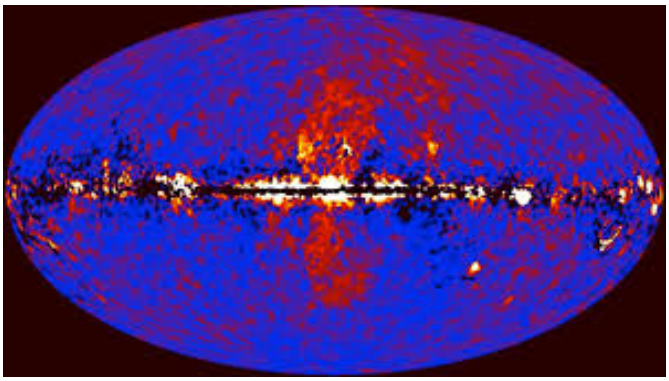

Figure 7: *Image of the Fermi "Bubbles" in Galactic coordinates (see e.g.* [50]*)*

rapid analysis of data carried out on the ground by the *Fermi* collaboration, by means of a series of algorithms developed for the purpose [51, 52] is in fact leading to several interesting results. We report only a few of them.

The research of the counterparts of the unidentified gamma sources has led the collaboration to the identification of new Pulsars with periods in the range of ms by various radio telescopes in the world [53]. A particular technique has led to the identification of pulsars that emit only in the gamma-ray band [54], including the first pulsar detected by *Fermi* [55] and the first so-called ms-pulsar emitting only in the gamma-ray band [56]. The study of pulsars also allowed the identification in the Large Magellanic Cloud of the first extragalactic gamma-ray pulsar [57].

A new class of sources revealed by LAT is the class of novae, galactic transients lasting a few weeks associated with explosive events related to white dwarfs in binary systems [58]

The study of variability of the emission by AGNs has led to the identification, for example, of a possible periodicity, detectable also in other bands, by the AGN PG1553+113 [59] whose origin is still widely discussed. A further interesting observation by LAT was the gravitational lensing of the blazar B0218+357 [60], observable not through multiple images but through the repetition of its temporal features.

Another unexpected result was also the detection of long duration GRBs

and Solar Flares, such as GRB130427A [61] or the Solar Flare of March 2012 [62], both lasting up to 20 hours. Their study is shedding light on the emissive mechanisms of respectively leptonic and hadronic nature at work in such sources.

The most unexpected temporal variability, however, was certainly the identification of the flare emission by the Crab Nebula (see fig. 8, by both AGILE [63] and *Fermi* [64, 65], which is leading to a profound revision of the theoretical processes at work in Pulsar Wind nebulae.

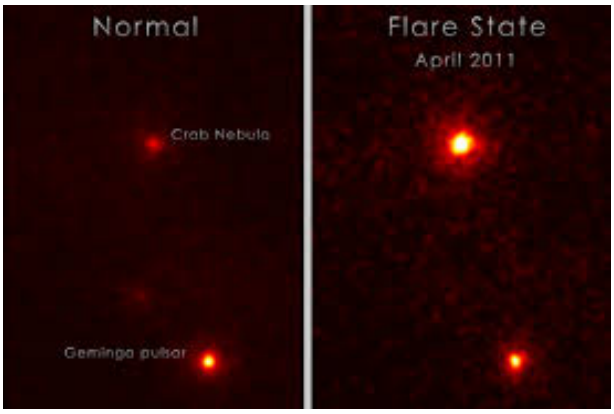

Figure 8: *Image of the Crab in its Quiet and Flaring state of 2011*

6 Multimessenger Astrophysics

The most exciting results have been achieved in recent years thanks to the identification of electromagnetic counterparts of other signals, in particular that of very high energy neutrinos, in the case of blazar B1424-418 [66] and with a larger multifrequency coverage the more recent one (see fig. 9, the one of blazar PKS 0506+056 [3].

A fundamental result for the *Fermi* mission was the identification by the GBM instrument on board of *Fermi* of the electromagnetic counterpart of the gravitational wave GW170817 [67], associated with the merger of two neutron stars. In this last case the LAT instrument was in the South Atlantic Anomaly and therefore could not observe GRB 170817A, of which it could investigate

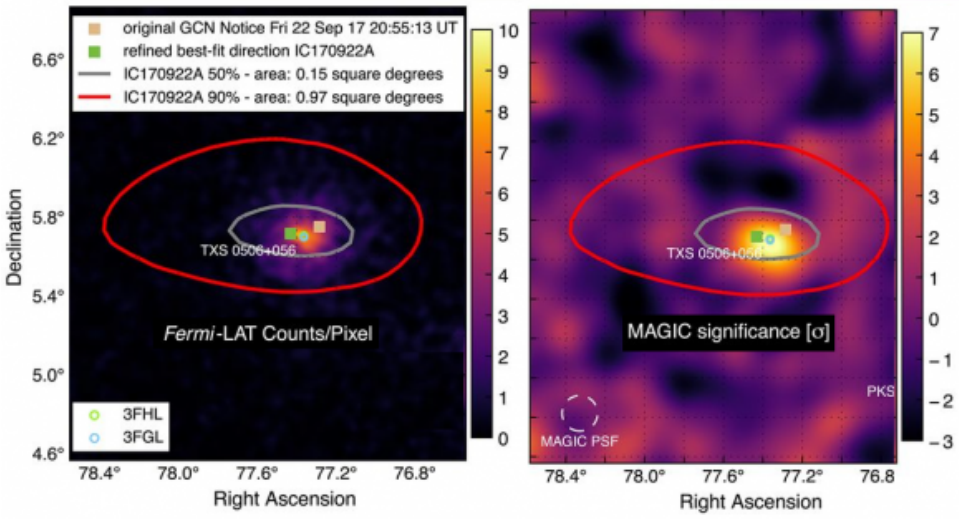

Figure 9: *Identification of the candidate EM counterpart of the Icecube Neutrino 170922A* [3)]

the high-energy emission [68)].

7 Towards the future

The LAT onboard the *Fermi* mission has certainly brought great light in the field of high-energy gamma-ray astrophysics. Its role in multiwavelength astrophysics and in newborn multimessenger astronomy has been really decisive in these years. The design and construction of new very high-energy instruments such as CTA [69)] is underway, from which we expect a more profound coverage of the gamma-ray observation from Earth with energies above 20 GeV. Surely the road traced by LAT, thanks to the identification of new classes of sources and new traces of emissive phenomena is making the gamma-ray band more and more a cornerstone for the astrophysics of the future. Hopefully the LAT will still be operational when CTA will fully operational. Finally, various proposals are being studied to create new structures on satellites such as the eASTROGAM satellite [70)] or the AMEGO [71)] instrument.

8 Conclusions

Fermi is still a very active astroparticle mission exploring the high to very high energy gamma-ray sky. The results in its first 10 years of operatations raised significant interest in a broad community of scientists, including astrophysicsists and particle and nuclear physicists. After Fermi, the Gamma-ray Astrophysics from space has reached its full maturity.

References

1. M. Tavani *et al*, Astronomy and Astrophysics **502**, 995 (2009).
2. W.B. Atwood *et al*, The Astrophysical Journal **697**, 1071 (2009).
3. M.G. Aartsen *et al*, Science **361**, 1378 (2018).
4. B.P. Abbott *et al*, Physical Review Letters **119**, 161101 (2018).
5. M. Ackermann *et al*, The Astrophysical Journal Supplement, **203**, 4 (2012).
6. W.B. Atwood *et al*, The Astrophysical Journal **774**, 76 (2013).
7. D.L. Band *et al* The Astrophysical Journal **701**, 1673 (2009)
8. E.A. Baltz *et al*, Journal of Cosmology and Astroparticle Physics **07**, 013 (2008).
9. G. Kanbach *et al*, Space Science Reviews, **49**, 69, (1988)
10. R.C. Hartman *et al*, The Astrophysical Journal Supplement Series **123**, 79 (1999).
11. E.J Schneid *et al*, Astronomy and Astrophysics Supplement **120**, 299 (1996).
12. D.F. Torres *et al*Physics Reports **382**, 303 (2003).
13. J.K. Daugherty and A.K. Harding, The Astrophysical Journal **458**, 278 (1996).
14. J. Chiang and R.W. Romani, The Astrophysical Journal **436**, 754 (1994).
15. R.C. Hartman *et al*, The Astrophysical Journal Letters **385**, L1 (1992).

16. K. Hurley *et al*, Nature **372**, 652 (1994).

17. W. de Boer *et al*, Astronomy and Astrophysics **444**, 51 (2005).

18. Web site: https://fermi.gsfc.nasa.gov/ssc/data/analysis/documentation/Cicerone/

19. A.A. Abdo *et al*, The Astrophysical Journal Supplement Series **183**, 46 (2009).

20. A.A. Abdo *et al*, The Astrophysical Journal Supplement Series **188**, 405 (2010).

21. P.L. Nolan *et al*, The Astrophysical Journal Supplement Series **199**, 31 (2012).

22. F. Acero *et al*, The Astrophysical Journal Supplement Series **218**, 23 (2015).

23. M. Ackermann *et al*, The Astrophysical Journal Supplement Series **209**, 34 (2013).

24. M. Ackermann *et al*, The Astrophysical Journal Supplement Series **222**, 5 (2016).

25. M. Ajello *et al*, The Astrophysical Journal Supplement Series **232**, 18 (2017).

26. A.A. Abdo *et al*, The Astrophysical Journal Supplement **187**, 460 (2010).

27. A.A. Abdo *et al*, The Astrophysical Journal Supplement **208**, 17 (2013).

28. F. Acero *et al*, The Astrophysical Journal Supplement Series **224**, 8 (2016).

29. M. Ackermann *et al*, The Astrophysical Journal Supplement **209**, 11 (2013).

30. A.A. Abdo *et al*, The Astrophysical Journal **715**, 429 (2010).

31. M. Ackermann *et al*, The Astrophysical Journal **743**, 171 (2011).

32. M. Ackermann *et al*, The Astrophysical Journal **810**, 14 (2015).

33. F. Acero *et al*, The Astrophysical Journal Supplement Series, **223**, 26 (2016).

34. M. Ackermann *et al*, The Astrophysical Journal **799**, 86 (2015).

35. S. Abdollahi *et al*, Science **362**, 6418 (2018).

36. A. Giuliani *et al*, The Astrophysical Journal Letters **742**, L30 (2011).

37. M. Ackermann *et al*, Science **339**, 807 (2013).

38. M. Pesce-Rollins *et al*, The Astrophysical Journal Letters **805**, L15 (2015).

39. M. Ackermann *et al*, The Astrophysical Journal **835**, 219 (2017).

40. M. Ackermann *et al*, The Astrophysical Journal **820**, 72 (2016).

41. E. Charles *et al*, Physics Reports **636**, 1 (2016).

42. A. Albert *et al*, The Astrophysical Journal **834**, 15 (2017).

43. A.A. Abdo *et al*, Physical Review Letters **103**, 251101 (2009).

44. C. Weniger, Journal of Cosmology and Astroparticle Physics **08**, 007 (2012).

45. M. Ackermann *et al*, Physical Review D **91**, 122002 (2015).

46. F. Calore *et al*, Physical Review D **91**, 063003 (2015)

47. M. Ajello *et al*, The Astrophysical Journal **819**, 44 (2016).

48. M. Ackermann *et al*, The Astrophysical Journal **840**, 43 (2017).

49. M. Su, T.R. Slatyer and D.P. Finkbeiner, The Astrophysical Journal **724**, 1044 (2010).

50. M. Ackermann *et al*, The Astrophysical Journal, **793**, 64 (2014).

51. M. Ackermann *et al*, The Astrophysical Journal **771**, 57 (2013).

52. G. Vianello *et al*, The Astrophysical Journal Letters **841**, L16 (2017).

53. A.A. Abdo *et al*, Science **325**, 848 (2009).

54. W.B. Atwood *et al*, The Astrophysical Journal **652**, L49 (2006).

55. A.A. Abdo *et al*, Science **322**, 1218 (2008).

56. H.J Pletsch *et al*, Science **338**, 1314 (2012).

57. M. Ackermann *et al*, Science **350**, 801 (2015).

58. M. Ackermann *et al*, Science **345**, 554 (2014).

59. M. Ackermann *et al*, The Astrophysical Journal **813**, L41 (2015).

60. C.C. Cheung *et al*, The Astrophysical Journal Letters **782**, L14 (2014).

61. M. Ackermann *et al*, Science **343**, 42 (2014).

62. M. Ajello *et al*, The Astrophysical Journal **789** 20 (2014)

63. M. Tavani *et al*, Science **331**, 736 (2011).

64. A.A. Abdo *et al*, Science **331**, 739 (2011).

65. R. Buehler *et al*, The Astrophysical Journal **749** 26 (2012)

66. M. Kadler *et al*, Nature Physics **12**, 807 (2016)

67. B.P. Abbott *et al*, The Astrophysical Journal Letters **848**, L13 (2017).

68. M. Ajello *et al*, The Astrophysical Journal **861**, 85 (2018)

69. B.S. Acharya: arXiv e-print 1709.07997 (2017)

70. A. de Angelis *et al*, Journal of High Energy Astrophysics, **19**, 1 (2018).

71. A. Moiseev *et al*, 35th International Cosmic Ray Conference. Proceedings of Science, **301**. 798

Frascati Physics Series Vol. 66 (2018)
Frontier Objects in Astrophysics and Particle Physics
May 20-26, 2018

HIGHLIGHTS FROM AGILE

Carlotta Pittori[1,2], on behalf of the AGILE Collaboration
[1] *ASI - SSDC, Via del Politecnico snc, I-00133 Roma, Italy*
[2] *INAF-OAR, via Frascati 33, I-00078 Monte Porzio Catone (Roma), Italy*

Abstract

AGILE is an Italian Space Agency (ASI) space mission devoted to gamma-ray observations in the 30 MeV–50 GeV energy range, with simultaneous X-ray imaging in the 18–60 keV band. Launched in April 2007, the AGILE satellite is in its 11th year of operations in orbit, and it is substantially contributing to improve our knowledge of the high-energy gamma-ray sky. I will summarize some AGILE highlights, focusing in particular on compact objects emitting broad-band non-thermal electromagnetic radiation, also believed to be emitters of other multi-messenger signals, such as cosmic rays, neutrinos, and gravitational waves.

1 Introduction

I present an overview of the main AGILE γ-ray satellite scientific highlights during its 11 years of observations. AGILE (Astro-rivelatore Gamma a Im-

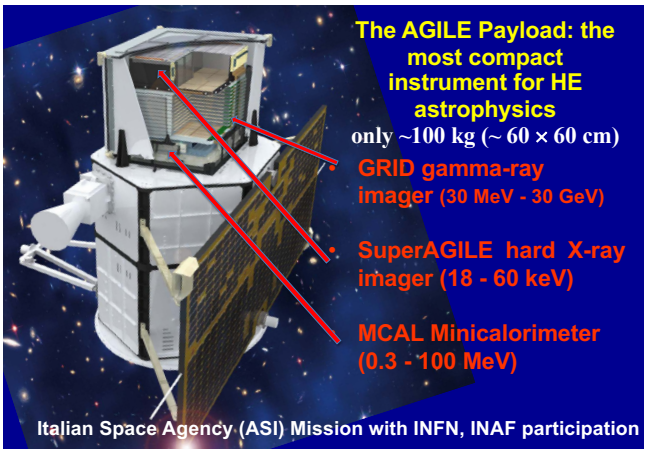

Figure 1: *The AGILE Payload: state-of-the-art Silicon detectors integrated in a very compact instrument for high-energy astrophysics in the 30 MeV - 30 GeV energy range, with simultaneous X-ray imaging capability in the 18-60 keV band.*

magini LEggero), launched on April 23, 2007, is a γ-ray astrophysics mission of the Italian Space Agency (ASI), with INAF, INFN and CIFS participation [1)]. The AGILE scientific payload consists of three independent instruments: the Gamma Ray Imager Detector (GRID) sensitive in the energy range 30 MeV–30 GeV, a hard X-ray imager on top (Super-AGILE) sensitive in the energy range 18–60 keV, and a Mini-Calorimeter (MCAL) sensitive in the energy range 350 keV to 100 MeV that works both as a slave of the GRID and as an autonomous detector for transient events. An anticoincidence system (AC) of segmented plastic scintillators is used for particle background rejection. The small high-tech telescope (see Fig. 1), designed for a nominal operative life of only two years, continues its exploration of the high-energy Universe, also providing a crucial contribution in the search of electromagnetic counterparts of gravitational waves (GW) and neutrinos.

2 New lessons from high-energy astrophysics

High-energy astrophysics has enjoyed a rapid development in the past decades, and recent important results and progress were achieved by the γ-ray AGILE [1)] and Fermi [2)] satellites observations. This branch of astrophysics studies the non-thermal emission in the Universe, mainly coming from violent astrophysical environments near compact objects, such as neutron stars and super-massive or stellar-size black holes.

Unexpected discovery of intense γ-ray transients at energies above 100 MeV on short timescales ($<$ minutes, days) are detected in different astrophysical systems, both Galactic and extragalactic, challenging current models of particle acceleration. The observation of brief and very bright flares of energetic γ-rays suggests that pairs are accelerated to PeV energies on short timescales, implying very fast and efficient acceleration mechanism from very small emission sites. Such rapid intra-day accelerations cannot be driven by shocks, and they may highlight the role of the magnetic field, the importance of relativistic magnetic reconnection and plasma instabilities in astrophysical sources.

Furthermore the compact objects emitting broad-band non-thermal electromagnetic radiation are also believed to be emitters of other multi-messenger signals, such as cosmic rays, neutrinos, and gravitational waves.

3 AGILE main scientific results

I present here a selection of the main AGILE science highlights after 11 years of operations.

3.1 AGILE detections of microquasar γ-ray emission

AGILE detected for the first time several γ-ray flares above 100 MeV from Cygnus X-3 microquasar, and also a weak persistent emission by integrating all available data collected at that time between November 2007 and June 23, 2009 [3)]. Galactic microquasars are binary systems with a neutron star or a stellar-mass black hole accreting gas from a companion star. They were already known to produce relativistic jets, generally together with radio flares. Before the AGILE discovery of γ-ray flares thousands of times more energetic than quiescent states, no systematic evidence for the acceleration of particles to GeV

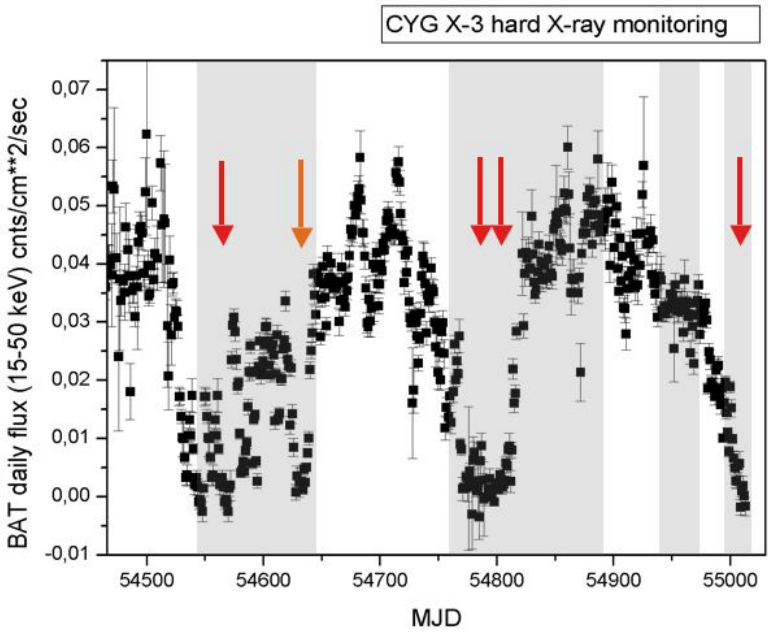

Figure 2: *Hard-X-ray flux from Cygnus X-3 from the Burst Alert Telescope (BAT) on board NASAs Swift spacecraft, between 1 January 2008 and 30 June 2009. The red arrows mark the major gamma-ray flares of Cygnus X-3 as detected by the AGILE instrument* [3].

or higher energies was known from such systems. A clear repetitive pattern of temporal correlations between the γ-ray flares and transitional spectral states of the radio and X-ray emission was identified by AGILE. Particle acceleration occurs in coincidence with low hard-X-ray fluxes or during transitions from low to high hard-X-ray fluxes, and the γ-ray flares usually appear before major radio flares, see Fig. 2.

This important AGILE discovery has been subsequently confirmed by the Fermi satellite [4], which was also able to unambigously identify the temporal signature of the binary system by measuring the the 4.8 hours orbital period in γ-rays.

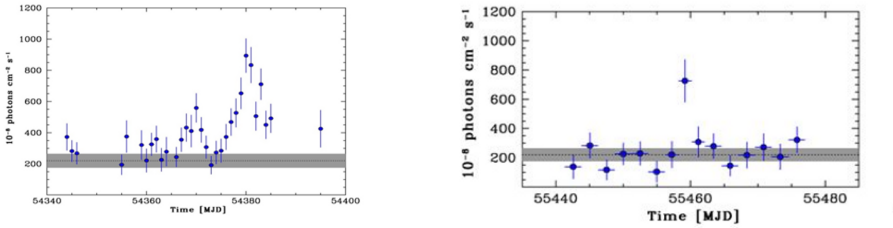

Figure 3: *Left panel: the first Crab Nebula flare seen by AGILE in 2007* [6, 7]. *Right panel: the Crab Nebula flare seen by AGILE in 2010, publicly announced to the Scientific Community with an Astronomer's Telegram* [5]. *Time is given in Modified Julian Day (MJD). The dotted line and grey band show the average Crab flux and the 3σ uncertainty range.*

3.2 The variable Crab Nebula

The prestigious High Energy Astrophysics Division (HEAD) Bruno Rossi International Prize has been awarded in 2012 to the AGILE PI, Marco Tavani, and the AGILE team for the unexpected discovery in 2010 of strong and rapid γ-ray flares from the Crab Nebula over daily timescales [5, 6].

The discovery of flaring activity from the Crab nebula was made possible also thanks to the sky monitoring capability and fast ground segment alert system of the AGILE satellite, which observed a previous giant flare from the Crab Nebula in October, 2007, reported in the First AGILE-GRID source catalog as a possible unexpected brief flux increase [7]. The Crab system was considered to be an almost ideal standard candle, a nearly constant source (at a level of few percent) from optical to γ-ray energies, with possible long-term nebular flux variations over a few-year timescale reported in the hard X-ray range. AGILE made the first public announcement of a rapid γ-ray flare from the Crab Nebula on September 22, 2010 [5, 6], which was confirmed the next day by the Fermi Observatory [8, 9].

In Fig. 3, the left panel shows the AGILE lightcurve during the period September 27 – October 12, 2007 with the satellite in pointing mode and 1-

day binning; the right panel shows the AGILE lightcurve during the period September 2 – October 8, 2010 in "spinning" observing mode and 2-day binning near the flare. Statistically significant evidence for week-long and less intense episodes of enhanced γ-ray emission, called "waves", was also identified by considering AGILE and Fermi-LAT gamma-ray data above 100 MeV [10].

Gamma-ray data provide evidence for particle acceleration mechanisms in nebular shock regions more efficient than previously expected from theoretical models. Plasma instabilities possibly related to magnetic field reconnection in specific sites in the Nebula can be envisioned. We estimate a recurrence rate for strong γ-ray Crab Nebula flares of about ~ 1/year.

3.3 Bright γ-ray flaring blazars

Blazars are a subclass of active galactic nuclei (AGN) with relativistic jets pointing towards the observer. Their emission is dominated by variable non-thermal processes, and it extends from the radio to the γ-ray band above 100 MeV, up to TeV γ-rays. Blazars are classified into flat-spectrum radio quasars (FSRQ) or BL Lacertae (BL Lac) objects, with very different optical spectra: FSRQs have strong, broad optical emission lines, while BL Lacs have a completely featureless optical spectrum, or at most weak emission lines and some absorption features (e.g., see [11]). The blazar spectral energy distribution (SED) is in general characterized by two broad bumps: a low-energy one, spanning from the radio to the X-ray band, attributed to synchrotron radiation, and the high-energy one, from the X-ray to the γ-ray band, thought to be due to inverse Compton (IC) emission. In the leptonic scenario this second component is due to relativistic energetic electrons scattering their own synchrotron photons (Synchrotron self-Compton, SSC) or photons external to the jet (External Compton, EC).

Blazars of both flavors have been found to be highly variable, and particularly so in γ-rays. Correlated variability between X-rays and γ-rays is usually well explained in the SSC or EC framework [12]. In fact, a new class of "orphan" γ-ray flares from FSRQ blazars is now emerging from observations. AGILE observations of strong γ-ray flares from FSRQ such as 3C 454.3 [13], PKS 1830-211 [14], 4C +21.35 [15], 3C 279 [16, 17], together with their multi-wavelength behavior show in general a very high Compton dominance, and do not correlate with optical and soft X-ray events of comparable power

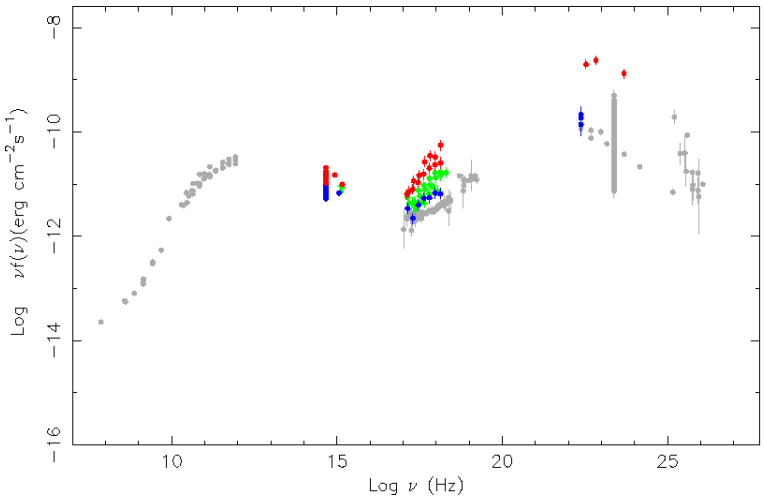

Figure 4: *The 3C 279 multi-wavelength spectral energy distribution.* **Red points:** *AGILE data during the June 2015 γ-ray flare (around MJD: 57187–57190), and simultaneous GASP-WEBT, Swift–UVOT and Swift–XRT ToO data.* **Green points:** *follow-up data covering approximately 48 hours after the γ-ray peak emission.* **Blue points:** *Post-flare 2015 data.* **Grey points:** *public non-simultaneous archival data from SSDC.*

and time scales, challenging simple one-zone leptonic theoretical models [18]. In Fig. 4 we report, as an example, the broad-band spectral energy distribution of the blazar 3C 279, obtained with the help of the ASI Space Science Data Center (SSDC) SED Builder tool[1], with AGILE data during a γ-ray flare observed in June 2015, together with simultaneous GASP-WEBT optical and Swift ultraviolet and X-ray observations highlighted in red [17].

3.4 Other important AGILE results

Other relevant scientific results for which AGILE should be remembered include:

[1]http://tools.ssdc.asi.it/SED. The Italian Space Agency data center SSDC was previously known as ASDC.

- **Vela-X**: the AGILE detection the first time of γ-ray emission above 100 MeV from a Pulsar Wind Nebula (PWN), the Vela-X PWN, as described in [19].

- **η-Carinae**: the first detection of a colliding wind binary system (CWB) above 100 MeV in the η-Carinae region [20].

- **SNR W44**: first evidence of cosmic-ray acceleration, the so-called "pion bump", from AGILE observations of the SNR W44 [21] (2017 Matteucci Medal of the National Academy of Sciences to M. Tavani).

- **MCW 656:**: AGILE detection of a new transient source AGL J2241+4454 [22], which led to the subsequent discovery of the first ever known hidden black hole in the Be star binary system MCW 656 [23].

- **Terrestrial Gamma-Ray Flashes**: the AGILE Minicalorimeter detects TGFs that last a few thousandths of a second, and produce γ-ray flashes up to 100 MeV, on timescales as low as < 5 ms [24]. The crucial AGILE contribution to TGF science is the discovery that the TGF spectrum extends well above 40 MeV, and that the high energy tail of the TGF spectrum is harder than expected.

4 AGILE and gravitational waves

The direct detection of gravitational waves (GW) by the LIGO-Virgo Collaboration (LVC) since September 14, 2015 [25] opened the exciting new field of the astronomy of gravitational wave sources and started a new era in astronomy.

Thanks to its fast ground segment alert system [26, 27], AGILE observations have provided the fastest response and the most significant upper limits in the energy range above 100 MeV to the first detected gravitational wave event GW150914 (see Fig. 5), and to all other GW events detected up to now with optimal gamma-ray sensitivity [28, 30, 31]. During the so-called LVC observing run "O2". from November 30th, 2016 to August 25th 2017, about 30 AGILE internalLVC-GCN Circulars were issued with reaction time of 2-3 hrs, including manual refined validation.

The already fast AGILE alert system has been recently further optimized for the search of electromagnetic counterparts of gravitational waves, allowing the AGILE Team to perform a full data reduction and the preliminary Quick

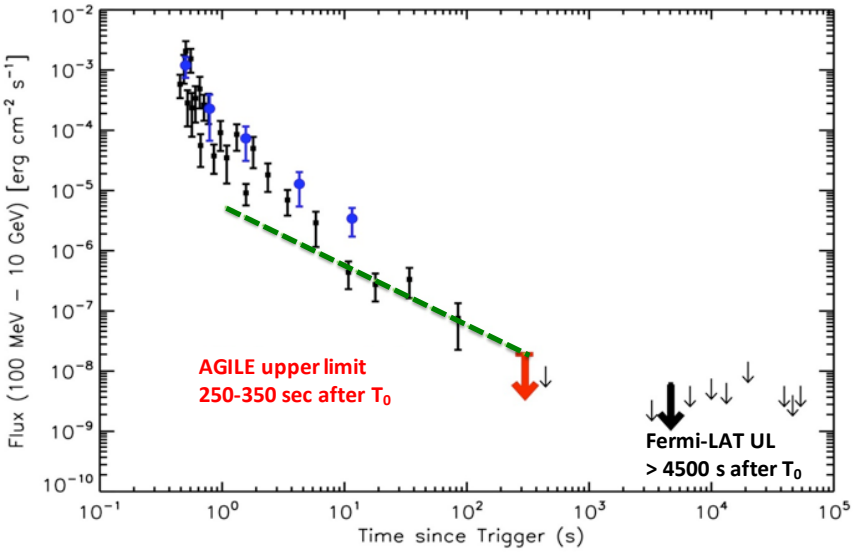

Figure 5: *The AGILE (in blue)* [28] *and Fermi-LAT (in black)* [29] *γ-ray lightcurves for the short GRB090510 used as a reference, scaled in flux and time as if it originated at the GW event GW150914 luminosity distance. The AGILE-GRID upper limit to γ-ray emission above 100 MeV is shown in red, the corresponding Fermi-LAT upper limit is marked in black.*

Look scientific analysis only 25/30 minutes after the telemetry download from the spacecraft. New processing pipelines for "sub-threshold" (very weak) events have been developed.

We look forward for future follow-up gamma-ray observations of GW sources with AGILE.

5 AGILE and neutrinos

Since April 2016, the IceCube Collaboration is alerting the astronomical community almost in real time whenever a single-track high-energy neutrino starting event (HESE) or an extremely high-energy (EHE) track event, with energy higher than several hundred TeV, is detected [32]. The origin of cosmic neutrinos is still largely unknown, and AGN of the blazar category are considered

as the main cosmic neutrino source candidates. The implementation of the IceCube alert system gives the possibility of fast follow-up observations both from space- and ground-based instruments, to search for transient electromagnetic emission spatially and temporally compatible with the IceCube neutrinos, crucial to identify their sources.

The main AGILE results in the multi-messenger field of neutrino astronomy may be summarized as follows:

- **AGILE and IC-160731:** The first possible association of γ rays with an IceCube neutrino was announced by AGILE in [33], and further investigated in [34].
- **AGILE and IC-170922:** Gamma-ray emission was observed by Fermi-LAT from the direction of the BL Lac blazar TXS 0506+056 [35], and confirmed by AGILE in [36]. The source was also detected by the MAGIC Cherenkov telescope and by other important follow-up observations, and TXS 0506+056 was globally announced as the 1st known source for high-energy neutrinos [37].
- **Systematic AGILE search on IC events**: A systematic search for transient γ-ray sources above 100 MeV in AGILE data coincident with 10 high-energy neutrino IceCube events has been recently performed. Three AGILE significant detections that can be considered possible counterparts to neutrino events have been found and discussed in [38]. Detecting 3 γ-ray/neutrino associations out of 10 IceCube events is shown to be unlikely due to a chance coincidence[2].

References

1. Tavani, M., Barbiellini, G., Argan, A., et al., 2009a, A.&A., 502, 995
2. Atwood, W.B. et al., 2009, ApJ, 697, 1071
3. Tavani, M. et al., 2009b, Nature 462, 620-623
4. Abdo A. A. et al., 2009, Sci, 326, 1512

[2]The joint post-trial false alarm probability corresponds to a number of Gaussian equivalent standard deviations of approximately 4.7 σ.

5. Tavani, M. et al., 2010, ATel #2855
6. Tavani, M. et al., 2011, Science Vol. 331, 736-739
7. Pittori, C. et al., 2009, A. & A., 506, 1563
8. Buehler, R. et al., 2010, ATel #2861
9. Abdo, A. A. et al., 2011, Science Vol. 331, 739
10. Striani, E. et al., 2013, ApJ, 765, 52
11. Giommi, P. et al., 2012, MNRAS, 420, 2899
12. Ghisellini, G. et al., 1998, MNRAS, 301, 451
13. Vercellone, S. et al., 2011, ApJ, 736, L38
14. Donnarumma, I. et al., 2011, ApJL, 736, L30
15. Verrecchia, F. et al., 2014, ATel #6733
16. Giuliani, A. et al., 2009, A. & A., 494, 509
17. Pittori, C. et al., 2018, ApJ, 856, 99
18. Tavani, M., Vittorini, V., and Cavaliere, 2015, ApJ, 814, 51
19. Pellizzoni, A. et al. 2010, Science, 327, 663
20. Tavani, M. et al. 2009c, ApJ, 698, L142
21. Giuliani, A. et al., 2011, ApJ 742, L30
22. Lucarelli, F. et al., 2010, ATel #2761, NASA ADS Bibliographic code: 2010ATel.2761....1L
23. Munar-Adrover, P., et al. 2016, ApJ, 829, 101
24. Marisaldi, M., et a. 2010, JGRA, 115, A00E13
25. Abbott B.P. et al., 2016a, Phys. Rev. Letters, 116, 061102
26. Pittori, C. 2013, Nuclear Physics B Proceedings Supplements, 239, 104

27. Bulgarelli, A., Trifoglio, M., Gianotti, F., et al. 2014, ApJ, 781, 19

28. Tavani, M., Pittori, C., Verrecchia, F., et al. 2016, ApJL, 825, L4

29. Ackermann, M., et al. 2016, ApJ, 823, L2

30. Verrecchia, F., et al. 2017, ApJ, 847, L142

31. Verrecchia, F., et al. 2017, ApJ, 850, L142

32. Aartsen, M. G. et al., 2017, APh, 92, 30

33. Lucarelli, F., Pittori, C., Verrecchia, F. et al., 2016, ATel #9295

34. Lucarelli, F., Pittori, C., Verrecchia, F., et al., 2017, ApJ, 846, 121

35. Tanaka, Y. T., Buson, S., Kocevski, D. et al., 2017, ATel #10791

36. Lucarelli, F., Piano, G., Pittori, C., et al., 2017, ATel #10801

37. Aartsen, M. G., et al., 2018, Science, 361, eaat1378

38. Lucarelli, F., et al., 2018, to appear on ApJ

Frascati Physics Series Vol. 66 (2018)
Frontier Objects in Astrophysics and Particle Physics
May 20-26, 2018

CALET: Calorimetric Electron Telescope

Pier Simone Marrocchesi *
Dept. of Physical Sciences, Earth and Environment, Univ. of Siena, Italy and INFN Sezione di Pisa

for the CALET collaboration

* *corresponding author: marrocchesi@pi.infn.it*

Abstract

The CALorimetric Electron Telescope CALET is collecting science data continuously since mid October 2015 on the JEM-EF external platform of the International Space Station. Equipped with a thick (30 X_0, 1.3 λ_I) calorimeter, comprised of a finely segmented 3 X_0 pre-shower section with excellent imaging capabilities followed by a 27 X_0 total absorption homogeneous calorimeter, and with two independent subsystems to identify the charge of the incident particle, CALET provides an excellent energy and angular resolution and electron/proton discrimination of order 10^{-5}. In addition to its primary goal of a direct measurement of the electron spectrum in the poorly known energy region above 1 TeV, CALET is carrying out extensive measurements of the energy spectra, relative abundances and secondary-to-primary ratios of elements from proton to iron and above (up to atomic number Z=40).
A brief overview of CALET observations is presented, based on the data taken during the first two-years. It includes the direct measurement of the electron+positron energy spectrum, preliminary spectra of cosmic-ray nuclei, gamma-ray observations and the search of an e.m. counterpart of LIGO/Virgo GW events.

1 Introduction

The CALorimetric Electron Telescope (CALET) [1, 2] is a high-energy astroparticle physics observatory on the ISS. The CALET mission, led by JAXA with the participation of the Italian Space Agency ASI and NASA, was launched on August 19, 2015 from the Tanegashima Space Center (Japan). CALET reached the ISS on August 24 with the transfer vehicle HTV5 (Kounotori) and was emplaced on the Exposure Facility of the Japanese Experimental Module (JEM-EF). The initial mission duration of two years is extendable to five years or more.

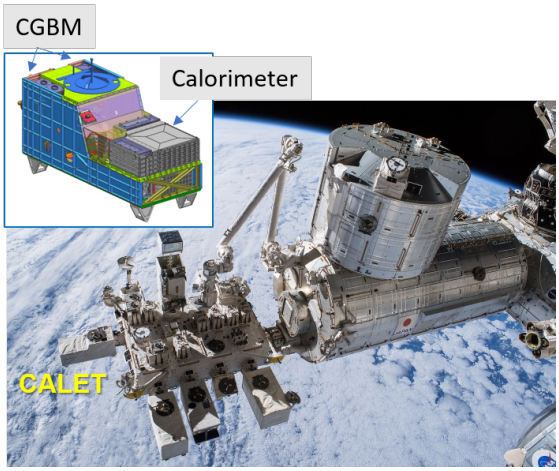

Figure 1: CALET payload attached at port #9 of the JEM-EF. The insert shows the main calorimeter and CALET Gamma-ray Burst Monitor (CGBM) subsystems [7].

CALET (Fig. 1) is an all-calorimetric instrument designed to achieve a large proton rejection capability ($> 10^5$) with a fine grained imaging calorimeter (IMC) followed by a total absorption calorimeter (TASC). Two independent subsystems identify the incoming particle via a measurement of its charge. The instrument CAL (IMC+TASC) amounts to a total of 30 X_0 and $\sim$1.3 proton interaction length (λ_I) at normal incidence.

The primary science goal of CALET [1, 2] is to carry out high precision measurements of the electron spectrum with an accurate scan of the energy region already covered by previous experiments [3] and to extend it to the unexplored

region above 1 TeV. The electron spectral shape might reveal the possible presence of nearby sources of acceleration. CALET has an extensive physics program that includes: searches for signatures of dark matter in the spectra of electrons and γ-rays; long exposure observations of cosmic nuclei from proton to iron and trans-iron elements (up to atomic numner Z $\sim$ 40); measurements of the CR relative abundances and secondary-to-primary ratios; monitoring of gamma-ray transients; studies of solar modulation and space weather phenomena.

2 Instrument

The IMC is a sampling calorimeter longitudinally segmented into 16 layers of scintillating fibers (with 1 mm^2 square cross-section) interspaced with thin tungsten absorbers. Alternate planes of fibers are arranged along orthogonal directions. It can image the early shower profile in the first 3 X_0 and reconstruct the incident direction of cosmic rays with good angular resolution (as shown in Fig. 2.

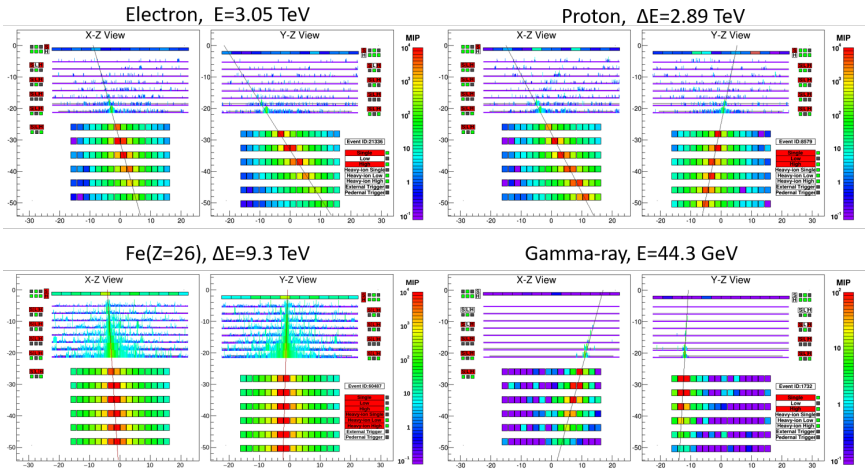

Figure 2: Examples of high-energy showers collected by CALET on the ISS. (*Top Left*) a 3 TeV electron candidate, (*Top Right*) a proton candidate with almost equivalent shower energy, (*Bottom Left*) an iron candidate with shower energy of 9.3 TeV, and (*Bottom Right*) a 44 GeV gamma-ray candidate.

The TASC is a 27 X_0 thick homogeneous calorimeter with 12 alternate X-Y layers of lead-tungstate (PWO) logs. It measures the total energy of the incident particle and discriminates electrons from hadrons with the help of the information from the CHD and IMC.

Charge identification of individual nuclear species is carried out by two independent subsystems: one dedicated two-layered hodoscope of plastic scintillators (CHD) positioned at the top of CALET, and the IMC which provides a redundant charge determination via multiple dE/dx measurements from the fibers. Together, they can measure the charge Z of the incident particle over a wide dynamic range ($Z = 1$ to ~ 40) with sufficient charge resolution to resolve individual elements [8, 9]. The geometrical factor of CALET is ~ 0.12 m^2sr and the total weight is 613 kg. Gamma-ray transients are detected by a dedicated Gamma-ray Burst Monitor (GBM) [7].
The instrument is described in more detail elsewhere [1, 10, 11]..

For an all-calorimetric instrument like CALET, energy calibrations are essential to achieve accurate flux measurements. In-flight calibrations using "MIP" signals from non-interacting protons and helium events were carried out and the linearity of the energy measurements up to 10^6 MIPs was established [12, 13]. Calibration uncertainties were carefully assessed and taken into account in the estimation of the actual energy resolution. As a result, a very high resolution of 2% or better was achieved for electrons above 20 GeV [13]. It should be noted that even with such a detailed calibration, the limiting factor for CALET energy resolution is the calibration uncertainty, as the intrinsic resolution of the instrument is close to 1%.

3 Inclusive Electron Spectrum

The CALET collaboration published a first electron paper reporting the measurement of the spectrum in the energy range from 10 GeV to 3 TeV [14]. Soon after, the DArk Matter Particle Explorer (DAMPE) collaboration published their all-electron spectrum in the energy interval from 25 GeV to 4.6 TeV [15]. The latter publication was followed by many papers speculating about the origin of a peak-like structure near 1.4 TeV in the DAMPE data.
Recently, an updated version of the CALET all-electron spectrum using 780 days of flight data and the full geometrical acceptance was published covering the energy range from 11 GeV to 4.8 TeV [16]. Figure 3 shows the updated spectrum obtained with CALET using the same energy binning as in our previous publication [14], except for adding one extra bin at the high energy end. The width of each bin is shown as a horizontal bar, the statistical errors as vertical bars, while the gray band is representative of the quadratic sum of statistic and systematic errors. A comprehensive study of the systematic uncertainties was performed as described in Refs. [14, 16] and Supplemental Material therein.

Taking the currently available experimental data at face-value we notice that: (i) the all-electron spectrum data seem to fork into two groups of measure-

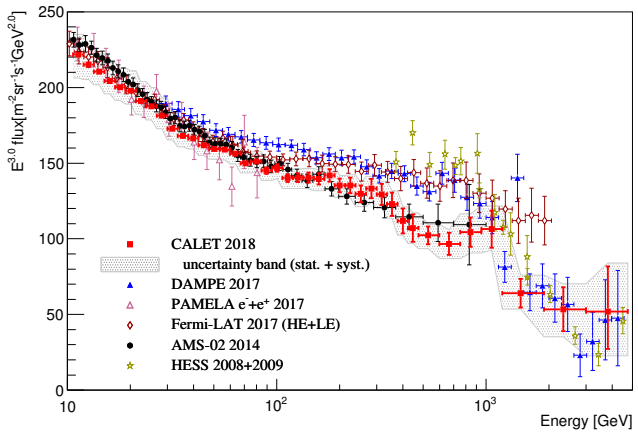

Figure 3: Cosmic-ray all-electron spectrum measured by CALET from 10.6 GeV to 4.75 TeV [16]. The gray band indicates the quadratic sum of statistical and systematic errors (not including the uncertainty on the energy scale). Also plotted are direct measurements in space [15, 17, 18, 19] and from ground-based experiments [20, 21].

ments: AMS-02 + CALET and Fermi/LAT + DAMPE, with good consistency within each group, but with only marginal overlap between the two groups, possibly indicating the presence of unknown systematic errors; (ii) CALET spectrum is consistent with AMS-02 below ∼1TeV where both experiments have a good electron identification capability albeit using different detection techniques; (iii) CALET observes a flux suppression above ∼1TeV consistent with DAMPE within errors; (iv) no peak-like structure was found at 1.4 TeV in CALET data, irrespective of energy binning.

After rebinning with the same set of energy bins as DAMPE, an inconsistency between the two measurements emerges with a 4 σ significance. The latter includes the systematic errors quoted from both experiments. Possible binning related effects in the CALET all-electron spectrum were also investigated by introducing a shift by 1/4 of the bin width. The deviation ascribed to the binning is well below our energy dependent systematic uncertainty or statistical fluctuations. Therefore, bin-to-bin migration and related effects turn out to be negligible compared to our estimated systematic uncertainties, as expected from the estimated CALET energy resolution of 2% above 20 GeV. The solid curves in Figure 3 show the energy dependent systematic uncertainty band.

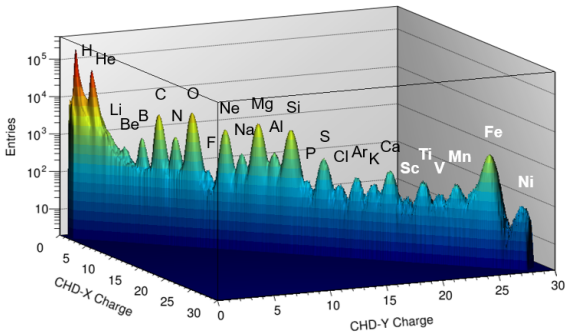

Figure 4: Charge identification capability of CHD shown as a scatter plot of the charge measured by the two layers.

4 Cosmic-ray nuclei

Direct measurements of the high-energy spectrum of each element present in the flux of charged cosmic rays [22], provide information that complements electron observations with additional insight into cosmic-ray acceleration and propagation phenomena. CALET is carrying out extensive measurements of the energy spectra, relative abundances and secondary-to-primary ratios of elements from proton to iron and above.

In particular, CALET is investigating the intermediate energy region from 200 GeV/A to 800 GeV/A where a deviation from a single power-law has been observed for both proton and helium spectra by CREAM [23, 24, 25], PAMELA [26, 27] and confirmed with high statistics measurements by AMS-02 [28] that reported a similar behavior also for Li and other light nuclei. CALET is performing an accurate scan of this energy region to verify the hypothesis of a progressive hardening of the proton spectrum by measuring accuratately the dependence of the spectral index as a function of energy.

By correlating the charge measurements from the two layers of CHD (Fig.4) and the independent charge measurement by IMC, well separated charge peaks emerge on top of a low background for individual elements. Taking advantage of the excellent charge identification capability and wide charge span of CALET, preliminary results from the current analysis of nuclei have been presented on protons [4] and heavier nuclei [5] including the spectra of carbon, oxygen, neon, magnesium, silicon and iron as shown in Fig.5 as a function of kinetic energy per particle.

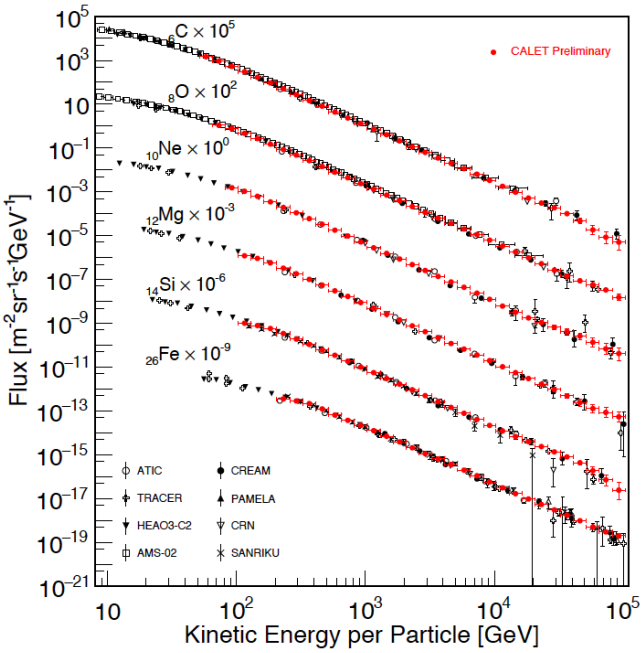

Figure 5: Preliminary energy spectra of carbon, oxygen, neon, magnesium, silicon and iron as a function of kinetic energy per particle compared with previous observations. Only statistical errors are shown.

5 Gamma-Rays, Transients and Counterparts Searches

CALET can identify gamma-rays and measure their energies up to the TeV region. Both CHD and the first IMC layers are used in the offline analysis as anti-coincidence against incoming charged particles, taking advantage of the high granularity of the IMC. In addition to the HE trigger, CALET uses a LE-γ trigger extending the sensitivity to gamma rays with primary energies down to $\sim$1 GeV. This dedicated trigger is activated only at low geomagnetic latitudes (to avoid an increase of the dead-time) and it is also enabled whenever a gamma-ray burst is triggered onboard by the CGBM.

The gamma-ray data from the first 24 months of on-orbit scientific observations allowed a complete characterization of the performance of the calorimeter [29]. Optimization of the event selection criteria and the determination of the effective area, Point Spread Function (PSF) and absolute pointing accuracy lead to the observation of bright point sources and the study of diffuse components. CALET gamma-ray sky seen with LE-γ trigger is shown in Fig. 6 (top

panel), where both the galactic emission and bright gamma-ray sources are clearly identified. Fig. 6 (bottom panel) shows the projection of the observed and expected number of photons onto the galactic latitude for the galactic plane region $|l| < 80^o$.

Gamma-ray transients were detected by the dedicated CGBM instrument which collected, as expected [30], an average of nearly 60 GRBs per year in the energy range of 7 keV–20 MeV. About 20% of them were classified as short GRBs. A search for GeV-energy gamma-ray counterparts detected by other instruments was carried out by checking the CAL data at the reported trigger times based on CGBM, Swift, and Fermi/GBM triggers. No significant counterparts have been detected at this stage for timescales ranging from 1 s to 1 hr [29]. Combined analyses of CGBM and calorimeter were performed for the search of counterpart emission related to gravitational wave events. In particular, for GW151226 upper limits on X-ray and gamma-ray counterparts were established [31]. A review of the search results with the CALET calorimeter

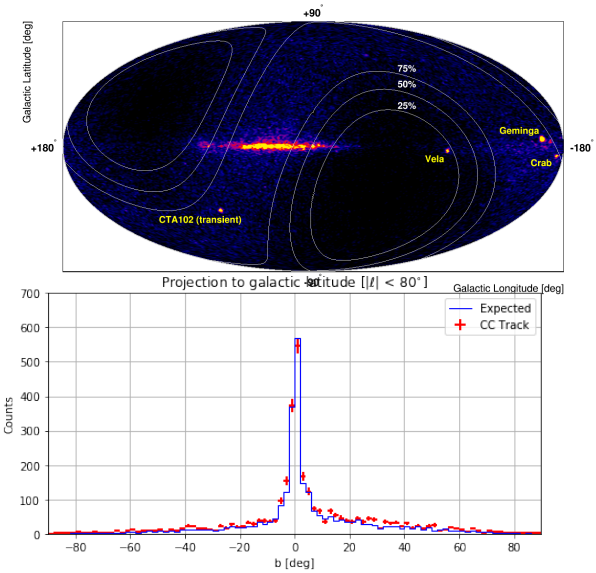

Figure 6: (*Top*) Gamma-ray sky map shown in a Mollweide projection of galactic coordinates. White contours show the relative level of exposure compared to the maximum on the sky. (*Bottom*) Projection of the observed and expected number of photons onto galactic latitude for the galactic plane region $|l| < 80^o$ for the energy range from 1 to 100 GeV.

during the LIGO/Virgo's Observation Run 2 has been published recently [32].

6 Summary

CALET was successfully launched on Aug. 19, 2015. The instrument performance has been very stable during all the scientific observation period from Oct. 13, 2015. CALET measurements of the electron spectrum [14, 16] were published in two papers, the latter with improved statistics and extended energy range from 11 GeV to 4.8 TeV. In perspective, the extension to five years (or more) of CALET electron observations is expected to increase the available statistics by a factor ∼3 thereby contributing to a better understanding of the detector and a possible reduction of the systematic errors. This will make possible a refined search for possible spectral features in the region from a few hundred GeV to ∼1 TeV, which are currently not significant. Preliminary results on protons [4], as well as primary and secondary nuclei up to $Z = 26$ and their ratios (for example, boron to carbon) have been recently presented [5], demonstrating CALET's wide energy span from 1 GeV to 1 PeV and its excellent charge identification capability. The relative abundance of the ultra heavy nuclei up to $Z = 40$ has also been preliminarly analyzed [6].
The performance of the gamma-ray measurements has been characterized [29] confirming CALET's capability to observe gamma rays in the energy range from ∼1 GeV to above 100 GeV. CALET's current results on the search of electromagnetic counterparts to gravitational wave events [31, 32] confirm the great potential of follow-up observations during the upcoming LIGO/Virgo's third observation run (Observation Run 3). High statistics detection of MeV electrons originating from the radiation belt [33] allowed the study of relativistic electron precipitation. This is one of the topics of Space Weather studies which were added as additional observational targets for CALET after the start of on-orbit operations.
The so far excellent performance of CALET and the outstanding quality of the data suggest that a 5-year (or more) observation period will most likely improve our current knowledge of cosmic-ray phenomena.

References

1. Torii S *et al.* (CALET Collaboration) 2015 *Proceeding of Science (ICRC2015) 581*
2. Torii S *et al.* (CALET Collaboration) 2017 *Proceeding of Science (ICRC2017) 1092*
3. Asaoka Y, *et al.* (CALET Collaboration) 2017 *Proceeding of Science (ICRC2017) 205*

4. Marrocchesi P S *et al.* (CALET Collaboration) 2017 *Proceeding of Science (ICRC2017) 156*
5. Akaike Y *et al.* (CALET Collaboration) 2017 *Proceedings of Science (ICRC2017) 181*
6. Brian R, Akaike Y *et al.* (CALET Collaboration) 2017 *Proceeding of Science (ICRC2017) 180*
7. Yamaoka K *et al.* 2013 *Proc. 7th Huntsville Gamma-Ray Burst Symposium, GRB 2013* p 41
8. Shimizu Y. et al., Proc. 32nd ICRC, **898** (2011)
9. Marrocchesi P S *et al.* 2011*Nucl. Instrum. Methods Phys Res., Sect. A* **659** 477–483
10. Marrocchesi P S *et al.* 2011, *Nucl. Instr. and Meth. A* **692**, 240-245 (2012)
11. Asaoka Y. *et al.* 2017, *Astropart. Phys.* **91**, 1 (2017)
12. Asaoka Y, Ozawa Y, Torii S *et al.* (CALET Collaboration) 2018 *Astropart. Phys.* **100** 29
13. Asaoka Y, Akaike Y, Komiya Y, Miyata R, Torii S *et al.* (CALET Collaboration) 2017 *Astropart. Phys.* **91** 1
14. Adriani O *et al.* (CALET Collaboration) 2017 *Phys. Rev. Lett.* **119** 181101
15. Ambrosi G *et al.* (DAMPE Collaboration) 2017 *Nature* **552** 63
16. Adriani O *et al.* (CALET Collaboration) 2018 *Phys. Rev. Lett.* **120** 261102
17. Adriani O *et al.* 2017 *La Rivista del Nuovo Cimento* **40** 473
18. Abdollahi S *et al.* (The Fermi-LAT Collaboration) 2017 *Phys. Rev. D* **95** 082007
19. Aguilar M *et al.* (AMS Collaboration) 2014 *Phys. Rev. Lett.* **113** 221102
20. Aharonian F *et al.* (H.E.S.S. Collaboration) 2008 *Phys. Rev. Lett.* **101** 261104
21. Aharonian F *et al.* (H.E.S.S. Collaboration) 2009 *Astron Astrophys.* **508** 561
22. Marrocchesi P S *et al.* 2017, Charged Cosmic Rays: a Review of Balloon and Space Borne Measurements *arXiv:1704.00304 [astro-ph.HE]* (2017)
23. Ahn H. S. et al., *Astrophys. J.* **714**, 89-93 (2010)
24. Yoon Y.S. et al., *Astrophys. J.* **728**, 122 (2011)
25. Yoon Y.S. et al., *arXiv:1704.02512v1 [astro-ph.HE]* (2017)
26. Adriani O., et al., *Science* **332**, 69 (2011)
27. Adriani O., et al., *Astrophys. J.* **765**, 91-98 (2013)
28. Aguilar M. et al., *Phys. Rev. Lett.* **114**, 171103 (2015)
29. Cannady N, Asaoka Y *et al.* (CALET Collaboration) 2018 *ApJS* **238** 5
30. Yamaoka K *et al.* (CALET Collaboration) 2017 *Proceeding of Science (ICRC2017) 613*
31. Adriani O *et al.* (CALET Collaboration) 2016 *ApJL* **829** L20
32. Adriani O *et al.* (CALET Collaboration) 2018 *ApJ* **863** 160
33. Kataoka R *et al.* 2016 *Geophys. Res. Lett.* **43** doi:10.1002/2016GL068930

Frascati Physics Series Vol. 66 (2018)
Frontier Objects in Astrophysics and Particle Physics
May 20-26, 2018

SEARCH FOR ULTRA-HIGH ENERGY COSMIC RAYS FROM SPACE - THE JEM-EUSO PROGRAM

Mario E. Bertaina
Department of Physics, University of Torino & INFN Torino
for the JEM-EUSO Collaboration
http://jem-euso.roma2.infn.it

Abstract

The origin and nature of Ultra-High Energy Cosmic Rays (UHECRs) remain unsolved in contemporary astroparticle physics. To give an answer to these questions is rather challenging because of the extremely low flux of a few per km^2 per century at extreme energies such as $E > 5 \times 10^{19}$eV. The objective of the JEM-EUSO program, Extreme Universe Space Observatory, is the realization of a space mission devoted to scientific research of cosmic rays of highest energies. A super-wide-field telescope will look down from space onto the night sky to detect UV photons emitted from air showers generated by UHECRs in the atmosphere. The JEM-EUSO program includes different experiments using fluorescence detectors to make a proof-of-principle of the UHECR observation from space and to raise the technological level of the instrumentation to be employed in a space mission: EUSO-TA, EUSO-Balloon, EUSO-SPB, Mini-EUSO and TUS. The main results obtained so far by such experiments are summarized and put in prospect of future space detectors such as K-EUSO and POEMMA.

1 Introduction

The origin and nature of Ultra-High Energy Cosmic Rays (UHECRs) remain unsolved in contemporary astroparticle physics [1]. To give an answer to these questions is rather challenging because of the extremely low flux of a few per km^2 per century at extreme energies such as $E > 5 \times 10^{19}$ eV (EECRs). The objective of the JEM-EUSO program, Extreme Universe Space Observatory, is the realization of a space mission devoted to scientific research of EECRs [2]. Its super-wide-field telescope will look down from space onto the night sky to detect UV photons emitted from Extensive Air Showers (EAS) generated by EECRs in the atmosphere.

The JEM-EUSO program includes several missions from ground (EUSO-TA [3]), from stratospheric balloons (EUSO-Balloon [4], EUSO-SPB [5, 6]), and from space (TUS [7], Mini-EUSO [8]) employing fluorescence detectors to make a proof-of-principle of the EECR observation from space and to raise the technological level of the instrumentation to be employed in space missions such as K-EUSO [9] and POEMMA [10] (see Fig. 1). A space project devoted to the study of EECRs such as JEM-EUSO should have enough quality in terms of exposure determination and EAS parameter reconstruction to satisfy the scientific requirements of such an ambitious mission. A review of the key results obtained by each experiment of the JEM-EUSO program in this respect is described in the following (details can be found in [3] - [17]). The future K-EUSO and POEMMA missions are briefly introduced at the end.

2 EUSO-TA

EUSO-TA is a ground-based telescope, installed at the TA site in Black Rock Mesa, Utah, USA. This is the first detector to successfully use a Fresnel lens based optical system and Multi-Anode Photomultipliers (MAPMT, 64 channels per tube, 2304 channels encompassing a 10.6° × 10.6° field of view - FoV) for detection of UHECRs. The telescope is located in front of one of the fluorescence detectors of the TA experiment (see Fig. 2). Since its operation in 2015, the detector has observed several UHECRs and, in addition, meteors. The limiting magnitude of 5.5 on summed frames (∼3 ms) has been established. Measurements of the UV night sky emission in different conditions and moon phases have been performed. These observations serve as a proof of concept

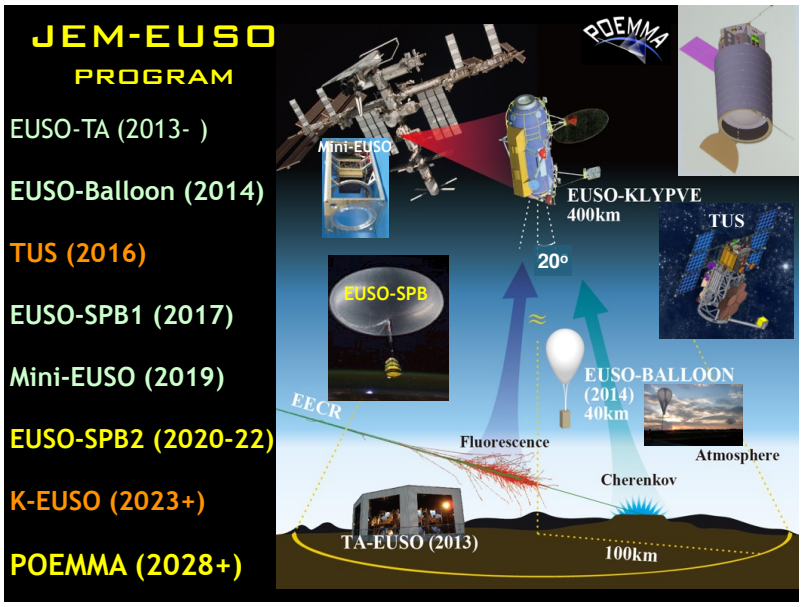

Figure 1: Roadmap of the JEM-EUSO program. See text for details.

for the future application of this detector technology for space-based missions.

Fig. 3 shows an example of a UHECR which has been detected by EUSO-TA, using TA external trigger. It can be seen that re-binning of the images significantly increases the visibility of the tracks making EUSO-TA data more similar to those of ground-based UHECR telescopes, which have much larger pixel sizes. However, such a pixel size is not suited for space-based observations, to which EUSO-TA has been tuned. Simulations of the events made with the OffLine package [11] are also presented. The shower image can be reproduced to very fine detail, taking into account the uncertainties in EAS reconstruction by the Fluorescence Detector of Telescope Array (TAFD) and intrinsic modeling of the detector response. With the implementation of the external trigger, data is collected for each TAFD event. Therefore, an event is considered as detected if a linear trace is found in the EUSO-TA data and a corresponding event in TAFD results. To date, 9 UHECR events (see Fig. 4) have been identified in 130 hours of UHECR-dedicated observations. The distances of these

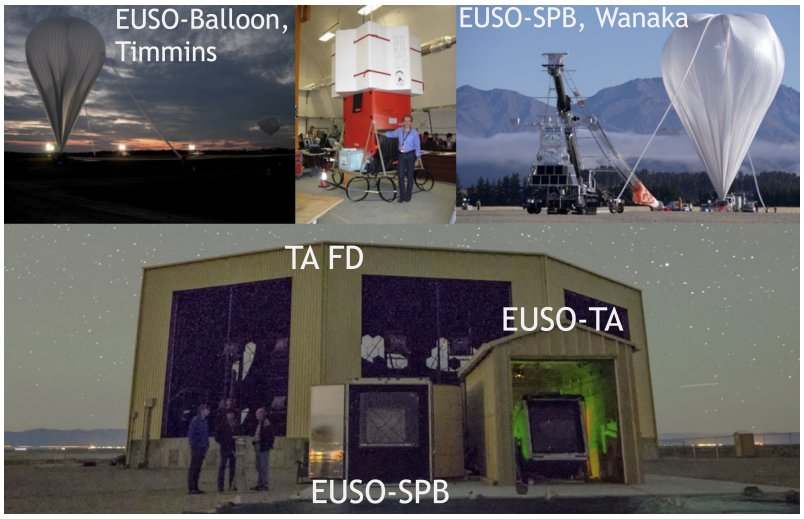

Figure 2: EUSO-TA and stratospheric balloon missions of the JEM-EUSO program. See text for details.

events from the detector vary between approximately 1 and 9 km, while the energy is between $10^{17.7}$ - $10^{18.8}$ eV, according to the TAFD reconstruction. In 2016, simulations were performed, using the updated detector parameters and ESAF (EUSO Simulation and Analysis Framework) simulation code [11], resulting in 8 predicted events, consistent with the 9 UHECRs observed to date, even though some indepedent assumptions had to be made on EUSO-TA intrinsic sensitivity to UHECRs. Nevertheless, this result confirms the general understanding of the detector response through simulations. The proximity of the events and the dead time between frames makes 8 events visible in the detector for a duration of a single frame, and one event for two frames. EUSO-TA does not usually observe the EAS maximum, but a late stage of the shower development, and as such the number of registered photons corresponds to an EAS of lower energy than if the instrument was optimally pointed towards the shower maximum. Therefore, to estimate the instrument's capabilities it was necessary to calculate the equivalent energies of the events (E_{eq}), corresponding to the reconstructed energy assuming that EUSO-TA observed the event's

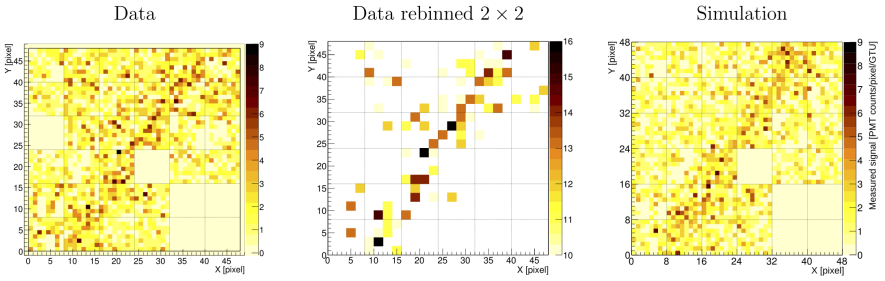

Figure 3: Example of a UHECR observed by EUSO-TA (E $\sim 10^{18}$ eV, impact parameter 2.5 km with respect to the telescope, zenith angle of the axis of 35° and azimuth angle of 7°) with different pixel binning and comparison with simulations The left plot shows the real data in photoelectron counts, in the centre 2×2 rebinning of the data is shown and in the right plot the simulation made with the OffLine package [11] (see text for details).

shower maximum. This calculation is based on the parameters measured by TA for each individual shower. The corresponding points can be used to form a conservative estimate of the detector's energy threshold. In a very simplified approach, one can assume that the minimal number of counts on the focal surface for the UHECR to be detected is constant, proportional to its energy and reversely proportional to the square of the distance from the shower axis (R_p). Based on this assumption, $R_p = A \cdot \sqrt{(E_{eq})}$ is fit to detected events, where A is a free parameter. It can be seen that the strong signals of the TA Central Laser Facility (CLF) shots (EAS equivalent energy of $\sim 10^{19.4}$ eV at a distance of 21 km) and Ground Laser System (GLS) shots (EAS equivalent energy of $\sim 10^{19.7}$ eV and $\sim 10^{20}$ eV at a distance of 33 km) are on the right side of the curve, i.e. in the detectable region, as expected. Moreover, the ground-field tests performed with EUSO-SPB employing an internal trigger logic, indicate that its energy threshold lies on top of the fitting curve supporting the conclusions derived with such method, though EUSO-SPB overall detector efficiency is ∼2 times better than EUSO-TA (see details in section 3).

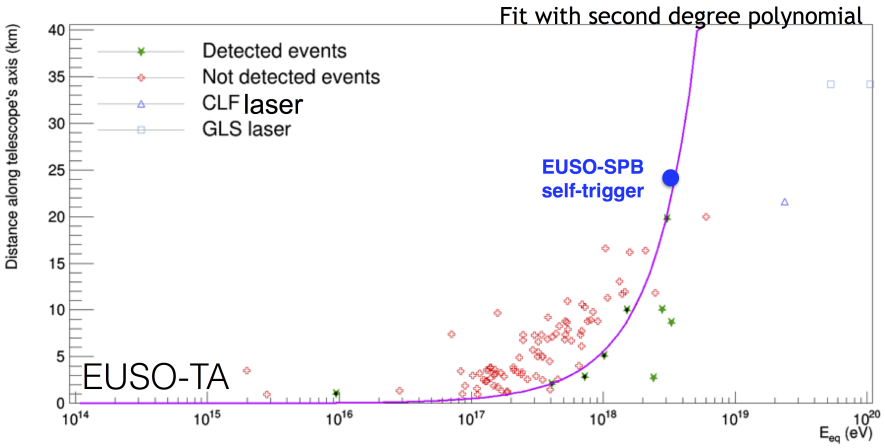

Figure 4: All UHECRs detected by TAFD in the EUSO-TA FoV during its operation with non-detected events and laser shots superimposed. The vertical axis shows the distance to the shower axis. The horizontal axis shows the events equivalent energy. The fit to the detected points suggests an estimate of EUSO-TA detection energy threshold. The blue point indicates the estimated energy threshold of EUSO-SPB determined during the field tests (see text for details).

3 EUSO-Balloon & EUSO-SPB

EUSO-Balloon [4] was launched by CNES from the Timmins base in Ontario (Canada) on the moonless night of August 25, 2014 UT. After reaching the floating altitude of ∼38 km, EUSO-Balloon imaged the UV intensity in the wavelength range 290 - 430 nm for more than 5 hours before descending to ground. The refractor telescope consisted of a similar apparatus as EUSO-TA (two Fresnel lenses of ∼1 m^2 size and a Focal Surface (FS) filled with MAPMTs). The spatial and temporal (GTU) resolutions of the detector were 130 m and 2.5 μs, respectively. The full FoV in nadir mode was $\sim 11^\circ$. During 2.5 hours of EUSO-Balloon flight, a helicopter circled under the balloon operating UV flashers and a UV laser to simulate the optical signals from UHECRs, to calibrate the apparatus, and to characterise the optical atmospheric conditions. During flight EUSO-Balloon took more than 2.5 million images that have

been analysed to infer different information: study of the performance of the different parts of the detector; response of the detector to the UV flasher and laser events; UV radiance from the Earth atmosphere and ground in different conditions: clear and cloudy atmosphere, forests, lakes, as well as city lights.

The measurement of UV light intensity is relevant for a JEM-EUSO-like mission as it is one of the key parameters to estimate the exposure curve as a function of energy [12]. However, EUSO-Balloon uses a very different approach compared to previous measurements as it is based on an wide-FoV and wide-bandwidth optical refractive system with very fine spatial and temporal resolutions, which requires a careful computation of the optics and detector response to translate the detected counts into an absolute measurement. From the point of view of the capability of a space-based observatory for EECRs the essential point is the number of counts per GTU at pixel level which is the pedestal that should be dark enough to detect a EECR track on top. Fig. 5 shows the average normalized count rates $\langle \hat{N} \rangle$ as a function of the packet time (breaks are due to technological tests foreseen for this flight). The count rate, $\hat{N}_0$, for clear atmosphere conditions is an input parameter to the EAS simulations used to estimate the reference aperture for EECR observations. The corresponding absolute intensity (I_0) is useful for the design of any space-based EECR observatory, independent of the configuration of the instrument. In EUSO-Balloon, only the back-scattered light from the airglow and extraterrestrial light contributes to the measured diffuse light. The reflectivity of the clouds is expected to be higher than clear atmospheric conditions. Thus, the interval and area with lowest count rates is assumed to represent clear atmosphere. Such conditions were assumed to be present between 04:38 and 04:52. Based on the average of the distribution in that time window, the reference $\hat{N}_0$ value is $\sim$0.65, the FWHM of the pixel distribution being $\sim$0.03. Between 04:20 and the end of measurement, when the artificial lights of Timmins and surroundings were out of the FoV, the count rate varies within a factor of $\sim$2. This gives the maximal difference of UV intensity between clear and cloudy sky conditions during flight. Ray trace simulations were then performed using the OffLine code to translate $\hat{N}_0$ in I_0 values. In the area with no artificial light sources, based on the airglow and starlight models, the measured count rate from the diffuse light under clear atmosphere conditions corresponds to I_0 = 300 - 320 photons m^{-2} sr^{-1} ns^{-1} in the 300 – 500 nm band. This value is in

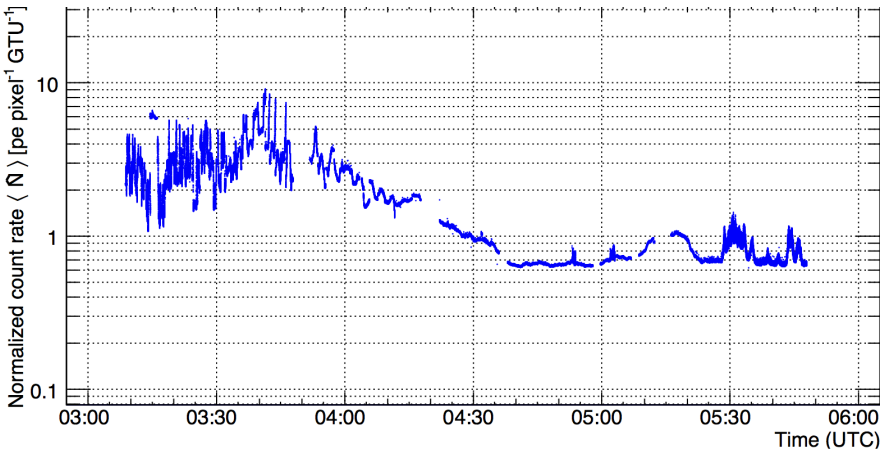

Figure 5: Average normalized count rates $\langle \hat{N} \rangle$ as a function of the packet time [13].

the band of previous measurements and confirms a good understanding of the detector performance also in this respect, which is very important in view of JEM-EUSO.

The helicopter events revealed to be extremely useful to understand the system's performance and to test the capability of EUSO-Balloon to detect and reconstruct EAS-like events. Laser tracks are used to test the reconstruction algorithms [14]. The analysis is based on the geometry of the triggered pixels. The typical time fit of a laser event and the direction reconstruction are shown in Fig. 6 after requiring basic quality cuts: a) a set of events of same energy (15 mJ, equivalent to $\sim 10^{20}$ eV EAS); b) a track lasting at least 4 GTUs. It is important to remember that the read-out period of 2.5 μ is optimised for JEM-EUSO, which is expected to detect EAS at ∼400 km distance, instead of ∼35 km as in case of EUSO-Balloon. The fact that EAS-like tracks can be reconstructed in EUSO-Balloon is quite promising in view of JEM-EUSO.

EUSO-SPB was launched April 25 2017 from Wanaka New Zealand as a mission of opportunity on a NASA SPB test flight planned to circle the southern hemisphere [5]. The primary scientific goal was to make the first observation of UHECR-EASs by looking down on the atmosphere with an optical fluorescence detector from the near space altitude of 33 km. After 12 days 4 hours aloft,

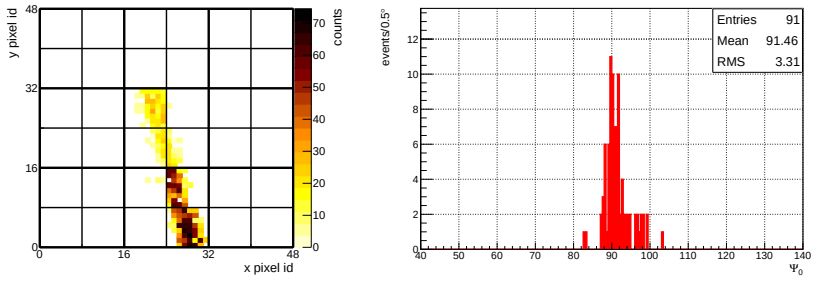

Figure 6: Left: Example of a laser track detected by EUSO-Balloon. Right: Zenith angle reconstruction of the helicopter laser shots with the 2-parameter fit method and laser energy of 15 mJ [14].

the flight was terminated prematurely in the Pacific Ocean about 300 km SE of Easter Island due to a leak in the balloon. The telescope was similar to EUSO-Balloon. An autonomous internal trigger was implemented according to [15] to detect UHECRs. About 30 hours of useful data have been collected during night time.

In October 2016, the fully assembled EUSO-SPB detector was tested for a week at the EUSO-TA site to measure its response and to calibrate it by means of a portable GLS. Observations of CLF, stars, meteors were performed. Fig. 7 shows an example of a GLS track detected by EUSO-SPB as well as the trigger efficiency curve of the 2 and 3 lens system as a function of GLS energy. With the 2 lens system, which is the one that flew from Wanaka, the ∼50% trigger efficiency is reached at laser energies whose luminosity is equivalent to ∼45° inclined EAS of E $\sim 3 \times 10^{18}$ eV seen from above by a balloon flying at 33 km altitude. This condition is represented by the blue point displayed in Fig. 4. Fig. 8 shows the average pixel count and trigger rates during flight. The pixel count rate will be used to determine the exposure and the UV intensity as performed for EUSO-Balloon. The different intensity levels are due to clear atmosphere, clouds and presence of moon light. The trigger rate was tipycally a few Hz, which is compliant with JEM-EUSO requirements. The analysis of the collected data is on going. Tracks of CRs directly crossing the detector have been recognized. However, no EAS track has been clearly identified yet. Simulations post-flight indicate that the number of expected events is ∼1 in

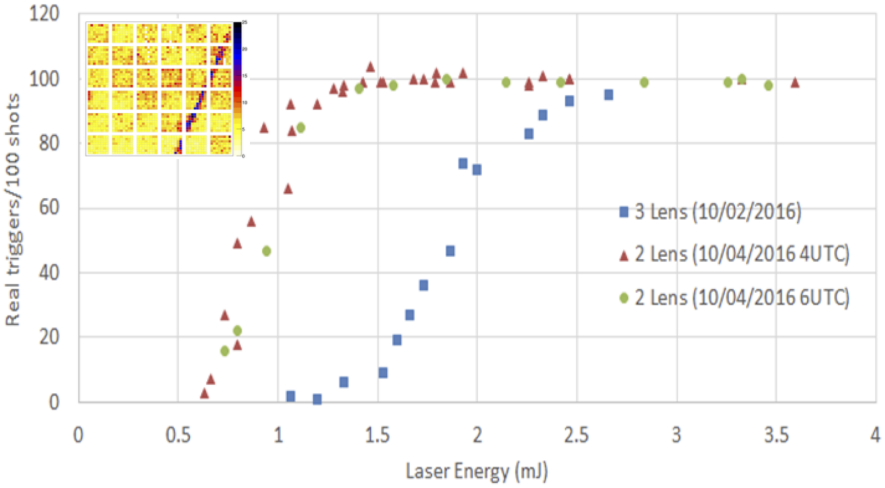

Figure 7: EUSO-SPB trigger efficiency as a function of GLS energy with 2 and 3 lens system for vertical shots during the field tests in Utah. An example of GLS track (2 mJ energy) is displayed on the top-left corner.

the available data sample indipendently of the balloon height and UV level confirming pre-flight expectations for such a flight duration. Analyses are on going to take properly into account the role of clouds and search for candidates.

A more ambitious mission is currently under development, EUSO-SPB2 [6]. It will be equipped with 2 telescopes. One telescope will be devoted to UHECR measurements using the fluorescence technique. The FS will be equipped with 3 PDMs to increase the UHECR collection power. A more performing optics (Schmidt camera) and a reduced GTU (1 μs) will lower the energy threshold of the instrument. The FS of the other telescope will be based on SiPMT sensors and a dedicated electronics to detect the Cherenkov emission in air by UHECR-generated EASs. In perspective they will test the capability to detect EAS generated by ν_τ interacting in the Earth crust. For this observation the detector will be pointing slightly below the limb. EUSO-SPB2 is expected to fly by 2022 from Wanaka, New Zealand on a NASA Super Pressure Balloon.

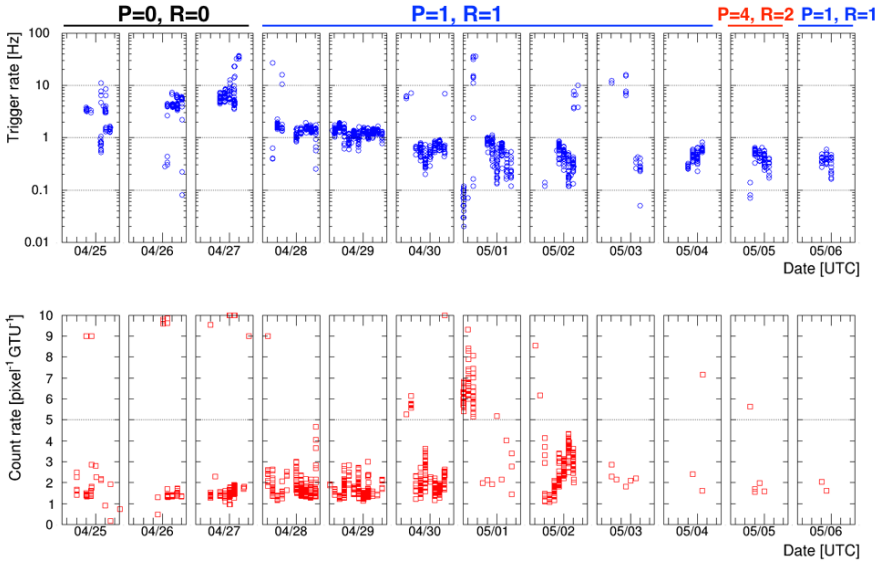

Figure 8: Trigger rate (top) and average count rate measured at pixel level (bottom) measured by EUSO-SPB in flight.

4 TUS & Mini-EUSO

The Track Ultraviolet Setup (TUS) detector was launched on April 28, 2016 as a part of the scientific payload of the Lomonosov satellite. TUS [7] is the world's first orbital detector aiming at detecting EECRs. The satellite has a sun-synchronous orbit with an inclination of 97.3°, a period of ∼94 min, and a height of 470 - 500 km. The telescope consists of two main parts: a modular Fresnel mirror-concentrator with an area of ∼2×2 m^2 and 256 PMTs arranged in a 16×16 photo-receiver matrix located in the focal plane of the mirror. The pixel's FoV is 10 mrad, which corresponds to a spatial spot of ∼5 km × 5 km at the sea level from a 500 km orbit height. Thus, the full area observed by TUS at any moment is ∼80 km × 80 km. TUS is sensitive to the near UV band with a time resolution of 0.8 μs in a full temporal interval of 256 time steps. During its operation TUS has detected about 8×10^4 events that have been subject to an offline analysis to select among them those satisfying basic temporal and spatial criteria of EECRs. A few events passed this first screening. In order to perform

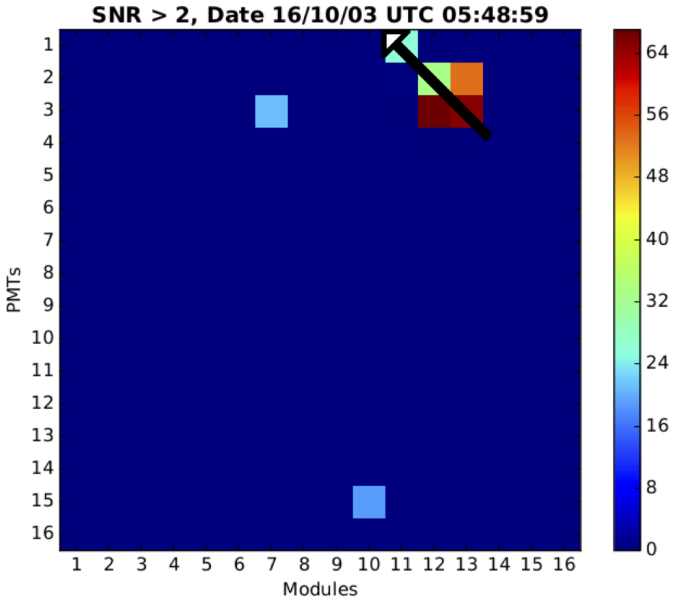

Figure 9: TUS Event 161003 occurring above Minnesota on October 3rd 2016.

a deeper analysis of such candidates, a dedicated version of ESAF as well as a detailed modeling of TUS optics and detector are being developed. Fig. 9 and Fig. 10 show an example of event which has passed first EECR selection criteria. A deeper analysis and comparison with simulations is still on going. A detailed study of this event is presented elsewhere [16] which includes also the study of weather conditions and presence of artificial lights. This example shows the importance of TUS measurements to determine analysis strategies in view of K-EUSO.

Mini-EUSO [8] is a UV telescope to be placed in 2019 inside the ISS, looking down on the Earth from a nadir-facing window in the Russian Zvezda module. Mini-EUSO will map the earth in the UV range (290 - 430 nm) with a spatial and temporal resolutions of $\sim$5 km (like TUS) and 2.5 μs, respectively. Mini-EUSO has a FS similar to EUSO-TA. The optical system consists of 2 Fresnel lenses of 25 cm diameter with a large FoV of $\sim$19°. A multiple level trigger [17] will allow the measurement of UV transients at different time scales,

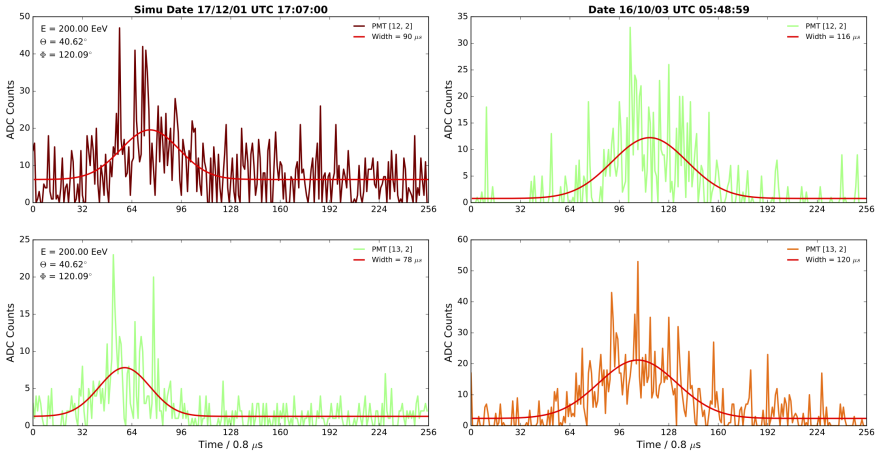

Figure 10: Comparison between signals from ESAF simulation and those from TUS 161003 event for corresponding PMTs. Left panels: Signals in PMTs [12,2] and [13,2] from ESAF simulation (EAS zenith angle $\theta = 41°$). Arbitrary units are used as the calibration of the detector response in simulation is still in progress. Bottom panels: Signals in the same PMTs taken from the candidate event.

complementing TUS observations. Laboratory experiments with Mini-EUSO engineering model and simulations confirm the sensitivity of Mini-EUSO to EECR-like transients around 10^{21} eV.

5 K-EUSO & POEMMA

K-EUSO [9] continues the Russian program for UHECRs studies, begun with the UV detectors installed on board Tatiana-1, Tatiana-2, and TUS. The fundamental objectives of K-EUSO are the demonstration of the space-based observation of EECRs and the study of the anisotropy in arrival direction of EECRs across the whole celestial sphere. K-EUSO is a result of the joint efforts to improve the performance of the Russian KLYPVE mission, by employing the technologies developed for the JEM-EUSO mission, such as the focal surface detectors and the readout electronics. Since its first conception as KLYPVE, K-EUSO project has passed various modifications aimed to increase FoV and EECR statistics. It will be the first detector with a real capability for EECR

spectrum and anisotropy study with a sufficient statistics and the full celestial sphere coverage. The adopted optical layout is a Schmidt camera covering a FoV of 40 degree with an entrance pupil diameter of 2.5 m, a 4 m diameter spherical mirror and a focal length of 1.7 m. The temporal and spatial evolution of UV light recorded by K-EUSO will allow the reconstruction of the EAS, allowing the energy and arrival direction of the EECR to be determined. The camera focal plane is covered by 1.2×10^5 pixels, each smaller than 3×3 mm, giving a 0.066° angular resolution per pixel; a pixel covers about 0.8 km on the surface of the Earth for ISS altitude of 400 km. Sampling time is 2.5 μs. Attached to the Russian MRM-1 module on-board ISS, it will detect EECRs with a yearly exposure of about 4 times Auger, with an exposure flat over the whole sky. K-EUSO is planned to operate for minimum of 2 years and it can function more than 6 years if the lifetime of the ISS is extended.

The Probe Of Extreme Multi-Messenger Astrophysics (POEMMA) mission [10] is being designed to establish charged particle astronomy with UHECRs and to observe cosmogenic tau neutrinos (CTNs). The study of UHECRs and CTNs from space will yield orders-of-magnitude increase in statistics of observed UHECRs at the highest energies and the observation of the cosmogenic flux of neutrinos for a range of UHECR models. These observations should solve the long-standing puzzle of the origin of the highest energy particles ever observed, providing a new window onto the most energetic environments and events in the Universe, and on studies of particle interactions well beyond accelerator energies. The discovery of CTNs will help solve the puzzle of the origin of UHECRs and begin a new field of Astroparticle Physics with the study of neutrino properties at ultra-high energies. The POEMMA design combines the concept developed for the OWL mission [18] and the experience of the JEM-EUSO fluorescence detection camera. POEMMA is composed of two identical satellites flying in formation at 525 km altitude with the ability to observe overlapping regions during moonless nights at angles ranging from Nadir to just above the limb of the Earth, but also with independent pointing strategies to exploit at maximum the scientific program of the mission. Each POEMMA satellite consists of a 10-meter diameter Schmidt telescope with a deployable mirror similar to the OWL concept. The POEMMA optical aperture is $\sim$14 m^2. Each POEMMA telescope monitors a 45° FoV. The POEMMA FS is composed of a hybrid of two types of cameras: about 90% of the FS is dedicated to

the POEMMA fluorescence camera (PFC), while POEMMA Cherenkov camera (PCC) occupies the crescent moon shaped edge of the FS which images the limb of the Earth. The PFC is composed of EUSO PDMs based on MAPMTs. The typical time between images for the PFC is about 1 μsec. The much faster POEMMA Cherenkov camera (PCC) is composed of Silicon photo-multipliers (SiPMs) also flown in EUSO-SPB1 and soon to be tested in space with Mini-EUSO. The PFC registers UHECR tracks from Nadir to just below the Earth's limb, while the PCC registers light within the Cherenkov emission cone of upgoing showers around the limb of the Earth and also from high energy cosmic rays above the limb of the Earth.

6 Acknowledgments

This work was partially supported by Basic Science Interdisciplinary Research Projects of RIKEN and JSPS KAKENHI Grant (22340063, 23340081, and 24244042), by the Italian Ministry of Foreign Affairs and International Cooperation, by the Italian Space Agency through the ASI INFN agreement n. 2017-8-H.0, by contract contract 2016-1-U.0, by NASA award 11-APRA-0058 in the USA, by the Deutsches Zentrum für Luft- und Raumfahrt, by the French space agency CNES, the Helmholtz Alliance for Astroparticle Physics funded by the Initiative and Networking Fund of the Helmholtz Association (Germany), and by Slovak Academy of Sciences MVTS JEMEUSO as well as VEGA grant agency project 2/0132/17. Russia is supported by ROSCOSMOS and the Russian Foundation for Basic Research Grant No 16-29-13065, and the Olle Engkvist Byggmästare Foundation.

References

1. B.R. Dawson, M. Fukushima and P. Sokolski P., Prog. Theor. Exp. Phys. **12** 12A107 (2017).

2. J.H. Adams *et al* (JEM-EUSO Coll.), Experimental Astronomy **40** 3 (2015).

3. G. Abdellaoui *et al* (JEM-EUSO Coll.), Astroparticle Physics **102** 98 (2018).

4. J.H. Adams *et al* (JEM-EUSO Coll.), Experimental Astronomy **40** 281 (2015).

5. L. Wiencke and A. Olinto for the JEM-EUSO Coll., PoS(ICRC2017), **1097** (2017).

6. J.H. Adams *et al*, ArXiv e-prints [[arXiv]1703.04513 (2017).

7. P. Klimov *et al* (TUS Coll.), Space Science Reviews **8** 1 (2017).

8. F. Capel *et al*, Advances in Space Research 10.1016/j.asr.2017.08.030 (2017).

9. M. Casolino M. *et al* (JEM-EUSO Coll.), PoS(ICRC2017) **368** (2017).

10. A. Olinto *et al* (POEMMA Coll.), PoS(ICRC2017) **542** (2017); A. Olinto *et al* (POEMMA Coll.), This conference proceedings (2019).

11. F. Bisconti F. *et al* (JEM-EUSO Coll.), PoS(ICRC2017) **463** (2017).

12. J.H. Adams *et al* (JEM-EUSO Coll.), Astroparticle Physics **44** 76 (2013).

13. M. Bertaina *et al* (JEM-EUSO Coll.), PoS(ICRC2017) **445** (2017).

14. G. Abdellaoui *et al* (JEM-EUSO Coll.), J. of Instrumentation **13** 05023 (2018).

15. G. Abdellaoui *et al* (JEM-EUSO Coll.), Nucl. Instr. & Meth. A **866** 150 (2017).

16. P. Klimov *et al* (TUS Coll.), This Conference Proceedings (2018).

17. A. Belov *et al*, Advances in Space Research, 10.1016/j.asr.2017.10.044 (2017).

18. F.W. Stecker *et al*, Nucl. Phys. B **136C**, 433 (2004).

Frascati Physics Series Vol. 66 (2018)
Frontier Objects in Astrophysics and Particle Physics
May 20-26, 2018

Fast Radio Bursts as cosmological probes

Marta Burgay
INAF - Osservatorio Astronomico di Cagliari, via della Scienza 5, 09047 Selargius (CA), Italy

Abstract

Fast Radio Bursts (FRBs) are powerful, millisecond duration flashes of radio waves of yet unknown origin. The frequency-dependent dispersion delay imparted on their impulsive signal by the free electrons along their path is well in excess of that expected from the Milky Way Galaxy in the burst direction, stronlgly suggesting an extragalactic origin for these transient events. If this is the case, FRBs can be used as cosmological probes and help solving many open questions such as the location and distribution of the missing baryonic matter in the Universe, the era of Helium reionization, and more.

1 A brief history of FRBs

Fast Radio Bursts (FRBs [1)]) are very short, intense flashes of radio waves whose disperion measure, the integrated electron density along the line of sight

to the source, is greatly in excess of that predicted (e.g. [2, 3]) for our Galaxy in their direction. Because of that, FRBs are believed to be extragalactic in origin.

The first extragalactic radio burst, known as the Lorimer Burst from the name of its discoverer, was found back in 2007 [4] while searching for extragalactic single pulses from pulsar and Rotating Radio Transients [5] in archival data of the Parkes radio telescope. It was only in 2013, though, that FRBs were recognised as a genuine family of astronomical signals, when four more highly dispersed pulses [1], one of which is shown in Figure 1 (left), were found in the data of the Parkes High Time Resolution Universe Survey [6]. Until then, in fact, despite deep searches in many more archival data and despite repeated observations of the Lorimer Burst location, no further similar signal had been detected (e.g. [7]). In the mean time, again at Parkes, a new type of radio flashes, resembling in many ways the Lorimer Burst were discovered [8]. These transients, however, were clearly local (terrestrial or atmospheric) in origin, being detected at the same time in all 13 beams of the 20-cm multibeam receiver [9] and casted serious doubts on the genuine astrophysical nature of the Lorimer burst. It was later discovered [10] that those strange signals, dubbed Perytons - the name of a mythological animal casting the shadow of a man - were caused by a microwave oven being opened before stopping the timer; Peryton detections, at a closer look, were indeed clustered around lunch time (see Fig. 1, right), and, simultaneously with their 20-cm quasi-dispersed signal, there was a 2.5 GHz signal (in the microwave part of the electromagnetic spectrum!), not present at the time of the genuine FRBs. All remaining doubts were cleared when more transient, dispersed bursts were detected also at telescopes other than Parkes (e.g. [11, 12]).

2 What are FRBs?

The observational characteristics of published Fast Radio Bursts are listed in the on-line catalogue at http://www.frbcat.org [13]. Among the most important ones we cite here:

- the burst dispersion measure: 2 to 200 times larger than the Galactic contribution along the line of sight (covering the range $\sim$ 100-2500 pc/cm^3)

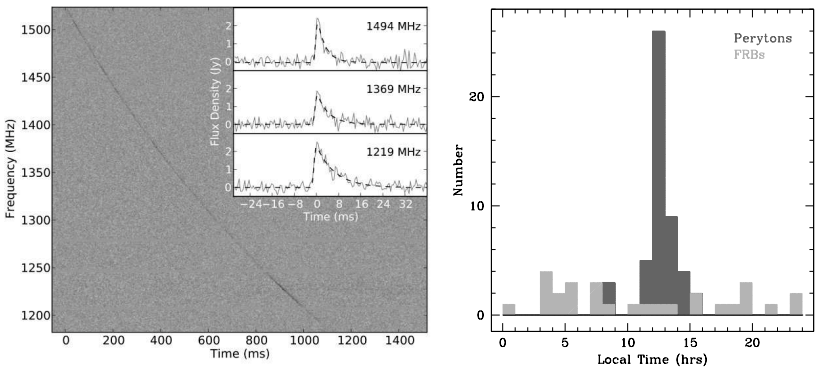

Figure 1: *Left: dynamic spectrum of FRB110220 showing the frequency-dependent time of arrival of the signal, going as ν^{-2} due to the dispersion of radio waves travelling through an ionised medium. In the inset, the frequency-dependent scatter-broadening of the pulse is shown. Right: time of occurrence (in local time) of Perytons (dark gray) and Parkes' FRBs (light grey). The first* [10]*, being produced by a microwave oven, are clustered around lunch time, while the latter, of astrophysical origin, do not show any particular correlation with the time of the day.*

- the burst duration: from a few tenths to a few tens of milliseconds, although most FRBs are not resolved in time because of the dispersion smearing in the single observing frequency channel
- the peak flux density: from 0.04 to 200 Jy, with an average vaue of ~ 23 Jy

In the cases in which it is measureable with high enough accuracy, the dispersion index very precisely matches the value of -2 expected from a radio signal travelling through a cold ionised medium (in Perytons this was not true!). This fact also rules out the possibility that the high DM of FRBs may derive from a dense but close-by environment (e.g. nearby flaring stars, as suggested by [14]), in which the terms beyond the quadratic one, would become important in the DM law [15].

As a further observational clue, pointing towards an extragalactic origin for FRBs, is the fact that, in a dozen bursts, a broadening of the pulse due to

scattering is also measured (see e.g. inset of Fig. 1, left panel). Its cause could either be the turbulent inter-galacictic medium (IGM) or an intervening galaxy (e.g. [1]). In the handfull of cases where the scattering index is also measured, it is compatible with the ~ -4.4 value expected from a radio wave travelling through an inhomogeneous, turbulent medium with a Kolmogorof spectrum.

The excess dispersion measure $\mathrm{DM_E}$, i.e. the DM not coming from our Galaxy and its halo, can be ascribed to the intergalactic medium (IGM) and to the host galaxy. The contribution from the latter, however, unless FRBs are produced in the very centre of galaxies, is expected to be small and the DM of the IGM to be the dominant ingredient. From $\mathrm{DM_E}$, hence, assuming a given set of cosmological parameters and a given Universal ionisation fraction, we can derive an estimate of the FRB's redshift z and co-moving distance [16, 17]. Using concordance cosmological parameters, the obtained values of z range from 0.03 [18] to 2.1 [19], corresponding to comoving distances from 128 Mpc to 5.4 Gpc. This, in turn, implies large isotropic emitted energies, up to 10^{40} erg. Another important, although difficult to precisely assess, derived parameter is the birth rate for the FRBs: the most recent estimate, based on the sample of FRBs discovered at the Parkes telescope, is $1.7^{+1.5}_{-0.9} \times 10^3$ events per sky per day, above a fluence of ~ 2 Jy ms [20].

On the basis of these observed and derived characteristics, several authors proposed a large number of possible theories and progenitors for FRBs. Until very recently, when the discovery of 20 new FRBs was announced [18], the number of theoretical models was larger than the number of FRBs themselves! A comprehensive list of proposed theories and progenitors for these transients signals can now be found at https://frbtheorycat.org. Broadly speaking the models can be divided into two main categories: those in which a cataclismic event (a merger, an explosion, etc) is responsible for the production of one single burst of radio emission, and those in which the progenitor is not destroyed and can produce multiple bursts on different time-scales (magnetar flares, giant pulses from pulsars, etc). Despite very extensive follow-up campaigns, only one FRB so far [11] has shown repeated bursts [21], opening the possibility that there may be multiple progenitors for these highly dispersed bursts.

3 FRBs as cosmological probes

Regardles of their specific nature, if they have indeed a cosmological origin FRBs could have a large number of applications. We have mentioned above that we can link FRBs DMs to their redshifts "assuming a given set of cosmological parameters". Reversing the reasoning, if we independently measure the redshift of FRBs host galaxies, we can, through their DM, put constraints on cosmological parameters. One such application is, for instance, the detection of (the ionised part of) the missing baryonic matter in the Universe [22, 23]: all of the ionised gas along the line of sight, including that not directy observed, but inferred by CMB observations (i.e. the '"missing baryons"), concurs to the dispersion of the radio signal and can be hence measured through the dispersive effect. The barionic mass energy density parameter Ω_b enters, indeed, in the equation linking z to DM [16, 17]: localising and measuring the redshift for a few hundreds of FRBs would hence allow us to measure Ω_b [24] and to understand whether the missing baryons lie in fact in the IGM.

With a much larger sample of localised FRBs (10^4), one could also study the probability density function of the DM as a function of redshift and understand how baryons are distributed with respect to galaxy halos (wether closely following them or on different scales); this, in turn, is an important ingredient to understand galaxy accretion and feedback mechanisms [24]. Studying how the DM varies with z for a large sample of FRBs up to high redshifts, can also probe the era of He reionization (EoR) expected between z 3 and 4. At the EoR we indeed expect an observable variation in the steepnes of the DM-z relation [25].

4 Localising FRBs: current and future efforts

In order to undesrtand what FRBs are and to fully exploit them as cosmological probes, it is now clear that we need to find, localise and measure the redshift for many hundreds, or even thousands, of them.

So far only FRB 121102 [11], thanks to its repeated bursts, has been firmly localised in a dwarf irregular galaxy at $z = 0.2$ [26] through radio interferometric observations. Another possible way to find the host galaxy to an FRB, without the need to use arrays of telescopes to get high angular resoultion directly in the radio band, is to detect FRBs in real time and trigger observations at other

wavelengths to search for an associated transient event (e.g. a supernova, a magnetar flare, a gamma-ray burst, a gravitational wave...). The SUrvey for Pulsars and Extragalactic Radio Bursts SUPERB [27], an experiment using the 13-beam 20-cm receiver [9] at the Parkes radio telescope to search for pulsars and fast transients, does exactly this: though an on-line GPU pipeline it searches for FRBs in real time sending e-mail alerts to the SUPERB team. The SUPERB pipeline is now widely used at Parkes in piggy-back along with most other pulsar observations. Thanks to this, more than a dozen FRBs have now been detected in real time and multiwavelength campaigns have followed for many of them (e.g. [28, 29, 30, 20]). None so far has revealed a transient event that could be firmly associated to the FRB itself, putting, however, some interesting limit on the possible progenitors.

The Parkes telescope, to date, has been the most succesful in finding FRBs, with a score of 27 discoveries, but new telescopes have recently, or will in the near future, enter the game with new capabilities and technologies, opening new perspectives to the field. The Australian Square Kilometre Array Pathfinder ASKAP [31], for instance, as mentioned above, has recently found 23 new bright FRBs [32] (with an average peak flux density 4 times higher than that of Parkes' FRBs), and the Canadian Hidrogen Intensity Mapping Experiment CHIME [33], who started observations a few months ago, has detected at least one FRB at low frequencies already [34] and promises to find several per day. Both these instruments, despite their different configurations — ASKAP is an array of 12-m dishes equipped with Phased Array Feeds, while CHIME is a transit telescope — have a large field of view, a crucial ingredient to catch fast transients such as FRBs, which can occur at any time in any patch of the sky.

The next step forward will be to also have an high angular resolution (Parkes, ASKAP and CHIME all have tens of arcminutes resolutions), to allow us a direct localization of the FRBs and the subsequent detection of their host galaxies. One of the new instruments that will deploy this capability is MeerKAT [35], the South African precursor of the SKA, whose observations will start in the next months. MeerKAT has an angular resolution of $0.52'$ over a 1.27° field of view, providing a much better precision to identify FRBs host galaxies, and is expected to detect hundreds of new fast transients in the next 5 years [36].

On a longer time-scale, the Square Kilometre Array SKA will certainly be the most important instrument for fast transient science, putting together a large collecting area, a large field of view and a high angular resolution, and promising to solve the FRB mystery and to allow to exploit these fascinating, powerfull flashes of radio waves as cosmological probes [37].

5 Acknowledgements

We thank the Autonomous Region of Sardinia (RAS) for the financial support through the Regional Law 7 August 2007 n. 7 (year 2015) "Highly qualified human capital:, in the context of the research project CRP 18 "General relativity tests with the Sardinia Radio Telescope" (P.I. M. Burgay).

References

1. D. Thornton, *et al.*, *Science* **341**, 53 (2013).
2. J. M. Cordes, T. J. W. Lazio, *arXiv:astro-ph/020715* (2002). Preprint (arXiv:astro-ph/0207156).
3. J. M. Yao, R. N. Manchester, N. Wang, *ApJ* **835**, 29 (2017).
4. D. R. Lorimer, M. Bailes, M. A. McLaughlin, D. J. Narkevic, F. Crawford, *Science* **318**, 777 (2007).
5. M. A. McLaughlin, *et al.*, *Nature* **439**, 817 (2006).
6. M. J. Keith, *et al.*, *MNRAS* **409**, 619 (2010).
7. J. S. Deneva, *et al.*, *ApJ* **703**, 2259 (2009).
8. S. Burke-Spolaor, M. Bailes, R. Ekers, J.-P. Macquart, F. Crawford, III, *ApJ* **727**, 18 (2011).
9. L. Staveley-Smith, *et al.*, *PASA* **13**, 243 (1996).
10. E. Petroff, *et al.*, *MNRAS* **451**, 3933 (2015).
11. L. G. Spitler, *et al.*, *ApJ* **790**, 101 (2014).
12. K. Masui, *et al.*, *Nature* **528**, 523 (2015).

13. E. Petroff, *et al.*, *PASA* **33**, e045 (2016).

14. A. Loeb, Y. Shvartzvald, D. Maoz, *MNRAS* **439**, L46 (2014).

15. A. V. Tuntsov, *MNRAS* **441**, L26 (2014).

16. K. Ioka, *ApJ* **598**, L79 (2003).

17. S. Inoue, *MNRAS* **348**, 999 (2004).

18. R. M. Shannon, *et al.*, *Nature* **562**, 386 (2018).

19. M. Caleb, *et al.*, *MNRAS* **478**, 2046 (2018).

20. S. Bhandari, *et al.*, *MNRAS* **475**, 1427 (2018).

21. L. G. Spitler, *et al.*, *Nature* **531**, 202 (2016).

22. J. N. Bregman, *Annual Review of Astronomy & Astrophysics* **45**, 221 (2007).

23. J. M. Shull, B. D. Smith, C. W. Danforth, *ApJ* **759**, 23 (2012).

24. M. McQuinn, *ApJL* **780**, L33 (2014).

25. Z. Zheng, E. O. Ofek, S. R. Kulkarni, J. D. Neill, M. Juric, *ApJ* **797**, 71 (2014).

26. S. Chatterjee, *et al.*, *Nature* **541**, 58 (2017).

27. E. F. Keane, *et al.*, *MNRAS* **473**, 116 (2018).

28. E. Petroff, *et al.*, *MNRAS* **447**, 246 (2015).

29. E. F. Keane, *et al.*, *Nature* **530**, 453 (2016).

30. E. Petroff, *et al.*, *MNRAS* **469**, 4465 (2017).

31. S. Johnston, *et al.*, *PASA* **24**, 174 (2007).

32. J.-P. Macquart, *et al.*, *Submitted to ApJ Letters* (2018).

33. CHIME/FRB Collaboration, *et al.*, *ApJ* **863**, 48 (2018).

34. P. C. Boyle, Chime/Frb Collaboration, *The Astronomer's Telegram* **11901** (2018).

35. J. Jonas, *Panoramic Radio Astronomy: Wide-field 1-2 GHz Research on Galaxy Evolution* (2009), p. 4.

36. B. Stappers, *Proceedings of MeerKAT Science: On the Pathway to the SKA. 25-27 May, 2016 Stellenbosch, South Africa (MeerKAT2016). Online at ¡A href="href="¿href="https://pos.sissa.it/cgi-bin/reader/conf.cgi?confid=277¡/A¿, id.10* (2016), p. 10.

37. J. P. Macquart, *et al.*, *Advancing Astrophysics with the Square Kilometre Array (AASKA14)* p. 55 (2015).

Frascati Physics Series Vol. 66 (2018)
Frontier Objects in Astrophysics and Particle Physics
May 20-26, 2018

Confirming the Detection of two WHIM Systems along the Line of Sight to 1ES 1553+113

F. Nicastro[1,2]
[1] *INAF - Osservatorio Astronomico di Roma,*
Via Frascati, 33, 00078 Monte Porzio Catone (RM), Italy
[2] *Harvard-Smithsonian Center for Astrophysics, Cambridge, MA, USA*

Abstract

We present a re-analysis, with newly acquired atomic data, of the two detections of two highly ionized intervening OVII absorbers reported by Nicastro and collaborators (2018). We confirm both intervening Warm-Hot Intergalactic Medium OVII detections, and revise statistical significance and physical parameters of the absorber at $z = 0.4339$ in light of its partial contamination by Galactic interstellar medium NII Kα absorption.

1 Introduction

Hydrodynamical simulations for the formation of structures in the Universe predict that, starting at redshift of $z \sim 2$, diffuse baryons in the intergalactic medium (IGM) condense into a filamentary web and undergo shocks that heat

them up to temperatures T$\simeq 10^5 - 10^7$ K, making their by far largest constituent, hydrogen, mostly ionized (e.g. [1,2]). At the same time, galactic outflows powered by stellar and AGN feedback, enrich these baryons with metals (e.g. [2]). How far from galaxies these metals roam, depends on the energetics of these winds but it is expected that metals and galaxies will be spatially correlated. This shock-heated, metal-enriched medium, known as Warm-Hot Intergalactic Medium (WHIM), is made up of three observationally distinct phases: (1) a warm phase, with T$\simeq 10^5 - 10^{5.7}$ K, where neutral hydrogen is still present with ion fraction $f_{HI} > 10^{-6}$ and the best observable metal ion tracers are OVI (with main transitions in the FUV) and CV (with transitions in the soft X-rays); (2) a hot phase with T$\simeq 10^{5.7} - 10^{6.3}$ K, where $f_{HI} \simeq 10^{-6} - 10^{-7}$ and OVII (with transitions in the soft X-rays) largely dominates metals with ion fractions near unity; and (3) an even hotter phase (T$\simeq 10^{6.3} - 10^7$ K), coinciding with the outskirts of massive virialized groups and clusters of galaxies, where HI and H-like metals are present only in traces (e.g. [1]).

The warm phase of the WHIM has indeed been detected and studied in detail in the past few years and is estimated to contain an additional 15% fraction of the baryons (e.g. [3,4] and references therein). This brings the total detected fraction to 61% but still leaves us with a large (39%) fraction of elusive baryons, which, if theory is correct, should be searched for in the hotter phases of the WHIM. In particular, the diffuse phase at T$\simeq 10^{5.7} - 10^{6.3}$ K should contain the vast majority of the remaining WHIM baryons, and it is traced by OVII. Optimal signposts for this WHIM phase are then OVII Heα absorption lines, which however are predicted to be relatively narrow (Doppler parameter $b(O) \simeq 20 - 46$ km s^{-1}), extremely shallow (rest-frame equivalent widths EW$\lesssim 10$ mÅ), and rare. Such lines are unresolved by current X-ray spectrometers and need a signal to noise ratio per resolution element SNRE$\gtrsim 20$ in the continuum to be detected at a single-line statistical significance$\gtrsim 3\sigma$. This requires multi-million second exposures against the brightest possible targets available at sufficiently high redshift ($z \gtrsim 0.3$).

In this contribution we first summarize the fidings from our recent discovery of two intervening OVII-bearing absorption systems along the line of sight to the blazar 1ES 1553+113, at redshifts $z = 0.3551$ and $z = 0.4339$ [5], then introduce a slight revision of our recently published results[5] in light of newly

determined measurements of wavelengths and oscillator strengths of the NII Kα complex (McLaughlin, private communication) that make our own Galaxy's ISM contamination likely for the OVII Kα line of the system at $z = 0.4339$, and finally discuss the implications of our finding.

Throughout the paper uncertainties are quoted at 68% significance, unless explicitly stated.

2 Intervening WHIM Systems along the Line of Sight to 1ES 1553+113

The detections of two WHIM systems at $z = 0.4339$ and $z = 0.3551$ in the XMM-*Newton* RGS spectrum of 1ES 1553+113, have been presented by [5]. Here we briefly summarize their main findings.

The 8-33 Å RGS spectrum shows a number of narrow (unresolved) line-like negative features (Fig. 1 in Extended Data - ED, hereinafter - of [5]), eight of which are securely identifiable as Galactic absorption lines (marked and labeled in blue in Fig. 1 of ED of [5]). Two additional unresolved absorption lines are detected in both RGSs at combined single-line statistical significances of $4.1-4.7\sigma$ and $3.7-4.2\sigma$ (Fig. 1 and Table 1 in ED of [5]) [1] , at wavelengths where (1) no strong Galactic absorption is expected (but see §3 for likely NII Kα ISM contamination for one of these two lines) and (2) neither of the two spectrometers is affected by instrumental features due to cool-pixels in the dispersing detector (Fig. 1). These are the lines identified by [5] as intervening WHIM OVII Heα at $z = 0.4339 \pm 0.0008$ and $z = 0.3551^{+0.0003}_{-0.0015}$ (Table 1 in ED of [5]). An additional lower significance ($1.7-2\sigma$) line is detected at a $\lambda = 26.69 \pm 0.09$ Å, and is identifiable as OVII Heβ at a redshift consistent with $z = 0.4339 \pm 0.0008$ (Table 1 in ED of [5] and Fig. 1, where the sizes of the arrows are proportional to the relative strengths of the lines [2]).

Here we confirm these identifications, but in light of new laboratory-experiment revised positions and oscillator strengths of the lines of the NII

[1] here, and throughout the paper, we report a range of statistical significance, where the upper boundary is the actual measured single-line statistical significance, while the lower boundary is the measured significance conservatively corrected for observed systematics in the RGS spectrum (details in [5]).

[2] in particular, the size of the arrows of low-ionization lines are relative to the strength of the NI Kα transition, while those of the high-ionization lines are relative to the strength of the Heα transition.

Kα triplet (McLaughlin, private communication: see §3), we slightly revise the physical parameters of the $z = 0.4339$ WHIM system (and thus the implied WHIM OVII cosmological mass density estimate) and its statistical significance (see §3).

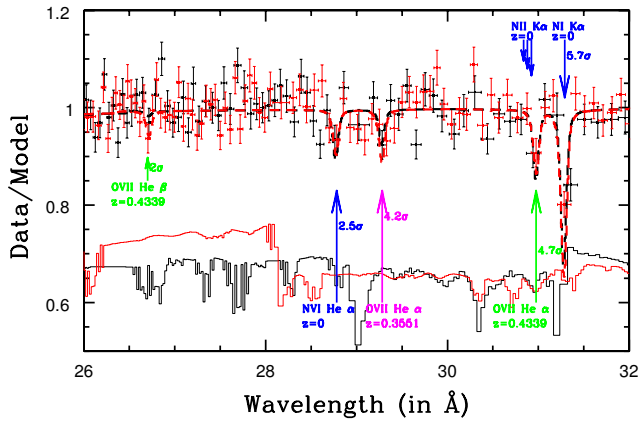

Figure 1: *Normalized raw RGS1 (black points) and RGS2 (red points) data of the blazar 1ES 1553+113, in the wavelength interval $\lambda = 6-32$ Å. Thick dashed curves are RGS1 (black) and RGS2 (red) best-fitting model folded through the RGSs response functions. Thin solid curves at the bottom of the graph are RGS1 (black) and RGS2 (red) effective areas (in arbitrary units), showing instrumental features due to cool-pixels in the dispersing detectors.*

3 Galactic NII Contamination for the $z = 0.4339$ WHIM System

In Fig. 1 the relatively strong line present in the data at a centroid $\lambda = 30.975 \pm 0.017$ Å, is ≥ 50 mÅ ($\geq$ one RGS resolution element) inconsitent with the theoretical (i.e. computed with the Hebrew University Lawrence Livermore Atomic Code - HULLAC[6] ; E. Behar, private communication) rest-frame wavelengths of the NII Kα triplet (three blue arrows at $\lambda = 30.836$, 30.879 and 30.924 Å) available to us at the time of publication of [5]. For this reason, this

line was safely identified by [5] as the OVII Heα transition imprinted by an intervening WHIM system $z = 0.4339$.

Laboratory positions and strengths of the three main NII Kα lines, were already available in 2011[7], but were the outcome of the first early experiments done at the Optimized Light Source of Intermediate Energy laboratory (SOLEIL [3]) when the instability of synchrotron beam profiles was still poorly understood. New measurements for wavelengths and cross-sections of the NII ion have recently been perfomed at SOLEIL and results from the analysis of these new data have been made available to us (McLaughlin, private communication) and are shown (graphically) in Fig. 2. Fig. 2 shows two narrow portions of the RGS spectrum of 1ES 1553+113, $\lambda = 30.5 - 31.5$ Å (top panel) and $\lambda = 23 - 24$ Å (bottom panel). These are the spectral regions were the Kα transitions of NI and NII (top panel) and OI and OII (bottom panel), lie. The arrows in Fig. 2 mark the positions of these lines and, as for Fig. 1, their relative size is proportional to the relative strengths of the transitions. The new laboratory measurements of the NII Kα triplet indicate that the centroids of these lines are now consistent with the $\lambda = 30.975 \pm 0.017$ line present in the data (Fig. 2, top panel).

The question thus arises: can this line be entirely due to Galactic ISM absorption? A first problem with this hypothesis is that the centroids of the three NII Kα lines are about 1 RGS resolution element apart from each other and the lines have different strengths. Thus, Galaxy's ISM NII Kα absorption should imprint a relatively shallow, broad and skewed profile trough in the data, rather than the unresolved, symmetric, line-like feature present in the data.

To test this possibility further, we used our *galabs* model[8] to self-consistently model the cold and mildly ionized ISM absoprtion components of our Galaxy along the line of sight to 1ES 1553+113

3.1 Modeling the Cold-Neutral and Warm-Ionized ISM components in the RGS spectra of 1ES 1553+113

The insterstellar medium of our Galaxy contains both Cold-Neutral and warm-ionized Metal-rich Medium (CNMM and WIMM[8]) which attenuates the soft

[3] https://www.synchrotron-soleil.fr/en/about-us/what-soleil/soleil-3-questions

X-ray spectrum of both Galactic X-ray binaries and AGNs. The line of sight to 1ES 1553+113 is no exception. The RGS spectrum of 1ES 1553+113 clearly shows metal photo-electric absorption by neutral and mildly ionized oxygen and nitrogen (Fig. 2).

We model both the bound-free (flattening of the long-wavelength X-ray powerlaw) and bound-bound (Kα resonant lines from neutral metal ions) photo-electric absorption by the CNMM with a Tuebingen-Boulder ISM absorption component (*tbabs* in XSPEC), with solar abundances set to [9] and lower boundary of the hydrogen column density frozen to the weighted average measurement along this line of sight: $N_{HI} = 3.7 \times 10^{20}$ cm^{-2} [10]. The best-fitting N$_H$ is pegged to its lower boundary and the model reproduces well both the broad-band attenuation of the continuum at low energies and the Kα lines of OI and NI (Fig. 2, blue histogram).

This CNMM component does not include absorption by non-neutral metal species and thus cannot model either the strong OII Kα (Fig. 2, bottom panel) or the weaker NII Kα (Fig. 2, top panel) triplets [4] . We thus add a WIMM component[8] to our model, with relative abundances set to Solar-like[9] and absolute metallicity free to vary, and refit the data. The best-fitting WIMM component has typical physical parameters (T$\sim 3000 - 5000$ K; N$_H = 1.85 \pm 0.07 \times 10^{20}$ cm^{-2}) and metallicity ($Z = (0.52 \pm 0.09) Z_{\odot}$) and, together with the CNMM component, model excellently the OI Kα line, the OII Kα triplet and the NI Kα line in the data, but cures only modestly the narrow line-like absorption deficit seen near the NII Kα triplet (Fig. 2, red histogram).

To model this additional feature, we add an unresolved (FWHM frozen to 10 mÅ) negative Gaussian to our model and refit the data. The best-fitting Gaussian has centroid $\lambda = 30.975 \pm 0.010$ Å and EW$= 10 \pm 3$ mÅ (i.e. a single line significance of $2.9 - 3.3\sigma$). We therefore confirm the identification of this line as an intervening WHIM OVII Kα line at $z = 0.4339$, as in N18. Our final best-fitting model is the green histogram of Fig. 2.

We note that the best-fitting profile of the unresolved NII Kα absorption triplet (red histogram), is in all (i.e. in wavelenths, shape and strength) similar

[4]In Fig. 2 the arrows, and their relative sizes, shows the latest laboratory-measurement positions and relative strengths of the OII Kα (Bizau et al., 2015) and NII Kα (McLaughlin, private communication) transitions.

to the gentle curvature seen in the continuum folded through the RGS effective area (blue histogram). This is an effective area feature and has been introduced by a recent correction made by the RGS calibration team (J. Kaastra, private communication) based on the data of the calibration sources Mkn 421 and PKS 2155-304. We think, instead, that this relatively narrow curvature in the data of calibration sources has an astrophysical (not instrumental) origin and is due to the ubiquitous ISM NII Kα absorption bound to be imprinted in the X-ray aspectra of any astrophyscal source. By adopting this correction, thus, we are conservteily underestimating the actual strength and statistical significance of the intervening WHIM OVII Kα absorption line at $z = 0.4339$.

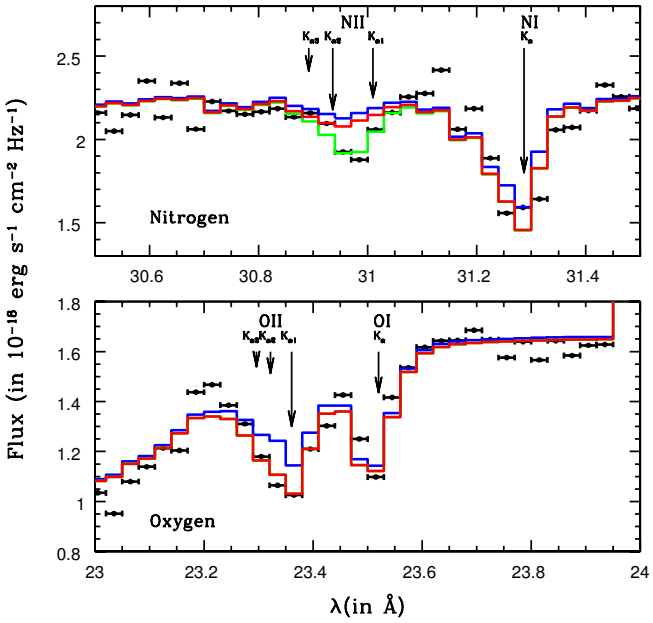

Figure 2: *RGS spectrum of 1ES 1553+113 at* $\lambda = 30.5 - 31.5$ *Å (top panel) and* $\lambda = 23 - 24$ *Å (bottom panel). These are the spectral regions were the K*α *transitions of NI and NII (top panel) and OI and OII (bottom panel), lie.*

4 Revised Comsological Mass Density of OVII Kα WHIM Absorbers

The revised (compared to [5]) equivalent H column density and metallicity of the $z = 0.4339$ WHIM system, are: $N_H = 0.7^{+0.5}_{-0.3} \times 10^{19}$ cm$^{-2}(Z/Z_\odot)^{-1}$ and $0.05 < (Z/Z_\odot) < 0.2$ (see [5]). This gives an OVII WHIM cosmological mass density estimate $0.002 < \Omega_b^{WHIM} < 0.016$ (i.e. 9-70% of the Universe's baryons).

5 Acknowledgements

FN thanks B. McLaughlin for providing the new laboratory and theory data of the NII Kα transitions.

6 References

References

1. Cen, R. & Ostriker, J. P., ApJ, **650**, 560 (2006).
2. Davé, R. et al., ApJ, **552**, 473 (2001).
3. Shull, J. M. et al., ApJ, **759**, 23 (2012).
4. Nicastro, F. et al., AN, **338**, 281 (2017).
5. Nicastro, F. et al., Nature, **558**, 406 (2018).
6. Bar-Shalom, M. & Klapisch, J. O., JQSRT, **71**, 169 (2001).
7. Gharaibeh, M. F. et al., JoPB, **44**, 175208 (2011).
8. Nicastro, F. et al., MNRAS, **457**, 676 (2016).
9. Wilms, J., Allen, A. & McCray, R., ApJ, **542**, 914 (2000).
10. Kalberla, P. M. W. et al., A&A, **440**, 775 (2005).
11. Branchini, E. et al., ApJ, **697**, 328 (2009).
12. Schaye, Y. et al., MNRAS, **446**, 521 (2015).

Frascati Physics Series Vol. 66 (2018)
Frontier Objects in Astrophysics and Particle Physics
May 20-26, 2018

Recent results from the TUS/LOMONOSOV Space Mission

Pavel Klimov for the Lomonosov-UHECR/TLE Collaboration
Lomonosov Moscow State University, Skobeltsyn Institute of Nuclear Physics, GSP-1, Leninskie Gory, Moscow, 119991, Russia

Abstract

TUS (Tracking Ultraviolet Set-up) is the first orbital detector of extreme energy cosmic rays (EECR). It was launched into orbit on April 28, 2016, as a part of the scientific payload of the Lomonosov satellite mission. The detector is aimed to test the technique of measuring UV fluorescent and Cherenkov radiation of extensive air showers (EAS) generated by primary cosmic rays with energies above 50 EeV. The TUS detector is a UV telescope looking in the nadir direction from the altitude of ∼500 km. It consists of a 2 m^2 mirror and a 256-pixel photo detector and has a $\pm 4.5^\circ$ field of view with 5×5 km^2 spatial resolution in the atmosphere. During more than a year of operation, a number of EAS-like events were measured by the detector. Some of them are caused by atmospheric phenomena of anthropogenic sources, some are considered as EAS candidates. We report results of a search for EAS-like events in the TUS data and their analysis with an emphasis on a strong extreme energy cosmic ray candidate registered on October 3, 2016. Conditions of the measurements were studied to exclude thunderstorm atmospheric events. An arrival direction

and energy of a primary particle were estimated basing on results of extensive simulations and new reconstruction algorithms.

1 Introduction

Measurements of the energy spectrum, nuclear composition and arrival directions of ultra-high-energy cosmic rays (UHECRs, $E \gtrsim 50$ EeV[1]) are an important part of modern astrophysics and particle physics [?]. The first cosmic ray particles of such high energy were detected [?] and a cut-off of the energy spectrum was predicted (GZK cutt-off) [?, ?] more than 50 years ago. However, the nature and origin of UHECRs are still not understood. The problem relates to extremely low flux of particles with energies above GZK: the Pierre Auger Observatory and the Telescope Array–registered less than two dozen events with energies $E > 100$ EeV in 13 and 7 years of operation respectively [?, ?]. Moreover, these ground-based detectors observe two different portions of the sky, making a comparison of the results more difficult. The idea to expand the UHECR experimental studies to space was suggested by Benson and Linsley [?, ?]. Fluorescence and Cherenkov ultraviolet (UV) radiation of an extensive air shower (EAS) generated by an UHECR in the nocturnal atmosphere of Earth can be detected from a satellite similar to the way how it is observed from the ground with fluorescence telescopes but with a much larger exposure. Space-based observations have the potential for an increase in statistics, up to several orders of magnitude, and would be able to cover the whole sky uniformly, allowing for a direct comparison of spectra and direction of arrival on the celestial sphere.

The primary goal of the TUS project, first announced in 2001 [?], is to test the possibility of UHECR measurements from space and study the UV background phenomena which will influence EAS detection. The TUS detector on board the Lomonosov satellite was launched into orbit from the Vostochny Cosmodrome (Russia) on 28th April 2016. The satellite has a sun-synchronous orbit with an inclination of 97°.3, a period of ≈ 94 min, and a altitude of about 470–500 km above Earth surface.

[1] 1 EeV $= 10^{18}$ eV

2 Design of the TUS detector

TUS is a UV telescope looking downward into the atmosphere. It consists of the two main parts: a modular Fresnel mirror-concentrator and 256 photomultiplier tubes (PMTs) arranged in a 16×16 photodetector pixels located in the focal plane of the mirror. The TUS detector on board Lomonosov satellite is presented in Fig. 1.

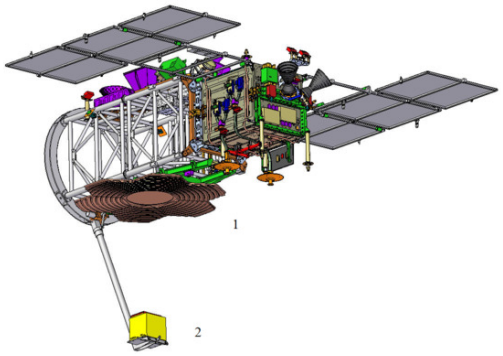

Figure 1: Artists's view of the TUS detector on-board the Lomonosov satellite: number 1 marks the mirror-concentrator, and 2 marks the photodetector.

The TUS mirror is composed of 7 hexagonal segments made of a carbon plastic with the total area of 2 m^2. The focal distance of the mirror equals 1.5 m. The effectiveness of the TUS optics was estimated to be of the order of 70% based on tests performed at the stage of manufacturing. This means about 70% of all UV photons approaching the entrance pupil are focused in a spot. Other 30% are diffused scattered producing a uniform illumination of the focal surface. The shape of a spot is determined by the point spread function (PSF) of the mirror. The PSF was measured during pre-flight tests of the mirror for different angles of incidence, see [?]. A typical root-mean-square (RMS) radius of a spot varies from approximately 7–8 mm on axis to 8–10 mm at the edge of the field of view (FOV) (at 4.5°)

The photodetector is built of 16 modules, each consisting of 16 channels. Each channel (pixel) is a Hamamatsu R1463 PMT with the quantum efficiency in the near-UV band (300–400 nm) of approximately 20%. A multi-alcali cathode is covered by a UV glass filter of the UFS1 type and a reflective light

guide with a square entrance of 15 mm size located in the focal plane of the mirror. The angular resolution (the field of view of one pixel) is 10 mrad, which corresponds to a spatial spot of about 5 km×5 km at the sea level from a 500 km orbit height. Thus, the full instantaneous area observed by TUS is approximately 80 km×80 km.

Each pixel of the photo detector measures UV light from the part of the FOV with a time resolution of 0.8 μs in a full temporal interval of 256 time steps. This allows to measure the EASs track as a source radiating in the near UV band and moving rectilinearly at the speed of light. The trajectory of the EAS axis, coincides with the arrival direction of a primary particle, given by azimuth and zenith angles (ϕ, θ).

The TUS electronics can operate in four modes intended for registering various fast optical phenomena at different time scales with different time sampling. In addition to the EAS mode with a 0.8 μs temporal resolution, TUS performed observations with the sampling time of 25.6 μs (TLE-1 mode), 0.4 ms (TLE-2 mode) and 6.6 ms (METEOR mode). EAS mode is efficient not only for EAS events but for the shortest type of TLE (Transient Luminous Events) – Elves. Three other modes are aimed for studying atmospheric phenomena such as lightning discharges, TLEs (sprites, blue jets, gigantic jets, etc.) and for detecting micro-meteors, space debris. METEOR mode, is also used for the relative calibration of PMTs.

It turned out to be necessary, because an emergency situation occurred with the detector during the first orbits after it was switched on. The calibration that was performed before the launch of the satellite were lost.

A signal in METEOR mode has a duration of a record equal to 1.68 s and has small fluctuations due to being integrated over 8192 time steps of the EAS mode. The FOV of a pixel shifts during a record because of the satellite movement so that an area observed by a pixel at the beginning of the record is later observed by an adjacent one. This allows to calculate relative sensitivity of neighbor pixels.

The absolute calibration can be made by the comparison with previous UV background measurements, for example in MSU satellite missions Tatiana-1, Tatiana-2 and Vernov [?, ?, ?]. This work is currently in progress.

The TUS on-line selection system is provided by a two-level trigger [?, ?], which allows selecting events in terms of both the intensity of the signal (a

threshold trigger) and the specific space-time pattern (an adjacency trigger). Data of all 256 channels for 256 consecutive time steps are recorded in case of both triggers conditions are satisfied, thus forming a TUS event. The data is represented by 10-bit ADC codes A_k, $k = 1, \ldots, 256$.

More details about the TUS detector can be found in [?].

Experimental data on EAS were compared with EAS data from simulations in ESAF software package. ESAF was originally developed for the Extreme Universe Space Observatory (EUSO) Mission [?] and has been maintained through the JEM-EUSO program [?].

Figure 2 presents an example of the expected detector response to EASs generated by a primary proton with the energy of 200 EeV arriving from 60 ° zenith angle. ESAF (EUSO Simulation and Analysis Framework) [?] software was used to simulate fluorescence and Cherenkov light from extensive air showers as they are observed by TUS. The graph represents a light curve, i.e., the overall signal falling onto the focal surface. For simplicity of the figure, zero background illumination is assumed, all pixels have equal sensitivities with quantum efficiency 0.2 and the PMT gain 10^6.

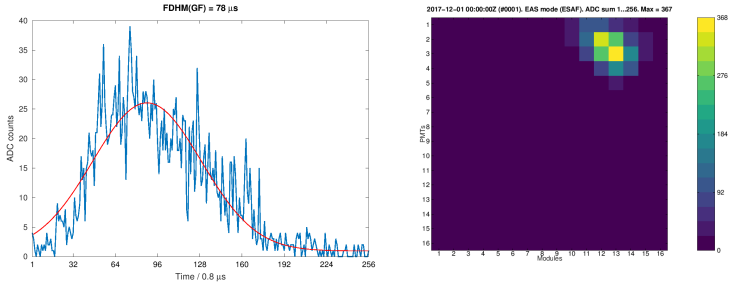

Figure 2: Light curve (sum of ADC counts) of typical EASs originating from a 200 EeV proton arriving at zenith angle $\theta = 60°$ as seen by TUS, according to simulations with ESAF.

3 Some results of the TUS detector measurements

In what follows, we present the selected results of an analysis of data obtained with TUS detector in the EAS mode of operation: background measurements, transient luminous events and EAS candidate. We discuss all these measure-

ments in application to future UHECR missions, like KLYPVE [?] or JEM-EUSO [?].

3.1 Non-uniform noise-like illumination

The majority of events registered thus far by TUS have noise-like waveforms with ADC counts of all PMTs fluctuating around some average values. The trigger is caused by random fluctuations of the background in this case. There is a subset of events with noise-like waveforms but strongly non-uniform illumination of the focal plane. Sometimes it is a local spot due to anthropogenic source in the atmosphere (city, industrial center). But in some of them a significant part of focal plane is illuminated. This effect is observed during full moon nights. In some cases the moonlight arrives at the focal surface directly, without previous scattering in the atmosphere. Example of such an event is presented in Figure 3. This measurement was done above the Atlantic ocean in the northern hemisphere not far from equator.

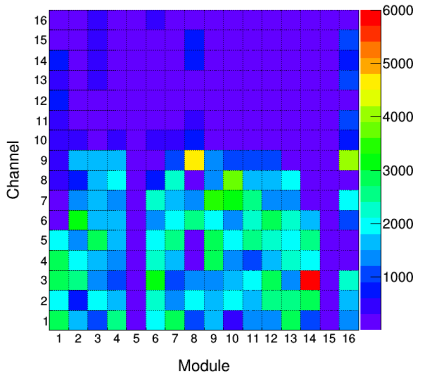

Figure 3: Pixel map of the event measured on July 16, 2018. A part of FS directly illuminated by the Moon light.

This is an important result for the next UHECR detector KLYPVE-EUSO. At the beginning of the project it was planned as a single mirror telescope as TUS. But now we see that it can lead to a direct moonlight and sunlight to the photo detector. The detector should have a significant shield to protect sensors. The best solution was found to use a Schmidt camera. In addi-

tion to a very wide field of view in this optical scheme photo detector is placed inside the telescope between entrance pupil and mirror and totally protected from direct moonlight by a shell of the telescope.

3.2 Instant flashes in the EAS mode

As mentioned above random UV signals are the main type of EAS triggers. Their rate has been minimized in compromise with a "low" EAS energy threshold and it is of about 1 per minute. Much lower in rate are "EAS imitating background" events technically selected by EAS trigger but in most cases do not following all features of EAS.

One of unexpected type of events during the TUS operation in space is instant (i.e., happening in one or, rarely, two time samples of 0.8 μs) and as a rule intensive flashes that produce tracks or, sometimes, small spots in the focal surface. From the first days of the TUS operations they were producing near 15 % of triggers and a new algorithm aimed to exclude these events was developed and implemented during flight. Figure 4 shows two different examples of such events. The first one represent a so called instant track (hit pixels form a line). Simulations performed using the Geant4 software toolkit have revealed that protons with energies from 100–200 MeV up to a few GeV that hit the UV filters approximately parallel to their plane can produce fluorescence and Cherenkov radiation and result in tracks similar to those observed by TUS. The second type of events has another shape of the image. This is a "spot" with a size near the PSF. These events can be caused by other phenomena, for example direct Cherenkov light of upward going EAS. This EAS can be produced by a neutrino crossing the Earth. It is difficult to prove this hypotheses and to distinguish on the basis of TUS data the signal from the neutrino EAS from the signal from charged particles crossing the detector UV filter. But this type of measurements is of great interest in frame of multi-messenger astrophysics (see, for example, POEMMA project description in this volume).

3.3 Thunderstorm related monotonous flashes

Many TUS triggers are caused by thunderstorm lightning effects. These signals are usually represents "monotonous" flashes - relatively slow (hundred microsecond) rise of a signal. If the event is placed inside the FOV then it looks like an expanding bright spot - a joint effect of the event geometry, scattered

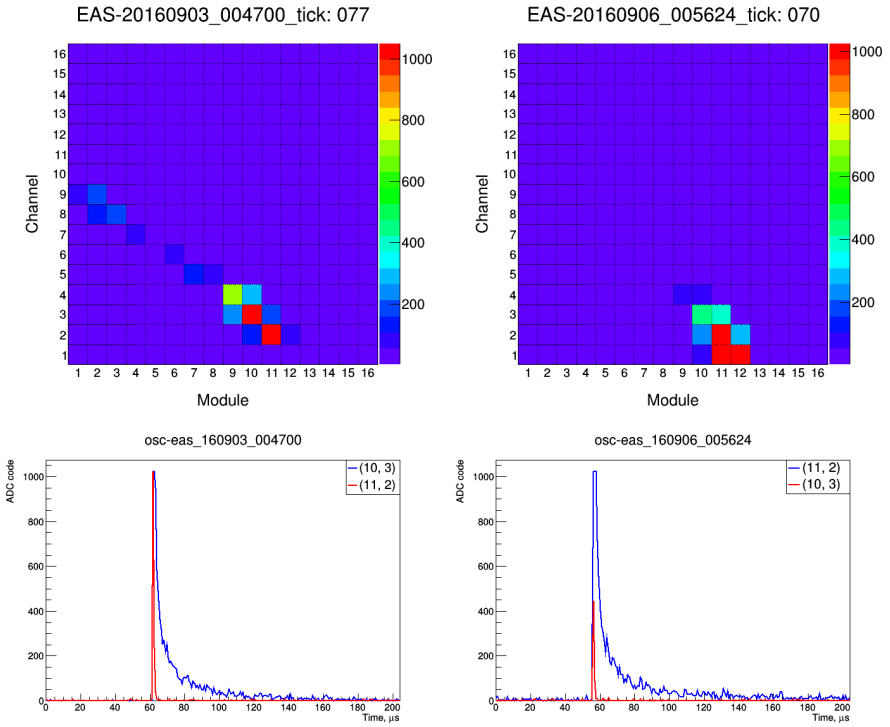

Figure 4: Left: instant track event. Right: instant spot event. Upper panel represent pixel maps of two events, bottom – oscillogams of two hit pixels.

light and mirror PSF. But many of them evolves simultaneously in majority of pixels presenting an almost uniform illumination of the focal plane. An analysis of geographical distribution of these flashes demonstrates their correlation with well known regions of thunderstorm activity. A comparison with lightning flashes measured by the World Wide Lightning Location Network (WWLLN) has been performed. It demonstrated that the majority of them occur in more than 100 km from the TUS FOV within 1 s time interval. The distribution of distance between the TUS "monotonous" flash event and closest lightning discharge (from WWLLN data) measured during one hour time interval is shown in figure 5. The large time interval was chosen to identify the thunderstorm because WWLLN has just 10% detection efficiency and can miss the lightning

directly in the moment of TUS measurements.

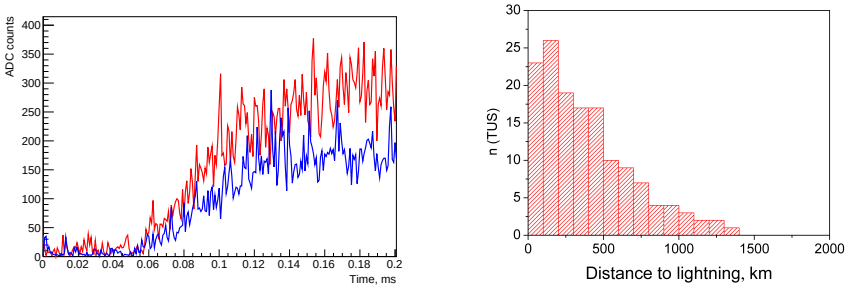

Figure 5: Left: Example of a "monotonous flash" oscillogram in two pixels. Right: The distribution of distance between the TUS "monotonous" flash event and closest lightning discharge measured by WWLLN.

This demonstrates that the TUS detector is sensitive to lightning discharges that occur rather far from TUS FOV. The reason for this effect is a diffuse scattering of the TUS mirror (almost 30 % of light are scattered and illuminate the whole photo detector. This is one more argument to chose Schmidt design for next UHECR missions to decrease stray light on the mirror and suppress triggering rate nearby thunderstorms.

3.4 Fine time-spatial structure of elves

The TUS detector measured numerous UV TLEs in the EAS mode with different temporal dynamics and spatial structure. The most common type of TLEs with a specific geometry of the development in the ionosphere are Elves – the result of the ionosphere heating by an expanding electromagnetic wave from a powerful lightning. A number of such events were measured by the TUS detector.

Single elve is a result of cloud-to-ground discharge and various measurements of single elves were described previously [?, ?].

Number of ground based experiments measured elves with more complicated spatial structure – events witch have two rings and called them double elves [?, ?]. In the work [?] simulations of double elves are made and demonstrated that these elve doublets are the ionospheric signature of compact intracloud discharges (CIDs).

In the TUS data a number of double elves was found. One example is presented in figure 6. On the pixel map two separated rings are obviously seen. These rings correspond to two peaks in the oscillogram. The first one is brighter and it is a result of interaction of ionosphere with a direct electromagnetic wave from lightning. The second ring is caused by a reflected from ground electromagnetic lightning emission.

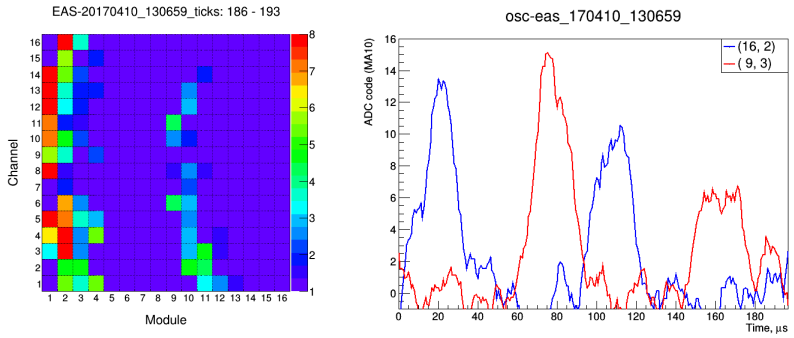

Figure 6: A double elve measured by the TUS detector on April 10, 2017. Left: pixel map, two bright rings are seen. Right: oscillograms of two hit pixels (blue and red lines), two peaks with a delay of ~ 75 μs are seen in both waveforms.

The analyses of thunderstorm in nearby region was performed with use of data of Vaisals GLD360, a ground-based lightning location network with a relatively high detection efficiency [?, ?] data [?]. A number of lightning were found in the North direction to the TUS FOV. It is coincides with the direction of expected elve source. Next generation of orbital UV telescopes like KLYPVE-EUSO will be able to measure fine time-spatial structure of such events with larger FOV which will allow to see the whole ring but not just an arc as TUS does.

3.5 The EAS candidate event registered on 3rd October 2016

The event which is considered as the most strong candidate for EAS in the TUS data was registered on 3rd October 2016 at 05:48:59 UTC, 00:48:59 local time. The center of the FOV of TUS at the moment of registration was located at 44.08°N, 92.71°W above Minnesota, USA, in approximately 100 km south-east from Minneapolis. The location is a part of the Richard J. Dorer Memorial

Hardwood State Forest. [2] There are no cities, airports or other settlements that could be sources of the signal below the hit channels.

The measurement was performed over the clear sky and far from thunderstorms. Thunderstorm activity was studied in the region using the Vaisala Global Lightning Dataset GLD360. No lightning strikes were registered within 930 km and during ±10 s from the event. This witnesses in favour of a non-thunderstorm origin of the signal.

A study of the cloud coverage was performed using the Modern-Era Retrospective analysis for Research and Applications-2 (MERRA2) project. [3] It was found that the atmosphere was clear at the time of observation of the event without any noticeable cloud except some small low-altitude ones.

Waveforms of all ten hit pixels and a pixel map for the event are shown in Fig. 7. Here a stacked histogram is used to represent the light curve, i.e., the total signal falling onto the focal surface. To minimize statistical fluctuations, the signal is represented as a moving average of the original signal with the base level subtracted calculated over three time steps.

The signal demonstrates a spatio-temporal dynamics similar to what is expected for an EAS. Hit pixels are grouped in an oblong spot, the shape of which might be a "convolution" of two factors, namely, the asymmetric PSF of the mirror and a linear track. A position of the maximum of the signal in each pixel has some shift from one pixel to another. It is natural to interpret this as a movement of the signal in the FOV of the detector.

A reconstruction of the arrival direction of a relativistic particle can be defined as a determination of parameters of a track, i.e., a straight line segment on the focal plane (FP), along which the image center (a "point") moves at a constant velocity. The most simple approach called Linear Track Approximation (LTA) was used for the first attempt of reconstruction. Details can be found, for example in [?]. As a result, the LTA gives the arrival direction $(\phi, \theta) \approx (51^\circ, 43^\circ)$ for the mean distance from satellite to EAS $R = 480$ km.

A detailed study of kinematics of the event were performed using simulations of the events with similar position in FOV made in the ESAF.The best agreement with the kinematics of the discussed event is found for zenith angles around 45°, and energy of primary particle near 300 EeV.

[2] $https://www.dnr.state.mn.us/state_forests/forest.html?id=sft00033$
[3] $https://gmao.gsfc.nasa.gov/reanalysis/MERRA-2/$

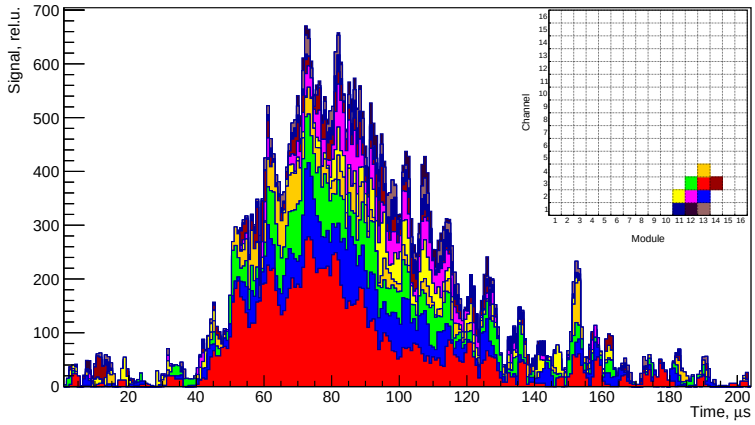

Figure 7: The light curve of the event as the signal of ten hit pixels stacked together and expressed in rel.u.The signal is smoothed with a moving average calculated for three time steps.

The reconstruction of the arrival direction of the event registered with TUS on 3rd October 2016 are in a good agreement with the estimates obtained by an analysis of kinematics of simulated EASs. On the other hand, the algorithm developed for the reconstruction was found to be sensitive to the choice of active channels in case some of them have low signal-to-noise ratio. For this reason a more reliable reconstruction algorithms are under development. This work is especially important in view of the future orbital missions like KLYPVE-EUSO (K-EUSO) [?].

The main difficulty in interpreting the event as an UHECR cascade is the high amplitude of the signal and thus the estimated energy of the primary particle. It is clear from Fig. 2 and this can be verified analytically that the amplitude of the light curve expected for a 200 EeV primary particle "registered" with TUS is one order of magnitude less than it is observed in the discussed event. Thus, the energy of a primary particle should also be higher if the event is considered as an EAS. This makes the probability of such an event rather low as long as one considers "traditional" cosmic rays.

Another argument against the hypothesis of a ZeV CR origin of the registered event is that a Cherenkov peak should be present in the waveform of such an energetic EAS with a zenith angle $\sim 45^\circ$ and the same position in the

FOV unless the zenith angle is larger than estimated (more than 60°) so that the reflection point is outside the FOV of the detector.

4 Conclusion

The TUS orbital UHECR detector was successfully operating on board the Lomonosov satellite in 2016 and 2017 and provided very important measurements of UV atmospheric emission in various time scales. Signals from lightning discharges and upper atmospheric transient phenomena with high temporal resolution are seen. It allows to study a fine time-spatial structure of various phenomena occurring in the atmosphere. The TUS detector provided the first registration of an event with specific kinematics that can be interpreted as a movement of a relativistic UV light source (namely EAS particle disc) in the detectors FOV downward to the ground in the nocturnal atmosphere of Earth. The reconstructed zenith angle equals approximately 40°–50° and agrees with results of simulations. On the other hand the absolute calibration of the TUS detector for EAS signal is rather uncertain and evaluation of EAS energy is not reliable. Analysis of pixel absolute calibration is in progress.

This measurement is of great importance for the future orbital missions aimed for registering UHECRs from space. Being a pathfinder with a relatively low sensitivity, narrow field of view and only the 5-km spatial resolution, TUS proves the possibility of observing EASs from space and highlights the necessary improvements for the next generations missions like KLYPVE-EUSO.

5 Acknowledgements

The work was done with partial financial support from the State Space Corporation ROSCOSMOS, M.V. Lomonosov Moscow State University through its Prospects for Development program (Perspektivnye Napravleniya Razvitiya) and the Russian Foundation for Basic Research grant No. 16-29-13065. We thank Vaisala Inc. company for providing the data on lightning strikes.

Frascati Physics Series Vol. 66 (2018)
Frontier Objects in Astrophysics and Particle Physics
May 20-26, 2018

Constraining Dark Matter models with extremely distant galaxies

Marco Castellano
INAF - Osservatorio Astronomico di Roma
Nicola Menci
INAF - Osservatorio Astronomico di Roma
Andrea Grazian
INAF - Osservatorio Astronomico di Roma
Alexander Merle
Max-Plank-Institut für Physik (Werner-Heisenberg-Institut)
Norma G. Sanchez
CNRS LERMA, Observatoire de Paris PSL, Sorbonne Universités
Aurel Schneider
Institute for Astronomy, Department of Physics, ETH Zurich
Maximilian Totzauer
Max-Plank-Institut für Physik (Werner-Heisenberg-Institut)

Abstract

The investigation of distant galaxy formation and evolution is a powerful tool to constrain dark matter scenarios, supporting and in some cases surpassing other astrophysical and experimental probes. The recent completion of the Hubble Frontier Field (HFF) programme combining ultra-deep Hubble Space Telescope observations and the magnification power of gravitational lensing produced by foreground galaxy clusters has enabled the detection of the faintest primordial galaxies ever studied. Here we show how the number density of such primordial galaxies allows to constrain a variety of DM models alternative to CDM. In particular, it provides stringent limits on the mass of thermal WDM candidates, on the parameter space of sterile neutrino production models, and on other DM scenarios featuring particles in the keV mass range which is also supported by recent detections of a 3.5keV X-ray line. These constraints are robust and independent of the baryonic physics modeling of galaxy formation and evolution. Fuzzy DM (ultralight DM particles) results strongly disfavored.

1 Introduction

Understanding the nature of the Dark Matter (DM) component of the Universe constitutes a key issue in fundamental physics and in cosmology. During the last two decades, investigations of the formation and growth of cosmic structures have progressively led to the adoption of the Cold Dark Matter (CDM) paradigm, where DM particles are characterized by thermal velocities small enough to produce negligible free streaming on the scales relevant to structure formation (e.g. Peebles, 1982). Typically, this corresponds either to assuming DM particles to be massive ($m_X > 0.1$ GeV) or to be constituted by condensates of light axions (with mass $\sim 10^{-5} - 10^{-1}$ eV). However, as of now, both direct (see, e.g., Aprile et al., 2012) and indirect (see, e.g., Ackermann et al., 2015) CDM detection experiments have failed to provide a definite confirmation of such a scenario. On the structure formation side, several critical issues are affecting the CDM scenario at the mass scales of dwarf galaxies ($M \approx 10^7 - 10^9$ $M_\odot$). These are all connected to the excess of power in the CDM power spectrum at such scales compared to a variety of observations.

The combination of astrophysical issues with the lack of detection of candidate particles has stimulated the interest toward different DM scenarios, characterized by power spectra with suppressed amplitude at small mass scales ($M \lesssim 10^8 - 10^9$ $M_\odot$) with respect to the CDM case. In particular, great attention has been given to Warm Dark Matter (WDM) scenarios, which assume DM to be composed by particles with masses m_X in the keV range that potentially provide a Dark Matter interpretation of the claimed detection of an X-ray line in stacked observations of galaxy clusters and in the Perseus cluster (Bulbul et al., 2014; Boyarsky et al., 2014). While WDM candidates may result from the freeze-out of particles initially in thermal equilibrium in the early Universe (like, e.g., gravitinos, see Steffen, 2006, for a review), a similar suppression at these scales can be obtained by a variety of models featuring particles in the keV mass range with *non-thermal* spectra, like sterile neutrinos. Finally, another proposed solution to the small-scale problems in galaxy formation is based on Bose condensates of ultra-light (pseudo) scalar field DM with mass $m_\psi \approx 10^{-22}$ eV , often referred to as "Fuzzy" DM.

Existing astrophysical bounds on the thermal relic mass m_X, have been set with a variety of techniques (e.g. Polisensky & Ricotti, 2011; Schultz et al., 2014), the tightest constraints achieved so far being the $m_X \geq 3$ keV, derived by comparing small scale structure in the Lyman-α forest of high- resolution ($z > 4$) quasar spectra with hydrodynamical N-body simulations (Viel et al., 2013).

The abundance of low-mass cosmic structures provides an important key to constrain DM scenarios. In this context, the Hubble Frontier Field (HFF) programme has recently provided important information through the detection of ultra-faint, lensed galaxies at very high-redshifts. In fact, estimates of the UV luminosity function down to unprecedented faint magnitudes $M_{\rm UV} = -12.5$ at $z = 6$ in (Livermore et al., 2016), can be used to derive limits on the total number density of galaxies at early epochs.

In the present paper we summarise the results presented in Menci et al. (2016b, 2017a) where stringent constraints on DM models with suppressed power spectra by have been derived by comparing the maximum number density of DM halos $\overline{\phi}$ expected at redshift $z = 6$ to the observed number density ϕ_{obs} of galaxies at the same redshift in the HFF. The condition that observed galaxies cannot outnumber their host DM halos ($\overline{\phi} \geq \phi_{obs}$) directly leads to constraints on the set of parameters admitted for each DM model. *Remarkably, this technique provides a conservative approach which is not affected by uncertainties in the baryonic physics*, at variance with most of previous investigations of DM scenarios alternative to CDM.

2 The halo mass function in dark-matter models with suppressed power spectra

2.1 Warm Dark Matter thermal relics

The simplest alternative to CDM is provided by Warm Dark Matter models assuming DM to be the result from the freeze-out of particles with mass in the keV range initially in thermal equilibrium in the early Universe. In these models, the population of low-mass galaxies is characterized by lower abundances and shallower central density profiles compared to Cold Dark Matter (CDM) due to the dissipation of small-scale density perturbations produced by the free-streaming of the lighter and faster DM particles. In this case, the mass of the DM particle completely determines the suppression of the density power spectrum compared to the CDM case

The computation of the halo mass function for the WDM scenario is based on the standard procedure described and tested against N-body simulations in, e.g., Schneider et al. (2013); Angulo et al. (2013). The differential halo mass function (per unit $log\, M$) based on the extended Press & Schechter approach (e.g. Bond et al., 1991) reads:

$$\frac{d\,\phi}{d\,log M} = \frac{1}{6}\,\frac{\overline{\rho}}{M}\,f(\nu)\,\frac{d\,log\,\sigma^2}{d\,log r}\,. \tag{1}$$

Here $\nu \equiv \delta_c^2(t)/\sigma^2$ depends on the linearly extrapolated density for collapse in the spherical model $\delta_c = 1.686/D(t)$ and $D(t)$ is the growth factor of DM perturbations.

A spherical collapse model for which $f(\nu) = \sqrt{2\nu/\pi}\, exp(-\nu/2)$ is assumed.

The key quantity entering Eq. 1 is the variance of the linear power spectrum $P(k)$ of DM perturbations (in terms of the wave-number $k = 2\pi/r$). Its dependence on the spatial scale r of perturbations is:

$$\frac{d\, log\, \sigma^2}{d\, log\, r} = -\frac{1}{2\,\pi^2\,\sigma^2(r)}\,\frac{P(1/r)}{r^3}. \tag{2}$$

In WDM scenarios the spectrum P_{WDM} is suppressed with respect to the CDM case P_{CDM} below a characteristic scale depending on the mass m_X of the WDM particles. In the case of relic thermalized particles, the suppression factor can be parametrized as (Bode et al., 2001):

$$\frac{P_{WDM}(k)}{P_{CDM}(k)} = \left[1 + (\alpha\, k)^{2\mu}\right]^{-10/\mu}. \tag{3}$$

where $\mu = 1.12$ and the quantity α is linked to the WDM free-streaming scale:

$$\alpha = 0.049 \left[\frac{\Omega_X}{0.25}\right]^{0.11} \left[\frac{m_X}{\mathrm{keV}}\right]^{-1.11} \left[\frac{h}{0.7}\right]^{1.22} \frac{h^{-1}}{\mathrm{Mpc}}, \tag{4}$$

where m_X is the WDM particle mass, Ω_X is the WDM density parameter (Ω_X) and h the Hubble constant in units of 100 km/s/Mpc.

The mass function is computed through Eq. 1 after substituting Eq. 2, with a power spectrum $P(k) = P_{WDM}(k)$ determined by the WDM particle mass m_X after Eqs. 3 and 4.

2.2 Sterile neutrinos

2.2.1 Resonant production from mixing with active neutrinos

A suppression to the power spectrum similar to the WDM case can be obtained by a variety of models featuring particles in the keV mass range with *non-thermal* spectra, like sterile neutrinos, the main difference being that in the case of non-thermal spectra, the production mechanism is essential in determining the suppression with respect to CDM. The minimal setup for sterile neutrino DM is the production via mixing with one or several active neutrino flavors. Active neutrinos are weakly interacting and are therefore in thermal equilibrium with other Standard Model particles in the early Universe. During that epoch, the sterile neutrino abundance builds up gradually via occasional oscillations from the active to the sterile sector. Combined limits from

structure formation and X-ray observations (e.g. Merle et al., 2016) have recently ruled out *non-resonant* production (Dodelson-Widrow (DW) mechanism, Dodelson & Widrow, 1994).

However, active-sterile oscillation may be enhanced by a resonance (Shi & Fuller (SF) or *resonant* production mechanism, RP, Shi & Fuller, 1999), provided there exists a significant lepton asymmetry L in the early Universe. Such a resonance allows for significantly smaller mixing angles θ, relaxing the tight limits from X-ray observations. In this scenario, for any given sterile neutrino mass, the mixing angle is related to the adopted lepton asymmetry L, such that the parameter space of RP sterile neutrino models can be described in terms of combinations of sterile neutrino masses m_ν and mixing amplitudes $sin^2(2\theta)$. Each one of such combinations corresponds to a different momentum distribution, which strongly differs from a generic Fermi-Dirac form (Abazajian et al., 2001).

2.2.2 Production from scalar decay

Production from scalar decay (SD) is described by a generic model that invokes one real scalar singlet S and (at least) one sterile neutrino N beyond the Standard Model. The scalar singlet couples to the SM Higgs doublet Φ via a *Higgs portal*, while the interaction between the scalar and the sterile neutrino is described by a Yukawa-type coupling.

The free parameters of the scalar decay model are: 1) the Higgs portal coupling λ, which determines the production rate and the kinematics of the scalar from the SM degrees of freedom of the Higgs doublet; 2) the Yukawa coupling y, which enters into the decay rate of the scalar and hence controls how fast the scalar decays into sterile neutrinos; 3) the mass of the scalar singlet, m_S, which determines which channels contribute to the production of scalars and thereby finally to the abundance of sterile neutrinos (see Sect. 2 of König et al. 2016); 4) the mass of the sterile neutrino m_ν, strongly influencing the effects on cosmological structure formation.

In Menci et al. (2017a), we treated λ, y, and m_S as free parameters. For each triple of (λ, y, m_S), we fixed the mass of the sterile neutrino by requiring it to reproduce the observed relic DM abundance. The interplay between the Higgs portal and the Yukawa coupling results in two different regimes: 1) for small Higgs portal couplings, the scalar itself is produced by freeze-in and is always strongly suppressed compared to its would-be equilibrium abundance. In this case, the relic abundance of sterile neutrinos (and hence the mass m_ν) are independent of the Yukawa coupling y for a

fixed pair (m_S, λ). 2) When λ is large enough to equilibrate the scalars, they will be subject to the well-known dynamics of freeze-out. In this regime, sterile neutrinos can be produced from scalars in equilibrium and from those decaying after freeze-out. Accordingly, the number density of steriles and thereby their mass m_ν can strongly depend on y even for fixed (m_S, λ).

2.2.3 The halo MF of sterile neutrino models

An approach similar to the one adopted for thermal WDM is used for the sterile neutrino RP and SD models, but in this case the power spectrum is computed directly by solving the Boltzmann equation after computing the distribution function for all points of the parameter space. The resulting differential mass functions are characterized by a maximum value at masses close to the "half-mode" mass (e.g., Schneider et al., 2012; Angulo et al., 2013), the mass scale at which the spectrum is suppressed by 1/2 compared to CDM. This function depends strongly on the sterile neutrino mass; for RP models it also depends on the lepton asymmetry assumed and, hence, on the resulting mixing angle θ; typical power spectra in such models yield half-mode masses ranging from $M_{hm} \approx 10^{10}\, M_\odot$ to $M_{hm} \approx 10^{8}\, M_\odot$. Correspondingly, the cumulative mass functions saturate to a maximum value $\overline{\phi}(z) \approx \phi(M_{hm}, z)$, defining the maximum number density of DM halos associated to the considered power spectrum.

2.3 Fuzzy Dark Matter

Fuzzy DM models assume the DM to be composed of a non-relativistic Bose-Einstein condensate, so that the uncertainty principle counters gravity below a Jeans scale corresponding to the de Broglie wavelength of the ground state. In this case, the suppression of small scale structures and the formation of galactic cores in dwarf galaxies is in fact entirely due to the uncertainty principle, which counteracts gravity below the Jeans scale, corresponding to a mass scale $M_J = 10^7\, M_\odot\, m_{22}^{-3/2}$ (Marsh & Silk, 2014), where $m_{22} \equiv m_\psi / 10^{-22}$ eV. In such models, the DM mass m_ψ ultimately determines all the relevant DM physical scales in structure formation, since it determines the scale below which an increase in momentum opposes any attempt to confine the particle any further.

In the Fuzzy DM case, dedicated N-body simulations (Schive et al., 2016) yield for the differential mass function the form

$$\frac{\mathrm{d}\,\phi}{\mathrm{d}(\ln M)} = \left.\frac{\mathrm{d}\,\phi}{\mathrm{d}(\ln M)}\right|_{\mathrm{CDM}} \cdot \left[1 + \left(\frac{M}{M_0}\right)^{-1.1}\right]^{-1.2}, \tag{5}$$

where $|\mathrm{d}\,\phi/\mathrm{d}\,(\ln M)|_{\rm CDM}$ is the halo mass function in the CDM scenario. The auxiliary mass scale $M_0 = 1.6{\times}10^{10}\,(m_\psi/10^{-22}\ \mathrm{eV})^{-4/3}\,M_\odot$, determining the suppression of the halo mass function compared to the CDM case, depends on the Fuzzy DM candidate mass, and it plays a role analogous to the half-mode mass scale for sterile neutrino models.

3 The observed galaxy number density at z∼6

The above mentioned halo number densities are compared to the observed number density ϕ_{obs} of galaxies derived by integrating the galaxy luminosity function (LF) at $z = 6$ by Livermore et al. (2016) down to the faintest bin $M_{\rm UV} = -12.5$. Constraints on DM models are simply put by requiring that observed galaxies cannot outnumber their host DM halos ($\overline{\phi} \geq \phi_{obs}$). The reference luminosity function has been estimated from objects in the Abell 2744 and MACS 0416 cluster fields, selected on the basis of their photometric redshift. The UV LF with the corresponding 1-σ uncertainties in each magnitude bin is estimated on the basis of the median magnification for each galaxy in the sample and is reported in Fig. 10 of Livermore et al. (2016). From this we have derived the observed cumulative number density ϕ_{obs} (and its confidence levels) through a Monte Carlo procedure. We extracted random values $\Phi_{random}(M_{UV})$ of the luminosity function in each magnitude bin according to a Gaussian distribution with variance given by the relevant error bar. Thus, for each simulation we produced a new realization of the luminosity function at $z = 6$. From this, a cumulative number density ϕ_{random} has been derived by summing up the values of $\Phi_{random}(M_{UV})$ in all the observed magnitude bins in the range $-22.5 \leq M_{UV} \leq -12.5$. We carried out $N_{sim} = 10^7$ simulations to compute the probability distribution function (PDF) of the cumulative number density ϕ_{random}. We obtain a median value $log\,\phi_{obs}/\mathrm{Mpc}^{-3} = 0.54$, while from the relevant percentiles of the PDF we derive lower bounds 0.26, 0.01, and -0.32 at 1, 2, and 3-σ confidence levels, respectively.

4 Results

4.1 Thermal WDM

In Fig. 1 we show the cumulative mass function $\phi(> M)$ at $z = 6$ for different assumed WDM particle masses. All the mass functions saturate to a maximum number density $\overline{\phi}_{m_\chi} \approx \phi(M_{hm})$. This is compared with the observed number density ϕ_{obs} of galaxies

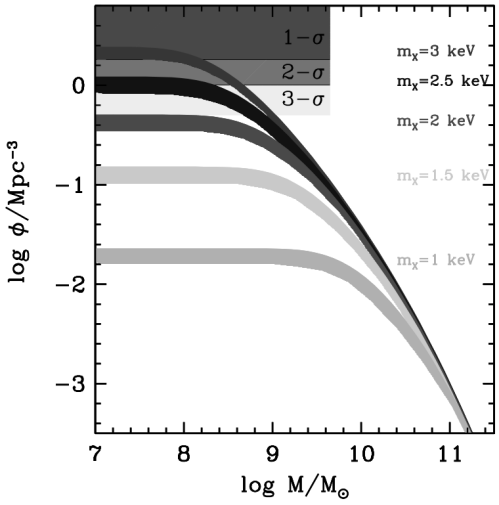

Figure 1: *Adapted from Menci et al. (2016b): the cumulative mass functions computed at $z = 6$ for different values of the WDM particle mass m_X from 1 to 3 keV (bottom to top). The shaded areas correspond to the observed number density of HFF galaxies within 1-σ, 2-σ, and 3-σ confidence levels.*

with $M_{UV} \leq -12.5$. The condition $\phi_{obs} \leq \overline{\phi}_{m_X}$ yields $m_X \gtrsim 2.9$ keV at 1-σ level, $m_X \geq 2.4$ keV at 2-σ level, and $m_X \geq 2.1$ keV at 3-σ level.

4.2 Sterile Neutrino from resonant productions

In the case of resonantly produced sterile neutrino DM, we choose the free parameters to be the mass, m_ν, and the mixing amplitude $\sin^2(2\theta)$. We first investigate the effect of varying the mixing angle for a fixed sterile neutrino mass by focusing on the case $m_\nu = 7.1$ keV, corresponding to a sterile neutrino whose decay could be at the origin of the potential 3.5 keV line in X-ray spectra of clusters. For such a case, the spectra yield the cumulative halo mass functions shown in Fig. 2 (left panel) for different values of $\sin^2(2\theta)$. The condition on the number density of DM halos to be larger than the observed abundance $\overline{\phi} \geq \phi_{obs}$ restricts the mixing angle in the range $2 \times 10^{-11} \leq \sin^2(2\theta) \leq 10^{-9}$ (at 2-σ confidence level).

We also explore the whole range of free parameters using a grid of values for

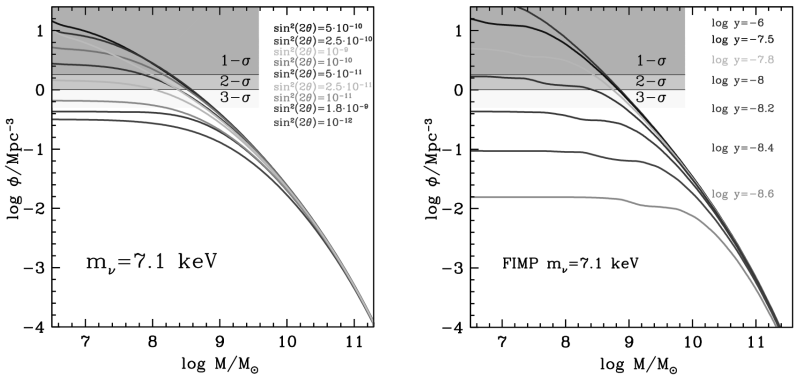

Figure 2: *Adapted from Menci et al. (2017a): same as Fig. 1 for Resonant Production (left) and Scalar Decay with small Higgs portal coupling (right) sterile neutrino DM models. The illustrative case with $m_\nu = 7.1$ keV, corresponding to a particle whose decay could be at the origin of the potential 3.5 keV line in X-ray spectra of clusters, is considered. The cumulative mass functions are derived at varying mixing amplitude (from 10^{-12} to 5×10^{-10}, bottom to top) and Yukawa coupling y (log(y) from -8.6 to -6, bottom to top) for the RP and SD case respectively.*

both m_ν and $\sin^2(2\theta)$. After computing the corresponding power spectra, the condition $\overline{\phi} \geq \phi_{obs}$ leads to the exclusion region in the plane $m_\nu - \sin^2(2\theta)$ shown in Fig. 3. We exclude all models with a sterile neutrino mass below $m_\nu \leq 5$ keV and also large parts of the parameter space above.

4.3 Sterile Neutrino from scalar decay

In the case of SD sterile neutrinos the parameter space is three-dimensional, since it includes the mass of the scalar m_S, the Higgs portal coupling λ and the Yukawa coupling with the scalar y. We show in Fig. 2 (right panel) a comparison between the model cumulative halo distributions and the observed number density of galaxies in the illustrative case of a sterile neutrino with $m_\nu = 7.1$ keV (the candidate origin of the potential 3.5 keV line) in the limit of small Higgs portal coupling $\lambda \ll 10^{-6}$. In this case, the present data allow to set a constraint $y \geq 9\times10^{-9}$ at 2-σ confidence level.

We then extend our exploration to cover the whole parameter space of SD production model for sterile neutrinos. To this aim, we consider a grid of λ and y values

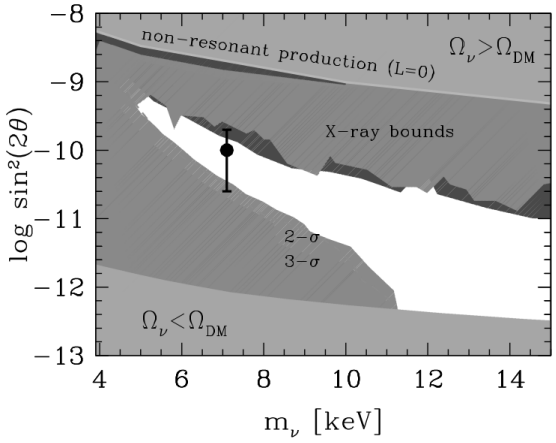

Figure 3: *Adapted from Menci et al. (2017a): the constraints on the RP sterile neutrino parameter space from our method are represented as exclusion regions, with 3-σ and 2-σ limits represented by darker and lighter colors, together with other constraints from the literature (see Menci et al., 2017a, for details). The tentative line signal at 7.1 keV is shown by the point with error bars.*

for six different values of the scalar mass m_S / GeV $= 60, 65, 100, 170, 500, 1000$. For each value of m_S, we compute the power spectrum corresponding to each point in the $\lambda - y$ plane. In Fig. 4 of Menci et al. (2017a) we show the regions of the parameter space consistent with the galaxy number densities measured in the HFF ($\overline{\phi} \geq \phi_{\rm obs}$). These regions clearly split into a freeze-out (for $\lambda \geq 10^{-6}$) and freeze-in (for $\lambda \ll 10^{-6}$) family. For the freeze-out family, decreasing the scalar mass m_S leads to a tighter bound on y, while yielding an approximate lower bound of $\lambda \gtrsim 10^{-5.2}$ for the Higgs portal coupling. For the freeze-in family, decreasing the scalar mass m_S pushes the admitted values of λ to progressively smaller values, while providing progressively stronger limits on y.

4.4 Fuzzy DM

The large observed number density of high redshift galaxies turns out to provide particularly strong constraints on Fuzzy DM. In Fig. 4 we show the cumulative halo mass function for different values of the DM particle mass (in units of 10^{-22} eV). The

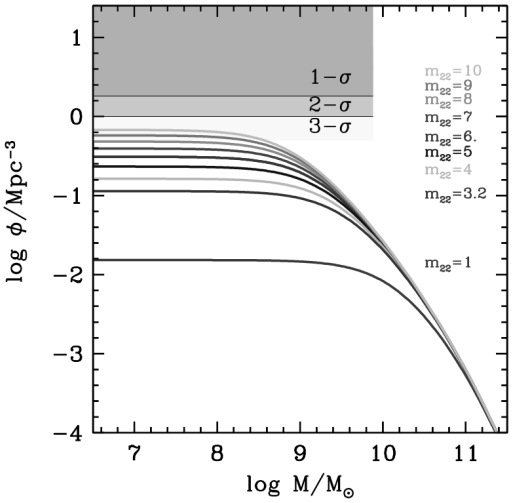

Figure 4: *Adapted from Menci et al. (2017a): same as Fig. 1 for Fuzzy DM models with varying particle mass from 1 to 10 in units of* 10^{-22} *eV (bottom to top).*

strong suppression in the number of low-mass halos compared to the CDM case yields a lower limit $m_\psi \geq 10^{-21}$ eV for the DM particle mass at 3-σ confidence level. Our results constitute the *tightest constraint on Fuzzy DM particles derived so far*, and have a strong impact for the whole class of models based on Fuzzy DM. In fact, all results in the literature indicate that the mass of Fuzzy DM particles should be in the range $m_\psi = (1-5.6)\cdot 10^{-22}$ eV to explain the observed density profile of nearby dwarf galaxies (e.g., Gonzáles-Morales et al., 2016). This is inconsistent at more than 3-σ confidence level with our lower limits, strongly disfavoring such scenarios.

5 Summary and conclusions

The recently measured UV luminosity functions (LFs) of ultra-faint lensed galaxies at $z \approx 6$ provide strong constraints on DM models with suppressed power spectra. The comparison of the predicted maximum number density of DM halos $\overline{\phi}$ to the observed number density ϕ_{obs} provide robust constraints through the simple condition that observed galaxies cannot outnumber their host DM halos ($\overline{\phi} \geq \phi_{obs}$). Remarkably, these constraints are conservative, and independent of the modeling of baryonic

physics in low-mass galaxies. The mass of WDM thermal relic candidates is constrained to be $m_X \geq 2.9$ keV at 1σ confidence level, and $m_X \geq 2.4$ keV at $2-\sigma$ level. The parameter space for RP and SD sterile neutrino models is significantly restricted. By taking the notable case of sterlie neutrinos whose decay can explain the potential 3.5 keV line ($m_\nu = 7.1$ keV), the mixing amplitude in the RP case is restricted to $-11.4 \leq \log \sin^2(2\theta) \leq -10.2$, while the Yukawa coupling y for SD production is constrained to $y \geq 9 \times 10^9$ at 2-σ confidence level.

While our method is robust and independent of the baryon physics entering galaxy formation, we note that the measurements of the luminosity functions from strongly lensed galaxies are particulary delicate at the faint end where large magnifications are involved and where the computation of effective volumes is prone to subtle systematic effects. As an example, Bouwens et al. (2016b) have adopted a different estimate of the impact of lensing magnifiction finding not only a lower median value for the number density of galaxies at $M_{UV} = -12.5$ compared to Livermore et al. (2016), but also larger error bars, resulting in looser constraints on the parameters of DM models. A thorough discussion of the impact of observational uncertainties on our constraints is provided in Menci et al. (2016b) and Menci et al. (2017a).

The main step to provide more stringent constraints is thus clearly a deeper understanding of the systematics associated with the lensing observations of faint, high-redshift galaxies. Refined lensing models and more accurate determinations of the source redshifts, together with the inclusion of observational data from other strong-lensing cluster will certainly enable an improved comparison between the observed galaxy number density and predicted halo number density in a variety of DM scenarios. In a few years from now a significant leap will be made possible by deep JWST imaging reaching absolute magnitudes of $M_{\rm UV} \approx -11$ on 5 times larger samples of high-redshift galaxies.

References

Abazajian, K., Fuller, G. M., & Patel, M. 2001, Phys. Rev., D64, 023501, astro-ph/0101524

Ackermann, M., et al. 2015, Phys. Rev. Lett., 115, 231301, 1503.02641

Angulo, R. E., Hahn, O., & Abel, T. 2013, Mon. Not. Roy. Astron. Soc., 434, 3337, 1304.2406

Aprile, E., et al. 2012, Phys. Rev. Lett., 109, 181301, 1207.5988

Bode, P., Ostriker, J.P., Turok, N. 2001, ApJ, 556, 93

Bond, J.R., Cole, S., Efstathiou, G., & Kaiser, N., 1991, ApJ, 379, 440

Bouwens, R. J., Oesch, P. A., Illingworth, G. D., Ellis, R. S., & Stefanon, M. 2016b, ArXiv e-prints, 1610.00283

Boyarsky, A., Ruchayskiy, O., & Iakubovskyi, D. 2009, JCAP, 0903, 005, 0808.3902

Boyarsky, A., Ruchayskiy, O., Iakubovskyi, D., & Franse, J. 2014, Phys. Rev. Lett., 113, 251301, 1402.4119

Bulbul, E., Markevitch, M., Foster, A., Smith, R. K., Loewenstein, M., & Randall, S. W. 2014, Astrophys. J., 789, 13, 1402.2301

Dodelson, S., & Widrow, L. M. 1994, Phys. Rev. Lett., 72, 17, hep-ph/9303287

Gonzáles-Morales, A. X., Marsh, D. J. E., Peñarrubia, J., & Ureña-López, L. 2016, ArXiv e-prints, 1609.05856

König, J., Merle, A., & Totzauer, M. 2016, 1609.01289

Livermore, R. C., Finkelstein, S. L., & Lotz, J. M. 2016, ArXiv e-prints, 1604.06799

Marsh, D. J. E., & Silk, J. 2014, Mon. Not. Roy. Astron. Soc., 437, 2652, 1307.1705

Menci, N., Sanchez, N. G., Castellano, M., & Grazian, A. 2016b, ApJ 818, 90, 1601.01820

Menci, N. and Merle, A. and Totzauer, M. and Schneider, A. and Grazian, A. and Castellano, M. and Sanchez, N. G., ApJ 836, 61, 1701.01339

Merle, A., Schneider, A., & Totzauer, M. 2016, JCAP, 1604, 003, 1512.05369

Peebles, P. J. E. 1982, Astrophys. J., 263, L1

Polisensky, E., & Ricotti, M. 2011, Phys. Rev., D83, 043506, 1004.1459

Schive, H.-Y., Chiueh, T., Broadhurst, T., & Huang, K.-W. 2016, Astrophys. J., 818, 89, 1508.04621

Schneider, A., Smith, R. E., Maccio, A. V., & Moore, B. 2012, Mon. Not. Roy. Astron. Soc., 424, 684, 1112.0330

Schneider, A., Smith, R. E., & Reed, D. 2013, Mon. Not. Roy. Astron. Soc., 433, 1573, 1303.0839

Schultz, C., Onorbe, J., Abazajian, K. N., & Bullock, J. S. 2014, Mon. Not. Roy. Astron. Soc., 442, 1597, 1401.3769

Shi, X.-D., & Fuller, G. M. 1999, Phys. Rev. Lett., 82, 2832, astro-ph/9810076 xs

Steffen, F. D. 2006, JCAP, 9, 001, hep-ph/0605306

Viel, M., Becker, G. D., Bolton, J. S., & Haehnelt, M. G. 2013, Phys. Rev., D88, 043502, 1306.2314

Frascati Physics Series Vol. 66 (2018)
Frontier Objects in Astrophysics and Particle Physics
May 20-26, 2018

EXPERIMENTAL DIRECT DARK MATTER SEARCH

Alfredo D. Ferella
Oskar Klein Centre, Department of Physics, Stockholm University, Sweden

Abstract

Dark Matter is one of the most challenging puzzles of modern physics. Its indisputable evidence so far comes solely from its gravitational interaction, but it is believed to have particle nature. The Weakly Interacting Massive Particle (WIMP) still remains the best-motivated candidate. After a brief introduction and motivation to the WIMP paradigm, the WIMP direct detection principles will be explained, and a review of the leading experiments and their recent results will be given.

1 Introduction

The solution to the Dark Matter puzzle is surely one of the main challenges of modern particle and astroparticle physics. Strong observational evidences provide a picture of a Universe in which Dark Matter constitutes about 85%

of the total matter. Yet Dark Matter has not been directly detected. In this review the Dark Matter problem will be discussed and the approaches to directly detect it, in the form of a special category of particles, will be presented.

The evidence of Dark Matter comes from astrophysical observations at different scales and with completely different techniques. From galactic to cosmological scale [1, 2, 3, 4] all evidences strongly suggest that more than 95% of the Universe is made of invisible and unknown types of matter and energy.

1.1 Particle Dark Matter

The existence of Dark Matter having been assessed, one question arises: what are the Dark Matter characteristics and nature? Moving from experimental evidences and astronomical observations, with the help of theoretical predictions we can attempt to depict the "identikit" of an hypothetical Dark Matter particle.

As already highlighted above, the Dark Matter interacts gravitationally, meaning that it is constituted by **massive** particles that are definitely **non-baryonic** and **electrically neutral** (being invisible to any radiation sensitive device). Furthermore, having been there also at the time when the Universe became transparent to light, as measured from the cosmic microwave background, Dark Matter particles have to be **stable** or at least have a lifetime longer than the age of the Universe.

Dark Matter candidates may be classified as 'hot' (relativistic) or 'cold' (non-relativistic) according to their energy at the time when they decoupled from the rest of the Universe. The observations on the present Universe suggest Dark Matter being predominantly cold, i.e. **non-relativistic**. This is derived from the relation between the tiny fluctuations in the matter-density of the early Universe and the large scale structures observed nowadays: if Dark Matter were hot it would not be able to assemble in confined regions and the Universe structures observed today would have been much more isotropic.

1.2 WIMPs and their Miracle

The evolution of the number density of any particle χ over the age of the Universe t follows the Boltzmann equation [5] in which annihilation and creation of χ is modeled in terms of the temperature (i.e. kinetic energy) of the particle

species and of the Universe expansion rate. In the early instants the temperature is high enough that the production rate equals the annihilation rate and $n_\chi = n_\chi^{eq}$. As soon as the thermal kinetic energy of χ particles falls below their mass ($= m_\chi$) the production is suppressed and n_χ decays exponentially until the expansion term starts dominating and there is no more annihilation.

At this point in time the total density of χ particles (Ω_χ) is then found to be: $\Omega_\chi = 1.66\ g^{1/2} \frac{T_0^3}{\rho_c m_{Pl} \langle \sigma_A | v \rangle}$. Substituting $T_0 = 2.35 \cdot 10^{-4}$ eV (the current Universe temperature), $\rho_c \simeq 1 \times 10^4\ h^2$ eV$\cdot$ cm^{-3} (the critical density), $m_{Pl} = 1.22 \cdot 10^{28}$eV (Planck mass) and $g^{1/2} \sim 1$, we obtain:

$$\Omega_\chi h^2 = \frac{m_\chi n_\chi}{\rho_c} \simeq \frac{3 \cdot 10^{-27} cm^3 s^{-1}}{\langle \sigma_a v \rangle}$$

Therefore, in the case of Dark Matter particles we find that $\langle \sigma_a v \rangle \sim 10^{-26} \div 10^{-25}$cm^{3}s^{-1}. Incidentally this value is very close to what is expected from a "weak-scale" ($m_\chi \sim 100$ GeV c^{-2}) particle interacting through electroweak force ($\langle \sigma_a v \rangle \sim 10^{-25}$cm^{3}s^{-1}), therefore dubbed "**Weakly Interacting** Massive Particle" (WIMP). Many supersymmetric extensions of the Standard Model of particle physics predict the existence of a particle with similar characteristics. For this reason this coincidence of Cosmology and Particle Physics predictions is not seen as actually "accidental", rather as a *(WIMP) miracle*.

1.3 Detection of WIMPs

Dark Matter particles can be searched via three different methods:

1. **Indirect detection:** by looking for excesses of standard model particles in large, heavy astrophysical objects (galaxies, stars, etc...), possibly coming from Dark Matter annihilation;
2. **Collider production:** by searching for missing energy at colliders, possibly coming from Dark Matter production;
3. **Direct detection:** by detecting signals of low energy deposits coming from Dark Matter particle scattering off nuclei in low background detectors placed underground.

2 Direct Dark Matter Detection

If WIMPs exist and are the dominant constituent of Dark Matter, they must be present also in the Milky Way [6)] and, though they very rarely interact with

conventional matter, should nonetheless be detectable in sufficiently sensitive experiments on Earth. Assuming a local density of $\rho_0 = 0.3$ GeV$\cdot$ cm^{-3} and a WIMP mass of $m_\chi = 100$ GeV$\cdot$ c^{-2}, the WIMP flux on Earth is expected to be of the order of 10^5 cm^{-2}s^{-1} [7], large enough to allow the detection of a significant number of nuclear recoils caused by their elastic scatterings off target nuclei of Earth based detectors [8]. Direct Dark Matter search experiments, indeed, aim to detect the interactions of WIMPs in dedicated low background detectors, by measuring the rate, R, the energy, E_R and possibly, in directional experiments, the direction of the WIMP-induced nuclear recoils. Since the WIMP$-$nucleon relative velocity v is non-relativistic, the recoil energy E_R can be expressed in terms of the scattering angle in the center of mass frame, θ as [9]:

$$E_R = \frac{|\vec{q}|^2}{2m_N} = \frac{\mu_{\chi-N}^2 v^2}{m_N}(1-\cos\theta), \tag{1}$$

where m_N and m_χ are the masses of the target nucleus and of the WIMP respectively, $|\vec{q}| = \sqrt{2m_N E_R}$ is the momentum transfer and $\mu_{\chi-N} = \frac{m_\chi m_N}{m_\chi + m_N}$ is the WIMP-nucleus reduced mass.

2.0.1 The Rate

The differential nuclear recoil rate induced by the WIMPs can be written as:

$$\frac{dR}{dE_R}(E_R, t) = \frac{\rho_0 \sigma_0}{m_N m_\chi} \int_{v_{min}}^{v_{esc}} v \cdot f(\mathbf{v}) \cdot F^2(E_R, \mathbf{v}) \cdot d^3v. \tag{2}$$

Here E_{th} is the energy threshold of the detector, ρ_0 is the local Dark Matter density, σ_0 is the cross section at zero momentum transfer, $f(v)$ is the WIMP velocity distribution in the halo, v_{min} is the minimum velocity required for the WIMP to generate the recoil energy E_R and v_{esc} is the galactic escape velocity. $F^2(E_R)$ is the nuclear form factor, that accounts for the fact that the de Broglie wavelength associated with the momentum transfer is of the same order as the nuclear dimensions; thus the bigger the nucleus the stronger its effect.

The main astrophysical uncertainties lie in the velocity distribution $f(v)$ (commonly assumed to be Maxwellian) and in the local Dark Matter density ρ_0 (usually assumed equal to 0.3 GeVc^{-2}cm^{-3}). Detecting the direction of the WIMPs would provide a viable solution to the velocity distribution function problem.

2.0.2 The Cross Section

In order to provide an interpretation of the outcome of a Dark Matter direct detection experiment some assumption on the specific particle-physics model needs to be made. If WIMPs are neutralinos, i.e. Majorana fermions, for example, they can have only scalar or axial coupling with quarks, which, in this specific non-relativistic regime, translates into a spin-independent coupling and a coupling between the neutralino spin and the nucleon spin. In the spin-independent case, the full coherence results in a cross section $\sigma_0 \propto A^2$, for a target nucleus of mass number A, while in the spin-dependent case the cross section is dominated by the total net spin of the nucleus. In most cases, the coherent term will dominate because of the A^2 enhancement. However, neutralinos with dominantly gaugino or higgsino states, for example may only couple through the spin-dependent term.

In the generalized framework of non-relativistic effective field theories (EFT), the WIMP-baryon possible couplings can be worked out. In this case six possible nuclear response-functions are present, described by 14 different operators [10, 11, 12].

2.0.3 The Modulation of the Rate

As a result of the Earth motion relative to the WIMP halo, the event rate is expected to modulate with a period of one year with the maximum on the 2$^{\text{nd}}$ of June. To detect this characteristic modulation signature, large masses are required, since the effect is of the order of $\sim 3\%$ with respect to the total event rate [13]. A stronger diurnal direction modulation of the WIMP signal is also expected. The Earth rotation about its axis, oriented at an angle with respect to the WIMP "wind", changes the signal direction by 90 degrees every 12 hours, with a resulting 30% modulation with respect to the total rate [14].

2.1 General experimental considerations

Several experimental effects are in common with all the technologies employed for direct detection of Dark Matter, some due to the nature of the interaction and others related to the common sources of background. In the remaining part of this section some general experimental considerations are discussed to help the understanding of the case, while specific detector related effects need

to be considered separately in the discussion of the individual experimental approach.

Nuclear recoils induced by WIMPs are detected exploiting the three basic phenomena associated with the energy loss of charged particles in target media: scintillation, ionization and heat. All the detectors used to perform this rare event search are also sensitive to the environmental radiation associated with cosmic rays and radioactivity in construction materials and the environment. At the current limits [15] the expected WIMP rate is ~ 1 event per ton per year and significant SUSY parameter space still exists down to such rates that will be accessible by upcoming multiton-scale detectors with nearly vanishing backgrounds.

Because of such small expected signal rates, Dark Matter search experiments are usually located in deep-underground sites, where the cosmic muons' flux is attenuated by a factor 10^5 to 10^8 with respect to the surface. In addition, such detectors are typically enclosed in thick layers of (active or passive) shielding materials, in order to reduce the contribution to signals from environmental (background) radiation. Moreover shielding and detector components have to be selected with the lowest possible radioactivity.

The signals recorded by a WIMP-search experiment are of two types: nuclear recoils **(NR)** and electronic recoils **(ER)**.

NR are the looked-for-signals, but can also be induced by (background) fast neutrons. Such neutrons may either be the product of spontaneous fission and/or (α, n) reactions from environmental and detector construction materials (mainly induced by natural primordial radionuclides ^{238}U and ^{232}Th), or arise from the hadronic showers produced by the highly energetic residual cosmic ray muons. The neutron contribution to the signal is usually modeled via Monte Carlo simulations including detector response, detailed detector and surrounding geometry and using, for the global normalization scaling, the cosmic muon flux and spectrum, and measurements of the radioactivity content of the materials surrounding the detector. Coherent scattering of solar, diffused supernovae and atmospheric neutrinos off target nuclei will also soon become an important background that mimics the DM signal [16].

ER are the dominant background in direct WIMP search experiments and are produced by the interaction of γ-rays originating from the decays of the uranium and thorium chains as well as from other radioactive isotopes present

in the vicinity of the detector. Techniques for background reduction need to be employed in order to be able to isolate the signal in sensitive experimental data. In the following a general discussion on background reduction and ER rejection is given. For a more detailed description of background sources and reduction techniques the reader is referred to reference [17].

Since the mean free path of a high energy γ-ray or of a fast neutron is of the order of centimeters, while the mean free path of a WIMP is of the order of light-years, the identification of multiple scatters, sometimes referred to as multi-site events, constitutes a powerful background rejection tool. Moreover some detectors have the advantageous ability of reconstructing the interaction verteces, allowing volume fiducialization, that helps both with self-shielding and with rejection of spurious events coming from surface contamination. Finally in many Dark Matter direct search experiments background discrimination mechanisms are used, based on the fact that nuclear recoils (signals) and electronic recoils (backgrounds) have different signatures in the detector, due to their different nature. Electronic recoil rejection techniques are mainly based on the principle that NR have much denser energy losses than ER. Therefore one can exploit this effect either with hardware solutions or with software (analysis) active rejection. In particular a detection technology that is not sensitive to weakly ionizing charged particles is employed in superheated liquid detectors (see section 3.2). Two main analysis approaches are used in off-line software rejection: *pulse shape discrimination* and *combination of two detection channels* (ionization and scintillation, for example).

Dedicated calibrations are used to define the signal (neutron source) and background (γ or β source) regions in the parameter space usually defined by the readout signals.

3 A biased selection of WIMP search experiments

A large variety of experiments aiming at direct WIMP detection are deployed in underground laboratories all around the world. Many have finished their research program and several ton or multi-ton scale are currently under construction. In this review it is not possible to give count of all and only a small selection of them is presented that should provide an overview of the current status and the direction the field is taking. For more details the reader is referred to a more general review. One of the most complete of the recent

reviews of the field is [18]; however being relatively old it misses some of the most recent results and proposed experiments.

The technologies employed in this experimental research field are: NaI(Tl) scintillator crystals (see section 3.1 for details), other scintillators [19], ionization germanium detectors [20, 21, 22], cryogenic bolometers [23, 24, 25], liquid noble elements-based detectors (see sec. 3.3), superheated liquid detectors (see sec. 3.2), directional detectors [26], gas based detectors [27, 28], paleodetectors [29]. The above list is probably not completely exhaustive and the author apologizes in advance in case some experiment or technology is not listed or not present in the provided bibliography.

3.1 DAMA/Libra: a longstanding, controversial signal

In a review of this type a mention is deserved by the DAMA/Libra longstanding claim [30] of a significant annually modulated signal, compatible (in period, phase and energy spectrum) with Dark Matter detection.

The project was designed in early 1990s by an Italian group, in collaboration with Chinese and French colleagues, and installed at Gran Sasso underground laboratory [31]. The detector (DAMA) was initially based on nine 9.7 kg of highly radio-pure NaI(Tl) scintillators shielded from radioactive background. The collaboration has then increased the sensitive mass to about 250 kg of NaI(Tl) (LIBRA). The threshold provided for both experiments was 2 keV.

More recently the LIBRA detector was upgraded [32] by replacing all the photomultiplier tubes (PMTs) with new ones with higher quantum efficiency and lower radioactivity. This upgrade resulted in a lower software threshold of 1 keV as well as a better energy resolution and a higher acceptance efficiency near the threshold.

The DAMA experiment belongs to the first generation of dark matter direct detection experiments, with no background rejection, therefore requiring a large detector exposure. Although the NaI(Tl) scintillator provides some discrimination between nuclear recoils and electronic recoils based on pulse shape, the collaboration published its data without any background reduction. Using a total exposure (2.46 ton$\times$year), combining old and new data the collaboration reported a 12.9σ C.L annual modulation in the energy range $[2, 6]$ keV. The modulation analysis carried out using a simple sinusoidal function

$A(t) = A_0 \cos[\omega(t - t_0)]$ results in the following outcome:
$A_0 = 0.0103 \pm 0.0008$ cpd/kg/keV
$t_0 = 145 \pm 5$ days
$T = \frac{2\pi}{\omega} = 0.999 \pm 0.001$ years

The DAMA/LIBRA evidence for the annual modulation is clear but only in the lowermost energy bins (2-6 keV corresponding to a nuclear recoil energy of 22-66 keV for interaction on Iodine nuclei) where the understanding of the efficiencies is particularly important. The origin of this clear modulation and its interpretation continue to be widely disputed, although many studies have been performed by the collaboration regarding various possible systematic effects.

The DAMA/LIBRA result is in strong tension with all other more sensitive WIMP search experiments employing different detection technologies, even when they give up any ER rejection [33]. Therefore several experimental efforts have started in different underground laboratories in order to confirm or refute the DAMA/LIBRA signal using the same NaI detection medium. The main challenge is to obtain crystals of kg-scaled sizes with the same (or lower) radioactive contamination as the DAMA/LIBRA crystals. An intensive investigation on low radioactive samples of NaI powder and on clean crystal growth procedures have led to the development of a specific process that has become a standard between all these experiments [34, 35]. There are NaI-based dark matter search experiments in operation (DM-Ice17 [36], ANAIS [37, 38]) or under development (DM-Ice [39], Kam-LAND-PICO [40], SABRE [41, 34], COSINUS [42]). These detectors are/will be located in both Northern and Southern hemispheres; therefore possible seasonal or site effects can be disentangled from the dark matter modulation. Definitive results are expected in the next three to five years.

3.2 Superheated liquid detectors

After their invention in 1952 [43] and the successful years of applications in accelerator experiments in 1960s and 1970s, classical bubble chambers have been outclassed by other detection technologies and for several decades they have been almost forgotten. However the relatively large use of superheated liquid "droplet" detectors in neutron dosimetry has likely inspired their application in the context of direct Dark Matter search [44].

In this technology the target is kept in liquid phase in a superheated state

slightly below its boiling point. Proto-bubbles are created by the thermal spikes of released heat on a particle track. The growth of such bubbles is dumped by various thermal processes. Therefore macroscopic liquid-to-vapor phase transitions can happen only if an amount of energy larger than a certain critical value (E_c) is deposited within a thermal spike length $L < 2R_c$, where R_c is the "critical radius", i.e. the minimal radius that the proto-buble should have to nucleate. Therefore the superheated liquid thermodynamical conditions can be tuned in such a way that only particles with $dE/dx > 50$ keV/μm (like scattered nuclei) can nucleate a bubble. In this way the detector is extremely insensitive to electronic recoil events ($> 10^{10}$ rejection power), since all other background particles (muons, γ-rays, X-rays and βs) are well below the nucleation threshold. The energy threshold for recoiling nuclei can be set as low as a few keV. Precautions are being taken in order to reduce the inhomogeneous bubble nucleation by mildly superheating the liquid. The bubbles forming in these detectors are usually photographed with CCD cameras, while the acoustic shock waves that accompany the nucleation are detected with piezoelectric transducers.

WIMP-search experiments using superheated liquids usually employ fluorine reach targets (CF_3I, C_2ClF_5, C_3ClF_8 and $C4F_{10}$). Fluorine has an unpaired number of protons and is, thus, sensitive to spin-dependent interactions. A notable source of background are the α particles from naturally occurring radioactive radioactive isotopes, mainly ^{222}Rn and its progenies, emanating from surfaces. However since α-particles have a louder acoustic emission they can efficiently ($< 99.3\%$) be rejected. Moreover, since the location of the nucleation is known with mm precision, efficient fiducialization can be applied in order to select only events in the inner core of the detector.

Five different experiments have been operating over the last years using bubble chamber (COUPP [45], PICO [46] and MOSCAB [47]) and droplet detector (PICASSO [48] and SIMPLE [49]) technologies.

PICO-60 is a 60 liter bubble chamber detector based on C_3F_8, located at SNOLAB. It ran for a few years until 2017. The experiment "set the most stringent direct-detection constraint to date on the WIMP-proton spin-dependent cross section at 3.4×10^{-41} cm^2 for a 30-GeV c^{-2} WIMP" [46].

The low background achievements and the technological developments in bubble chambers detectors for WIMP direct detection are remarkable. However

some specific effects limiting their sensitivity have been evidenced in the past 5 years that need to be addressed. In particular it has been shown by PICO-60, for example, that particulate contamination can create bulk bubbles that constitute a background signal for Dark Matter search. Although the mechanism remains largely uncertain, there are good indications that it is the interaction of the particulate with the buffer fluid to produce such events. Therefore future plans for bubble chamber detectors for WIMP search (PICO-40L, PICO-500 and MOSCAB [47]) moved from pressure (mechanical) to temperature stabilization. In this way after each event the detector-reset to the initial state is automatic. This determines the absence of any moving parts, reducing (if not eliminating) any possible particulate detachment.

3.3 Liquid noble elements based detectors

Liquid noble elements such as argon and xenon are excellent media to be used for non-segmented, homogeneous, compact and self-shielding detectors. Liquid xenon (LXe) and liquid argon (LAr) are good scintillators and have good charge conduction properties. The characteristic wavelength of the scintillation light is 175 nm and 128 nm for LXe and LAr respectively [50]. While LAr scintillation wavelength needs to be shifted to (usually blue) longer values to make this light detectable by traditional photo-sensors, that of LXe is in a relatively near ultraviolet region that allows quartz/fused silica photo-sensor transparent windows. Moreover the singlet (short-) and triplet (long-lived) states that generate the luminescence in such media are populated at different levels depending on the type of ionizing particle [51]. This provides a NR to ER discrimination tool based on pulse shape that is particularly efficient in LAr for which the characteristic times of the two components are 6 ns and 1.6 μs. For LXe the pulse shape analysis is not as effective since the lifetimes of the two components are much closer in value (4 ns and 22 ns). In order to profit of pulse shape discrimination a large number of measured photons is needed and therefore a higher threshold has to be used, making LAr based detectors mainly sensitive to relatively high mass WIMPs ($\gtrsim$ 20 GeV c^{-2}).

Moreover as already discussed above, the simultaneous detection of ionization and scintillation signals provides an additional rejection tool for ER events. This is possible when operating noble elements based detectors in dual phase time projection chambers (TPCs). In this configuration the detector

has a cylindrical geometry defined by a tube of reflective material and three optically transparent electrodes (cathode, anode and "gate grid") that define two regions with separately tunable electric field values. The liquid fills most of the volume and is the sensitive medium. The gas phase in thermal equilibrium with the liquid is above a well defined level between the gate grid and the anode. Two arrays of photo-sensors on top and bottom are usually present to detect the primary scintillation signal (S1) from particle interactions. Moreover the ionization electrons resulting from the same interaction are drifted along the electric field lines to reach the liquid-gas interface; in this region the electric field applied between gate grid and anode is strong enough to extract the electrons to the gas phase and accelerate them such that they can generate a secondary scintillation signal (S2) that is proportional to their number. In addition the 3D position of an interaction can be determined by measuring z from the time distance between S1 and S2 and $x - y$ from the S2 hit pattern on the top photo-sensor array.

LXe dual phase TPCs have shown the best performances and are leading the direct WIMP search field providing the most stringent limit on spin-independent WIMP-nucleon interaction [15]. Noble liquid elements based detectors that just finished operation successfully (or will be ending soon) are: (LAr) DarkSide-50 [52], DEAP-3600 [53], DarkSide-20k and Argo [54], (LXe) LUX [55], XMASS-I [56], PandaX-II [57], PandaX-4T [58], XENON1T and XENONnT [15, 59].

4 Beyond the WIMP paradigm

Although WIMP still remains a very well motivated Dark Matter candidate, the lack of convincing signal, combined with the increasingly stringent limits set by LHC searches for new physics has motivated in the recent years a large effort by the Dark Matter community to explore a broader set of dark matter candidates [60]. A big effort has brought to the development of innovative ideas in terms of theoretical results as well as new experimental concepts. In particular an extension of the sensitivity of current or purposely designed new detectors to lower energy deposits allows to probe DM with masses between meV to GeV scale. In Figure 4.1 the theoretical predictions from different models of a possible Dark Matter candidate mass are schematically shown, along with some of the experimental ideas for direct detection of low-mass DM

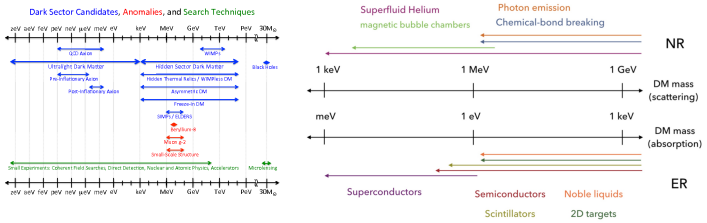

Figure 1: "Mass ranges for dark matter and mediator particle candidates, experimental anomalies, and search techniques described in this document" (left). Some new ideas on how to probe low mass Dark Matter with scattering or absorption (right). From [60]

via scattering off, or absorption by, nuclei (NR) or electrons (ER).

4.1 Low Energy Threshold: a possible reality

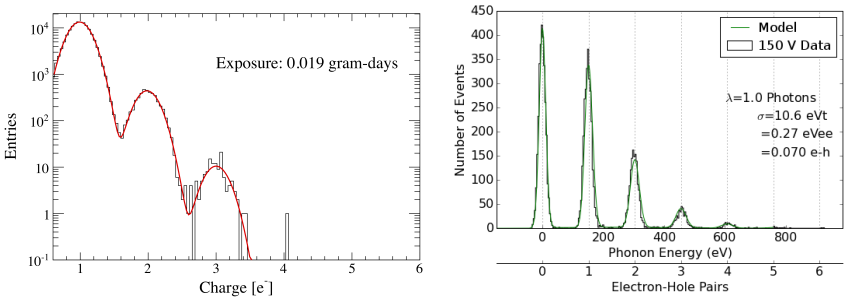

Figure 2: Recorded spectrum by the SENSEI experiment in a surface run at FermiLab [61] (left). Laser calibration data showing individual electron-hole pair sensitivity of a single crystal of silicon [62]

The low energy threshold required for low-mass Dark Matter direct detection is the main challenge in this new field. However the technology is mature to allow very low energy deposits. In particular two experiments have demonstrated single electron-hole pair sensitivity in silicon (see Figure 4.1), which

constitute a solid base for any future investigations.

5 Conclusions

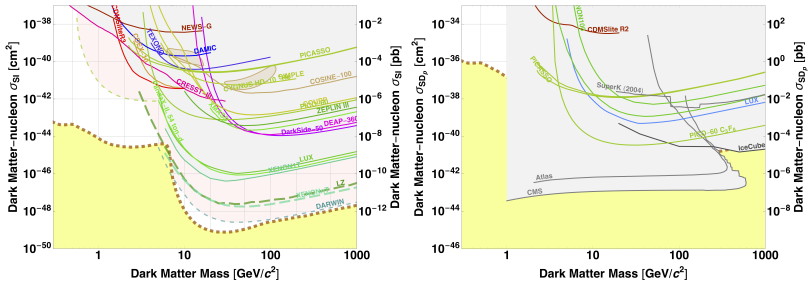

Figure 3: Limits from current experiments and DAMA/Libra allowed region and projected sensitivity of future direct WIMP search experiments. Spin-independent WIMP-nucleon (left) and spin-dependent WIMP-proton (right) cross section vs WIMP mass parameter space. Plot generated from [63]

The cold dark matter explaining all cosmological and astrophysical observations could be made of WIMPs, thermal relics from an early phase of our Universe. This hypothesis is testable with different approaches: direct detection, indirect detection and at accelerators. However so far it escaped detection in the laboratory. Liquid xenon experiments offer excellent prospects for discovery with an increase in WIMP sensitivity by ~ 2 orders of magnitude in the next decade The neutrino background will soon be on reach. Figure 5 summarizes the present status and future reach of this very competitive field. Should a future observation be made in one experiment a confirmation from at least another experiment would be required, preferably employing a different experimental technique, as well as cross checks from indirect and collider searches. Other direct searches of Dark Matter in a different lower mass particle form has already started, building on the technological achievements of past and current WIMP search experiments, but moving from nuclear to electronic scatters.

References

1. F. Zwicky. Die Rotverschiebung von extragalaktischen Nebeln. *Helv. Phys. Acta*, 6:110–127, 1933. [Gen. Rel. Grav.41,207(2009)].

2. Vera C. Rubin and W. Kent Ford, Jr. Rotation of the Andromeda Nebula from a Spectroscopic Survey of Emission Regions. *Astrophys. J.*, 159:379–403, 1970.

3. Douglas Clowe, Marusa Bradac, Anthony H. Gonzalez, Maxim Markevitch, Scott W. Randall, et al. A direct empirical proof of the existence of dark matter. *Astrophys. J.*, 648:L109, 2006.

4. N. Aghanim et al. Planck 2018 results. VI. Cosmological parameters. 2018.

5. Edward W. Kolb and Michael S. Turner. The Early Universe. *Front. Phys.*, 69:1–547, 1990.

6. Michael R. Merrifield. The Rotation curve of the milky way to 2.5-R(0) from the thickness of the HI layer. *Astron. J.*, 103:1552–1563, 1992.

7. Laura Baudis. Direct dark matter detection: the next decade. *Phys. Dark Univ.*, 1:94–108, 2012.

8. Mark W. Goodman and Edward Witten. Detectability of Certain Dark Matter Candidates. *Phys. Rev.*, D31:3059, 1985.

9. J.D. Lewin and P.F. Smith. Review of mathematics, numerical factors, and corrections for dark matter experiments based on elastic nuclear recoil. *Astropart. Phys.*, 6:87, 1996.

10. A. Liam Fitzpatrick, Wick Haxton, Emanuel Katz, Nicholas Lubbers, and Yiming Xu. Model Independent Direct Detection Analyses. 2012.

11. A. Liam Fitzpatrick, Wick Haxton, Emanuel Katz, Nicholas Lubbers, and Yiming Xu. The Effective Field Theory of Dark Matter Direct Detection. *JCAP*, 1302:004, 2013.

12. Nikhil Anand, A. Liam Fitzpatrick, and W.C. Haxton. Weakly interacting massive particle-nucleus elastic scattering response. *Phys. Rev.*, C89(6):065501, 2014.

13. A.K. Drukier, K. Freese, and D.N. Spergel. Detecting Cold Dark Matter Candidates. *Phys. Rev.*, D33:3495, 1986.

14. David N. Spergel. The Motion of the Earth and the Detection of Weakly interacting massive particles. *Phys. Rev.*, D37:1353, 1988.

15. E. Aprile et al. Dark Matter Search Results from a One Ton-Year Exposure of XENON1T. *Phys. Rev. Lett.*, 121(11):111302, 2018.

16. Louis E. Strigari. Neutrino Coherent Scattering Rates at Direct Dark Matter Detectors. *New J. Phys.*, 11:105011, 2009.

17. G. Heusser. Low-radioactivity background techniques. *Ann. Rev. Nucl. Part. Sci.*, 45:543, 1995.

18. Teresa Marrodán Undagoitia and Ludwig Rauch. Dark matter direct-detection experiments. *J. Phys.*, G43(1):013001, 2016.

19. S.C. Kim et al. New Limits on Interactions between Weakly Interacting Massive Particles and Nucleons Obtained with CsI(Tl) Crystal Detectors. *Phys. Rev. Lett.*, 108:181301, 2012.

20. C.E. Aalseth et al. Maximum Likelihood Signal Extraction Method Applied to 3.4 years of CoGeNT Data. 2014.

21. C.E. Aalseth et al. Search for An Annual Modulation in Three Years of CoGeNT Dark Matter Detector Data. 2014.

22. R.M. Bonicalzi et al. The C-4 Dark Matter Experiment. *Nucl. Instrum. Meth.*, A712:27, 2013.

23. G. Angloher et al. Results on light dark matter particles with a low-threshold CRESST-II detector. *Eur. Phys. J.*, C76(1):25, 2016.

24. R. Agnese et al. New Results from the Search for Low-Mass Weakly Interacting Massive Particles with the CDMS Low Ionization Threshold Experiment. *Phys. Rev. Lett.*, 116(7):071301, 2016.

25. E. Armengaud et al. Constraints on low-mass WIMPs from the EDELWEISS-III dark matter search. *JCAP*, 1605(05):019, 2016.

26. J. B. R. Battat et al. Readout technologies for directional WIMP Dark Matter detection. *Phys. Rept.*, 662:1–46, 2016.

27. Q. Arnaud et al. First results from the NEWS-G direct dark matter search experiment at the LSM. *Astropart. Phys.*, 97:54–62, 2018.

28. F. J. Iguaz et al. TREX-DM: a low-background Micromegas-based TPC for low-mass WIMP detection. *Eur. Phys. J.*, C76(10):529, 2016.

29. Andrzej K. Drukier, Sebastian Baum, Katherine Freese, Maciej Górski, and Patrick Stengel. Paleo-detectors: Searching for Dark Matter with Ancient Minerals. 2018.

30. R. Bernabei et al. Searching for WIMPs by the annual modulation signature. *Phys. Lett.*, B424:195–201, 1998.

31. C. Bacci et al. WIMPs search with low activity NaI crystals: Preliminary results. *Phys. Lett.*, B293:460–464, 1992.

32. R. Bernabei et al. First Model Independent Results from DAMA/LIBRA–Phase2. *Universe*, 4(11):116, 2018.

33. D. S. Akerib et al. Search for annual and diurnal rate modulations in the LUX experiment. *Phys. Rev.*, D98(6):062005, 2018.

34. M. Antonello et al. The SABRE project and the SABRE PoP. 2018.

35. P. Adhikari et al. Background model for the NaI(Tl) crystals in COSINE-100. *Eur. Phys. J.*, C78:490, 2018.

36. E. Barbosa de Souza et al. First search for a dark matter annual modulation signal with NaI(Tl) in the Southern Hemisphere by DM-Ice17. *Phys. Rev.*, D95(3):032006, 2017.

37. J. Amaré et al. Preliminary results of ANAIS-25. *Nucl. Instrum. Meth.*, A742:187–190, 2014.

38. J. Amare et al. Assessment of backgrounds of the ANAIS experiment for dark matter direct detection. *Eur. Phys. J.*, C76(8):429, 2016.

39. J. Cherwinka et al. First data from DM-Ice17. *Phys. Rev.*, D90(9):092005, 2014.

40. K. Fushimi et al. KamLAND-PICO Dark Mater Search Project. *Phys. Procedia*, 61:67–73, 2015.

41. Jingke Xu et al. Scintillation efficiency measurement of Na recoils in NaI(Tl) below the DAMA/LIBRA energy threshold. *Phys. Rev.*, C92(1):015807, 2015.

42. G. Angloher et al. The COSINUS project - perspectives of a NaI scintillating calorimeter for dark matter search. *Eur. Phys. J.*, C76(8):441, 2016.

43. Donald A. Glaser. Some Effects of Ionizing Radiation on the Formation of Bubbles in Liquids. *Phys. Rev.*, 87:665–665, 1952.

44. V. Zacek. Search for dark matter with moderately superheated liquids. *Nuovo Cim.*, A107:291–298, 1994.

45. E. Behnke et al. First Dark Matter Search Results from a 4-kg CF_3I Bubble Chamber Operated in a Deep Underground Site. *Phys. Rev.*, D86:052001, 2012.

46. C. Amole et al. Dark Matter Search Results from the PICO-60 C_3F_8 Bubble Chamber. *Phys. Rev. Lett.*, 118(25):251301, 2017.

47. A. Antonicci et al. MOSCAB: A geyser-concept bubble chamber to be used in a dark matter search. *Eur. Phys. J.*, C77(11):752, 2017.

48. E. Behnke et al. Final Results of the PICASSO Dark Matter Search Experiment. *Astropart. Phys.*, 90:85–92, 2017.

49. M. Felizardo, T.A. Girard, T. Morlat, A.C. Fernandes, A.R. Ramos, et al. Final Analysis and Results of the Phase II SIMPLE Dark Matter Search. *Phys. Rev. Lett.*, 108:201302, 2012.

50. O. Cheshnovsky, B. Raz, and J. Jortner. Temperature dependence of rare gas molecular emission in the vacuum ultraviolet. *Chem. Phys. Lett.*, 15:475, 1972.

51. Akira Hitachi et al. Effect of ionization density on the time dependence of luminescence from liquid argon and xenon. *Phys. Rev.*, B27:5279, 1983.

52. P. Agnes et al. DarkSide-50 532-day Dark Matter Search with Low-Radioactivity Argon. *Phys. Rev.*, D98(10):102006, 2018.

53. P. A. Amaudruz et al. First results from the DEAP-3600 dark matter search with argon at SNOLAB. *Phys. Rev. Lett.*, 121(7):071801, 2018.

54. C. E. Aalseth et al. DarkSide-20k: A 20 tonne two-phase LAr TPC for direct dark matter detection at LNGS. *Eur. Phys. J. Plus*, 133:131, 2018.

55. D. S. Akerib et al. Results from a search for dark matter in LUX with 332 live days of exposure. 2016.

56. K. Abe et al. Search for dark matter in the form of hidden photons and axion-like particles in the XMASS detector. *Phys. Lett.*, B787:153–158, 2018.

57. Xiangyi Cui et al. Dark Matter Results From 54-Ton-Day Exposure of PandaX-II Experiment. *Phys. Rev. Lett.*, 119(18):181302, 2017.

58. Hongguang Zhang et al. Dark matter direct search sensitivity of the PandaX-4T experiment. *Sci. China Phys. Mech. Astron.*, 62(3):31011, 2019.

59. E. Aprile et al. Physics reach of the xenon1t dark matter experiment. *JCAP*, 1604:027, 2016.

60. Marco Battaglieri et al. US Cosmic Visions: New Ideas in Dark Matter 2017: Community Report. In *U.S. Cosmic Visions: New Ideas in Dark Matter College Park, MD, USA, March 23-25, 2017*, 2017.

61. Michael Crisler, Rouven Essig, Juan Estrada, Guillermo Fernandez, Javier Tiffenberg, Miguel Sofo haro, Tomer Volansky, and Tien-Tien Yu. SENSEI: First Direct-Detection Constraints on sub-GeV Dark Matter from a Surface Run. *Phys. Rev. Lett.*, 121(6):061803, 2018.

62. R. Agnese et al. First Dark Matter Constraints from a SuperCDMS Single-Charge Sensitive Detector. *Phys. Rev. Lett.*, 121(5):051301, 2018.

63. http://cdms.berkeley.edu/limitplots/mm/wimp_limit_plotter.html.

Frascati Physics Series Vol. 66 (2018)
Frontier Objects in Astrophysics and Particle Physics
May 20-26, 2018

LOW ENERGY SOLAR NEUTRINOS WITH BOREXINO

Lea Di Noto
Dipartimento di Fisica, Università degli Studi e INFN, 16146 Genova, Italy
on behalf of the Borexino collaboration *

Abstract

Low energy solar neutrinos are a unique tool to investigate the nuclear reactions that fuel the Sun. The Borexino experiment, based on a 270 ton ultra-pure liquid scintillator detector at Laboratori Nazionali del Gran Sasso, was conceived to measure solar neutrino fluxes in the MeV and sub-MeV energy range. The data taking started on 2007 and thanks to the unprecedented level of radiopurity achieved in the inner part of the detector, a real time spectroscopy of the main components of the pp chain was possible. After a purification process, in the phase II data, the simultaneous fit of all the pp-chain components was performed and the interaction rates of pp, ^{7}Be and pep were extracted with the highest precision to date. In this paper, after a description of the main properties of Borexino detector, the most important analysis techniques, necessary for the data selection and for the final fit of the phase II data will be explained.

1 Introduction

Solar neutrinos, fundamental for the discovery of the neutrino flavor oscillation, can be exploited to study both the fundamental properties of the neutrino in the particle physics and to probe the interior of the Sun, for confirming the Standard Solar Model predictions. Low energy electron neutrinos are produced in the stars by nuclear reactions (pp chain or CNO cycle) in which the hydrogen is converted into helium. In the Sun, 99% of the energy comes from the pp chain, while the CNO neutrino flux is expected to fuel mainly stars with mass larger than the Sun (> 1.5 $M_{\odot}$) [1]. The solar neutrino spectrum [2, 3], shown in Fig.2a) extends from sub MeV (in the region of the pp flux) up to 15.5 MeV (the maximum energy of the ^{8}B neutrinos) and in the intermediate region two monochromatic lines of ^{7}Be ($E = 0.86\,\mathrm{MeV}$ and $E = 0.384$ MeV) and one mono-energetic line of pep ($E = 1.44\,\mathrm{MeV}$) are present. The prediction on the ν flux components depends on input values in the solar model and in particular the presence of the CNO flux and it is contribute in the solar luminosity is related to the abundance of elements heavier than the Hydrogen in the Sun surface, resulting 40% higher in the High Metallicity (HZ) (GS98) than in the Low Metallicity (LZ) (AGSS09) solar model [4].

In addition the study of the survival probability of electron neutrino P_{ee} as a function of the neutrino energy have evidenced the so called *Mikheyev Smirnov Wolfenstein effect* [5, 6], which is the resonant enhancement of flavor conversion in the coherent interaction of neutrinos in the solar medium. In particular measurements in the sub MeV - few MeV range energy allow to test the Large Mixing Angle (LMA) type flavor oscillations. In this framework the so called 'up-turn' of the P_{ee} is expected right below the ^{8}B solar neutrino energies, due to the transition between the region below $E \sim 1.9\,\mathrm{MeV}$, (where the oscillations are essentially in vacuum) and the region at higher energy, dominated by matter effect.

Solar neutrinos were firstly detected by pioneering radio-chemical experiments [7, 8] when the Solar Neutrino Problem arose and from then many large volume detectors were build [9, 10, 11] discovering the neutrino oscillations and providing the first measurement of the oscillation parameters in vacuum. Now solar neutrinos are entered in the precision era, where the precise measurement of the P_{ee} as a function of energy and of the solar fluxes can validate the current scenario, define the parameters of the solar model or search for new

physics.

2 The Borexino detector

The Borexino experiment is located underground (at about 3800 meters of water equivalent) in the Hall C of the Laboratori Nazionali del Gran Sasso in Italy [12]. As shown in Fig.1 the core of the detector is 278 ton of ultra-pure organic liquid scintillator contained in a 125 μm-thick nylon vessel of 4.25 m radius, surrounded by 2212 photomultipliers (PMTs) attached to a stainless-steel sphere (SSS) of 6.85 m radius. The organic scintillator is composed by PC (pseudocumene, 1,2,4-trimethylbenzene) as a solvent and 1.5 g/l of fluor PPO (2,5-diphenyloxazole) as a solute, while the region between the nylon vessel and the stainless-steel sphere is filled by a buffer composed of pseudocumene and 5.0 g/l (later reduced to 3.0 g/l) of DMP (dimethylphthalate), a light quencher for the residual scintillation of PC. The entire detector is enclosed in an external tank (of radius 9 m and height 16.9 m), filled with ultra-pure water and instrumented with 208 PMTs, which collect Cherenkov light for a muon veto. The water tank and the buffer region act as passive shield against external gammas and neutrons originating from the rock and from external material guaranteeing an high level of purity in the core of the detector.

Neutrinos can interact by weak elastic scattering off the electrons producing scintillation light seen by the PMT in a single photo-electron regime (~ 500 p.e./MeV). The electron recoil energy, proportional to the total number of the detected photoelectron, is reconstructed with an energy resolution of ~ 50 keV at 1 MeV, while the neutrino interaction position is obtained by means of the different detection time of the gamma rays to each PMT. The position reconstruction algorithm has been tuned using a Rn source, placed in different positions inside the active volume during the calibration measurements [13] and a position resolution of ~ 10 cm was achieved for events of 1 MeV energy.

The data taking started in 2007 and thanks to the very high level of radio-purity in Phase I Borexino measured the ^{7}Be [14, 15], pep [17] and ^{8}B neutrinos [18], while after a purification process in Phase II also the pp neutrinos have been detected [19] and an evidence of the annual modulation of the ^{7}Be neutrinos was observed [20]. In addition since Borexino has the capability to detect also anti-neutrinos from the inverse beta decay on protons or carbon, a

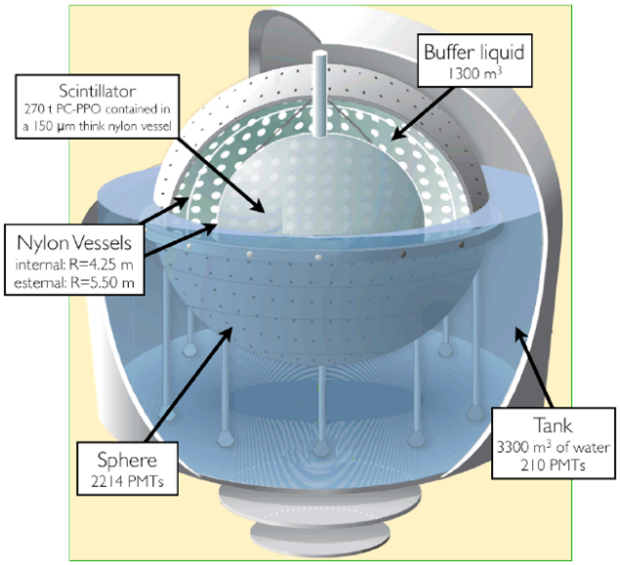

Figure 1: *Schematic drawing of the Borexino detector.*

precise geo-neutrino measurement was performed as well [21].

In the next section the main analysis tools developed for the simultaneous fit of the spectrum achieved in the Phase II data will be explained.

3 Data analysis

Borexino detects the solar neutrino fluxes together with other background components in the energy range from 190 keV to 10 MeV. The background events come from cosmogenic ^{11}C and neutron, from gamma rays from ^{208}Tl and ^{214}Bi from PMT and from internal background due to the ^{14}C present in the scintillator itself, ^{85}Kr in air ^{238}U (^{210}Bi and ^{210}Po) ^{232}Th, ^{40}K, ^{49}Ar ^{222}Rn coming from surfaces of inner materials [22]. Since the organic nature of the scintillator which yields the technical possibility to purify the material and thanks to a big work done in the construction phase the internal background sources were re-

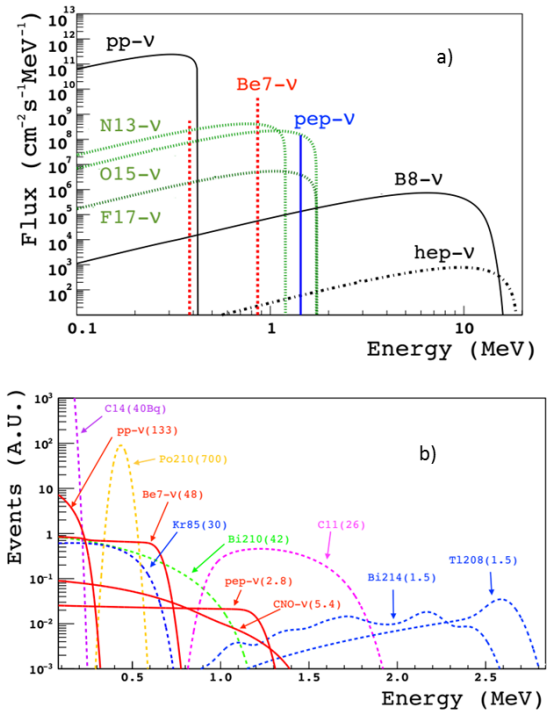

Figure 2: *a) Energy spectrum of the solar neutrino components of the pp chain (in blue, red and black) and of the CNO cycle (in green), b) Energy spectrum of the solar and background fluxes as expected observed by the Borexino detector. The spectral shapes are obtained by considering the electron recoil energy, the light quenching in the scintillator and other effects related to the detector response* [23].

duced well below the design goals. In addition a further purification campaign was performed between the Phase I and the Phase II allowing to achieve an unprecedented level of purity for ^{238}U ($< 9.5 \cdot 10^{20}$ g/g at 95% C.L.) and ^{232}Th ($< 7.2 \cdot 10^{19}$ g/g at 95% C.L.) and to further reduce the residual contamination of Kr and ^{210}Bi of a factor ~ 4.6 and ~ 2.3 respectively.

The main components of the Borexino spectrum are shown in Fig.2b), where both the solar and the background fluxes are shown. In the electron recoil energy spectrum, the monochromatic lines of ^{7}Be and pp appear as a broader peaks and in addition the light quenching effect, shifting of approximately 1/10th the alpha decaying events (as ^{210}Po) and the detector response were taken into account [23]. In the Borexino spectrum the residual background is mainly due to radioactive isotopes contaminating the scintillator itself, such as ^{14}C (β - decay, Q = 156 keV) and ^{210}Po (α decay, E = 5.3 MeV) influencing the lower region, and the ^{85}Kr (β - decay, Q = 687 keV), and ^{210}Bi (β - decay, Q = 1160 keV) from ^{210}Pb both present in the same energy window of the main pp solar fluxes. In addition in the low energy region (below 300 keV) also the pile-up of uncorrelated events has to be considered. On the contrary the region of the spectrum relevant for pep and CNO νs (between about 1.1 and 1.7 MeV) and for ^{8}B is mainly affected by the cosmogenic isotope ^{11}C and by residual external background, mainly due to ^{208}Tl and ^{214}Bi.

Proper analysis technique were developed in order to select the data set for the fit, where both the solar flux and the expected background are free parameters. The spectrum was divided in three regions: Low Energy Region (LER) ranging from 0.19 to 2.93 MeV and two High Energy Regions, HER-I, between 3.2 and 5.7 MeV and HER-II between 5.7 and 16 MeV. Firstly the internal and the external muons events were cut by combining the Outer Cherenkov Detector and a pulse shape analysis of the scintillator signals [24]. Then the cosmogenic background, related to all the radioactive elements produced in muon-induced nuclear spallation processes, was suppressed by applying a temporal Δt veto (equal to 300 ms for LER and 6.5 s for HER), following each muon events. Finally the fiducial volume cut was performed for selecting only events occurring in the inner core of Borexino defined by the coordinates $R < 2.8$ m and $-1.8 < z < 2.2$ m for LER region, while for HER-I the cut was done only as $z < 2.5$ m and for HER-II the entire scintillator was considered. However since the ^{11}C isotope produced by the muon spallation on ^{12}C cannot

be removed by the short Δt veto because of its long lifetime (τ = 29.4 min) a powerful strategy was developed based on the Three Fold Coincidence TFC method for allowing the pep neutrino flux measurement [25]. The technique exploits the fact that a single muon generates ^{11}C always together with neutrons (see eq.1), which produce a delayed scintillation signal (with 220 usec time constant) generated by the gamma of 2.2 MeV emitted after the capture of thermalized neutrons on proton or carbon atom in the scintillator.

$$\begin{aligned} \mu + {}^{12}C &\rightarrow \mu + {}^{11}C + n \\ {}^{11}C &\rightarrow {}^{11}B + e^{+} + \nu \end{aligned} \tag{1}$$

Thus, since the ^{11}C signal results to be time and spatial correlated with a muon and a neutron, the tagging procedure consists in identify the muon track and the neutron absorption and then put a veto on a region close to the neutron absorption position and to the muon track for a certain time window. With this technique a tagging efficiency of about 92 ± 4 % was reached [17] and this allowed to produce two different data sets, one with the ^{11}C subtracted and the other with the ^{11}C events tagged. Both the data sets were used for the final fit and for the estimation of the systematic uncertainties. In addition also the pulse shape analysis was adopted to disentangle the residual ^{11}C in the TFC subtracted spectrum. In fact since ^{11}C decays β^+ the scintillation time profile is significantly different from the β^- events due to the no point like energy deposit of β^+ and to the delayed annihilation ($\tau \sim 3$ ns) of the ortho-Positronium, formed in the 40% of the cases.

In Phase II a multivariate fit was performed in all the energy spectrum from 0.186 MeV to 2.927 MeV (recoil-electron kinetic energy) and the interaction rates of pp, ^{7}Be, and pep neutrinos were simultaneously achieved. Two complementary fit methods were adopted: the first one was based on Monte Carlo data, while the second one was performed by using an analytical energy response function. In the MC fit only the rate of the solar neutrino components and of the background components were free parameters, since the other parameters were carefully tuned on the calibration data. On the contrary in the analytical fit 6 additional effective parameters, related to the detector properties, were left free together with the neutrino and background fluxes. The multivariate fit was performed by fitting the TFC-subtracted and the TFC-tagged energy spectra, the spatial distribution of the events and the distribution of the pulse-shape discrimination variable. In the spatial distribution of the events the

two components coming from the uniformly distributed events in the scintillator (mainly due to solar neutrino interaction) and from the external components (due to the background events) were disentangled, while in the distribution of the pulse-shape discrimination, the contribution of the signal generated by the electrons with respect to the positrons was obtained [26]. Since the degeneracy of CNO and pep neutrinos in the same region of the spectrum, in the fit the CNO rates was fixed both to the HZ -SSM model and to the LZ- SSM with LMA oscillation solution, separately. Only the pep flux was influenced by the CNO constrain and for this component two values (one for the HZ model and one for the LZ model) were obtained. Finally the robustness of the results was checked by performing the fit in several configurations in term of binning and energy estimators (number of detected photon or number of triggered pmt in a certain time interval or total charge of collected hits) and the differences between the results were quoted as systematic errors. The results are shown in the ref [26] and they are in agreement with the numbers achieved from the Phase I, while the precision is improved for the ^{7}Be neutrinos and for the pep neutrinos. In addition, in order to extract an upper limit on the CNO flux, an indirect constrain on the pp and pep flux ratio was set and in this case the result has the same significance of previous one of phase I.

4 Conclusions

Thanks to the increase of the exposure, the reduction of the most relevant backgrounds, the development of powerful analysis technique and a more accurate tuning of the Monte Carlo code, a better precision was reached on the measurement of the solar neutrinos in Borexino. Since the very low energy range and the ability to disentangle all the solar flux components of the pp chain, these measurements were used to infer the electron neutrino survival probability at different energies and they showed a very good agreement with the MSW-LMA solution of neutrino oscillations, testing both the vacuum and the matter dominated regions.

References

1. W. A. Fowler. The Astrophysical Journal, **127**, 551556 (1958)
2. J. Bahcall and C. Pena-Garay, Journal of High Energy Physics **11**, 4 (2003)

3. N. Vinyoles et al. The Astrophysical Journal, **835 (2)**, 202 (2017)

4. J.N. Bahcall, A. Serenelli, and S. Basu, Ap. J. Suppl. **165**, 400 (2006)

5. L. Wolfenstein, Physical Review D **17**, 23692374, (1978)

6. S. Mikheyev and A. Smirnov, Sov. J. Nucl. Phys. **42**, 913 (1985)

7. R. Davis, Nobel Prize Lecture (2002)

8. W.Hampel et al. (GALLEX collaboration), Phys. Lett. B **447** 127 (1999)

9. Q.R. Ahmad et al (SNO collaboration), Physical Review Letters **87**, 071301 (2001)

10. Y. Fukuda et al, (Super-Kamiokande collaboration), Physical Review Letters **81**, 1562 (1998)

11. Q.R. Ahmad et al (SNO collaboration), Physical Review Letters **89**, 011301 (2002)

12. G. Alimonti et al., (Borexino collaboration), Nucl. Instr. and Methods A **600**, 568-593 (2009)

13. H. Back et al. (Borexino collaboration) Journal of Instrumentation **7** P10018, (2012)

14. C. Arpesella et al., (Borexino collaboration), Phys. Rev. Lett. **101**, 091302 (2008).

15. G. Bellini et al., (Borexino collaboration), Phys. Rev. Lett. **107**, 141302 (2011)

16. G. Bellini et al., (Borexino collaboration), Phys. Rev. D **89**, 112007 (2014)

17. G. Bellini et al., (Borexino collaboration), Phys. Rev. Lett. **108**, 051302 (2012)

18. G. Bellini et al., (Borexino collaboration), Phys. Rev. D **82**, 033006 (2010)

19. G. Bellini et al. (Borexino collaboration), Nature **512**, 383-386 (2014)

20. M. Agostini et al., (Borexino collaboration), Astroparticle Physics, **92**, 2129 (2017)

21. M. Agostini at al. (Borexino collaboration), Phys. Rev. D **92**, 031101 (2015)

22. G. Bellini et al., (Borexino collaboration), Phys. Rev. D **89**, 112007(2014)

23. M. Agostini et al., (Borexino collaboration), Astropart. Phys. **97**, 136-159 (2018)

24. G. Bellini et al., (Borexino collaboration), JINST **6**, P05005 (2012)

25. G. Bellini et al., (Borexino collaboration), Phys. Rev. D **89**, 112007 (2014)

26. M.Agostini et al. (Borexino collaboration), arXiv:1707.09279 (2017)

* **The Borexino collaboration**

M. Agostini[a], K. Altenmüller[a], S. Appel[a], V. Atroshchenko[b], Z. Bagdasarian[c], D. Basilico[d], G. Bellini[d], J. Benziger[e], D. Bick[f], I. Bolognino[d], G. Bonfini[g], D. Bravo[1 d], B. Caccianiga[d], F. Calaprice[h], A. Caminata[i], S. Caprioli[d], M. Carlini[g], P. Cavalcante[g,j], F. Cavanna[i], A. Chepurnov[k], K. Choi[l], L. Collica[d], S. Davini[i], A. Derbin[m], X.F. Ding[g,n], A. Di Ludovico[h], L. Di Noto[i], I. Drachnev[m,n], K. Fomenko[o], A. Formozov[d,k,o], D. Franco[p], F. Gabriele[g], C. Galbiati[h], M. Gschwender[q], C. Ghiano[g], M. Giammarchi[d], A. Goretti[h], M. Gromov[k], D. Guffanti[g,n], C. Hagner[f], T. Houdy[p], E. Hungerford[r], Aldo Ianni[g], Andrea Ianni[h], A. Jany[s], D. Jeschke[a], V. Kobychev[t], D. Korablev[o], G. Korga[r], T. Lachenmaier[q], M. Laubenstein[g], E. Litvinovich[b,u], F. Lombardi,[2 g], P. Lombardi[d], L. Ludhova[c,v], G. Lukyanchenko[b], L. Lukyanchenko[b], I. Machulin[b,u], G. Manuzio[i], S. Marcocci[3 n], J. Maricic[l], J. Martyn[x], E. Meroni[d], M. Meyer[y], L. Miramonti[d], M. Misiaszek[s], V. Muratova[m], B. Neumair[a], L. Oberauer[a], B. Opitz[f], V. Orekhov[b], F. Ortica[w], M. Pallavicini[i], L. Papp[a], Ö. Penek[c,v], L. Pietrofaccia[g], N. Pilipenko[m], A. Pocar[z], A. Porcelli[x], G. Raikov[b], G. Ranucci[d], A. Razeto[g], A. Re[d], M. Redchuk[c,v], A. Romani[w], N. Rossi[4 g], S. Rottenanger[q], S. Schönert[a], D. Semenov[m], M. Skorokhvatov[b,u], O. Smirnov[o], A. Sotnikov[o], L.F.F. Stokes[g], Y. Suvorov,[5 b,g], R. Tartaglia[g], G. Testera[i], J. Thurn[y], M. Toropova[b], E. Unzhakov[m], A. Vishneva[o], R.B. Vogelaar[j],

[1] *Present address: Universidad Autonoma de Madrid, Ciudad Universitaria de Cantoblanco, 28049 Madrid, Spain*

[2] *Present address: Physics Department, University of California, San Diego, CA 92093, USA*

[3] *Present address: Fermilab National Accelerato Laboratory (FNAL), Batavia, IL 60510, (USA)*

[4] *Present address: Dipartimento di Fisica, Sapienza Università di Roma e INFN, 00185 Roma, Italy*

[5] *Present address: Dipartimento di Fisica, Università degli Studi Federico II e INFN, 80126 Napoli, Italy*

F. von Feilitzsch[a], S. Weinz[x], M. Wojcik[s], M. Wurm[x], Z. Yokley[j], O. Zaimidoroga[o], S. Zavatarelli[i], K. Zuber[y], G. Zuzel[s]

[a] *Physik-Department and Excellence Cluster Universe, Technische Universität München, 85748 Garching, Germany*
[b] *National Research Centre Kurchatov Institute, 123182 Moscow, Russia*
[c] *Institut für Kernphysik, Forschungszentrum Jülich, 52425 Jülich, Germany*
[d] *Dipartimento di Fisica, Università degli Studi e INFN, 20133 Milano, Italy*
[e] *Chemical Engineering Department, Princeton University, Princeton, NJ 08544, USA*
[f] *Institut für Experimentalphysik, Universität Hamburg, 22761 Hamburg, Germany*
[g] *INFN Laboratori Nazionali del Gran Sasso, 67010 Assergi (AQ), Italy*
[h] *Physics Department, Princeton University, Princeton, NJ 08544, USA*
[i] *Dipartimento di Fisica, Università degli Studi e INFN, 16146 Genova, Italy*
[j] *Physics Department, Virginia Polytechnic Institute and State University, Blacksburg, VA 24061, USA*
[k] *Lomonosov Moscow State University Skobeltsyn Institute of Nuclear Physics, 119234 Moscow, Russia*
[l] *Department of Physics and Astronomy, University of Hawaii, Honolulu, HI 96822, USA*
[m] *St. Petersburg Nuclear Physics Institute NRC Kurchatov Institute, 188350 Gatchina, Russia*
[n] *Gran Sasso Science Institute, 67100 L'Aquila, Italy*
[o] *Joint Institute for Nuclear Research, 141980 Dubna, Russia*
[p] *AstroParticule et Cosmologie, Université Paris Diderot, CNRS/IN2P3, CEA/IRFU, Observatoire de Paris, Sorbonne Paris Cité, 75205 Paris Cedex 13, France*
[q] *Kepler Center for Astro and Particle Physics, Universität Tübingen, 72076 Tübingen, Germany*
[r] *Department of Physics, University of Houston, Houston, TX 77204, USA*
[s] *M. Smoluchowski Institute of Physics, Jagiellonian University, 30348 Krakow, Poland*
[t] *Kiev Institute for Nuclear Research, 03680 Kiev, Ukraine*
[u] *National Research Nuclear University MEPhI (Moscow Engineering Physics Institute), 115409 Moscow, Russia*

[v] *RWTH Aachen University, 52062 Aachen, Germany*
[x] *Institute of Physics and Excellence Cluster PRISMA, Johannes Gutenberg-Universität Mainz, 55099 Mainz, Germany*
[y] *Department of Physics, Technische Universität Dresden, 01062 Dresden, Germany*
[w] *Dipartimento di Chimica, Biologia e Biotecnologie, Università degli Studi e INFN, 06123 Perugia, Italy*
[z] *Amherst Center for Fundamental Interactions and Physics Department, University of Massachusetts, Amherst, MA 01003, USA*

Frascati Physics Series Vol. 66 (2018)
Frontier Objects in Astrophysics and Particle Physics
May 20-26, 2018

A REVIEW ON NEUTRINOLESS DOUBLE BETA DECAY

Stefano Dell'Oro
Virginia Polytechnic Institute and State University (VA, USA)
INFN, Laboratori Nazionali del Gran Sasso (Italy)

Abstract

The current status of the neutrinoless double beta decay ($0\nu\beta\beta$) search is summarized, exploiting the up-to-date knowledge of the oscillation parameters and of the recent theoretical developments in the understanding of the $0\nu\beta\beta$ process, especially those concerning the nuclear description and its limitations. This also allows to infer expectations and uncertainties for the experimental search for the $0\nu\beta\beta$. Looking ahead at the future of the search for $0\nu\beta\beta$, the challenges that the next generation of experiments will face in order to further improve the sensitivity are discussed, focusing in particular on the background abatement.

1 Introduction

In 1937, Majorana proposed a new way to represent fermions in a relativistic quantum field theory [?]. This formalism could be especially useful for neutral

particles, since a single Majorana quantum field characterizes the situation in which particles and antiparticles coincide and, in particular, it could be fully applied to the description of massive neutrinos. Within this theoretical framework, a new a new process was proposed [?]: the double beta decay without neutrino emission, or *neutrinoless double beta decay* ($0\nu\beta\beta$), namely

$$(A, Z) \rightarrow (A, Z + 2) + 2\mathrm{e}^{-}. \tag{1}$$

The main and evident feature of $0\nu\beta\beta$ is the explicit violation of the number of leptons, with the creation of an electron pair. The discovery of $0\nu\beta\beta$ would thus demonstrate that lepton number L is not a symmetry of nature. This, in turn, could support the exciting picture that leptons played a part in the creation of the matter-antimatter asymmetry in the universe.

The experimental observable in the search for $0\nu\beta\beta$ is the half-life time of the decaying isotope, whose theoretical expression is:

$$\left[t^{1/2}\right]^{-1} = G_{0\nu}\, g_{\mathrm{A}}^{4}\, |\mathcal{M}|^{2}\, \frac{m_{\beta\beta}^{2}}{m_{\mathrm{e}}^{2}} \tag{2}$$

where $G_{0\nu}$ is the phase space factor (PSF), g_{A} is the axial coupling constant, $\mathcal{M}$ is the nuclear matrix element (NME), while $m_{\beta\beta}$ is the *Majorana effective mass*, the key parameter that regulates the $0\nu\beta\beta$ rate (the electron mass m_{e} is conventionally taken as a reference).

The Majorana effective mass represents the absolute value of the ee-entry of the neutrino mass matrix and its expression takes the form

$$m_{\beta\beta} \equiv \left| \mathrm{e}^{i\alpha_1} |U_{ei}^{2}| m_1 + \mathrm{e}^{i\alpha_2} |U_{e2}^{2}| m_2 + |U_{e3}^{2}| m_3 \right| \tag{3}$$

where m_i are the masses of the individual neutrinos ν_i, $\alpha_{1,2}$ are the Majorana phases and U_{ei} are the elements of the mixing matrix that define the composition of the electron neutrino: $|\nu_{\mathrm{e}}\rangle = \sum_{i=1}^{3} U_{ei}^{*} |\nu_i\rangle$.

The knowledge of the oscillation parameters [?], allows to set a first series of constraints on $m_{\beta\beta}$. The result is shown in Fig. 1, where the representation $m_{\beta\beta}$ as a function of the mass of the lightest neutrino [?, ?] ha been adopted. It has to be noted that, since the complex phases $\alpha_{1,2}$ in Eq. (3) cannot be probed by oscillations and are unknown, the allowed regions for $m_{\beta\beta}$ are actually bands.

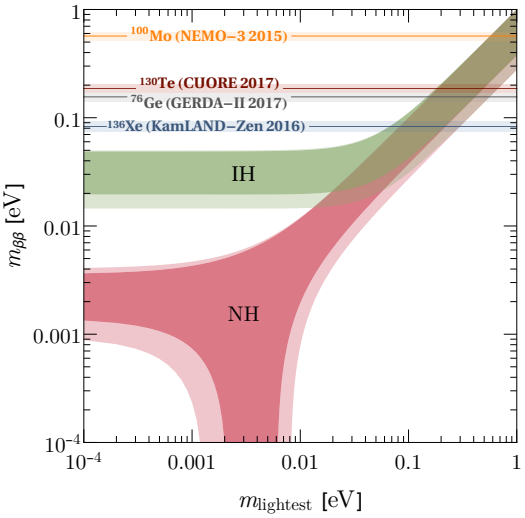

Figure 1: Majorana effective mass as a function of the lightest neutrino (3σ uncertainty regions). The horizontal lines show the current experimental limits from the searches for $0\nu\beta\beta$ of ^{76}Ge, ^{100}Mo, ^{130}Te and ^{136}Xe (see the text for the related references).

2 Considerations on the nuclear physics

The $0\nu\beta\beta$ transition is a nuclear process – it takes place inside the nuclei – and the momentum of the virtual nucleon is large, of the order $O(100\,\text{MeV})$, i. e. the inverse of the nucleonic size, therefore much larger than the neutrino mass. At the same time, the axial coupling of the nucleons is very importance, since the decay rate scales as g_A^4. Theory thus plays a fundamental role in extracting the information on the neutrino mass and, in a conservative approach, it is important to discuss the uncertainties of the quantities involved in Eq. (2) while passing from $t^{1/2}$ to $m_{\beta\beta}$.

The PSFs are known with accurate precision, about 7% for all the nuclei of interest [?], while the situation is more complicated for the NMEs. In fact, despite a relatively small intrinsic error of less than $\sim$ 20% is assessed for the latter parameters by the most recent calculations [?, ?], the disagreement between the results from different models is actually larger, up to a factor

~ 3. Moreover, when other processes than the $0\nu\beta\beta$ are considered (single β decay, electron capture, $2\nu\beta\beta$) and the calculations from the same models are compared to the measured rates, the actual differences are much larger than 20%.

The value of $g_{\rm A}$ remains an open issue: that actually measured in weak interactions and decays of nucleons ($g_{\rm A,nucl} \simeq 1.27$) could be indeed renormalized to the one appropriate for quarks inside the nuclear medium ($g_{\rm A,quark} = 1$). Or, even, the possibility of a further reduction (quenching) has been argued based on the systematic over-prediction of the β and $2\nu\beta\beta$ NMEs (worst scenario: $g_{\rm A,phen} \simeq g_{\rm A,nucl} \cdot A^{-0.18}$, where A is the mass number [?, ?]).

An experimental limit on $t^{1/2}$ thus translates into a range of values for $m_{\beta\beta}$. Referring to Fig. 1, the broadness of the horizontal bands depends on the adopted approach in discussing these theoretical uncertainties.

Looking ahead in the future of the $0\nu\beta\beta$ search, a large effort has to be put in the nuclear studies (NMEs and effective value of $g_{\rm A}$) in order to maximize the information that can be extracted from the experimental searches.

3 Experimental search for $0\nu\beta\beta$

The experimental search for a $0\nu\beta\beta$ signal relies on the detection of the two emitted electrons. Being the energy of the recoiling nucleus negligible, the sum of the kinetic energy of the two electrons is equal to the Q-value of the transition. Therefore, we expect to observe a monochromatic peak at $Q_{\beta\beta}$.

Despite the very clear signature, due to the rarity of the process, the detection of the two electrons is complicated by the occurrence of background events within the region of interest than can actually mask the $0\nu\beta\beta$ signal. Any event producing an energy deposition similar to that of $0\nu\beta\beta$ increases the background level, and hence spoils the experiment sensitivity. The main contributions to the background come from the environmental radioactivity, the cosmic rays, and the $2\nu\beta\beta$ itself. In particular, the latter one is unavoidable in presence of finite energy resolution, since it originates from the same isotope which is expected to undergo $0\nu\beta\beta$.

The choice for the best isotope to look for $0\nu\beta\beta$ is the first issue to deal with. A high $Q_{\beta\beta}$ is important, since it directly influences the background, the actual suitability depending on the detector resolution and rejection capabilities. A large isotopic abundance for either the natural or the enriched material

is needed in order to achieve a sufficient large mass. Finally, the isotope of interest has to be integrated in a working detector. These requirements result in a group of "commonly" studied isotopes among all the candidate $0\nu\beta\beta$ emitters: ^{48}Ca, ^{76}Ge, ^{82}Se, ^{96}Zr, ^{100}Mo, ^{116}Cd, ^{130}Te, ^{136}Xe and ^{150}Nd.

Regarding the detector, a good energy resolution is the first requirement, crucial to identify the sharp $0\nu\beta\beta$ peak and to protect against the (intrinsic) $2\nu\beta\beta$ induced events. Fundamental as well is a very low background. An underground location, a careful material selection for the detector and the surrounding parts, and the presence of passive and/or active shielding are therefore mandatory. The employed technique has also to guarantee the scalability to large masses, since tonnes of isotope of interest will be needed for the next generation of experiments.

It has to be noted that it is impossible to simultaneously optimize all these features in a single detector. Therefore, it is up to the experimentalists to choose which aspect to privilege in order to get the best sensitivity. Among the most successful examples of detectors, we find Ge-diodes, bolometers, Xe liquid and gaseous TPC, liquid scintillators loaded with the $0\nu\beta\beta$ isotope, tracker + calorimeter (external $0\nu\beta\beta$ source), ...

The sensitivity of a $0\nu\beta\beta$ experiment can be defined as the process half-life corresponding to the maximum signal that could be hidden by the background fluctuations n_B (at a given statistical C. L. n_σ) and can be parametrized as:

$$S^{0\nu} = \ln 2 \cdot T \cdot \varepsilon \cdot \frac{n_{\beta\beta}}{n_\sigma \cdot n_B} = \ln 2 \cdot \varepsilon \cdot \frac{1}{n_\sigma} \cdot \frac{x\,\eta\,N_A}{\mathscr{M}_A} \cdot \sqrt{\frac{M \cdot T}{B \cdot \Delta}} \qquad (4)$$

where B is the background level per unit mass, energy, and time, M is the detector mass, Δ is the FWHM energy resolution, x is the stoichiometric multiplicity of the element containing the $\beta\beta$ candidate, η is the $\beta\beta$ candidate isotopic abundance, N_A is the Avogadro number and, finally, $\mathscr{M}_A$ is the compound molecular mass. Despite its simplicity, Eq. (4) has the advantage of emphasizing the role of the essential experimental parameters.

3.1 Constraints on $m_{\beta\beta}$

Once the experimental sensitivities are known in terms of $S^{0\nu}$, it is possible to correspondingly find the lower bounds on $m_{\beta\beta}$ by inverting Eq. (2).

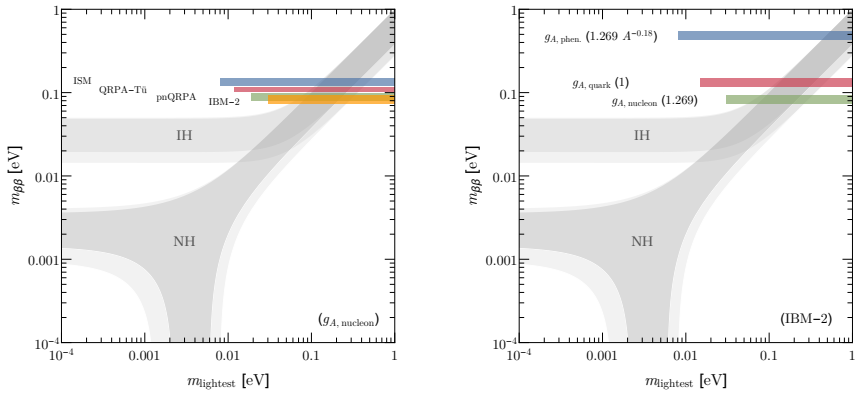

Figure 2: Uncertainty of the current $m_{\beta\beta}$ bound from ^{136}Xe. (Left) Dependence on the NME. (Right) Dependence on the value of the axial vector coupling constant. See the text for more details and references.

In the left panel of Fig. 1, the most stringent limits up to date are shown. They come from ^{76}Ge, ^{100}Mo, ^{130}Te and ^{136}Xe: $t^{1/2}_{\mathrm{Ge}} > 8.0 \cdot 10^{25}\,\mathrm{yr}$ [?], $t^{1/2}_{\mathrm{Mo}} > 1.1 \cdot 10^{24}\,\mathrm{yr}$ [?], $t^{1/2}_{\mathrm{Te}} > 1.5 \cdot 10^{25}\,\mathrm{yr}$ [?], $t^{1/2}_{\mathrm{Xe}} > 1.1 \cdot 10^{26}\,\mathrm{yr}$ [?] at 90% C. L..

In the figure, the case $g_A = g_{\mathrm{nucleon}}$ (unquenched value) is assumed. The error propagation on the NME (fixed to an arbitrarily chosen model) [?] and on the PSF [?] results in the broadening of the lines describing the limits. As the plot shows, the current generation of experiments is probing the quasi-degenerate part of the neutrino mass spectrum, down to a value for $m_{\beta\beta}$ of $\sim$ 85 meV.

The effect of the uncertainties is shown in Fig. 2, both for the choice of different NMEs (left panel) and different values of g_A (right panel). In particular, in the latter case it can be seen that the sensitivity for the same limit (that on ^{136}Xe [?]), in the two cases of g_{nucleon} and $g_{\mathrm{phen.}}$ differs of a factor $\gtrsim 5$. It is clear from the figure that this is the biggest uncertainty, with respect to all the other theoretical ones.

3.2 Towards the next generation of $0\nu\beta\beta$ experiments

The forthcoming generation of $0\nu\beta\beta$ experiments aims at sensitivities of the order of 10^{27} yr or more. This is crucial in order to begin to probe the Inverted Hi-

erarchy region of neutrino mass spectrum (refer to Fig. 1), i. e. $m_{\beta\beta} \lesssim 50\,\mathrm{meV}$.

All the experimental collaborations will be requested to demonstrate their capability to reach such a goal and the feasibility and effectiveness of the proposed technique will have to be tested by means of demonstrators and extensive R&D programs in order to stand a chance in continuing the challenge of the $0\nu\beta\beta$ search.

Unfortunately, the cost of the experiment will become even more a critical aspect and money, i. e. \$/mole of detectable isotope, will have to be included in the sensitivity studies,taking into account the technological costs: procurement, enrichment/purification, infrastructures, ... and projecting the efficiency of the detector at the tonne-scale. Politics will play a very central role in the experiment down-selection. From the experiment side, the possibility of merging of experiments sharing the same technology and that studying different nuclei with a specific setup should be considered.

A fundamental issue regards the background abatement. Referring to Eq. (4), when the background level B is so low that the expected number of background events in the region of interest along the experiment life is of order of unity, namely

$$M \cdot T \cdot B \cdot \Delta \lesssim 1, \tag{5}$$

the sensitivity begins to scale linearly with the exposure:

$$S_{0B}^{0\nu} = \ln 2 \cdot \varepsilon \cdot \frac{1}{N_{\mathrm{events}}} \cdot \frac{x\,\eta\,N_A}{\mathscr{M}_A} \cdot M\,T. \tag{6}$$

It is called the "zero background" experimental condition and it is likely the experimental condition that next generation experiments will face. It is fair to notice that, up to now, the constraints on the background in Eq. (5) has been fulfilled for a 1-tonne experiment only for ^{76}Ge **?)**, but other experiments are on the way.

3.3 Future players

Despite the very hard challenge, the study and search for $0\nu\beta\beta$ is a very active field and many experiments promise to populate the near future scenario **?)**:

- AMoRE-II (bolometer, 200 kg of ^{100}Mo), the latest in the AMoRE program;

- CUPID (bolometer, $\sim 1\,\mathrm{t}$ of ^{100}Mo or ^{130}Te), the upgrade of the CUORE experiment;
- LEGEND (Ge-diode, $200\,\mathrm{kg} \rightarrow 1\,\mathrm{t}$ of ^{76}Ge) the upgrade of the joint GERDA + MAJORANA experiments;
- KamLAND2-Zen (Xe-loaded liquid scintillator, $1\,\mathrm{t}$ of ^{136}Xe), the next phase of the KamLAND-Zen program;
- nEXO (Xe liquid TPC, $5\,\mathrm{t}$ of ^{136}Xe), the upgrade of EXO-200;
- NEXT-tone (Xe gas TPC, $1\,\mathrm{t}$ of ^{136}Xe), the latest in the NEXT program;
- PANDA-X (Xe gas TPC, $1\,\mathrm{t}$ of ^{136}Xe), the $0\nu\beta\beta$ search with the PANDA program;
- SNO+ (Te-loaded liquid scintillator, $4\,\mathrm{t}$ of ^{130}Te);
- SuperNEMO (tracker+calorimeter, $100\,\mathrm{kg}$ of ^{82}Se), the upgrade of NEMO-3.

As it can be seen, each of these experiment is either the upgrade of an existing one or it the result of an R&D program: staring with smaller setups, the goal becomes to reach sensitivities larger to $10^{27}\,\mathrm{yr}$, with detector mass of hundreds of kilograms.

3.4 Summary and outlook

The study of $0\nu\beta\beta$ offers a unique tool to study lepton number violation and neutrino masses.

Today, sensitivities of the order of $(10^{25} - 10^{26})\,\mathrm{yr}$ on the decay half-life time have been reached for multiple isotopes. The next generation of detectors aims at improving this values by more than one order of magnitude, starting to proble the Inverted Hierarchy region of the neutrino mass spectrum. The main challenge will be represented by the background abatement, and the cost and complexity of the setups will represent critical issues too.

On the theoretical side, a better understanding of the nuclear physics is needed in order to maximize the information that can be extracted from the experimental searches.

The field is very active, with ambitious experimental proposals and numerous R&D programs that will continue to guarantee excellent results.

Frascati Physics Series Vol. 66 (2018)
Frontier Objects in Astrophysics and Particle Physics
May 20-26, 2018

NUCLEUS-NUCLEUS INTERACTIONS AT LHC AND IN COSMIC RAYS AROUND AND ABOVE THE KNEE

A.A. Petrukhin, A.G. Bogdanov
National Research Nuclear University MEPhI
(Moscow Engineering Physics Institute)
115409, Russia, Moscow, Kashirskoe shosse 31

Abstract

At energies > TeV in the center of mass system, which correspond to energies $> 10^{15}$ TeV in cosmic rays, the production of quark-gluon plasma blobs is possible. This can drastically change the interaction picture, since the transition from quark-quark interaction to interaction of many quarks and gluons occurs. The experimental results obtained at LHC and in cosmic rays at corresponding energies (around and above the knee) are considered.

1 Introduction

The energy region above 10^{15} eV in cosmic rays corresponds to energies more than 1 TeV in the center of mass system, which are investigated in LHC. But namely at these energies both in cosmic rays and in LHC experiments some interesting and unusual events and phenomena begin to appear.

Table 1: *Relative abundances of cosmic-ray nuclei.*

Particles	Z	$< A >$	Energy per nucleon	Energy per nucleus
Protons	1	1	92%	42%
α-particles	2	4	7%	21%
Light nuclei	3-5	10	0.25%	1%
Medium nuclei	6-10	15	0.5%	18%
Heavy nuclei	≥ 11	15	0.25%	18%

At energies below 10^{15} eV measurements of mass, charge and energy of primary cosmic rays (PCR) are carried out using the equipment (mostly, thin calorimeters) placed on satellites or high-altitude balloons, i.e. outside of the Earth's atmosphere. Results are the following. Above 1 TeV energy spectrum of different nuclei can be described by a simple power law: $dN/dE \sim E^{-\gamma}$ with a slope $\gamma \approx 2.7$ [1)]. The abundance of protons in primary cosmic rays is about 40%, and almost all remaining particles 60% are heavier nuclei (tab.1).

At energies above 10^{15} eV the direct study of PCR becomes impossible due to the low flux. Therefore indirect method is used: registration of extensive air showers (EAS) on the surface of the Earth. Consequently, to two unknown functions – spectrum and composition of PCR – a third one is added: hadron interaction model, determining the development of EAS in the atmosphere. Such models are tuned according to the data of accelerator experiments and then are extrapolated by several orders of magnitude up to the region of ultrahigh energies of cosmic rays.

In accelerator experiments below 2 TeV (before LHC) various characteristics of hadron interactions were studied in detail. In LHC experiments, main characteristics of hadron interactions for *pp* collisions were confirmed. It should be noted, that the results of accelerator experiments are mainly related to *pp* interactions, while the collisions of primary cosmic rays with air are nucleus-nucleus (or proton-nucleus).

2 Results of EAS investigations above 10^{15} eV

For EAS investigations, systems of various detectors of charged particles (mainly scintillation counters) distributed over large area are applied, in addition detectors of different type radiations which are generated by EAS (Cherenkov

and fluorescence light, radio-emission, etc.) are used. The scheme of primary cosmic ray investigations by means of EAS observables is given in fig.1 [2]. Measured characteristics of EAS are: number of charged particles in each detector ($N_{\rm ei}$), number of muons in each muon detector ($N_{\mu \rm j}$), energy deposit of EAS core ($\Delta E_{\rm h}$), cascade curve (C.C., longitudinal profile of EAS development in the atmosphere) and maximum of EAS development ($X_{\rm max}$). These experimental values are used for recalculation to energy spectrum and mass composition of PCR taking into account different hadron interaction models.

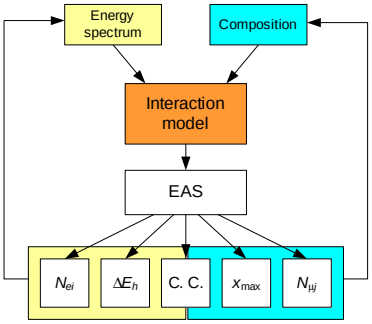

Figure 1: *Existing approach to EAS data analysis* [2].

In principle, two approaches to interpretation of results of EAS parameter measurements are possible. In cosmophysical approach, it is supposed that all serious changes in EAS parameters with increasing of energy are results of PCR spectrum and composition change. In particular, all changes in the number of charged particles reflect the changes of PCR energy spectrum (fig.2) and increasing in the number of muons and decreasing of $X_{\rm max}$ are interpreted as an increase of the mean mass of PCR composition. In nuclear-physical approach, corresponding changes are connected with hadron interaction model change. Now the most part of cosmic ray community follows the cosmophysical approach.

In frame of the cosmophysical approach, it is believed that primary cosmic rays with energies below the knee have galactic origin. The maximal energy of particles which can be accelerated and kept in the Galaxy gives the knee position. At the knee energies, protons begin to reach their acceleration limit or/and leave the Galaxy, and the slope of the energy spectrum becomes steeper.

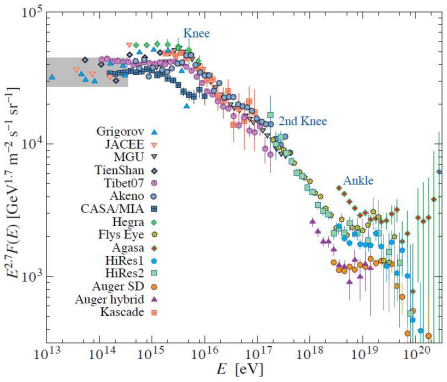

Figure 2: *The all-particle spectrum from air shower measurements* [1].

Then helium nuclei begin to leave the Galaxy, etc. Since the maximal energy of nuclei is proportional to Z, the observed composition above the knee becomes heavier. The flux of extragalactic cosmic rays is significantly less and can be observed at ultrahigh energy only. The energy at which the flux of extragalactic cosmic rays begins to prevail over the flux of galactic ones gives the ankle position.

3 Unusual events observed in cosmic rays above 10^{15} eV

The serious deviations from existing models of hadron interactions indicate unusual events which were detected at PeV energies and above in experiments with calorimeters and X-ray emulsion chambers at mountain altitudes ("Tien-Shan", "Pamir", "Chacaltaya") [3, 4, 5]: halos, alignment (see fig.3,a), Centauros, penetrating cascades (see fig.3,b), long-flying particles.

The enumerated unusual characteristics of observed events show that it is impossible to explain their appearance without rather serious changes of hadron interactions at PeV energies. Possible reasons of their appearance were discussed in many papers, and various ideas of their explanation were proposed, see e.g. [6, 7, 8, 9, 10]. But no idea for their explanation from a single point of view was proposed.

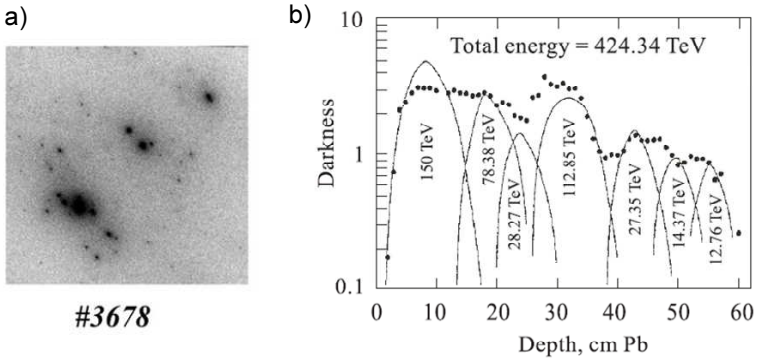

Figure 3: *a) Example of aligned event detected in Pamir experiment* [3]. *Three or more cascades are located in a practically straight line. b) Example of event with penetrating cascades. Shower transition curve in spot darkness is shown* [11].

4 "Muon puzzle"

During the last 10 years, a new problem in cosmic ray muon investigations appeared, which cannot be explained in the frame of existing hadron interaction models (so-called "muon puzzle" [12]). It includes two types of experimental results: an excess of muon bundles compared to calculations even for pure iron cosmic ray composition for any existing model of interaction, and an excess of very high energy (VHE) muons (more than 100 TeV) compared to calculations of inclusive muon energy spectrum.

It is interesting to mark that apparently firstly the excess of muon bundles was observed in LEP (CERN) detectors ALEPH and DELPHI at muon multiplicity about 100 particles [13, 14]. However in these experiments there was no possibility to study the dependence of this excess on primary particle energies.

This information was obtained in NEVOD-DECOR experiment in which muon bundles were measured at various zenith angles [15, 16]. A new approach to the study of the EAS — a method of local muon density spectra (LMDS) allows to estimate the energy of primary cosmic ray particles, which give the main contribution to events selected by muon density, according to the DECOR data (multiplicity of muons and zenith angle). Fig.4,a shows the differential spectra of local muon density D (ratio of the number of muons that hit the

setup to the detector area) for average zenith angle of 78°: experimental points and calculated using the CORSIKA code (curves). Five models of hadron interaction and limiting assumptions to the mass composition (protons and iron nuclei) were used in the calculations. At primary particle energies of $\sim 10^{18}$ eV and higher (corresponding to zenith angles $\theta \geq 75°$) an excess of muon bundles with high multiplicity ($m \geq 10$) is observed, even in comparison to the assumption that primary cosmic rays consist only of iron nuclei. This result was confirmed in Pierre Auger Observatory experiment [17], where the number of muons exceeds the expected values for pure iron composition, too, and the excess increases with increasing energy of primary particles (fig.4,b).

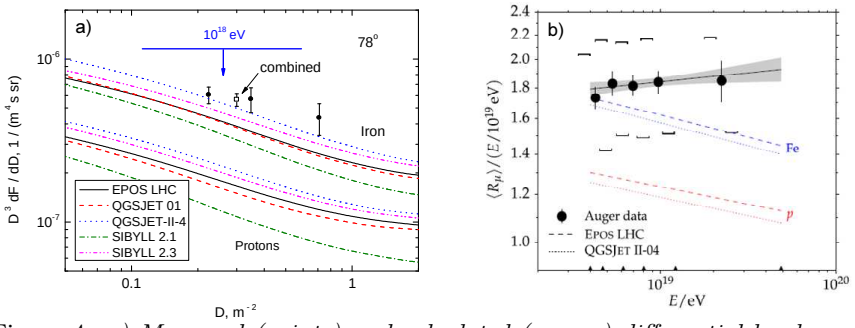

Figure 4: *a) Measured (points) and calculated (curves) differential local muon density spectra* [16]. *b) Average muon content as a function of the shower energy* [17]*; shown for comparison are theoretical curves for proton and iron showers.*

The first result of evaluation of muon energy spectrum in the region of higher than 100 TeV was obtained in the analysis of Baksan Underground Scintillation Telescope (BUST) data using the method of multiple interactions of muons (method of the pair meter) (see fig.5 [18]). Though statistics in this energy region is not high, serious deviations from usual energy spectrum (decays of π-, K-mesons) are observed.

5 Unusual phenomena in LHC experiments

It is important to underline that not only in cosmic rays, but even in LHC experiments serious deviations from existing models in the nucleus-nucleus interactions are observed. For example, in [19] a more fast increase of secondary

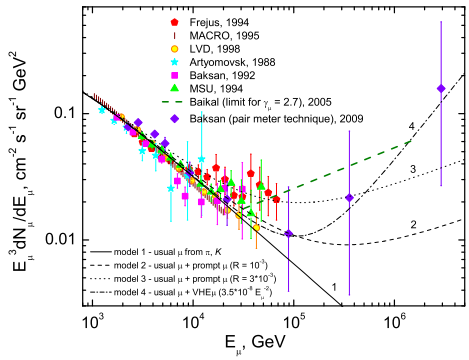

Figure 5: *Differential muon energy spectra for vertical direction measured in various experiments; the curves correspond to different spectrum models* [18].

particle multiplicity in Pb-Pb interactions compared to *pp* interactions was found. This result was confirmed in all LHC detectors. Another example are highly asymmetric dijet events (fig.6) detected in the ATLAS detector at Pb-Pb collisions [20]. Asymmetry both in jets and in the track numbers was observed.

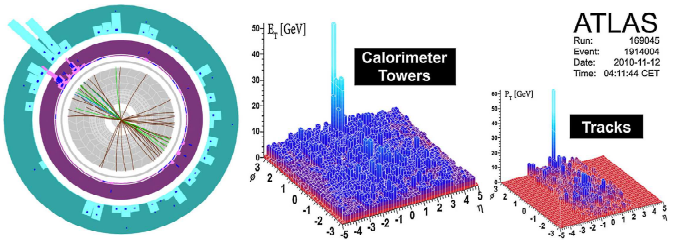

Figure 6: *Highly asymmetric dijet event in the ATLAS detector at Pb-Pb collision* [20].

Of course existing models are being improved and new models appear. But they do not include any serious deviations from existing conception that nucleus-nucleus interaction is a certain superposition of nucleon-nucleon interactions.

6 A new model of nucleus-nucleus interactions

Naturally, various interpretations of the anomalous events detected by the LHC and cosmic-ray experiments are possible. But in order to explain all anomalous phenomena from a single viewpoint, one needs a novel interaction model with the following features: 1) large cross section; 2) threshold behavior; 3) large orbital momentum; 4) large yield of HE leptons; 5) the change of EAS development and, as a consequence, appearance of a missing energy, increasing N_μ/N_e ratio, decreasing of X_max, etc.

We consider the production not of the particle but of some new state of matter, e.g. a blob of quark-gluon plasma (or better quark-gluon matter, since usual plasma is a gas, while quark-gluon plasma behaves like a liquid), the situation is changed. In this case a transition from quark-quark (quark-gluon, gluon-gluon) interactions to collective interaction of many quarks and gluons is required. This directly leads to the appearance of a large cross-section:

$$\sigma \sim \pi R^2, \tag{1}$$

where R is the size of quark-gluon blob.

The production of blobs of QGM provides also the threshold behavior, since for QGM formation a high temperature (energy) is required.

But to explain other observed phenomena a large value of orbital angular momentum is necessary. A possibility of its appearance in non-central ion-ion collisions was considered in paper [21]. Corresponding scheme is presented in fig.7,a. Further investigations showed [22] that the value of the orbital momentum can reach $L \sim 10^4$ (fig.7,b). A blob of a globally polarized QGM with a large orbital angular momentum can be considered as a usual (but very massive) resonance with a large centrifugal barrier. The centrifugal barrier:

$$V = L^2/2mR^2 \tag{2}$$

will be large for light quarks (u, d) but much less for top-quarks ($m_t/m_u \sim 10^5$) or other heavy particles. Though in interacting nuclei top-quarks are absent, the suppression of decays into light quarks gives time for the appearance of heavy quarks in the boiling quark-gluon matter in the blob.

How interaction is changed in frame of a new model?

Simultaneous interactions of many quarks change the energy in the center

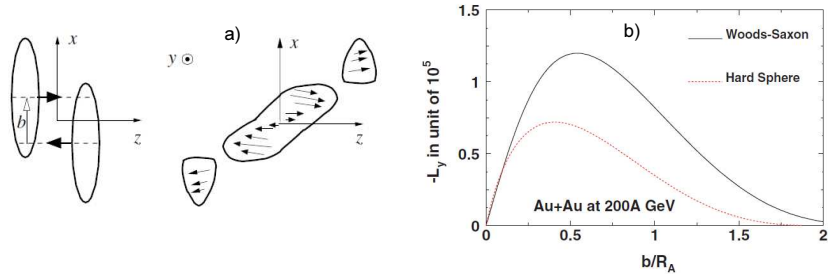

Figure 7: *a) Production of orbital angular momentum in non-central ion-ion collisions* [21]. *b) Total orbital angular momentum of the overlapping system in Au-Au collisions at the RHIC energy as a function of the impact parameter b* [22] *(right).*

of mass system drastically:

$$\sqrt{s} \sim \sqrt{2m_{\rm N}E_1} \to \sqrt{2m_{\rm c}E_1}, \tag{3}$$

where $m_{\rm N}$ is nucleon mass, $m_{\rm c} \approx nm_{\rm N}$ is compound mass of a part of target nucleus which together with a part of projectile nucleus is included in the blob of QGM. This point is important for new model, since it determines the conditions of transition from quark-quark interactions to interaction of many quarks.

Produced $t\bar{t}$-quarks take away from the QGM blob the energy $\varepsilon_t > 2m_t \approx$ 350 GeV, and taking into account fly-out energy $\varepsilon_t > 4m_t \approx 700$ GeV in the center of mass system. After this energy $\sqrt{s}$ and correspondingly orbital L momentum and centrifugal barrier are sharply decreased and the rest part of the blob decays into more light quarks.

Top-quarks very rapidly (10^{-25} s) decay into W-boson and b-quark: $t(\bar{t}) \to W^+(W^-) + b(\bar{b})$, W-bosons decay into leptons ($\approx 30\%$) and hadrons ($\approx 70\%$), b-quarks produce jets or can decay into c-quarks.

The proposed new model allow explain unusual experimental results obtained both in accelerator and cosmic ray experiments from a single point of view.

7 Explanation of CR results

The main supposition of nuclear-physical approach to interpretation of results of EAS study is the following. The energy spectrum and mass composition of primary cosmic rays are not changed seriously and all observed peculiarities of the energy spectrum (the knee, the ankle, etc.) must be explained by changes in the particle interaction. Of course, in this case the evaluated EAS energy (E_2) is not equal to primary particle energy (E_1) and some missing energy ($\Delta E = E_1 - E_2$) must appear. This missing energy must be taken away by the particles the energy of which is not measured by existing arrays for EAS investigations: three types of neutrinos and muons, since muon detectors used in EAS arrays can measure the number of muons, but not their energies.

Appearance of a large missing energy will change cosmic ray energy spectrum, more exactly, the spectrum of EAS in the number of charged particles. If not to take into account this change of interaction model and to use existing models for transition from EAS energy to energy of cosmic ray particles, a change of CR energy spectrum will be observed [23]. Fig.8,a illustrates the situation for sharp threshold energy. If not to take into account a difference between E_1 and E_2, some bump and the knee in the energy spectrum will be obtained (fig.8,b).

How the measured composition is changed in frame of the new model? Since for QGM production not only high temperature (energy) but also high density is required, threshold energy for production of the new state of matter for heavy nuclei will be less than for light nuclei and protons. Therefore heavy nuclei (e.g. iron) spectrum is changed earlier than light nuclei and proton spectra! And measured spectra for different nuclei will not correspond to the primary composition (fig.8,c). But the energy spectrum of all nuclei will be in a good agreement with experimental data (fig.8,d).

In frame of the considered nuclear-physical approach to interpretation of cosmic ray energy spectrum measurements it is easy to explain the ankle appearance. With the increase of the interaction energy, the mass and excitation energy of quark-gluon blob will be increased and can become larger than the centrifugal barrier; hence a resonance state will begin to decay into light quarks. Missing energy and other effects connected with production of heavy quarks will be decreased and the development of EAS will return to a normal behavior. Correspondingly, the measured spectrum must return to the primary

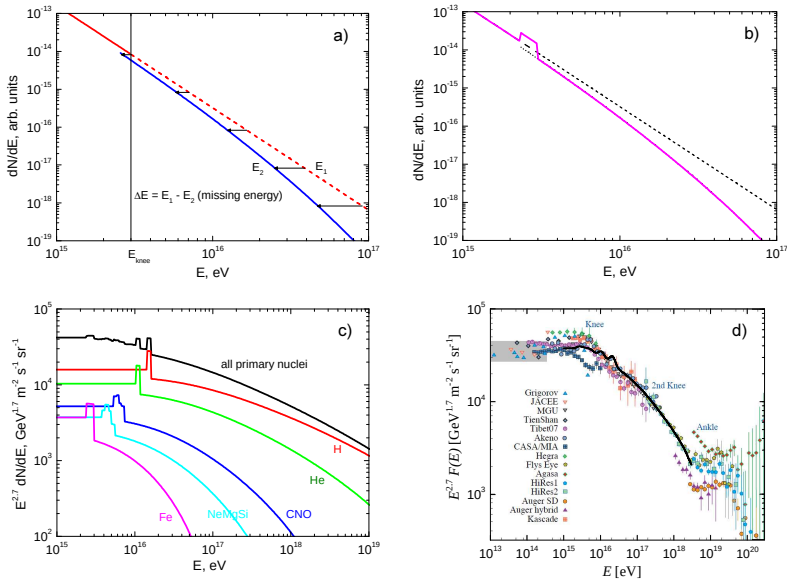

Figure 8: *a) The change in the CR energy spectrum at the appearance of the missing energy* [23] *b) The production of the knee with some "bump" in the nuclear-physical approach c) Changes of various CR nuclei spectra in the frame of the considered interaction model d) All-particle spectrum calculated in the frame of the new interaction model and experimental data.*

slope ($\gamma \approx 2.7$) and its behavior at higher energies will depend on the relation between positions of the ankle and the GZK cut-off. More detailed discussion of this problem is given in papers [24, 25].

In framework of this hypothesis, the so-called "muon puzzle" — the excessive number of measured EAS muons compared to the simulated number even for pure iron composition of primary CR – can be solved, since with 70% probability W-bosons decay into hadrons (mainly pions) with an average number of about 20, and the multiplicity of secondary particles (and also muons) begins to increase more sharply than the existing models predict.

There is a more interesting situation with the muon energy spectrum. In frame of the new interaction model, decays of W-bosons into leptons lead to excess of very high energy muons compared to conventional (from π, K-decays) energy spectra [26]. In fig.9, the results of calculations by means of CORSIKA

and PYTHIA codes of muon energy spectrum are presented. Similar energy spectra will be for three types of neutrinos. In this case cascade showers with energies of several hundred TeV and higher observed in the IceCube experiment [27] can be generated by atmospheric neutrinos too, if to take into account a possibility of formation of a new state of matter in nucleus-nucleus interactions of very high energy cosmic rays.

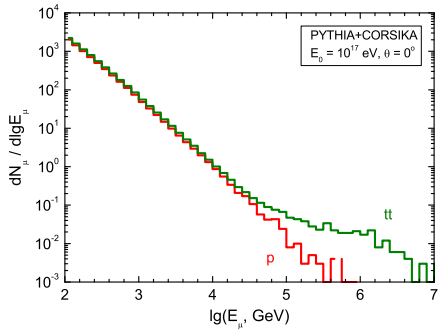

Figure 9: *The energy spectrum of EAS muons simulated by means of the CORSIKA taking into account $t\bar{t}$-quarks pair production according to PYTHYA* [26].

Also, using the proposed model of the production of QGM blobs most of the unusual experimental data in hadron experiments can be explained [28]. Here we consider only one of them.

Appearance of VHE muons allows explain not only results of muon observations, but also some unusual results in hadron experiments: penetrating cascades and long-flying component. Really in hadron calorimeters a "muon background" always exists (fig.10). In thin calorimeters this background cannot be observed without additional detectors to distinguish muons. But in thick detectors cascades generated by muons will increase the width of average hadronic cascade curve and will increase the observed value of absorption length (dotted line).

8 Explanation of LHC results

To illustrate possibilities of the new model for explanation of unusual phenomena observed in nucleus-nucleus collisions at LHC, let us consider two examples. The first example is observation of imbalance of jet energies at ATLAS in heavy

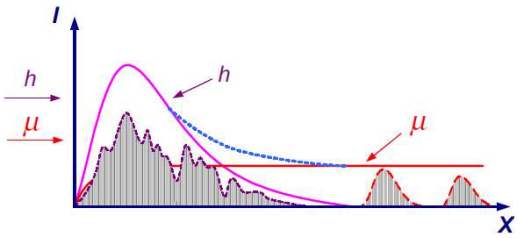

Figure 10: *Explanation of penetrating cascades. Hadron-muon cascade in a thick calorimeter.*

ion collisions (fig.6) [20]. If to take into account a possibility of $t\bar{t}$-quarks pair production, explanation will be the following: top-quark decays as $t \to W + b$, and kinetic energy of particles in the center-of-mass system will be equal to: $T_b \approx 65$ GeV, $T_W \approx 25$ GeV. If to take into account the fly-out energy, T_b may be more than 100 GeV which corresponds to jet energy in the observed event. In case of decay of the second W into pions (more than 10 particles), a picture observed by ATLAS will be obtained.

The second example is an excess of secondary particles observed in nucleus-nucleus (Pb-Pb) collisions compared to proton-proton collision at the same energy in the center-of-mass system $\sqrt{s}_{\rm NN} \approx 2.76$ TeV [19]. If to take into account collective interactions, the average mass of intersecting parts of nuclei will be larger than nucleon mass, and corresponding value $\sqrt{s}_{\rm AA}$ will be larger, too. Therefore, experimental point at the diagram must be moved to the right (fig.11). If to take into account that $\sqrt{s}_{\rm AA}$ cannot be more than $\sqrt{s}_{\rm NN}$, it allows evaluate limiting average number of interacting nucleus: $n_{\rm c} < 50$ TeV / 3.5 TeV ≈ 14. So in Pb-Pb interactions a blob of QGM can consist of up to 200 nucleons, though on average this value will be less.

9 How to check the new approach?

In cosmic ray experiments, there are two possibilities [15].

The first one is the measurement of the energy deposit of muon bundles. Changes of this value in dependence on primary particle energy will evident that some new processes of muon generation are included. These measurements are performed in the NEVOD-DECOR experiment in which the number of muons and their energy deposit are measured by different detectors: DECOR [29]

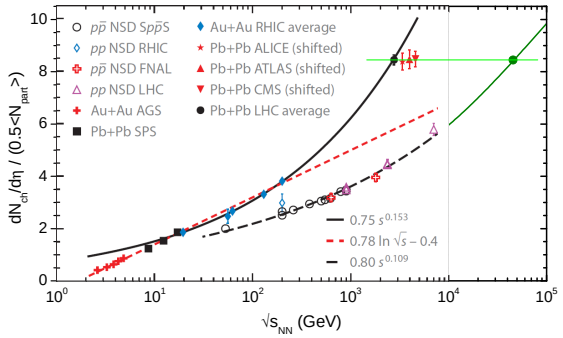

Figure 11: *Multiplicities of charged particles formed in nucleus–nucleus and proton–proton collisions as a function of collision energy* [19].

and NEVOD [30]. The first results are shown in fig.12 [31]. From the figure it is clear that the results of the calculations (curved) show a decrease of muon bundle energy deposit (and, accordingly, the average muon energies) with an increase of the primary particle energies. At the same time, the experimental data indicate to a possible increase of muon bundle energy deposit at densities $D > 1$ part./m^2, i.e. at primary particle energies $E_0 > 10^{17}$ eV.

The second one is careful measurement of the inclusive muon energy spectrum above 100 TeV with a good statistics. Detection of excess of VHE muons will evident for muon generation in decays of heavy particles (e.g., W-bosons). Such measurements can be performed in IceCube and HAWC (fig.13).

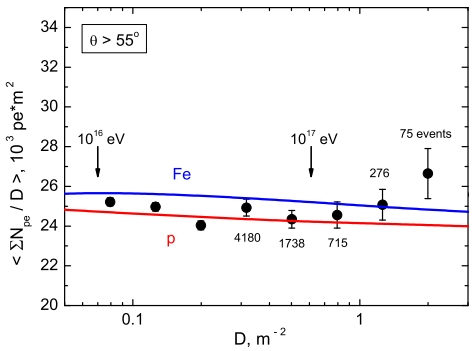

Figure 12: *Energy deposit of muon bundles measured in NEVOD-DECOR* [31].

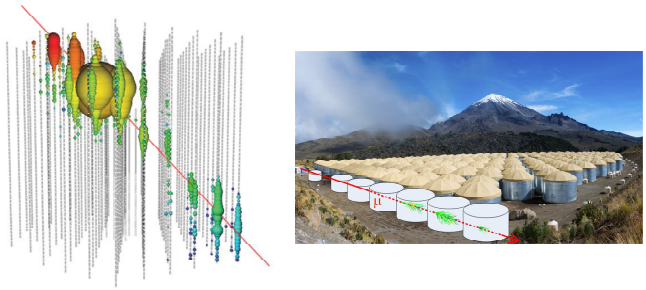

Figure 13: *Example of the high-energy muon registered in IceCube* [32] *(left). VHE muon in HAWC (right).*

Good possibilities to check the new model are available in LHC experiments, since such predictions as excess of t-quarks, excess of W-bosons, sharp increase of missing energy, etc. can be measured by the existing LHC detectors. But it is necessary to do these measurements in AA interactions (as in cosmic rays) not in pp interactions. Of course, the search of t-quarks and W-bosons in AA interactions is a more complex task compared to pp interactions, due to a very large multiplicity of secondary particles.

10 Conclusion

Many year attempts of explanation of all unusual events in the frame of cosmophysical approach were unsuccessful. Opposite, nuclear physical approach allows explain all unusual events and phenomena. Predicted in frame of this approach excess of very high energy muons which cannot be obtained in any other way, give an excellent possibility to check this approach and prove its truth. Comparison of possibilities of cosmic ray and accelerator (LHC) experiments shows that may be in the first time for the long period a new state of matter can be observed in CR earlier than at accelerators!

Acknowledgements

Authors thank R.P. Kokoulin for fruitful discussions and help in preparation of this paper. This work was supported by Ministry of Education and Science of the Russian Federation (government task and MEPhI Academic Excellence Project).

References

1. K. Nakamura *et al* (Particle Data Group), J. Phys. G: Nucl. Part. Phys. 37, 075021 (2010).
2. A. Petrukhin, Measurements of EAS muon energy – the key to solution of primary cosmic ray energy spectrum problem, in: Proc. 31st Int. Cosmic Ray Conf., 2009, Lodz, Poland (http://icrc2009.uni.lodz.pl/proc/pdf/icrc0884.pdf).
3. S.A. Slavatinski, Nucl. Phys. B (Proc.Suppl.) 122, 3 (2003).
4. M. Tamada, Nucl. Phys. B (Proc.Suppl.) 122, 349 (2003).
5. V.I. Yakovlev, Nucl. Phys. B (Proc.Suppl.) 122, 417 (2003).
6. S.I. Nikolsky, Nuclear Physics B (Proc. Suppl.) 60B, 144 (1998).
7. Yu.V. Stenkin, Phys. of Atomic Nuclei 71, 98 (2008).
8. I.M. Dremin, EPJ Web of Conferences 145, 10003 (2017).
9. M. Tamada *et al*, EPJ Web of Conferences 145, 15001 (2017).
10. S.B. Shaulov *et al*, EPJ Web of Conferences 145, 17001 (2017).
11. E. Gladysz-Dziadus, Phys. Elem. Part. Atom. Nucl. 34, 563 (2003).
12. A.A. Petrukhin, Nucl. Instrum. Meth. Phys. Res. A 742, 228 (2014).
13. V. Avati *et al*, Astropart. Phys. 19, 513 (2003).
14. J. Abdallah *et al* (DELPHI Collab.), Astroparticle Physics 28, 273 (2007).
15. A.G. Bogdanov *et al*, Nucl. Instrum. Meth. Phys. Res. A 588, 189 (2008).
16. A.G. Bogdanov *et al*, Astropart. Phys. 98, 13 (2018).
17. A. Aab *et al* (Pierre Auger Collaboration), Phys. Rev. D 91, 032003 (2015).
18. A.G. Bogdanov *et al*, Astropart. Phys. 36, 224 (2012).
19. K. Aamodt *et al* (ALICE Collaboration), Phys. Rev. Lett. 105, 252301 (2010).

20. G. Aad *et al* (ATLAS Collaboration), Phys. Rev. Lett. 105, 252303 (2010).

21. Z.-T. Liang, X.-N. Wang, Phys. Rev. Lett. 94, 102301 (2005).

22. J.-H. Gao *et al*, Phys. Rev. C 77, 044902 (2008).

23. A.A. Petrukhin, Nuclear Physics B (Proc. Suppl.) 212-213, 235 (2011).

24. A.A. Petrukhin, Nucl. Phys. B (Proc. Suppl.) 165, 145 (2007).

25. A.A. Petrukhin, Nucl. Phys. B (Proc. Suppl.) 175-176, 125 (2008).

26. A.A. Petrukhin, Acta Polytechnica 53 (Supplement), 707 (2013).

27. M.G. Aartsen *et al* (IceCube Collaboration), Phys. Rev. Lett. 111, 021103 (2013).

28. A. Petrukhin, Nuovo Cimento B 120, 837 (2005).

29. N.S. Barbashina *et al*, Instrum. Experim. Techniques 43, 743 (2000).

30. A.A. Petrukhin, Phys. Uspekhi 58, 486 (2015).

31. R.P. Kokoulin, EPJ Web of Conf. 145, 16002 (2017).

32. M.G. Aartsen *et al* (IceCube Collaboration), Astropart. Phys. 78, 1 (2016).

Frascati Physics Series Vol. 66 (2018)
Frontier Objects in Astrophysics and Particle Physics
May 20-26, 2018

THE CHERENKOV TELESCOPE ARRAY PROJECT: CURRENT STATUS AND SCIENCE GOALS

The CTA Consortium* represented by **A.Morselli**
INFN Roma Tor Vergata

Abstract

The Cherenkov Telescope Array (CTA) will be the next generation gamma-ray observatory, open to the scientific community, to investigate the very-high-energy emission from a large variety of celestial sources in the 20 GeV - 300 TeV energy range. The full array, distributed over two sites, one in the northern and one in the southern hemisphere, will provide whole-sky coverage and will improve the sensitivity with respect to the current major arrays such as H.E.S.S., MAGIC and VERITAS by a factor of five to twenty, depending on the energy. CTA will investigate a much higher number of already known classes of sources, going to much larger distances in the Universe. Along with accurate variability and spatially-resolved studies, these improvements will also enable population studies. Moreover, new light will be shed on new classes of TeV

* see
https://www.cta-observatory.org/consortium_authors/authors_2018_05.html
for full author list

sources, such as GRBs and clusters of galaxies. Furthermore, by pushing the high-energy limit to E > 100 TeV, CTA will allow a thorough exploration of the cut-off regime of the cosmic accelerators. The search for an annihilation signature of dark matter in the Galactic halo and in prominent dwarf spheroidal galaxies is one of the most important goals of CTA. We review the current status of the CTA project, introducing the highlights from the telescope prototypes and discuss the main CTA Key Science Projects, which will focus on major scientific cases, allowing us to provide legacy data sets of high value to a wider community.

1 Introduction

Very high energy gamma-ray astronomy (VHE; E> 100 GeV) is a relatively young field with great scientific potential. The current generation atmospheric Cherenkov telescopes (H.E.S.S., MAGIC, and VERITAS), along with air shower experiments (e.g. ARGO-YBJ, Milagro and HAWC) and with the *Fermi* and *AGILE* satellite instruments, have firmly established the field, discovering VHE radiation from more than 150 sources, comprising many source classes. A number of individual sources, both within and outside of our Galaxy, have been well-studied but there are many others that are not well-characterized or understood. It seems clear that our current knowledge represents just the tip of the iceberg in terms of the number of sources and source classes and in terms of our ability to confront the existing theoretical models. CTA will transform our understanding of the high-energy universe by discovering many hundreds of new sources, by measuring their properties with unprecedented accuracy, and also by exploring questions in physics of fundamental importance. The major scientific questions that can be addressed by CTA are the following, grouped into three broad themes:

Theme 1: Understanding the Origin and Role of Relativistic Cosmic Particles
- What are the sites of high-energy particle acceleration in the universe?
- What are the mechanisms for cosmic particle acceleration?
- What role do accelerated particles play in feedback on star formation and galaxy evolution?

Theme 2: Probing Extreme Environments
• What physical processes are at work close to neutron stars and black holes?
• What are the characteristics of relativistic jets, winds and explosions?
• How intense are radiation fields and magnetic fields in cosmic voids, and how do these evolve over cosmic time?

Theme 3: Exploring Frontiers in Physics
• What is the nature of dark matter? How is it distributed?
• Are there quantum gravitational effects on photon propagation?
• Do axion-like particles exist?

2 Core Programme

Over the lifetime of CTA, most of the available observation time will be divided into the Guest Observer (GO) Programme, where time will be awarded based on scientific merit, and a Core Programme of a number of major legacy projects. Director's Discretionary Time and host country reserved time will comprise the remaining time. The CTA Consortium has developed the Core Programme that consists of proposed Key Science Projects (KSPs) that are characterized by having an excellent science case and clear potential to advance beyond the state of the art, the production of legacy data sets of high value to the wider community, and clear added value for the project to be done as a KSP rather than part of the GO Programme (e.g. because of the scale of the project or the expertise required in carrying it out). This Core Programme has been described in the document "Science with the Cherenkov Telescope Array" [1)]

The proposed CTA Key Science Projects include: (i) Dark Matter Programme, (ii) Galactic Centre Survey, (iii) Galactic Plane Survey, (iv) Large Magellanic Cloud Survey, (v) Extragalactic Survey, (vi) Transients, (vii) Cosmic-ray PeVatrons, (viii) Star Forming Systems, (ix) Active Galactic Nuclei, and (x) Clusters of Galaxies. A few highlights from these projects are described here, focusing on the surveys and the search for dark matter:

• **The Galactic Centre Survey** consists primarily of a deep (525 h) exposure with pointings on a small grid centered on Sgr A*; this exposure covers the central source, the centre of the dark matter halo, the primary diffuse emission and multiple supernova remnant (SNR) and pulsar wind nebula (PWN) sources. An extended survey (300 h) of a 10° x 10° region around the

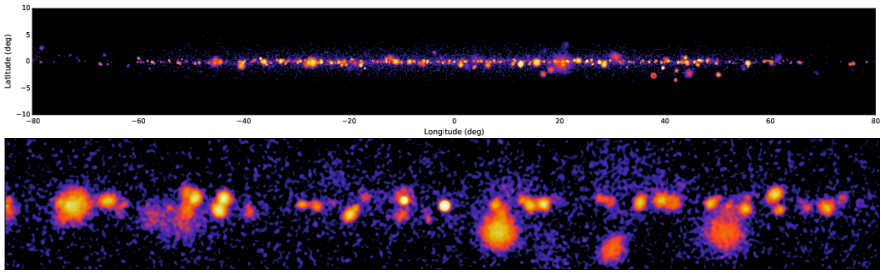

Figure 1: Top: simulated CTA image of the Galactic plane for the inner region, $-80° < l < 80°$, adopting the proposed Galactic Plane Survey observation strategy and a source model that contains supernova remnant and pulsar wind nebula populations as well as diffuse emission. Bottom: a close-in view of a 20° region in Galactic longitude.

Galactic centre would cover the edge of the Galactic bulge, the base of the Fermi Bubbles, the radio spurs and the Kepler SNR.

• **The Galactic Plane Survey** is a survey of the entire Galactic plane, with deeper exposure in the inner Galaxy and Cygnus region. The survey will be a factor of 5-20 more sensitive than previous surveys carried out at very high energies and is thus expected to sample a much larger fraction of the log N - log S distribution of Galactic sources, as shown in Figure 1. The discovery of many hundreds of sources in the Galactic Plane Survey will be an important pathfinder for later GO proposals.

• **The Large Magellanic Cloud (LMC) Survey** will cover this star-forming galaxy in its entirety, resolving regions down to 20 pc in size and with sensitivity down to a luminosity of $\sim 10^{34}$ erg/s. Long-term monitoring of SN 1987A will be carried out, provided the source is detected in the first phase of the survey.

• **The Extragalactic Survey** will be the first wide-field (one-quarter of the sky) survey of the VHE sky at high sensitivity. Aimed to provide an unbiased sample of galaxies (particularly active Galactic nuclei, AGN), the survey will also be sensitive to unexpected phenomena at high Galactic latitudes.

• **The Dark Matter Programme** is centered on the indirect search for dark matter via the weakly interacting massive particle (WIMP) annihilation signal [2]. As shown in Figure 2, the deep exposure of the Galactic centre region will allow CTA to reach a sensitivity to a thermal relic WIMP over a wide mass

region, thus nicely complementing searches done with the *Fermi* satellite, at the Large Hadron Collider and by direct-detection experiments. Additional dark matter targets include dwarf spheroidal galaxies, the LMC and the Perseus cluster. The effect of systematics is drastically reduced for dwarf spheroidal galaxies compared to the extended Galactic Halo, explaining the significant interest in observations of dwarfs.

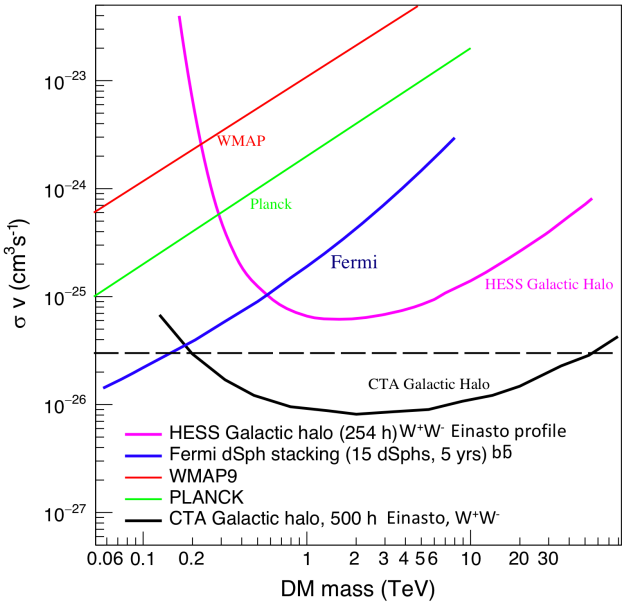

Figure 2: Current best limits on the annihilation cross-section from indirect detection (*Fermi*-LAT dwarf spheroidal galaxies stacking analysis, W^+W^- channel [3)], H.E.S.S. Galactic halo W^+W^- channel [5)]) and cosmic microwave background (WMAP and Planck $b\bar{b}$ channel [4)]) experiments compared with the projected sensitivity for CTA from observations of the Galactic halo for the Einasto profile, W^+W^- channel. The expectation for CTA is optimistic as it includes only statistical errors. The effect of the Galactic diffuse emission can affect the results by $\sim$ 50%. The dashed line shows the thermal relic cross section [2)].

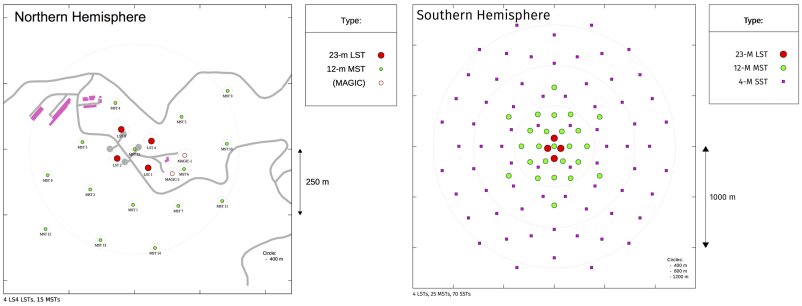

Figure 3: Possible layouts for the baseline arrays for CTA South (left) and CTA North (right). The LSTs are identified by the red circles, the MSTs by the green circles, and the SSTs by the purple squares.

3 CTA Design: Performance Goals, Concept, and Array Layouts

To achieve these broad science goals in a meaningful way, CTA must improve upon the performance of existing instruments in many areas simultaneously. The various performance goals, along with the science drivers that provide their impetus, are the following:

• **High sensitivity** (a factor of up to ten improvement over current experiments): impacts all science topics;

• **Wide Energy Coverage** (20 GeV to $\geq$ 300 TeV): low-energy sensitivity is needed to detect the most distant sources whose spectra are cut off from absorption on intergalactic radiation fields; very high-energy reach is needed to detect "PeVatron" sources that would help explain the origin of cosmic rays up to the knee in the spectrum;

• **Full-sky Coverage** (arrays in both hemispheres): enable the full characterization of the VHE universe and access to unique sources in both hemispheres;

• **Wide Field-of-View** ($\sim$ 8 deg): permits more rapid surveys and better study of extended sources;

• **Excellent Resolution** in angle (few arc-minutes) and energy ($\sim$10%): permits good reconstruction of source morphology and spectra,

• **Rapid Response** ($\sim$30 s slewing to/from anywhere in observable sky): enables rapid follow up of transient sources.

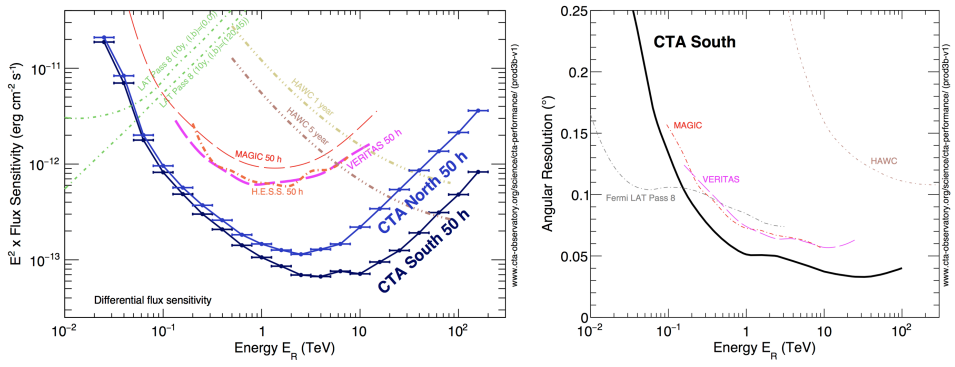

Figure 4: Left: Differential energy flux sensitivities for CTA (south and north) and selected existing gamma-ray instruments for five standard deviation detections in five independent logarithmic bins per decade in energy. For the CTA sensitivities, additional criteria are applied to require at least ten detected gamma rays per energy bin and a signal/background ratio of at least 1/20. The curves for *Fermi*-LAT and HAWC are scaled by a factor of 1.2 to account for the different energy binning. The curves shown give only an indicative comparison of the sensitivity of the different instruments, as the method of calculation and the criteria applied are different. Right: Angular resolution expressed as the 68% containment radius of reconstructed gamma rays (the resolution for CTA-North is similar).

To meet these performance goals, CTA will extend the atmospheric Cherenkov technique to its logical next level, by deploying large arrays of telescopes that cover an area on the ground that is significantly larger than the Cherenkov light pool. Compared to the existing instruments consisting of several telescopes separated by about 100m, the larger number of telescopes and the larger area covered by CTA will result in: i) a much higher rate of showers contained within the footprint of the array, ii) a better sampling of the showers from different viewing angles that will greatly improve the shower reconstruction and the cosmic-ray background rejection, and iii) a lower energy threshold since the central part of the shower (with the highest Cherenkov photon density) gener-

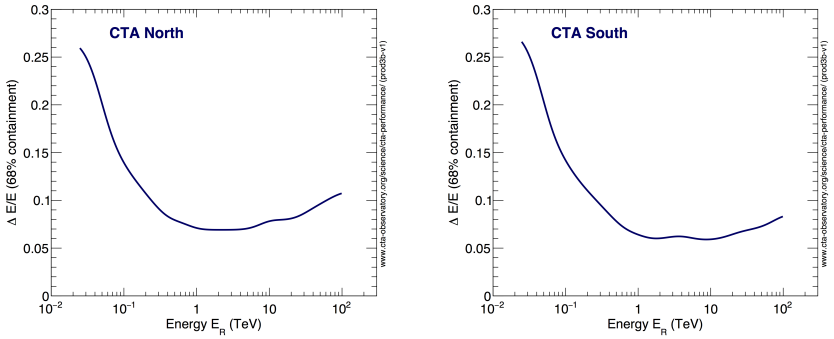

Figure 5: Energy resolution as a function of reconstructed energy (the result depends only weakly on the assumed gamma-ray spectrum). On the left for the North site and on the right for the South site.

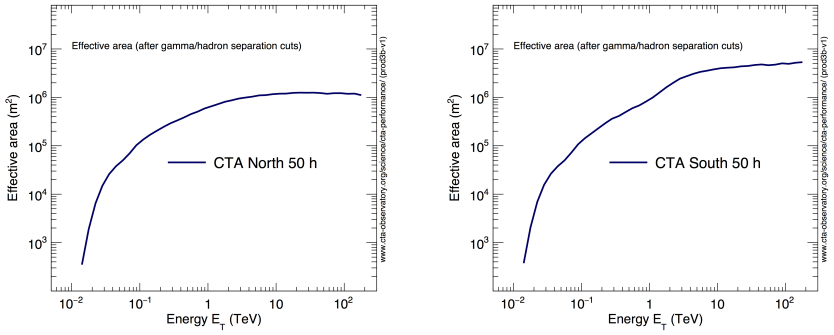

Figure 6: Effective collection area after gamma/hadron separation cuts but without any cut in the reconstructed event direction optimized for 50 h observation time for the North site (left) and the South site (right).

ally falls within the array. To achieve the goal of wide energy range within cost constraints leads to the logical choice of a graded array of telescopes of different sizes. In CTA, the lowest energies are covered by four large-sized telescopes (LSTs) that are capable of detecting gamma rays down to 20 GeV. The core

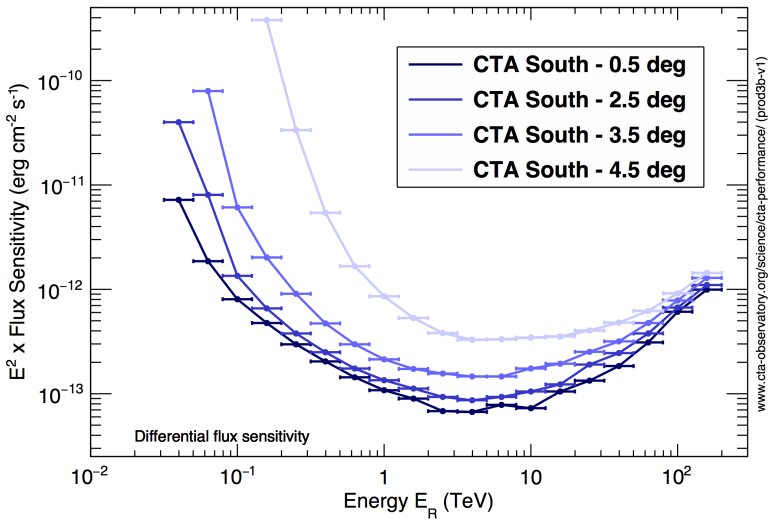

Figure 7: Differential sensitivity curves for a point-like source at increasing angular distances from the centre of the FoV.

energy range of 100 GeV to 10 TeV is covered by an array of 25 (South) or 15 (North) medium-sized telescopes (MSTs), and, for the Southern array, the highest energies are covered by a several km^2 array of 70 small-sized telescopes (SSTs). To achieve fast-response to low-energy transients such as gamma-ray bursts, the LSTs will incorporate very rapid slewing. Conversely, to achieve a wide field-of-view for surveys and extended Galactic sources, the MSTs and SSTs will employ wide-field cameras. To realize full-sky coverage, CTA arrays will be deployed in both hemispheres. The small-sized telescopes are only planned for the Southern array because the highest energies are most relevant for the study of Galactic sources. The layout of the telescopes in the CTA arrays has been determined over a number of years by a multi-step process starting with semi-analytic estimates and continuing with large-scale simulations that include full shower and detector modeling. The latest simulations incorporate site-dependent effects (including altitude, geomagnetic field, and telescope positioning constraints) to assess the performance attributes of CTA.

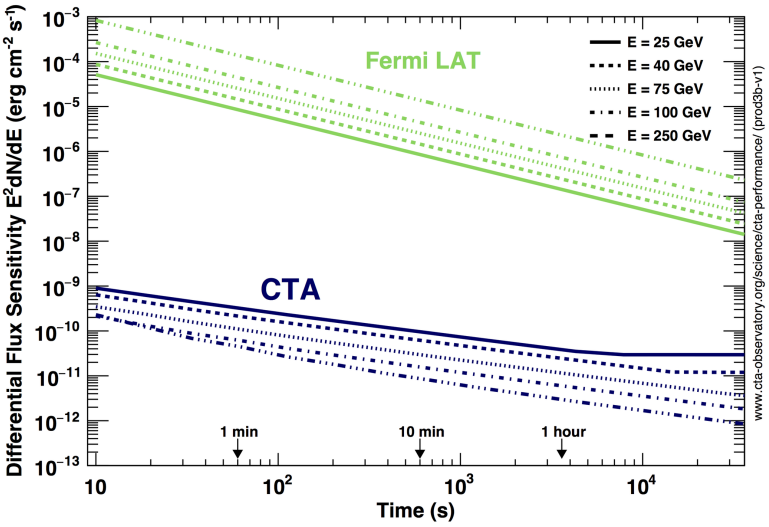

Figure 8: Differential flux sensitivity of CTA at selected energies as a function of observing time in comparison with the *Fermi*-LAT instrument (Pass 8 analysis, extragalactic background, standard survey observing mode).

Figure 3 shows the current baseline array layouts for the Southern and Northern CTA sites resulting from this optimization process. Figure 4 shows on the left the differential energy flux sensitivities for CTA (South and North) and on the right the angular resolution expressed as the 68% containment radius of reconstructed gamma rays. Figure 5 shows on the left the energy resolution as a function of reconstructed energy for the North site and on the right for the South sites. Figure 6 shows the effective collection area after gamma/hadron separation cuts but without any cut in the reconstructed event direction optimized for 50 h observation time for the North site (left) and the South site (right). Figure 7 shows the differential sensitivity curves for a point-like source at increasing angular distances from the centre of the FoV. The radius of the FoV region in which the sensitivity is within a factor 2 of the one at the centre is around 2 degrees near the CTA threshold, and >3 degrees above a few 100 GeV. Figure 8 shows the differential flux sensitivity of CTA at selected energies as a

function of observing time in comparison with the *Fermi*-LAT instrument (Pass 8 analysis, extragalactic background, standard survey observing mode). The differential flux sensitivity is defined as the minimum flux needed to obtain a 5-standard-deviation detection from a point-like gamma-ray source, calculated for energy bins of a width of 0.2 decades. An additional constraint of a minimum of 10 excess counts is applied. Note that especially for exposures longer than several hours, the restrictions on observability of a transient object are much stricter for CTA than for the *Fermi*-LAT. CTA will be able to observe objects above 20 degrees elevation during dark sky conditions.

4 Current Status of CTA

CTA was conceived and is being designed by the CTA Consortium (CTAC), a collaboration of more than 1400 scientists and engineers from 32 countries around the world. The Consortium has developed the primary science themes of CTA and Consortium Institutes are expected to provide the bulk of the CTA components, including telescopes, cameras and software. The CTA Observatory (CTAO) was established in 2014 to provide the legal entity to oversee the CTA Project Office that manages the construction of CTA. Governed by a Council of country representatives, CTAO will be responsible for observatory operations and data management. During the last several years, the progress towards realization of CTA has been accelerating. The baseline design and core technologies are now established, several prototype telescopes have been completed and are undergoing testing, the two CTA sites have been selected, and a large portion of the required funding has now been identified. Thus, the project is well positioned for a construction start in 2018 and the turn-on of full operations by the middle of the next decade.

4.1 CTA Sites

CTAO activities will be carried out at the two CTA array sites and at the CTA Headquarters (HQ) and Science Data Management Centre (SDMC). Pending successful completion of hosting agreements, the CTA HQ will be hosted at the INAF site in Bologna, Italy and the CTA SDMC will be on the DESY campus in Zeuthen, Germany. Following a lengthy process that included detailed assessment and external review, the CTA Resource Board (a precursor to the CTA Council) selected the following two sites to host CTA arrays:

• South: European Southern Observatory (ESO) Paranal site in Chile
• North: Instituto de Astrofisica de Canarias (IAC) Roque de los Muchachos Observatory site in La Palma, Spain.
Activities to prepare the sites are well underway in both hemispheres. Technical and infrastructure studies are being carried out in the context of the Royal Institute of British Architects (RIBA) process. CTA is currently in the advanced design phase (RIBA-3) and is approaching the technical design phase (RIBA-4). Specific activities include power, lightning protection, geotechnical, ground investigation, and general infrastructure (roads, buildings, foundations, etc.) studies. On La Palma, the construction of the first prototype LST has started and presently (May 2018) 123 mirrors have been installed. This prototype is expected to become the first LST in the Northern CTA array.

Figure 9: Prototype telescopes being developed for CTA. Top row (left to right): LST in construction (May 2018), MST-DC in Germany, MST-SCT in USA. Bottom row (left to right): SST-1M in Poland, SST-2M-GCT in France, and SST-2M-ASTRI in Italy.

4.2 Prototype Telescopes

Extensive work has been carried out within the CTA Consortium over a number of years to prototype the hardware and software for all three telescope types. This work builds on the successes and experiences of the current generation of imaging atmospheric Cherenkov telescopes, but it also makes use of new techniques. For example, in the telescope design, both single mirror (based on the traditional Davies-Cotton, or DC, design) and dual mirror (based on the Schwarzschild-Couder, or SC, design) approaches are being developed. For the photosensors in the cameras, both photomultiplier tubes (PMTs) and Silicon photomultipliers (Si-PMs) are being evaluated. In all camera designs, the read-out electronics (typically using 1 GS/s high-speed sampling ASICs) are contained in the focal-plane box. Figure 9 shows recent photos of the various prototype CTA telescopes. For the LST, the requirement of a large mirror area to reach the lowest gamma-ray energies has led to a single mirror design using a 23 m diameter parabolic reflector. This very large telescope will use PMTs. For the MST, two designs are being considered. A single mirror DC design has been developed at a site in Adlershof, Germany that makes use of a 12 m diameter dish with a focal length of 16 m and a PMT camera. Two read-out schemes are being prototyped that make use of 250 MS/s Flash-ADCs with digital storage and 1 GS/s ASICs. A dual mirror SC MST prototype is being built at the Whipple Observatory in Arizona, USA that will employ a 9.7 m primary mirror and a compact high-resolution camera using Si-PMs. For the SST, three approaches are being considered, with each having a primary mirror size of 4 m diameter and cameras using Si-PMs. Two of these use the SC design: the SST-2M-ASTRI prototyped at Serra La Nave, Sicily, Italy and SST-2M-GCT in Meudon, France. The third SST prototype, SST-1M, is being developed in Krakow, Poland and makes use of the DC design.

5 Synergies

CTA will have important synergies with many of the new generation of astronomical and astroparticle observatories. As the flagship VHE gamma-ray observatory for the coming decades, CTA plays a similar role in the VHE waveband as the SKA in radio, ALMA at millimetre, or E-ELT/TMT/GMT in the optical wavebands, providing excellent sensitivity and resolution compared to

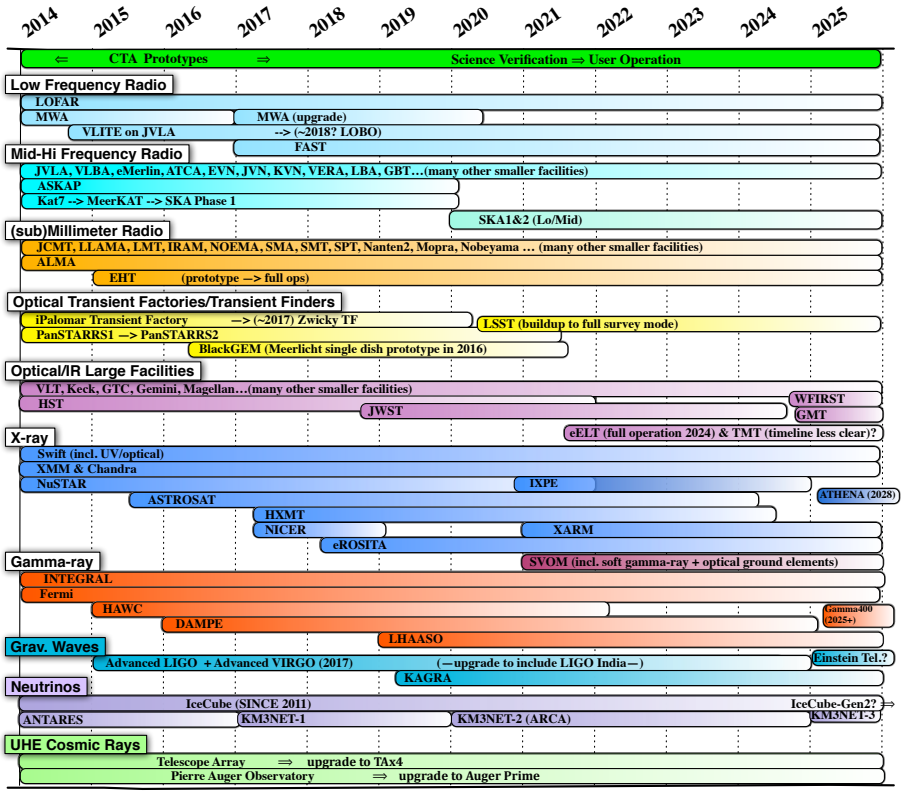

Figure 10: Timeline of major multi-wavelength/multi-messenger facilities over the next decade. Note that the lifetimes of many facilities are uncertain, contingent on performance and funding. We indicate this uncertainty via the gradient, but have chosen timelines based on the best information currently available.

prior facilities. At the same time, the scientific output of CTA will be enhanced by the additional capabilities provided by these instruments (and vice-versa). Multi-wavelength (MWL) and multi-messenger (MM) studies using CTA provide added value to the science cases in two main ways:

• Non-thermal emission: To understand the origin of cosmic rays and the ex-

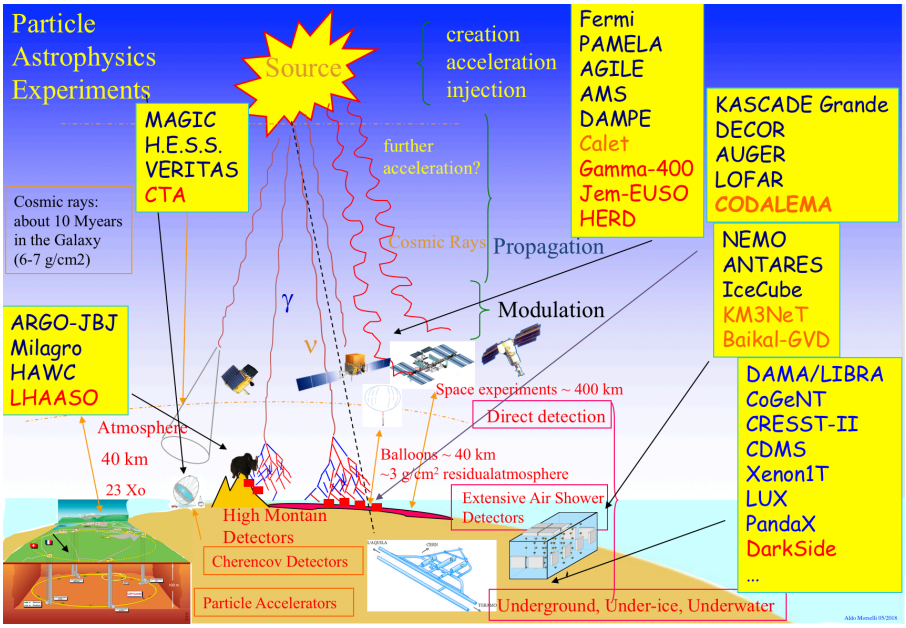

Figure 11: Indirect, direct and accelerator experiments for the study of the fundamental laws of nature and the search of dark matter (future experiments are in red).

treme physical environments that produce them, it is necessary to study non-thermal signatures that span many orders of magnitude in frequency in the broad-band spectral energy distribution (SED) of a given object. In the case of time-variable emission, such studies require simultaneous observations and/or alerts and triggers between observatories.

• Source properties: Information on the nature of gamma-ray emitting sources can be provided by MWL observations, enabling, for example, the object class, environmental conditions or the distance to be established. For this purpose, simultaneous observations are in general not required, except for the need to characterize transient sources, for example in the case of gamma-ray burst redshift measurements.

The need for (simultaneous) MWL and MM observations has been considered as a factor in the site selection process for CTA and in the preparations for CTA science. A summary timeline of major facilities is shown in Figure 10.

All these facilities will contribute together with all the indirect, direct and accelerator experiments to the study of the fundamental laws of nature and the search for dark matter in the sky, on-ground, in the water, in ice, underground and at accelerator machines, as shown in Figure 11 (future experiments are in red).

6 Acknowledgments

We gratefully acknowledge financial support from the agencies and organizations listed here: http://www.cta-observatory.org/consortium_acknowledgments.

References

1. B.S. Acharya et al., [CTA Consortium], Science with the Cherenkov Telescope Array, World Scientific, https://doi.org/10.1142/10986 [arXiv:1709.07997]

2. A.Morselli, The Dark Matter Programme of the Cherenkov Telescope Array, PoS(ICRC2017)921 [arXiv:1709.01483]

3. M.Ackermann et al., [Fermi Coll.], Searching for Dark Matter Annihilation from Milky Way Dwarf Spheroidal Galaxies with Six Years of Fermi-LAT Data, PRL 115, 231301 (2015) [arXiv:1503.02641]

4. P.A.R. Ade et al. [Planck Collaboration], Planck 2015 results. XIII. Cosmological parameters A&A 594, A13 (2016) [arXiv:1502.01589]

5. H. Abdallah et al., [H.E.S.S. Collaboration] (2017). Search for dark matter annihilations towards the inner Galactic halo from 10 years of observations with H.E.S.S., Phys. Rev. Lett. 117, 111301 [arXiv:1607.08142]

Frascati Physics Series Vol. 66 (2018)
Frontier Objects in Astrophysics and Particle Physics
May 20-26, 2018

THE PTOLEMY PROJECT: FROM AN IDEA TO A REAL EXPERIMENT FOR DETECTING COSMOLOGICAL RELIC NEUTRINOS

Marcello Messina
New York University Abu Dhabi
On behalf of the PTOLEMY project

Abstract

The PTOLEMY project aims at showing the feasibility to detect Cosmological Relic Neutrinos. The discussion on this topic, after a quick mention by S. Weinberg on 1962 about the principle [1)], was renewed in the paper [2)], where the speaker is among the authors. The paper gives a detailed treatment of the relic neutrino detection, based on the calculation of the neutrino interaction on beta unstable nuclei. The appearance of the cross sections evaluation, for the process under consideration, for the fist time in literature revitalized the discussion on the subject after many years of silence. The neutrino mass was included in the kinematic and this was crucial to conceive the idea of relic neutrino detection and more in general of neutrinos of vanishing energy. Subsequently, an experimental program has started to overcome the technological difficulties imposed by the physics topic, and the preliminary results of this program are reported in this paper.

1 Introduction

The Cosmic Neutrino Background (CNB) is the oldest relic particle originating from the Big Bang. It decoupled one second after the Universe was born, 350000 years before the well known Cosmic Microwave Background (CMB). As such the discovery of relic neutrinos and the measurement of their actual content in the present Universe are of outmost importance in every model that aims at describing the Universe evolution. The Universe has expanded by a factor of over one billion between the present-day and the early thermal epoch known as the neutrino decoupling. The CNB, produced in the epoch of neutrino decoupling, is a pillar of confirmation of the Universe evolution.

Experimental advances both in the understanding of massive neutrino physics and in techniques of high sensitivity instrumentation have opened up new opportunities to directly detect the CNB, an achievement which would profoundly confront and extend the sensitivity of precision cosmology data. Furthermore, the first picture of the Universe as it was one second after the start will be provided. This would be a constraint of unprecedented value to any cosmological model.

2 The PTOLEMY detection concept

The PTOLEMY detection concept is based on a process depicted in [2] where the interaction of relic neutrinos has been evaluated and the fundamental features of reaching a plateau value ([5], [6]) independently by the neutrino energy, when this approaches to zero, have been shown for the first time. It is worth pointing out the this is a common features of any exothermic reaction in which when the energy of the bullet particles vanishes the cross section diverges and the interaction rate (i.e. $\sigma \cdot v$) gets to a plateau value. This is the reason why in [2] $\sigma \cdot v$ is presented instead of the σ of the process.

In Fig. 2 the cross section of neutrino interaction on beta unstable elements, for the case of beta-minus and beta-plus unstable elements, are shown and the mentioned plateau value towards the region of very low neutrino energy can be seen. The two sets of interaction cross sections show that the neutrino and anti-neutrino feature the same capture process on the beta-minus and beta-plus decaying elements, respectively. The detailed kinematic calculation gave the possibility to point out what is depicted in Fig. 2 where the

process of neutrino capture of of vanishing kinetic energy produce a monochromatic electron with energy $2 \cdot m_\nu$ above the end-point of the Kurie spectrum of the unstable element under consideration.

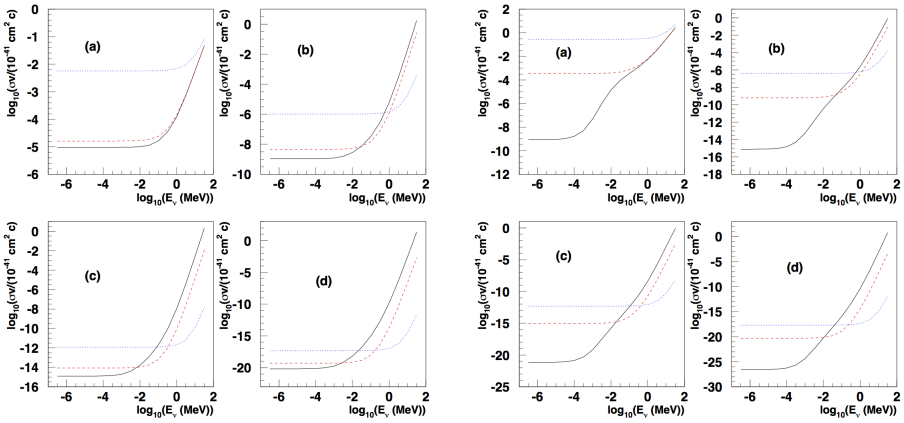

Figure 1: *The plot show the cross section on neutrino capture for nuclei undergoing different nuclear transitions for beta minus (left) and beta-plus (right) unstable elements. The labels a), b), c) ,d) correspond to the nuclear spin transition* $\Delta J = 0, 1, 2, 3$. *The three curves refer to different* Q_β*-values, solid line for* $Q_\beta = 10^{-3}$ MeV, *dashed line for* $Q_\beta = 10^{-1}$ MeV, *dotted line for* $Q_\beta = 10$ MeV. *Curves are for* $Z = 21$ *and nuclear radius given by* $R = 1.2A1/3$ *fm, where* $A = 2.5Z$

If the energy resolution (Δ) of a possible detection apparatus is good enough to disentangle the electron energy line-spectrum of relic neutrino interaction from the spectrum of the beta decay process, relic neutrino interactions can be unambiguously detected. The function reported in 1 gives the signal over background ratio. In this expression the key parameters are the neutrino temperature T_ν and the ratio $\frac{m_\nu}{\Delta}$.

$$\frac{S_\nu}{B_\beta(\Delta)} = \frac{9}{2}\zeta(3)\left(\frac{T_\nu}{\Delta}\right)^3 \frac{1}{(1+2m_\nu/\Delta)^{3/2}} \left(\frac{1}{\sqrt{2\pi}}\int_{2m_\nu/\Delta-1/2}^{2m_\nu/\Delta+1/2} e^{-x^2/2}dx\right)^{-1} \tag{1}$$

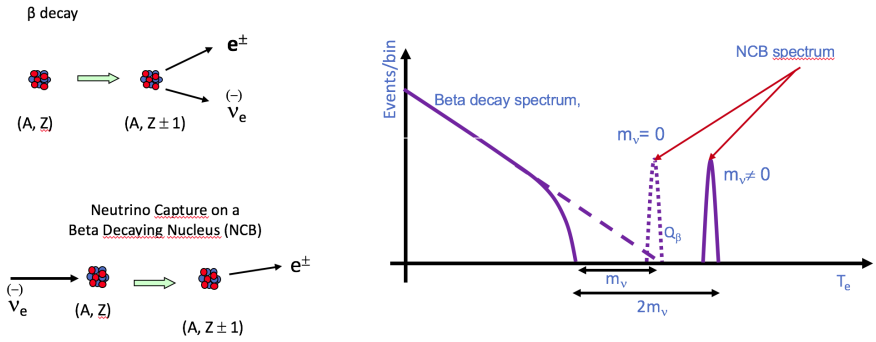

Figure 2: *(Left) The two competing processes, which share the same invariant amplitude, where the out-coming neutrino in the beta decay process is considered as incoming particle in the case of neutrino capture. (Right) The expected decay spectrum are depicted in the case of beta decay and neutrino capture.*

Thus, if a detector is capable to exploit enough target material and has the required energy resolution few events per year of relic neutrino interactions are expected. It is worth pointing out, as also underlined in [2], that the best target elements for this measurement are those with the largest value of $\tau_\beta \cdot (\sigma_{capture} v_\nu)$, so tritium comes out to be the most suitable when used in quantity on the mass scale of grams.

Tritium brings to our mind the KATRIN experiment [7] devoted to the direct neutrino mass measurement. Unfortunately, it exploits an amount of tritium, 100 μg, which results in a negligible number of expected relic neutrino interactions. The KATRIN detector is based on the technique of electrostatic filter, where electrons follow the field lines of a static B field with large gradient. This imposes that to increase the amount of tritium (i,e, grams), the volume must be increased proportionally, thus few 10^4 times larger volume which makes the KATRIN's technology not suitable for relic neutrino detection. The increase in volume is need not only to prevent inelastic scattering of tritium molecules, the pressure can not be as high as we like, but also by the fact that the electrons follow an adiabatic motion across field lines where the B flux must be conserved, i.e. $B \cdot S = const$. Thus if B decrees across particle

trajectory the surface on which the the field lines are spread out must increase proportionally. The need of the field decrease is imposed by the fact that the $F = \vec{\nabla} \cdot (\vec{\mu} \cdot \vec{B})$, where μ is the magnetic moment of the particle, straighten up the particle momentum on the the direction of the field lines. Once the straightening process has reached the desired precision, an electrostatic barrier can select the electrons of interest for the measurement, in this case those very close to the endpoint. Unfortunately, the KATRIN technology has several limitation factors such has the width (3 eV) of the tritium molecular bound which smears the electron energy and put an upper limit to the precision ($\sim$ 0.2 eV [7]) of the energy measurement. The responsible of that smearing are the rotational and vibrational modes of the molecule that can be excited when the electron is emitted.

The PTOLEMY project ([3]) aims at addressing all experimental limitations mentioned so far with a new beta-decay electron measurement technology. The first experimental feature that makes the detection principle presented in [2] feasable is the possibility to store the tritium atoms in a monoatomic layer of graphene. A tritium atom is covalently bounded to the graphene plane and in principle one atom of tritium per carbon atom can be stored. So far only a loading capability of 40% has been achieved [8] and R&D activities to improve this value are ongoing. The employment of graphene as support of tritium has a twofold advantage. The first one is to store large amount of tritium in surfaces of square meters (190 μg/m^2 in case of full loading) folded in sandwich structure with many layers. In this case the electron form beta decay or neutrino capture emerges from the monatomic layer without experiencing an inelastic scattering. A suited configuration of electric and magnetic fields must be studied in order to drive the electron towards the measuring point and avoid hitting any other layer of the graphene substrate.

The second key features of the tritium storage in a monoatomic graphene substrate is that the bound state has no degree of freedoms that can be activated thus the well in which the tritium atom is confined has negligible width. Those are topics addressed in the framework of theoretical chemistry and must be clarified with dedicated measurements. In the Letter of Intent to the Laboratori Nazionali del Gran Sasso (LNGS) [4] it is presented the whole R&D program needed prior to design of the PTOLEMY experiment.

Another important features that the PTOLEMY project aims at imple-

menting in its detector is the capability to pick up RF signal of an electron undergoing giro-motion in a given magnetic field. This idea, presented by the Project8 experiment [9], in the PTOLEMY case allows not only to realize a preliminary measurement of the electron energy but even more important gives a trigger that an electron in the relevant energy range is present. Subsequently, an electrostatic filter will allow only the interesting events to pass and reach the final measuring point. In Fig.3 all the steps mentioned so far are depicted even though in a preliminary way. In fact, the filtering process is shown to happen before the RF detection. Actually, a new filter concept has been recently

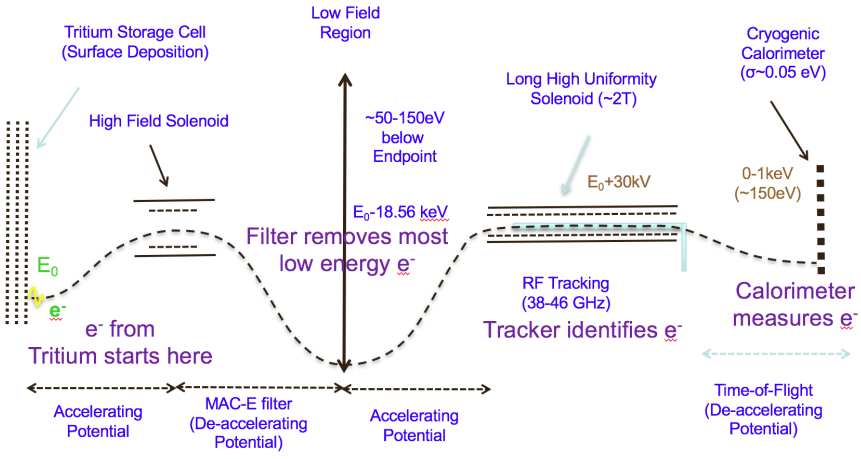

Figure 3: *The figure shows the conceptual steps of the measurement of a possible PTOLEMY detector.*

described in [10] and the paper is going through the publishing process. In this paper the electrostatic filter exploits the preliminary measurement from the RF antenna and instead of straightening the electron momentum across the field line, the momentum component transverse to the B field line is reduced by a known amount. In this way the limitation of the KATRIN filter concept are surpassed. The final energy measurement will be realized by a micro-calorimeter, actually a Transition-Edge-Sensor (TES) that given the low kinetic energy of

the electron can function as sensor and absorber, simultaneously. In Fig.3 the micro-calorimeter is positioned on the extreme right, after the filtering stage where the electron is also slowed down to a speed, i.e. kinetic energy, of few eV. This is needed to exploit the TES at the best of their performance given at the energy scale of few eV. The starting point for the development of the TES of the PTOLEMY project will be TES built and operated at the Italian National Institute of Metrology (INRiM, Turin, Italy) where an energy resolution of 0.12 eV FWHM has been achieved by measuring IR photons of 0.8 eV at 300 mK. In Fig. 4 the main results obtained at the INRiM are shown together with a photographs of the film of TiAu which a TES bulk is made of. The

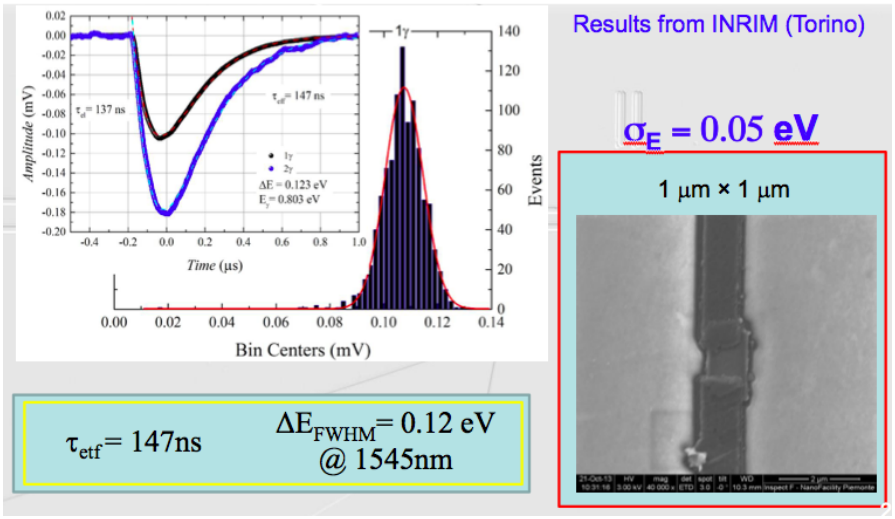

Figure 4: *(Left) Pulse shape and the histogram of events generated by IR photons of 0.8 eV energy. (Right) Photograms of the TiAu film which the TES is made of.*

results are also summarised in [11], [12].

3 Conclusions

To conclude what 10 years ago appeared to be impossible is presently much closer to be feasible even though challenging. A long R&D program is set to have the technology mature enough to be able to design a full size detector however, the steps are very clear.

References

1. Weinberg, Steven, Phys. Rev., **128**, 1457 (1962).
2. A.G. Cocco, G. Mangano and M. Messina, JCAP, **16**, 015 (2007).
3. S. Betts *et al*, Proceedings, Community Summer Study 2013: Snowmass on the Mississippi (CSS2013): Minneapolis, MN, USA, July 29-August 6, 2013, arXiv1307.4738 (2013).
4. E. Baracchini *et al*, arXiv1808.01892 (2018).
5. R. Lazauskas, P. Vogel, C. Volpe, J.Phys. **G35**, 025001 (2008).
6. L. D. Landau, E. M. Lifshitz, Quantum Mechanics: Non-Relativistic Theory, 3rd ed., Pergamon Press, Oxford (1977).
7. https://www.katrin.kit.edu/
8. Ehemann et al., Nanoscale Research Letters **7**, 198 (2012).
9. A. Ashtari Esfahani et al, J.Phys. **G44**, 054004 (2017).
10. M.G. Betti et al., arXiv:1810.06703.
11. L. Lolli et al., Appl. Phys. Lett., **103** (2013).
12. C. Portesi et al., IEEE Trans App. Supercond, **3**, 25 (2015).

Frascati Physics Series Vol. 66 (2018)
Frontier Objects in Astrophysics and Particle Physics
May 20-26, 2018

TESTING GRAVITY WITH THE MOON AND MARS

S. Dell'Agnello G. Delle Monache, L. Porcelli, L. Salvatori, M. Tibuzzi, C. Mondaini, R. Vittori, R. March, M. Muccino, O. Luongo, L. Ioppi
Nat. Inst. for Nuclear Physics-Frascati Nat. Labs (INFN-LNF) , Italy
D. Currie
University of Maryland (UMD) at College Park, MD, USA
G. Bianco, D. Dequal, C. Benedetto, F. Pasquali, R. Mugnuolo
Italian Space Agency-Space Geodesy Center (ASI-CGS), Matera, Italy
P. Villoresi, G. Vallone
INFN-Padua and Dep. Information Engineering (DEI), Univ. of Padua, Italy
J. Chandler
Harvard-Smithsonian Center for Astrophysics (CfA), Cambridge, MA, USA

Abstract

We present tests of fundamental relativistic gravity performed with solar systems experiments based on next-generation laser retroreflectors, lunar laser ranging and Mars surface missions.

1 Lunar Laser Ranging and Retroreflectors

There are laser retroreflectors on the Moon since 50 years ago (deployed in 1969 by Apollo 11 astronauts) and there were no laser retroreflectors on Mars, until the Italian *microreflectors* were recently deployed on Mars (next section). These instruments are positioned by time-of-flight measurements of short laser pulses (the so-called "laser ranging" technique) shot by ground stations of the International Laser Ranging Service (ILRS, see https://ilrs.gsfc.nasa.gov) or by orbiting spacecrafts equipped, for example, with laser altimeters (like NASA's

Lunar Reconnaissance Orbiter, LRO). Lunar laser ranging is performed by three currently acrive ILRS station: MLRO, the Matera Laser Ranging Observatory of the Italian Space Agency, the French station in Grasse and the US station, APOLLO (Apache Point Lunar Laser-ranging Operation). INFN-LNF and ASI-CGS work as a synergetic Joint Lab on laser retroreflectors, Satellite Laser Ranging (SLR), Lunar Laser Ranging (LLR) and their extension for Mars exploration and science. For 50 years LLR to Apollo/Lunokhod Cube Corner laser Retroreflector (CCR) arrays supplied accurate tests of General Relativity (GR) and new gravitational physics: possible changes of the gravitational constant $\dot{G}/G$, weak and strong equivalence principle, gravitational self-energy (Parametrized Post Newtonian parameter β), geodetic precession, inverse-square force-law [1) 2) 3)], spacetime torsion [4) 5)] and nonminimally couple gravity [6) 7)]. LLR has also provided significant information on the composition of the deep interior of the Moon, complementary to that of NASA's mission GRAIL (Gravity Recovery And Lunar Interior Laboratory). In fact, already in the later 1990s LLR first provided evidence of the existence of a fluid component of the deep lunar interior [1)], confirmed later by a re-analysis of Apollo lunar seismometry data in 2011 [8)]. Therefore, Apollo/Lunokhod CCRs form the first realization of a passive Lunar Geophysical Network (LGN) for lunar science, exploration and precisions tests of GR [9)]. For Moon missions we have developed two classes of next-generation CCR payloads: microreflectors of 25 gr mass for observation by orbiters and full-size payloads (order of kg mass) for direct LLR from Earth. In 1969 CCR arrays contributed a negligible fraction of the LLR error budget. Since laser station range accuracy improved by more than a factor 100, now, because of lunar librations, the Apollo/Lunokhod CCR payloads dominate the error due to their multi-CCR geometry and large geometric size. For direct LLR by ILRS, we developed a next-generation, single, large CCR, MoonLIGHT (Moon Laser Instrumentation for General relativity high-accuracy test) unaffected by librations that supports an improvement from a factor 10 up to a factor 100 of the space segment of the LLR accuracy (see [2)] for details). Performance testing of next-gen payloads with two specialized OGSE (Optical Ground Support Equiment) space facilities [10)] at INFN-LNF has been performed; for MoonLIGHT positive results are reported in [11)]. Lunar landing mission opportunities for our next-generation laser retroreflectors in the international context are described in [12)].

2 Laser Retroreflectors for the Mars Geophysical Network

There were no laser retroreflectors on Mars until the NASA InSight mission landed and started operating successfully on the surface of the red planet on Nov. 26, 2018 [13) 14)]. The ESA ExoMars Schiaparelli mission, which unfortunately failed Mars landing in 2016, was carrying a laser retroreflector like InSight [15)]. These instruments are positioned by laser ranging from Mars orbiters. The image of figure 1, taken in December 2018, shows LaRRI (Laser RetroReflector for InSight) on the lander deck in front of the camera calibration targets.

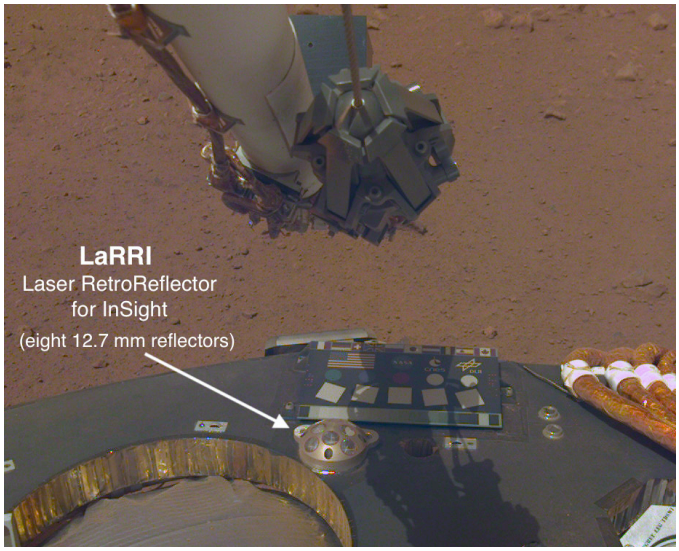

Figure 1: *LaRRI on InSight (December 2018).*

Starting from 2015 we initiated the delivery to ASI, ESA-ESTEC and NASA-JPL of several miniature laser retroreflector payloads (microreflectors) designed for Mars, Moon and other planetary missions. to be observed by orbiters capable of laser ranging measurements. Examples of the latter are the past Mars Global Surveyor (MGS), the currentLRO and similar future spacecrafts, like Hera (ESA's proposed mission to the Dydimos double asteroid, which is foreseen to carry a lidar/altimeter instrument onboard). The notional con-

cept of microreflectors for solar system exploration research (a pillar of the INFN-ASI Affiliation-Association to NASA-SSERVI, http://sservi.nasa.gov) is shown in figure 2 below. The goals of the microreflectors and their role as the

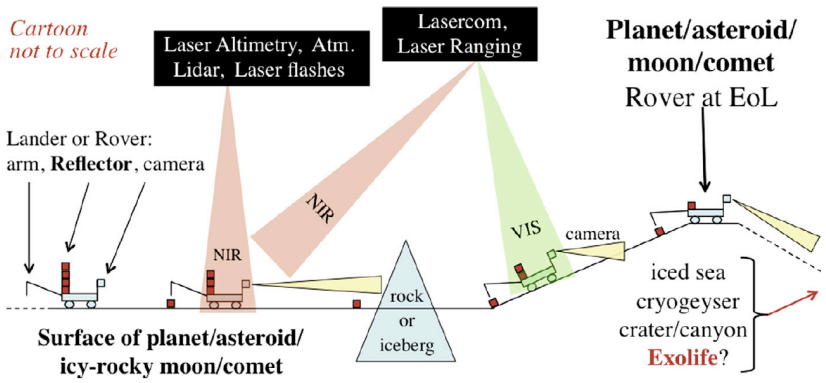

Figure 2: *Microreflectors for the solar system.*

passive, maintenance-free, long-lived instrument component of a future international Mars Geophysical Network (MGN) are described in [14) 15)]. InSight is the first, core node of such an MGN. Science and exploration applications of microreflectors include surface geodesy, geophysics (when combined with seismometers, heat flow probes, etc., like the instrument suites of InSight [13)] and Apollo[1] [16) 8)]) and the test of fundamental relativistic gravity.

To address the latter with Mars surface missions, we performed test physics simulations of the contribution of a 5-microreflector MGN to test General Relativity by means of the Planetary Ephemeris Program (PEP) developed by I. Shapiro et al (see for ex. [17)]). Under specific and conservative assumptions (described below) the contribution of this MGN is found to improve the measurements of $\dot{G}/G$ and of β (see table 1). γ is used as a control observable, by comparing its estimate with measurements by Cassini or the ESA missions GAIA (Global Astrometric Interferometer for Astrophysics) and BepiColombo (M. T. Crosta and L. Iess, these proceedings).

[1]EASEP, Early Apollo Scientific Experiment Package/Payload for Apollo 11 and ALSEP, Apollo Lunar Surface Experiments Package for Apollo 12-17.

Table 1: *Test of gravity with a laser retroreflector MGN (PEP simulations).*

Time/σ(CCR)	$\lvert\beta-1\rvert$ accuracy	$\lvert\gamma-1\rvert$ accuracy	$\dot{G}/G$ accuracy
10 years / 10 m	1.5×10^{-4}	7.0×10^{-4}	3.5×10^{-14}
10 years / 1 m	3.4×10^{-5}	1.4×10^{-5}	1.1×10^{-14}
10 years / 10 cm	7.1×10^{-7}	3.0×10^{-6}	2.6×10^{-15}
Accuracy now	$<1\times10^{-4}$	2.3×10^{-5}	9×10^{-13}
With data/mission	LLR/Messenger	Cassini	LLR

Table 1 is obtained under the following assumptions:

- Hypothetical MGN with coordinates: Phoenix (68N, 234E), Viking 1 (22N, 50W), Viking 2 (48N, 258W), Curiosity roving region (4S, 137E), Opportunity roving region (2S, 354E). This is a non-ideal MGN, since almost all nodes are in the northern hemisphere.

- One laser orbiter observation every 7 Sols. This takes into account weather conditions, although for example the visibility of Curiosity from MRO (Mars Reconnaissance Orbiter) is about once/Sol (source: NASA).

- $\sigma(CCR)$ is the positioning accuracy of the MGN node (the microreflector) on Mars. This is obtained by adding the Earth-Mars orbiter positioning by radio science, or with laser ranging/lasercom (*à la* LLCD, Lunar Laser Communications Demo, on NASA's LADEE, Lunar Atmosphere and Dust Environment Exploration) and the orbiter-reflector positioning by laser ranging/altimetry. The current accuracy of Mars ephemeris is 50-100 m (see [15] for a discussion).

This GR test with Mars will be complementary to (and with experimental errors independent of) the one performed [18] [2] with current large-size lunar laser retroreflectors (Apollo 11, 14, 15; Lunokhod 1, 2) observed by LLR.

For Mars (and Moon) missions we designed, built, qualified for surface missions, and delivered six microreflector payloads of 25 gr mass, each equipped with eight 0.5 inch (12.7 mm) diameter laser retroreflectors of fused silica:

- INRRI [15] (INstrument for landing-Roving laser Retroreflector Investigations) for ESA Schiaparelli 2016 [19] (delivered to ESA on September 2015 for integration by Thales Alenia Space - Italy)

- LaRRI [14) 22)] for NASA InSight 2018 (delivered to JPL on August 2017 for integration by Lockheed Martin Co.)
- INRRI for ESA ExoMars Rover 2020 [20)] (delivered to ESA-ESTEC on October 2018; the second identical spare is available at INFN for other international mission opportunities in the whole solar system; for example in partnership with ESA and NASA-SSERVI or with/for others)
- LaRA (Laser Retroreflector Array) for NASA Mars 2020 Rover [21)] (see figure 3; two flight models delivered to JPL in 2019; after Mars 2020 launch one will be returned to INFN for other mission opportunities).

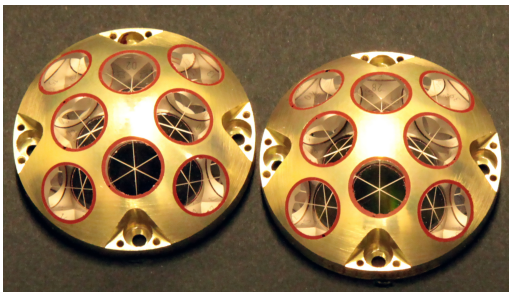

Figure 3: *The two LaRA flight models for Mars 2020.*

Prior to delivery the optical performance and thermal behavior of laser retroreflectors is characterized at the SCF_Lab [23)] of INFN-LNF in environmental conditions accurately representative of their deployment at their respective destinations. For LaRRI on InSight see [22)]. See [10)] for a detailed description of the general approach, OGSE equipment and test procedures and applications to LAGEOS (Laser GEOdynamics Satellite by NASA in 1976, LAGEOS-2 by ASI in 1993) and for CCR payloads for the GNSS (Global Navigations Satellite System constellations), like GPS, Galileo, IRNSS, the Indian Regional Navigation Satellite System). For Galileo see also [24) 25)]; for IRNSS see also [26)].

3 Acknowledgements

The INFN authors wish to thank the support of the INFN National Scientific Committee n. 2 on astroparticle physics research, through funding of the

MoonLIGHT-2 experiment. We also wish to thank ASI-NASA for the agreements signed on InSight and Mars 2020, and ASI-ESA for similar agreements on the ExoMars Schiaparelli and Rover missions.

References

1. J. G. Williams *et al*, Adv. Space Res. **37**(1), 67-71 (2006).
2. M. Martini and S. Dell'Agnello, in Springer DOI 10.1007/978-3-319-20224-2_5, R. Peron *et al* (eds.) (2016).
3. D. Currie, S. Dell'Agnello, G. Delle Monache, B. Behr, J. Williams, Nucl. Phys. **B** (Proc. Suppl.) 243-244 (2013) 218-228.
4. Constraining spacetime torsion with the Moon and Mercury, R. March, G. Bellettini, R. Tauraso, S. Dell'Agnello, R, Phys. Rev. D **83**, 104008 (2011).
5. R. March, G. Bellettini, R. Tauraso, S. Dell'Agnello, Constraining spacetime torsion with LAGEOS, Gen. Relativ. Gravit. (2011) **43**:3099-3126.
6. R. March, J. Pramos, O. Bertolami, S. Dell'Agnello, 1/c expansion of nonminimally coupled curvature-matter gravity models and constraints from planetary precession, Phys. Rev. **D** 95, 024017 (2017).
7. O. Bertolami, R. March, O, Pramos, Solar System constraints to nonminimally coupled gravity, Phys. Rev. D **88**, 064019 (2013).
8. R. Weber *et al* (2011) Sci. **331**, 309.
9. C. R. Neal *et al* (2019), The Lunar Geophysical Network Mission, 50^{th} LPSC (LPI Contrib. n. 2132).
10. S. Dell'Agnello et al., Adv. Space Res. **47**, 822-842 (2011).
11. E. Ciocci *et al*, Performance analysis of next-generation lunar laser retroreflectors, J. Adv. in Space Res. **60** (2017), 1300-1306.
12. S. Dell'Agnello. D. G. Currie et al (2019), The Return of Laser Retroreflectors to the Moon, Lunar Exploration Renaissance Conf., Brussels, Belgium.
13. W.B. Banerdt, C.T. Russell, Editorial on: Topical Collection on InSight Mission to Mars. Space Sci. Rev. **211**, 1-3 (2017).

14. S. Dell'Agnello, G. Delle Monache, *et al*, LaRRI: Laser Retro-Reflector for InSight Mars Lander, Space Research Today **200**, 25-32 (2017).

15. S. Dell'Agnello, G. Delle Monache, L. Porcelli *et al*, INRRI-EDM/2016: the first laser retroreflector on the surface of Mars. Adv. Space Res. **59**, 645-655 (2017), doi.org/10.1016/j.asr.2016.10.011.

16. J. G. Williams *et al* (2009), 16^{th} International Workshop on Laser Ranging.

17. I.I. Shapiro, R.D. Reasenberg, J.F. Chandler and R.W. Babcock, Measurement of the de Sitter precession of the Moon: A relativistic three-body effect, Phys. Rev. Lett., **61**, 2643-2646 (1988).

18. J.G. Williams, S.G. Turyshev and D.H. Boggs, Progress in Lunar Laser Ranging Tests of Relativistic Gravity, Phys. Rev. Lett. **93**, 261101 (2004).

19. Baldwin, E., Clark, S., Scuka, D. *et al*, March 2016. Europe's new era of Mars exploration, ESA, SCI-A-COEG-2016-001.

20. J. Vago *et al*, Habitability on Early Mars and the Search for Biosignatures with the ExoMars Rover, Astrobiology, Volume **17**, N. 6 and 7 (2017).

21. K.H. Williford *et al*, Chapter 11: The NASA Mars 2020 Rover Mission and the Search for Extraterrestrial Life, From Habitability to Life on Mars, 275-308 (2018), doi.org/10.1016/B978-0-12-809935-3.00010-4.

22. L. Porcelli, M. Tibuzzi, C. Mondaini *et al*, Optical-Performance Testing of the Laser RetroReflector for InSight, Space Sci Rev (2019) **215**:1.

23. Http://www.lnf.infn.it/esperimenti/etrusco/.

24. S. Dell'Agnello *et al*, ESA Proc. of the "3^{rd} Intern. Colloquium on Scientific and Fundamental Aspects of Galileo", Copenhagen, Denmark (2011).

25. S. Dell'Agnello *et al*, Thermo-optical vacuum testing of Galileo In-Orbit Validation laser retroreflectors, J. Adv. in Space Res. **57** (2016) 2347-2358.

26. S. Dell'Agnello *et al*, Thermo-optical vacuum testing of IRNSS laser retroreflector array qualification model, J. Adv. in Space Res. **60** (2017) 1054-1061.

Frascati Physics Series Vol. 66 (2018)
Frontier Objects in Astrophysics and Particle Physics
May 20-26, 2018

Testing Gravity with Gaia

Mariateresa Crosta
INAF-OATo, Astrophysical Observatory of Turin, Pino Torinese 10125

Abstract

On April 25th (2018) the second release of the Gaia catalogue (DR2) became available to the scientific community worldwide. It contains the five-parameter astrometric solution (positions on the sky, parallaxes, and annual proper motions) for more than 1.3 billion sources, within the Gaia magnitude range $3 < G < 20.7$, and median radial velocities for more than 7.2 million stars. Uncertainties of the DR2 astrometry are still too high to detect clearly the varying relativistic effects associated with the received null geodesic from within the multi-gravitational fields of the Solar System. However, a method of differential astrometry applied to the individual observations appears capable of spotting the complex light deflection by Jupiter; and this technique could be extended to consider passing gravitational waves that affect photon propagation.

Moreover, the independent astrometric solution underway at the Italian data processing center in Turin (DPCT), for verification purposes, is based on a high-accuracy general relativistic treatment of the data that implements, in

a sophisticated high-performance computing infrastructure, theoretical models for the observables and the observer.

This implies that the five-parameter global astrometric solution, made available with each release of the Gaia catalog, must be understood as providing relativistic kinematics demanding in turn, at least for consistency, a relativistic representation of the Galaxy's dynamics.

1 Introduction

The extraordinary advancement in astronomical observations and instrumentation brought about by Gaia requires coding light propagation, i.e. null geodesic, at an unprecedented level of precision. Gaia-like measurements, in fact, need to take into account the ever present and ever changing overlapping local gravitational fields in which the observer is embedded to the accuracy level required by the measurements, i.e., whenever these are comparable to the local curvature (even if weak) due to the gravity source or background geometry. Once the observer is properly defined, null geodesics represent the real physical link through space-time up to the star. As far as Gaia is concerned, this has been renamed as "Relativistic Astrometry" providing, already at the micro-arcsecond level (μas), a fully general-relativistic analysis of the inverse ray-tracing problem, from the observational data (e.g., stellar images on a digital detector) back to the position of the light-emitting star [1)] (Crosta et al. and references therein).

Gaia is already delivering [2, 3)] a huge amount of spectroscopic, photometric and, most importantly, astrometric data of unprecedented quality (to 100 μ as for brighter stars), and much more is to come till the final release (to 25 μas for brigther stars).

In summary DR2 contains: median radial velocities (i.e. the median value over the observation epochs) for more than 7.2 million stars with a mean G magnitude between 4 and 13; G magnitudes for more than 1.69 billion sources, with precisions varying from around 1 milli-mag at the bright (G<13) end to around 20 milli-mag at G=20; GBP (blu) and GRP (red) magnitudes for more than 1.38 billion sources, with precisions varying from a few milli-mag to around 200 milli-mag at G=20; epoch astrometry for 14,099 known solar system objects based on more than 1.5 million CCD observations; about 87 million sources with line-of-sight extinction AG and reddening E(BP-RP); for

a part of this last subset (around 76 million sources) luminosity and radius as well; finally, classifications for more than 550,000 variable sources consisting of Cepheids, RR Lyrae, Mira. Details can be read on the ESA web portal dedicated to the mission [4].

Nonetheless, all the goals of Gaia will not be achieved without the correct characterization and exploitation of the relativistic astrometric data.

Nowadays, our modeling of the Universe depends critically on our understanding of gravity; despite the fact General Relativity (GR) is the standard theory of gravity, deviations from GR could profoundly impact our conclusions on the best theory suitable to explain the "dark" ingredients that make up the Universe. On the other hand, experimental verifications of the GR weak effects are difficult, but could be as fundamental and complementary as any other observations that test manifestly the validity of Einstein's field equations, which underpin strong gravity. The recent LIGO observations of a merging binary black hole (Abott et al. 2016 [5]) further strengthen the confidence in GR in the strong-field regime; however, tests of GR in the weak-field regime remain very difficult on astronomical scales.

Gaia-like missions are offering the unique possibility of being a multi laboratory for extensively testing weak gravitational fields at local (Solar System) and more distant (MIlky Way) scales. In particular, the potential of Gaia is to probe the validity of GR by testing: i) PPN parameters and possibly new tiny relativistic effects on the light deflection due to the Solar System bodies; ii) the structure of our Galaxy as a product of the cosmological evolution shaped by gravity (Local Cosmology), namely the relations among baryonic structures (and their evolution) and the dark components of the Universe.

2 Solar System tests

While GR is currently the preferred theory of gravity, indeed any subtle deviations from GR should be predicted in experiments and the solar system represents the most natural arena to carry out such tests. For any alternative theory of gravity should present at least the same predictions of GR in the Solar System.

The first independent verification of GR in the solar system was made by Dyson, Eddington, and Davidson during the solar eclipse of 1919 to verify Einstein's General Relativity prediction of a 1.75" astrometric deflection of

light by the Sun. However, Eddington-like measurements of light deflection by the Sun during eclipses remain with large uncertainty; the best constraint to date is about 20%. Nearly a century later, astrometry remains one of the most fundamental and sensitive methods to test the validity of GR in the weak-field regime. The Gaia global astrometry will provide a massive repetition of the Eddington astrometric test of GR with 21st century technology, and this thanks to a combination of analytical and numerical relativistic methods [1]. As the systematic errors in DR2 [3] are still relatively large, the expectation is to estimate a deviation, from the GR predicted value of 1, for the PPN γ at the level of 10^{-6} when final calibrations after DR3: at the end of the mission astrometric accuracies are expected to be better than 5-10as for the brighter stars and 130-600μas for fainter targets.

Given the absolute character of such releases of the Gaia catalogs, the Consortium constituted by ESA for the Gaia data reduction (DPAC) agreed to set up two independent astrometric sphere solutions: AGIS and GSR. Beside the determination of the most fundamental PPN parameter, which enters as unknown the global reduction process, the Gaia observable relies on completely different relativistic observation equations and least-squares solution methods, namely AGIS, adopted as the baseline, that uses the GREM relativistic model, and GSR that is based on the RAMOD modeling of GR. This in itself represents a powerful test of General Relativity thanks to the billions of observation equations delivered by Gaia. Any discrepancy between the relativistic models, if it can not be attributed to errors of different nature, will mean either a limit in the modeling/interpretation - that a correct application of GR should fix, therefore validating GR - or provide a new stringent limit on GR validity.

Focusing on RAMOD, the fundamental step toward the realization of the Gaia catalogue is the global astrometric sphere reconstruction (GSR), which determines the celestial reference frame using the observations of a selected subset of up to 100 million stars (primary sources), among those observed by Gaia, in order to validate the baseline method adopted for Gaia. Recent blind simulations show that GSR works as expected in the range of accuracy required for Gaia [6]. In order to make the comparison useful, the largest degree of independence between the two solutions had to be guaranteed. Basically AGIS and GSR present: independent relativistic astrometric model; independent relativistic attitude model; independent (iterative) least-squares solution method

(all-unknowns solved).

Observations from global astrometry can be used also to create small stellar reference frames against which tiny relativistic light deflection effects due to a single source can be tested.

Thanks to the multiple observations over a few consecutive scans and the appropriate statistical analysis of the local coordinates on the two Gaia fields of view (FOVs), differential astrometry is used to adjust all the frames to a common frame by means of translations, rotations and possible distortion terms if necessary [7]. The first application has been the detection of the apparent shift in the position of bright stars during their near-occultation by Jupiter to test light deflection due to both the monopole and the quadrupole (never measured before, i.e. the oblateness of the planet). Jupiter offers an optimal target for second order light deflection experiments, thanks to its precisely known mass, relatively large deflection, and the ability to observe a target very close to the limb without the difficulties posed by the Sun. For Jupiter the magnitude of the monopole deflection for a grazing ray is $\sim$16 milli-arcsecond (mas), to which a component from the quadrupole moment is superimposed with an amplitude of $\sim 240\mu$as (Crosta and Mignard, 2006).

On the same subject we have a multi-epoch, multi-orbit HST proposal (PI S. Casertano, STScI). Therefore, this study is accomplished by comparing the performances expected, respectively, with Gaia and WFC3 on the Hubble Space Telescope, in spatial scan mode. The actual GAREQ (for GAia Relativistic Experiment on Quadrupole) experiment was carried out by the satellite on February 22th, 2017 and by HST on April, 6, 2017.

Gaia's spin axis orientation was optimized to catch a star close to the limb of Jupiter in 2017. Actually, the initial spin phase axis orientation was decided in 2014 to maximize the measurement success and on 8 Feb 2017. At the beginning of 2017, and towards the end of February 2017, Gaia provided measurements for 31 bright reference stars (G <13 mag) all lying within a field of 0.8×1.3 degree surrounding the target star (G= 12.68 mag). The target star was seen a total of 26 times over a 2-month period out of which we use 15 transits over a time interval of a couple of days surrounding the observation at closest approach.

Both observation epochs were executed successfully and are under reduction (Abbas et al. 2017 [9]). Results are still embargoed and will be published

as soon as possible.

Moreover, the GAREQ experiment provides an important science case and a conspicuous potential for assessing the health of the main astrometric payload during the mission. The operational importance resides in the fact that, thanks to the precise predictions of GR, we can compare the reconstructions of the relativistic deflections done with the Gaia observations to absolute numbers providing the means for accurate external tests on the satellite actual astrometric performances.

The differential astrometry technique can be utilized also to detect astrometric shifts on the light-of-sight over small stellar fields due to passing gravitational waves. The critical aspect in this case is the implementation of an appropriate retrieval and calibration procedure at DPCT, which is on-going.

3 Milky Way tests

The Milky Way (MW) is the product of the cosmological evolution at z=0. In the field of Local Cosmology, Gaia can provide tests on galactic models for their comparison with ΛCDM predictions.

The purpose is to check if it is worth pursuing a GR coherent phase-space picture of the MW against which theories, simulations, predicting dark matter components or possible deviations from GR (and not only from Newtonian or Keplerian mechanics) can be tested. Given the relativistic reduction process for the Gaia data, for the sake of consistency, a weakly relativistic scenario should be considered while dealing with the application of Gaia's data to test GR.

Gaia directly measures the kinematics of the stellar component of the MW. Provided that the Galaxy is not a point source but an extended source, the first attempt is to apply the relativistic kinematics delivered by Gaia to trace the MW rotation curves without any a priori assumption on the origin of its observed flatness at large radii from the galactic center, which is actually explained as a deviation from the Newtonian velocity profile possibly because of the presence of dark matter or of a modified gravity law (see MOND for example).

The Ansatz to be tested assumes an axially symmetric, stationary and asymptotically flat Galaxy-scale metric and, in parallel, the mass inside a large portion of the Galaxy, far away from the central bulk, can be simplified as a

pressure-less perfect fluid (i.e. "dust" for GR) avoiding the bulge where resides the axis of symmetry. Although a pressureless fluid is not a pure vacuum, however it may be considered an approximation very close to a low energy density regime. A co-rotating dust is defined to be a continuous distribution of matter with stress-energy tensor $T_{\alpha\beta}$ in the form of (in geometrizied units): $T_{\alpha\beta} = \rho u^{\alpha} u^{\beta}$, where the time-like vector field u^{α} represents the 4-velocity of the co-rotating fluid proportional to the killing vector k^{α} (namely a static observer), which in virtue of the definition of $T_{\alpha\beta}$, and in the limit of small density (ρ) results geodetic. The considerations above constitute the basis of the metric solution found by Balasin and Grumiller (BG) [10] in order to trace the velocity profiles for galactic curves in a weakly relativistic scenario. As argued by these authors, those assumptions simplify the dynamics to be solved as compared to the vacuum case.

Solving the nonlinear partial differential equations from Einstein's field equation, and by removing all the unphysical values which could violate the weak energy condition, the singularity along the axis at the center of the Galaxy, and the assumption of vanishing pressure, the functional expression for the BG velocity profile results (with z=0, on the galactic plane)

$$V_{\phi}^{BG}(R) = \frac{V_0}{r}\left(R_{out} - r_{in} + \sqrt{r_{in}^2 + R^2} - \sqrt{R_{out}^2 + R^2}\right) \qquad (1)$$

where the three parameters V_0, R_{out}, r_{in} have been chosen respectively as the flat regime velocity, the maximum extension of the Galaxy, and to the bulge size, i.e the parameters that define the upper and lower radial validity limits of the model.

The study of the rotation curve profile of our Galaxy requires the selection of the most suitable stellar tracers of the bulk circular velocity around the galactic center, i.e., of early type stars like, e.g. OB stars. To this end, we selected DR2 sources according to the requirements for a proper 6-dimensional reconstruction of the phase-space location occupied by each individual star as derived by the same observer, namely: (i) availability of the complete astrometric set, and of its corresponding error (covariance) matrix; (ii) availability of the Gaia-measured velocity along the line of sight, RV, and its error; (iii) parallaxes good to 20%, i.e., $p/\sigma_p \geq 5$; (iv) avalaibility of a cross-matched entry in the 2MASS catalog for the materialization of the sample [11].

The BG fit to the MW rotational data has been compared with well-

studied classical models for the MW (MWC), which is comprised of a bulge, a stellar disk and a Navarro-Frenk-White (NFW) dark matter (DM) halo.

To quantitatively asses this, a Monte Carlo Markov Chain (MCMC) analysis was done and compared the results for the two models. For the likelihood analysis the BG and MWC models appear almost identically consistent with the data (see [11]). For the MWC model, the estimated parameters are, within the errors, compatible with the very latest literature values. This is important in itself, proving that the 11 kpc range in (galactocentric) cylindrical radius covered by our DR2 sample of disk stars is sufficiently large already for the task.

As for the BG model, we obtain the important result on the lower limit parameter r_{in}, which is estimated below 1 kpc confirming *a posteriori*, the hypothesis of validity the BG model. In fact, inward of $R \sim 1$ kpc it would not be possible to neglect the z-dependence of velocity due to the presence of the MW bulge.

As for the local baryonic matter density, estimated via the 00-term of then Einstein field equation, we obtain $\rho_{\odot}(R = R_{\odot}, z = 0) = 0.088 \pm 0.005 M_{\odot} pc^{-3}$ that is perfectly in line with current estimates. Then, it appears that no extra-mass is required for the GR rotational curve!

Details on this study are under publication. References and full text are available in Crosta et al. [11].

4 Conclusion

Gaia-like missions are offering the unique possibility of being a multi laboratory for extensively testing weak gravitational fields both at the Solar System and Milky Way scales. Much more will be expected after DR3.

While after the first detections of GWs many efforts are concentrated on the strong field sources, the large amount of highly precise data from Gaia offers also the unique opportunity to test "complementary" weak gravitational regime and the subtle nonlinear effects as provided by the Einstein equation itself.

To trace light trajectories back to the emitting stars requires an appropriate treatment of local gravity and a relativistic definition of the observable, according to the measurement protocol of GR. Individual distances, phase-space stellar distributions can be achieved only from *in situ* investigations, i.e.

from within the local universe: the μas accuracy is not enough to probe directly Mpc scale, the nanoarcsecond regime will be needed, which comprises also the detection of GWs due to binary sources.

After Gaia, null geodesics should be as fundamental in astrophysics as the equations of stellar evolution.

5 Acknowledgements

The works described have made use of data from the European Space Agency (ESA) mission Gaia [12], processed by the Gaia Data Processing and Analysis Consortium (DPAC, https://www.cosmos.esa.int/web/gaia/dpac/consortium).

Funding for the DPAC has been provided by national institutions, in particular those participating in the Gaia Multilateral Agreement. As one of such institutions, the author is indebted to the Italian Space Agency (ASI) for their continuing support through contract 2014-025-R.1.2015 to INAF.

References

1. M. Crosta, A. Geralico, M. G. Lattanzi, A. Vecchiato, Phys. Rev. D. **96**, 104030 (2017).

2. Gaia Collaboration, T. Prusti, J. H. J. de Bruijne, A. G. A. Brown, A. Vallenari, C. Babusiaux, C. A. L. Bailer-Jones, U. Bastian, M. Biermann, D. W. Evans and *et al.*, The Gaia mission. A&A **595**, pp. A1. (2016).

3. Gaia Collaboration, A. G. A. Brown, A. Vallenari, T. Prusti, J. H. J. de Bruijne, C. Babusiaux, C. A. L. Bailer-Jones and *et al.*, Gaia Data Release 2. Summary of the contents and survey properties. A&A **616**, pp. A1. (2018).

4. https://www.cosmos.esa.int/web/gaia/dr2.

5. B. Abbott and *et al.* (the LIGO Scientific Collaboration), Phys. Rev. D **72**, 042002 (2015).

6. A. Vecchiato, M.G. Lattanzi, B. Bucciarelli and *et al.*, GAIA-C3-TN-INAF-AVE-027-01 (2017).

7. U. Abbas, B. Bucciarelli, M.G. Lattanzi and *et al.*, PASP **129**, 054503 (2017).

8. M. Crosta and F. Mignard, Class.Quantum Grav. **23**, 4853 (2006).

9. U. Abbas, B. Bucciarelli, M. Crosta, M.G. Lattanzi, D. Busonero *et al.*, GAIA-C3-TN-INAF-UA-005-0 (2017).

10. H. Balasin and D. Grumiller, Int. Journal of Mod. Phys. D **17**, 475 (2008).

11. M. Crosta, M. Giammaria, M.G. Lattanzi, and E. Poggio, http://arxiv.org/abs/1810.04445 (2018).

12. https://www.cosmos.esa.int/gaia.

Frascati Physics Series Vol. 66 (2018)
Frontier Objects in Astrophysics and Particle Physics
May 20-26, 2018

DARK SECTORS AT FIXED TARGETS: THE EXAMPLE OF NA62

Babette Döbrich*
CERN, 1211 Geneva 23, Switzerland

*On behalf of the NA62 Collaboration: R. Aliberti, F. Ambrosino, R. Ammendola, B. Angelucci, A. Antonelli, G. Anzivino, R. Arcidiacono, M. Barbanera, A. Biagioni, L. Bician, C. Biino, A. Bizzeti, T. Blazek, B. Bloch-Devaux, V. Bonaiuto, M. Boretto, M. Bragadireanu, D. Britton, F. Brizioli, M.B. Brunetti, D. Bryman, F. Bucci, T. Capussela, A. Ceccucci, P. Cenci, V. Cerny, C. Cerri, B. Checcucci, A. Conovaloff, P. Cooper, E. Cortina Gil, M. Corvino, F. Costantini, A. Cotta Ramusino, D. Coward, G. D'Agostini, J. Dainton, P. Dalpiaz, H. Danielsson, N. De Simone, D. Di Filippo, L. Di Lella, N. Doble, B. Dobrich, F. Duval, V. Duk, J. Engelfried, T. Enik, N. Estrada-Tristan, V. Falaleev, R. Fantechi, V. Fascianelli, L. Federici, S. Fedotov, A. Filippi, M. Fiorini, J. Fry, J. Fu, A. Fucci, L. Fulton, E. Gamberini, L. Gatignon, G. Georgiev, S. Ghinescu, A. Gianoli, M. Giorgi, S. Giudici, F. Gonnella, E. Goudzovski, C. Graham, R. Guida, E. Gushchin, F. Hahn, H. Heath, T. Husek, O. Hutanu, D. Hutchcroft, L. Iacobuzio, E. Iacopini, E. Imbergamo, B. Jenninger, K. Kampf, V. Kekelidze, S. Kholodenko, G. Khoriauli, A. Khotyantsev, A. Kleimenova, A. Korotkova, M. Koval, V. Kozhuharov,

Abstract

If new physics manifests itself in the existence of very weakly coupled particles of MeV-GeV mass-scale, fixed-target experiments can be an excellent instrument to discover it. In these proceedings, we review especially the sensitivity of the NA62 experiment to this physics scenario.

1 Weakly coupled particles at fixed target set-ups

Albeit we can describe our findings about elementary particles and their interactions to an incredible precision in the 'Standard Model of particle physics' (SM), it is clear that the particle content therein is likely not complete. One of the most blatant evidence for our insufficient knowledge is: we do not know what Dark Matter (DM) particles (constituting $\sim$80% of all matter) are. Exploration of the existence of particles at high energies (masses) is and will be performed, e.g., by the LHC. However, new particles might also be found at much lower energy scales but interaction strengths which are very tiny. If such particles exist, their feeble coupling would make them comparably long-lived and thus they could escape strong constraints from searches with colliders.

To search such long-lived particles, independently of whether they explain DM, a number existing and proposed fixed-target/beam-dump experiments

Z. Kucerova, Y. Kudenko, J. Kunze, V. Kurochka, V.Kurshetsov, G. Lanfranchi, G. Lamanna, G. Latino, P. Laycock, C. Lazzeroni, M. Lenti, G. Lehmann Miotto, E. Leonardi, P. Lichard, L. Litov, R. Lollini, D. Lomidze, A. Lonardo, P. Lubrano, M. Lupi, N. Lurkin, D. Madigozhin, I. Mannelli, G. Mannocchi, A. Mapelli, F. Marchetto, R. Marchevski, S. Martellotti, P. Massarotti, K. Massri, E. Maurice, M. Medvedeva, A. Mefodev, E. Menichetti, E. Migliore, E. Minucci, M. Mirra, M. Misheva, N. Molokanova, M. Moulson, S. Movchan, M. Napolitano, I. Neri, F. Newson, A. Norton, M. Noy, T. Numao, V. Obraztsov, A. Ostankov, S. Padolski, R. Page, V. Palladino, C. Parkinson, E. Pedreschi, M. Pepe, M. Perrin-Terrin, L. Peruzzo, P. Petrov, F. Petrucci, R. Piandani, M. Piccini, J. Pinzino, I. Polenkevich, L. Pontisso, Yu. Potrebenikov, D. Protopopescu, M. Raggi, A. Romano, P. Rubin, G. Ruggiero, V. Ryjov, A. Salamon, C. Santoni, G. Saracino, F. Sargeni, V. Semenov, A. Sergi, A. Shaikhiev, S. Shkarovskiy, D. Soldi, V. Sougonyaev, M. Sozzi, T. Spadaro, F. Spinella, A. Sturgess, J. Swallow, S. Trilov, P. Valente, B. Velghe, S. Venditti, P. Vicini, R. Volpe, M. Vormstein, H. Wahl, R. Wanke, B. Wrona, O. Yushchenko, M. Zamkovsky, A. Zinchenko

have set up corresponding programs. Amongst the ones that exploit a high-energy proton beam as primary beam are the proposed SHiP experiment, as well as running experiments SeaQuest at Fermilab and NA62 at CERN [1]. Results and prospects of the latter will be subject of this article, albeit some of our plots of Sect. 4 also include prospects for other experiments. Comprehensive projections for Seaquest can be found in [2] and for SHiP in [3].

In general, a primary beam of protons, electrons or even muons is used to produce such long-lived particles of a 'dark' or 'hidden' sector, which is motivated by different BSM physics, e.g. [4, 5, 6]. Typically, a higher primary beam energy is favored to achieve sizable production cross-sections. The experiment geometry then systematically shapes the accessible parameter space in the coupling-mass plane as it 'selects' the longevity of the particles that can be searched for. Importantly, the number of primary particles correlates with the feebleness of particles that can be probed.

If the exotic particles are stable and thus invisible for the experiment due to their small coupling, they could be found by missing-mass or missing energy techniques. Examples of such searches at NA62 are presented in sect. 3.

If the new particles decay, their final states will guide us in pin-pointing the new responsible interaction, see examples in sect. 4.

2 NA62 at CERN's SPS

The NA62 experiment aims at a precise measurement of the rare decay $K^+ \to \pi^+ \nu\bar{\nu}$. As the SM branching ratio of this decay is extremely small [7] $\mathcal{O}(10^{-10})$, the experiment is equipped with a hermetic detector system, cf. fig. 1. In addition, the experiment achieves a $\mathcal{O}(100)$ps timing resolution.

The SPS primary 400 GeV proton beam interacting in an upstream beryllium target (at 0m in fig. 1) produces a 75 GeV unseparated secondary beam (containing around 6 % Kaons) for NA62, selected by an achromat around 23m downstream the target. This beam is guided through a beamline into the experimental hall, with the first detector (KTAG) located at around 70 m.

Two trackers: The GTK (Si-pixel), and the STRAWs allow to determine the 3-momentum of the incident particles and their decay products, respectively. The GTK data is matched with the KTAG (differential Cerenkov counter) to obtain the full Kaon 4-momentum. The CHANTI station provides protection by vetoing inelastic interactions of the 75 GeV beam in the third

GTK tracker-station. A RICH positively identifies secondary charged pions. Further Hadron ID is provided by the calorimeters MUV1 and MUV2 . To veto unwanted decay modes, Muon ID is provided by the MUV3 plastic scintillator detector, placed after an iron absorber. Finally, photons can be vetoed at small angles by the IRC and SAC, at intermediate angles by the liquid krypton calorimeter (LKr) and, at large angles, by the lead-glass large-angle-veto (LAV) calorimeters.

First results of the analysis of the 2016 data set w.r.t. the decay $K^+ \to \pi^+\nu\bar{\nu}$ are presented at this conference [8]. After a commissioning phase, NA62 is taking quality data towards this measurement since 2016 and the current run of NA62 continues until the end of 2018, that is the end of 'Run 2'. NA62 then pauses with the pause of the CERN accelerator infrastructure. Restart of the experiment is expected in 2021 for 'Run3'.

To understand NA62's capability for Exotics searches, it is helpful to once again consider experiment and beamline shown in Fig. 1.

Besides magnets, the 'achromat' near 23m in the Fig. 1 comprises two move-able, $\sim$ 1.6m long blocks with a set of holes allowing passage of the narrow beam and allowing adjusting its intensity. These blocks are also dubbed 'Target Attenuator eXperimental areas': TAXes.

During data-taking in the configuration with the beryllium target in place (i.e. when the Kaon beam reaches the NA62 decay volume), a sizable fraction ($\sim$ 40 %) of the protons pass through the target without interaction. Thus these impinge on the front, copper-part of the TAXes. These protons are de-facto 'dumped' and can be the source of so-far undiscovered, weakly-interacting particles.

For this reason, during standard data-taking a number of parasitic trigger-lines have been implemented which might help to detect the presence of new particles. For example, an 'exotic' multi-track trigger has been employed during 2017 data-taking, built to trigger on events that did not originate from a Kaon decay. This exotic trigger runs in parallel with a number of triggers optimized for Kaon decays, notably $K^+ \to \pi^+\nu\bar{\nu}$.

To foster the production of weakly interacting, novel particles from dumped protons, NA62 can be run in 'pure' beam dump-mode by 'closing' the up-stream collimators and removing the beryllium target. 'Closing the collimators/TAXes' means that these are moved into a position that completely blocks

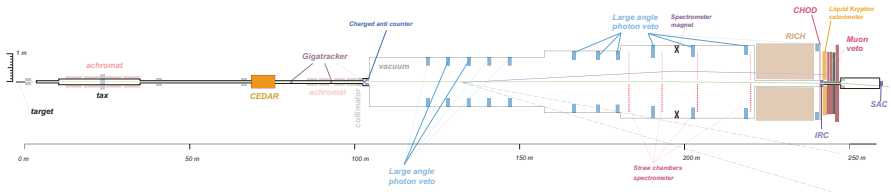

Figure 1: *Layout of NA62. See* [1] *for details on the detector. For closed-collimator runs the proton beam is dumped at* $\sim$ *23m (w.r.t. to the nominal target position at 0m, relevant in Kaon-mode).*

the primary SPS proton beam. Followingly, in 2016 and continuing in 2017, the experiment has started to take data samples in this 'pure' dump-mode to assess its capability and do first analyses for Dark Sector particles. The statistics here is on the order of $\mathcal{O}(10^{16})$ POT.

In summary, NA62 can search for hypothetical, very weakly-interacting particles, and thus illuminate the Dark Sector in at least three ways:

1. Meson decays: New Physics Particles can be produced in decays of the Kaon (see examples in sect. 3)

2. Parasitic dump production: In '$\pi^+\nu\bar{\nu}$' data taking, exotic particles can be produced by proton interactions far upstream the decay volume. This might be by direct interactions of the primary particle in a target material or in the decay of secondaries. Weakly interacting new-physics particles can travel interaction-less up to the decay volume. If they decay away from the main beam-line they can be found and recorded by the use of dedicated trigger lines, running parasitically to the trigger line for the main Kaon analysis (see examples in sect. 4)

3. Dedicated dump runs: To suppress backgrounds, NA62 can be run as 'proton dump experiment', making it even more sensitive any particle of appropriate life-time potentially produced in upstream proton interactions. (see examples in sect. 4)

3 NA62 results for exotics from Kaon decays

Let us first review some results and prospects of searches for exotic particles in NA62 from Kaon decays.

3.1 Invisibly decaying Dark Photons

The decay chain $K^+ \to \pi^+ + \pi^0$, with $\pi^0 \to \gamma + A'$ has been investigated using 5% of 2016 data. This corresponds to about 1.5×10^{10} Kaon decays. Here, A' is a Dark Photon (DP) decaying invisibly (see sect. 4.3 for visible DP decays). The squared missing mass $m^2 = (p_K - p_\pi - p_\gamma)^2$, peaks at 0 for the SM process $\pi^0 \to \gamma\gamma$ (where one of the γs is lost). By contrast, it should exhibit a peak around the A' mass for the $\pi^0 \to \gamma + A'$ decay, if the A' is sufficiently strongly coupled given the statistics. A data-driven background estimate, based on the tail with negative missing mass values, was used. No statistically significant excess has been observed and upper limits have been computed on the number of signal events.

The corresponding 90 % confidence level exclusion limit on the kinetic mixing parameter versus the mass of the DP is shown in Fig. 2 together with the limits from BaBar, NA64 and E949, as compiled in [9].

The "stalactite-like" shape shape of the NA62 exclusion region in fig. 2 can be understood as follows: Going to low A' masses, the search is limited by the SM background of π^0 decays with one photon lost. On the other hand, at high masses, the limiting factor is kinematics.

3.2 HNL from production search

A search for heavy neutral leptons (HNLs) that escape detection (see also section 4.4 for visible decay searches of HNLs) has been performed utilizing the decays $K^+ \to \mu^+/e^+ + N_{\mu/e}$, with N the HNL. The analysis proceeds through a "bump-hunt" in the positive squared missing mass region. This analysis was based on minimum-bias-triggered data from 2015 equivalent to $\sim 3 \times 10^8 K^+$ decays. No signal has been observed and upper limits have been placed [10]. This search considerably improves the sensitivity with respect to previous experiments for both the electron and muon modes above HNL masses $\gtrsim$300MeV, cf. Fig. 3. Note that the upper blue curve labeled NA62-2007 shows the limit from [11], based on data from 2007 (with the apparatus of

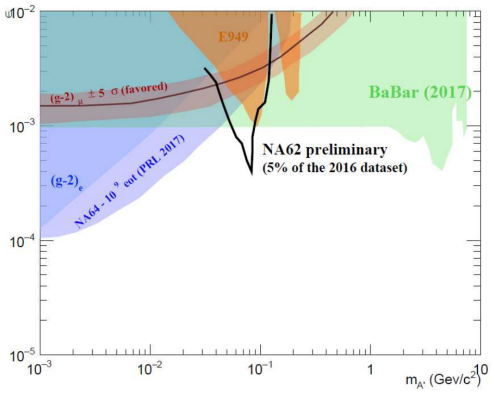

Figure 2: *90% CL exclusion limit in the coupling-mass plane for $\pi^0 \to \gamma A'$ with a Dark Photon A' that decays into invisible final states. The red band shows a region of the parameters suggested to explain the muon (g-2) anomaly (red band).*

the NA48/2 experiment) corresponding to $\sim 10^7 K^+$ decays exploited to search for the leptonic muon mode.

3.3 Further avenues for new particle searches from kaon decays

The above-mentioned examples do not constitute a comprehensive list of interesting channels and the around $3 \times 10^{12} K^+$ collected in 2017 and the ongoing 2018 data taking can be harvested for a plethora of new-physics signatures. For example, as by-product of the main analysis, a very intriguing possibility concerns flavored, ultralight axions such as the model of [12], or a bump hunt in $K^+ \to \pi^+ + X$, with X decaying further to $l^- l^+$ with $l = \mu, e$, see prospects in [13].

4 Prospects for upstream-produced exotics at 10^{18} POT at NA62

In this section we discuss the prospects to search for novel weakly interacting particles produced upstream the NA62 fiducial volume (TAX/target region in Figure 1).

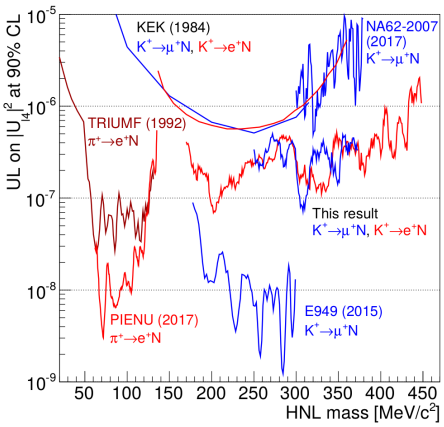

Figure 3: *90% CL exclusion limit in the plane of coupling ($|U_{l4}|^2$) versus mass from various pion and kaon leptonic decays. Limits from other production searches are shown together with the results from NA62 data taken in 2007 and 2015. The latter is labeled as "This result"* [10].

For definiteness, we show the sensitivity prospects for NA62 at 10^{18} POT for some new physics models that are also considered for a much wider set of experiments in the context of CERN's 'Physics beyond collider' (PBC) studies [14]. Thus, we heavily follow the benchmark sets provided in [15]. All plots show a potential 90% CL exclusion limit achievable by NA62, if full background rejection can be achieved.

4.1 ALPs with predominant photon coupling

For axion-like particles (ALPs) as portal particles, one has the possibility to write down couplings to gluons, quarks, leptons and other SM fields. Here only the prospect of a strictly predominant coupling to photons is shown. If this is realized, the pre-dominant production mechanism for ALPs would be via Primakov production through photons-from-protons in the target (favored by a coherent Z^2 enhancement over, e.g. an ALP-strahlung process [16]).

The relevant interaction term including the ALP a is

$$\mathcal{L}_{a,\mathrm{int}} = -\frac{1}{4}\, g_{a\gamma}\, a\, F^{\mu\nu} \tilde{F}_{\mu\nu} \,, \tag{1}$$

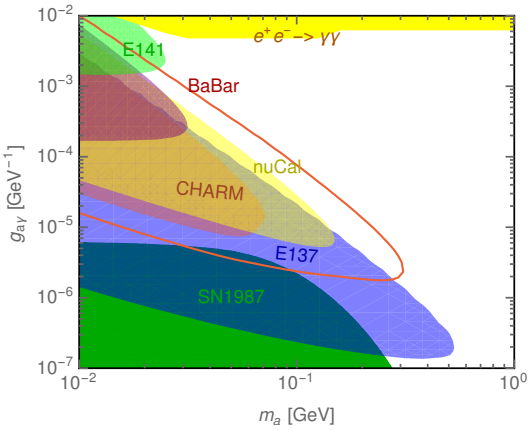

Figure 4: *Status of exclusions for ALPs coupled to photons in the MeV-GeV range. The shaded areas correspond to excluded regions, the red line denotes the NA62 prospect at* 10^{18} *POT.*

where $g_{a\gamma}$ denotes the photon ALP coupling.

The red, non-filled curve in Figure 4 shows the prospects of a search performed at NA62 at 10^{18} POT. Other curves are taken from [16] (with updates provided in [17, 18]). Projections are based on Primakov production through the equivalent photon approximation. In addition, detection of both photons from the ALP decay at a mutual distance of at least 10cm in the inner region of the LKr has been assumed in a toy MC. This toy MC has been cross-checked against the full NA62 MC. Note that this search needs to strictly be performed in beam-dump-mode as no tracking for the photons is available.

4.2 Higgs Portal

In the following we project the sensitivity for NA62 for a scalar S with an interaction

$$\mathcal{L}_{\text{int,scalar}} \sim \mu S H^\dagger H \quad , \theta = \mu v/(m_h^2 - m_S^2) \ , \tag{2}$$

where v is the Higgs VEV and a mixing parameter θ, valid for small mixings [19] is introduced. Above we have omitted the possibility of an additional S^2

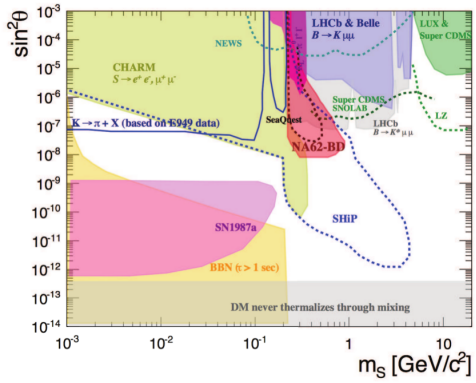

Figure 5: *Status of exclusions for scalars mixing with the Higgs as described in the text. Plot as in* [19] *with NA62 sensitivity projection in red, labelled 'NA62-BD'. Also indicated are projections for SeaQuest and SHiP.*

interaction. Our projection for NA62 at 10^{18} POT is given in Fig. 5.

The dominant production mode here is from B-Mesons produced in the dump, which subsequently decay into final states with S particles. The decay of S has been evaluated in a toy MC cross-checked against the full MC and considers final states $\mu\mu$, ee, $\pi\pi$, KK.

4.3 Dark Photons

The Dark Photon (vector) portal considered here is a minimal model in which an additional U(1) is introduced that mixes with the SM photon:

$$\mathcal{L}_{\text{int}} \sim \frac{\epsilon}{2\cos(\theta_W)} F'^{\mu\nu} B_{\mu\nu} \ , \tag{3}$$

with ϵ being the kinetic mixing.

Figure 6 shows the current state of exclusions together with the prospect sensitivity of NA62. Final states in ee, $\mu\mu$ have been considered, and plausible trigger and selection efficiencies have been accounted for. A toy MC has been set up and cross-checked against the full MC.

For this projection, only Dark Photon production via Meson decays of $D's, \pi^0, \eta, \eta', \Phi, \rho, \omega$ and in Bremsstrahlungs-production has been considered.

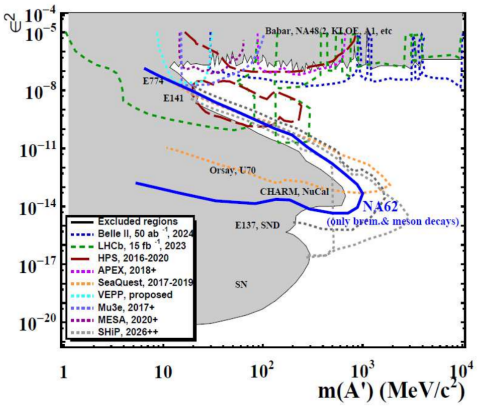

Figure 6: *Status of exclusions for Dark Photons. The blue line shows the sensitivity projection of NA62 based only on production of Dark Photons from Meson decays and Bremsstrahlung at* 10^{18} *POT from the Beryllium target.*

Additionally this production is assumed to take place in the Beryllium target only.

Considering production in the more downstream TAX will improve the projection further. Also, in principle, QCD processes such as $q\bar{q} \to A'$ can contribute, especially at higher masses [20]. Albeit this is plagued by theoretical uncertainties in the corresponding production cross-section. Such processes are not considered here. In this sense, our projection is rather conservative.

4.4 Heavy Neutral Leptons

For the neutrino portal

$$\mathcal{L}_{\text{int,HNL}} \sim \Sigma F_{\alpha i}(\bar{L}_\alpha H)N_i \tag{4}$$

with the sum over HNLs, N and the flavor of lepton doublets L. F denotes Yukawa couplings. More details can be found in [21, 5].

Figure 7 shows NA62 prospect sensitivity for 10^{18} POT in the coupling versus mass plane for a three theoretical scenarios of heavy neutral lepton models, corresponding to the highest possible couplings to electrons (left-most

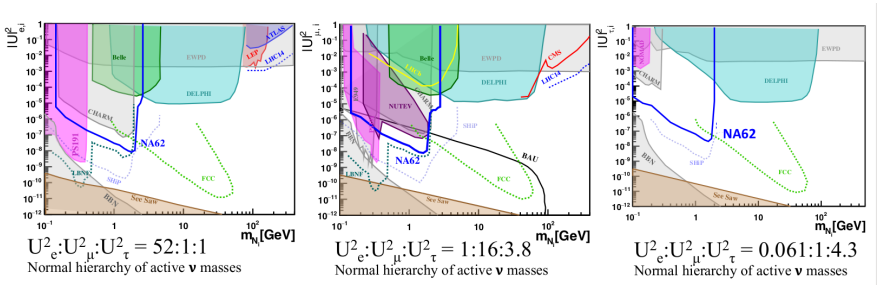

Figure 7: *Status of exclusions for HNLs coupled in the MeV-GeV range (together with some projections of a selected set of other experiments). In the plots, three extreme coupling scenarios are addressed separately, cf.* [21]*. The blue lines show the prospect of NA62 to test these scenarios if full background rejection can be achieved.*

panel), muons (central panel), and taus (right-most panel) and normal neutrino hierarchy.

5 A word on background rejection

The strategy and performance of background rejection for charged final states (Dark Photons, Scalars, and HNLs as discussed above) can be to some extent understood from fig. 8. In it, we show some results obtained in in parasitic mode (see also [22]). This sample is taken is during nominal data-taking, in a parasitic trigger stream that requires two coincident muons (10ns) window as well as an energy in the LKr calorimeter < 20 GeV. The statistics is $\sim 10^{15}$ POT.

On the l.h.s. of fig. 8 we show the distance of the extrapolation of the total vertex momentum to the nominal beam-line at the closest approach to the nominal beam-line. All two-track vertices are shown after a number of quality and track acceptance cuts. As expected, the majority of vertices and thus the background for exotic final states comes from K and π decays in and before the fiducial region. One can employ however, that the number of such vertices decreases steaply as one moves away from the beam-line.

The right-hand side of Figure 8 shows the same data after a number of

additional veto conditions, including the requirement that the vertex is located in the fiducial volume in between a z of 105m and 165m: Most importantly, the r.h.s. requires that the 2-d vertex distance ρ is between 10 and 50 cm from the beamline.

As can be seen, for this data set, no event is compatible with stemming from an exotic particle produced in the region between the NA62 Beryllium target and the TAX collimators in between 0 and $\sim$ 25m: The extrapolation of the total vertex momentum in the red-dashed signal box contains no entry.

Note, that for 'pure dump runs', a similar reasoning/analysis can be applied.

For the situation of fully neutral final states (such as ALPs) the above analysis is not useful, but in such a situation, it is feasible to exploit the fact that ALPs that exist in a still un-explored parameter region are necessarily very boosted when they reach the NA62 sensitive volume [22]. The probability to reach decay volume for an ALP is $\sim \exp(-l_{\text{absorber}}/l_d)$, where $l_d = \gamma\beta\tau \sim \frac{E_a}{m}\frac{64\pi}{m^3 g^2}$ and the "absorber" length for NA62 is $l_{\text{absorber}} \simeq 81$m. Following fig. 4, the yet-to-be discovered ALPs of interest have a short live-time (comparably large couplings) and will arrive at the NA62 sensitive volume at high E_a.

6 Conclusion: NA62 now and in run 3

The NA62 experiment, aimed at the measurement of $K^+ \to \pi^+\nu\bar{\nu}$ has released its first analysis on this decay channel based on 2016 data, validating its strict performance requirements on the detector. 2017 data is being analyzed and the 2018 run ongoing. To reach a measurement of $K^+ \to \pi^+\nu\bar{\nu}$ with a satisfactory precision, NA62 aims to continue to take data after LS2.

With this data, also exotic searches from Kaon decays can be performed. Recent results on production searches for heavy neutral leptons and preliminary results on invisible decays of dark photons were shown in this article.

The requirement of hermetic coverage and $\mathcal{O}(100)$-ps timing resolution allows also for a number of searches for new particles, potentially residing in a 'Dark Sector' being produced in the upstream TAX collimator. In these proceedings we have shown the prospects for some of these models at $\sim 10^{18}$ POT. This corresponds to a $\sim$ 1-year long data taking.

For this reason, the NA62 collaboration is currently discussing the possibility to use a fraction of the beam time during Run 3 (2021-2023) to operate

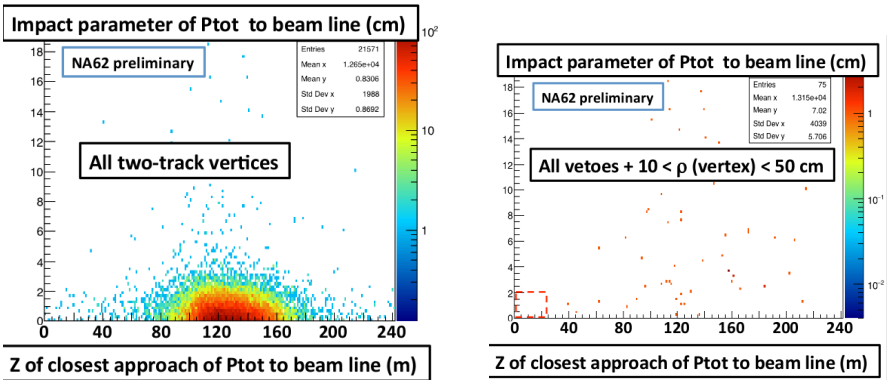

Figure 8: *Left-hand Plot: data corresponding to* 10^{15}*POT, after quality cuts described in text. Shown is the distance of the extrapolated total vertex momentum to the nominal beam-line at the position of the closest approach to the beam-line. Right-hand plot: Result after additional veto conditions and the requirement that the distance of the vertex to the nominal beamline is between 10 and 50cm. The red-dashed 'signal box' has no remaining event.*

NA62 with closed upstream collimators (beam-dump). The current NA62 run is exploited to evaluate background rejection capability and perform first searches for new physics for some of the presented channels.

7 Acknowledgements

The author would like to thank the organizers of the "Vulcano Workshop 2018 - Frontier Objects in Astrophysics and Particle Physics" for a thematically wide and intriguing conference in a wonderful setting.

References

1. E. Cortina Gil *et al.* [NA62 Collaboration], JINST **12**, no. 05, P05025 (2017) doi:10.1088/1748-0221/12/05/P05025 [arXiv:1703.08501 [physics.ins-det]].
2. A. Berlin, S. Gori, P. Schuster and N. Toro, arXiv:1804.00661 [hep-ph].
3. M. Anelli *et al.* [SHiP Collaboration], arXiv:1504.04956 [physics.ins-det].

4. R. Essig *et al.*, arXiv:1311.0029 [hep-ph].

5. S. Alekhin *et al.*, Rept. Prog. Phys. **79**, no. 12, 124201 (2016) doi:10.1088/0034-4885/79/12/124201 [arXiv:1504.04855 [hep-ph]].

6. J. Alexander *et al.*, arXiv:1608.08632 [hep-ph].

7. A. J. Buras, D. Buttazzo, J. Girrbach-Noe and R. Knegjens, JHEP **1511**, 033 (2015) doi:10.1007/JHEP11(2015)033 [arXiv:1503.02693 [hep-ph]].

8. G. Ruggiero, "$K^+ \to \pi^+ \nu\bar{\nu}$: First Result from the NA62 Experiment", these proceedings

9. D. Banerjee *et al.* [NA64 Collaboration], Phys. Rev. Lett. **118**, no. 1, 011802 (2017) doi:10.1103/PhysRevLett.118.011802 [arXiv:1610.02988 [hep-ex]].

10. E. Cortina Gil *et al.* [NA62 Collaboration], Phys. Lett. B **778**, 137 (2018) doi:10.1016/j.physletb.2018.01.031 [arXiv:1712.00297 [hep-ex]].

11. C. Lazzeroni *et al.* [NA62 Collaboration], Phys. Lett. B **772**, 712 (2017) doi:10.1016/j.physletb.2017.07.055 [arXiv:1705.07510 [hep-ex]].

12. L. Calibbi, F. Goertz, D. Redigolo, R. Ziegler and J. Zupan, Phys. Rev. D **95**, no. 9, 095009 (2017) doi:10.1103/PhysRevD.95.095009 [arXiv:1612.08040 [hep-ph]].

13. http://cds.cern.ch/record/2312430?ln=en

14. `http://pbc.web.cern.ch/`

15. M. Pospelov, "Notes on benchmark models for the PBC evaluation" (2018)

16. B. Döbrich, J. Jaeckel, F. Kahlhoefer, A. Ringwald and K. Schmidt-Hoberg, JHEP **1602**, 018 (2016) doi:10.1007/JHEP02(2016)018 [arXiv:1512.03069 [hep-ph]].

17. M. J. Dolan, T. Ferber, C. Hearty, F. Kahlhoefer and K. Schmidt-Hoberg, JHEP **1712**, 094 (2017) doi:10.1007/JHEP12(2017)094 [arXiv:1709.00009 [hep-ph]].

18. B. Döbrich, arXiv:1708.05776 [hep-ph].

19. G. Krnjaic, Phys. Rev. D **94**, no. 7, 073009 (2016) doi:10.1103/PhysRevD.94.073009 [arXiv:1512.04119 [hep-ph]].

20. P. deNiverville, D. McKeen and A. Ritz, Phys. Rev. D **86**, 035022 (2012) doi:10.1103/PhysRevD.86.035022 [arXiv:1205.3499 [hep-ph]].

21. D. Gorbunov and M. Shaposhnikov, JHEP **0710**, 015 (2007) Erratum: [JHEP **1311**, 101 (2013)] doi:10.1007/JHEP11(2013)101, 10.1088/1126-6708/2007/10/015 [arXiv:0705.1729 [hep-ph]].

22. `https://indico.cern.ch/event/523655/contributions/2246416/`

Frascati Physics Series Vol. 66 (2018)
Frontier Objects in Astrophysics and Particle Physics
May 20-26, 2018

The Muon g-2 experiment at Fermilab: Run 1 Status and Perspectives

Marco Incagli*
INFN Pisa
on behalf of the Muon $g-2$ collaboration

Abstract

Since more than 50 years the electron and muon anomalies, a_e and a_μ, defined in terms of the gyromagnetic factor g_i for particle i as $a_i = (g_i - 2)/2$, have provided a deep insight into the quantum structure of elementary particles. They have been, and continue to be, a milestone for the development of the Standard Model of Particle Physics against which all new theories have to be compared. For almost 20 years, the experimental value of a_μ has shown a tantalizing discrepancy of more than 3σ from the theoretical prediction making it mandatory for experimentalists to improve the current result, dominated by the E821 experiment at BNL [1)].

The Muon $g-2$ E989 experiment at Fermilab will use the same storage ring technique used at BNL, and previously in the CERN-III experiment, with the goal of decreasing by a factor of 4 the current error on a_μ, which will allow for a finer comparison with the theoretical prediction. E989 started collecting data in winter 2018 accumulating, in the period April-July 2018 (Run1) almost twice the statistics of the previous experiment (before application of data quality cuts).

In this document, the experiment will be briefly described, underlying the improvements which will allow to reduce the systematic error, and some preliminary result will be shown.

1 Introduction

A particle with electric charge Q and spin $\vec{s}$ is characterized by a magnetic moment

$$\vec{\mu} = g\frac{Q}{2m}\vec{s} \tag{1}$$

where g is the gyromagnetic factor.

For an elementary spin 1/2 particle, Dirac theory predicts that the gyromagnetic ratio is exactly $g = 2$. However, the development of the Quantum ElectroDynamic theory (QED) led to the prediction, and then to the observation, of virtual diagrams in which photons, as well as other particles, are emitted and reabsorbed. These diagrams modify the effective magnetic momentum and therefore the coupling of the particle to an external magnetic field.

This was first predicted by Schwinger [2)] and measured by Kusch and Foley [3)] in 1948. At first level in perturbation theory, the anomaly a was predicted by Schwinger to be:

$$a = \frac{g-2}{2} = \frac{\alpha}{2\pi} = 0.00116 \pm 0.00004 \tag{2}$$

The mesaured value was:

$$a = 0.00118 \pm 0.00003 \tag{3}$$

It was the first great success of QED.

With time, the measurement has been refined over and over reaching the astonishing value of

$$a_e = (115965218073 \pm 28) \times 10^{-14}$$

for the electron [4)] and

$$a_\mu = (116592080 \pm 63) \times 10^{-11}$$

for the muon [1)].

Although the muon anomaly can be measured less precisely than the electron one, mostly beacause of the particle lifetime, it was soon realized that a new particle (boson) contributing to the anomaly in a virtual correction would have an effect which, in general, can be proportional to the square of the mass ratio:

$$\alpha_{NP} \simeq \left(\frac{m_\mu}{M}\right)^2$$

This is due to the chirality flip in the boson emission. Therefore the muon anomaly, although less precisely measured, is more sensitive to New Phisics contributions than the electron one.

The current precision with which the anomaly is known is summarized in table 1. The QED contribution has been evaluated at 5 loops (more than 12000 diagrams!), the electroweak contribution is well under control while the hadronic vacuum polarizion and the light-by-light scattering are the largest sources of uncertainty in the a_μ^{theo} determination.

Table 1: *Theoretical determination of muon anomaly* a_μ.

contribution	value ($\times 10^{-11}$)	error ($\times 10^{-11}$)	reference
QED	11658471.90	0.01	5)
EW	15.36	0.10	6)
LO HLbL	9.80	2.60	7)
NLO HLbL	0.30	0.20	8)
LO HVP	693.27	2.46	9)
NLO HVP	-9,82	0.04	9)
NNLO HVP	1.24	0.01	10)
Total	11659182.05	3.56	9)

The theoretical prediction shows a tantalizing discrepancy of 3.7σ from the experimental result quoted above, which calls for a new experiment to possibly confirm, with a larger significance, the current difference.

The Muon $g-2$ experiment at Fermilab is designed to measure the muon anomaly with an error 4 times smaller than the current one by using the same experimental technique used in BNL as well as in the CERNIII experiment, briefly described in the next section, but improving both on the statistical and on the systematical error. In particular, the E821 total error was dominated by

the statistical component, therefore the first goal of the Fermilab experiment is to increase the collected statistics by a factor of 21, while the systematical error will have to be improved "just" by a factor of 3 to reach the final sensitivity.

2 The experiment

The experiment is based on the principle that the spin of a muon moving in a constant magnetic field $\vec{B}$, in the presence of a static electric field $\vec{E}$, precesses around $\vec{B}$ with an angular velocity ω_s which is slightly faster than the momentum precession (cyclotron frequency) ω_p around the same vector. More precisely, the spin vector projection on the momentum axis changes with time according to (from [12] eq.11.171):

$$\frac{d}{dt}(\hat{\beta}\cdot\vec{s}) = -\frac{e}{mc}\vec{s}_{\perp}\cdot\left[\left(\frac{g}{2}-1\right)\hat{\beta}\times\vec{B}+\left(\frac{g\beta}{2}-\frac{1}{\beta}\right)\vec{E}\right] \tag{4}$$

For a muon beam of momentum $p_\mu = 3.095$ GeV/c, called *magic momentum*, corresponding to a value of β which cancels out the second term of equation 4, and assuming that all muons follow the ideal circular path in a plane perpendicular to $\vec{B}$, then the above expression greatly simplifies into:

$$\omega_a = \frac{ea_\mu B}{m} \tag{5}$$

where $\omega_a = \omega_s - \omega_p$ is the difference between the spin precession and the cyclotron frequency and where quantities are taken as absolute values (no sign). By inverting the simplified equation 5, the the muon anomaly a_μ is given by:

$$a_\mu = \frac{m\omega_a}{eB} \tag{6}$$

In reality, the beam will have dimensions both in the radial and in the vertical directions, as well as a momentum spread, therefore the simple expression given above is only a first order approximation which will need to be carefully corrected. The most evident correction to the motion is the so-called *Coherent Betatron Oscillation* (CBO), which is due to the radial and vertical movement of particles within the beam. This will be briefly discussed in section 4.

3 The E989 experiment at Fermilab

The E989 experiment at Fermilab is largely built on the legacy of E821. During the summer of 2013, the 14-m diameter superconducting coils from the E821

storage magnet were moved from Brookhaven National Laboratory in New York to Fermilab, near Chicago. Performing the experiment at Fermilab provides a number of advantages, including the ability to produce more muons and to eliminate the pion contamination of the muon beam injected into the storage ring, which was a major limiting factor for E821.

The upgraded linear accelerator and booster ring structure of FNAL will deliver proton pulses (8 GeV, 4×10^{12} protons per pulse, 1.3 s pulse separation) impinging on the production target. The secondary π^+ beam will be focused with a pulsed lithium lens into the transport beam line which accepts π^+ with a momentum spread of $\pm 0.5\%$ around 3.11 GeV/c. In the transport beam line and in the delivery ring section the in-flight-decay of π^+ generates the μ^+ beam, polarized due to the V-A structure of the weak current. The $\simeq 10$ times longer flight distance at FNAL compared to BNL allows the residual hadronic contamination in the muon beam to decay away before it reaches the muon storage ring. This will essentially eliminate the so called hadronic flash in the positron calorimeters after muon beam injection which was a major source of background for the BNL experiment. The muons are injected into the storage ring through an inflector magnet which locally cancels out the main dipole field, thus allowing the muons to enter the storage ring perpendicularly to its radius at a value which is 77 mm larger than the nominal one. A set of kickers then kicks the muons into the right orbit. Muons then circulate in the storage ring decaying with a lifetime $\tau = \gamma\tau_0 \simeq 64\,\mu$s. The high-energy positrons from the muon decay are emitted preferentially along the spin direction, again because of the V-A structure of the weak current, with an asymmetry A which depends on the positron fractional energy.

Twenty-four individual calorimeter stations [11], each consisting of an array of 6×9 PbF2 crystals (25.4 mm $\times$ 25.4 mm $\times$ 152.4 mm) will be spaced equidistantly around the inner radius of the storage ring in order to capture the emitted positrons. Each crystal is individually instrumented with a silicon photomultiplier (SiPM) to detect the Cerenkov light generated by the high energy positrons. The high segmentation allows hit position discrimination while the fast SiPM response can separate events as close as 3 ns (800 MHz digitization rate) which will allow to address pile-up related systematic effects.

A sophisticated laser system will be used to calibrate in energy and to align in time the response of the 1296 crystals. This is of paramount importance

as the single largest systematic error in the BNL experiment was the calorimeter "gain stability", corresponding to 120 ppb error contribution out of a total of $\sigma_{\omega A}^{syst} = 180$ ppb [1]. Thanks to the laser system and to the new calorimeter, the budget for this error is 20 ppb: a reduction of a factor 6!

Straw tracker stations will be operated in front of two positron calorimeters which will allow for the precise reconstruction of the positron flight path and of the muon beam distribution. Retractable fiber harp detectors will be installed in the muon storage region to measure the muon distribution in the storage region.

4 Current status

E989 started collecting data in February 2018. After few months of commissioning, the first real data started to accumulate in April of the same year which allowed to reach by the end of Run1 in July 2018, a raw integral number of positrons which is almost twice the total sample of the previous BNL experiment.

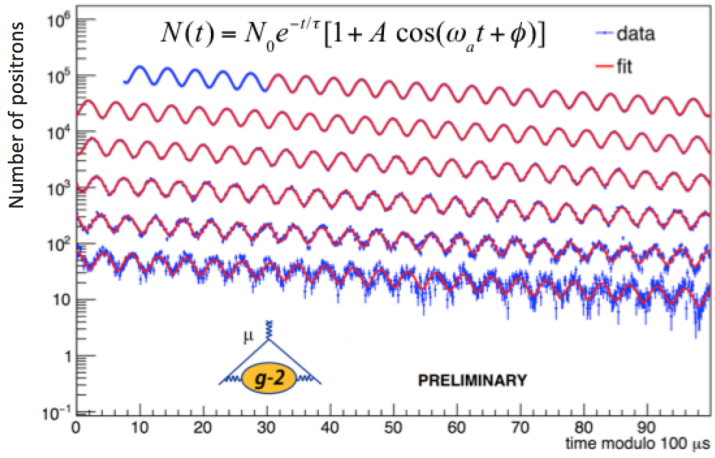

Figure 1: Arrival time spectrum of high energy positrons from a subset of data. The data are fit with an exponentional decay modulated by a sinusoidal function describing the muon spin precession.

Although Data Quality Cuts have still to be applied, with some simple cuts it is possible to produce the plot of fig.1 obtained by selecting positrons events with an energy larger than 1.7 GeV in a sample corresponding to one day of data taking acquired at the beginnig of April 2018. The plot shows the spin precession with respect to the cyclotron frequency modulating the muon exponential decay. The modulation is characterized by an amplitude A which depends on the specific energy cut applied to data.

The higher the energy cut, the higher the asymmetry parameter A. At the same time, however, by increasing the energy threshold the number of observed positrons N decreases, thus reducing the statistical significance. The optimal value is obtained by maximizing the product A^2N, which corresponds to a threshold $E_{thr} = 1.7$ GeV.

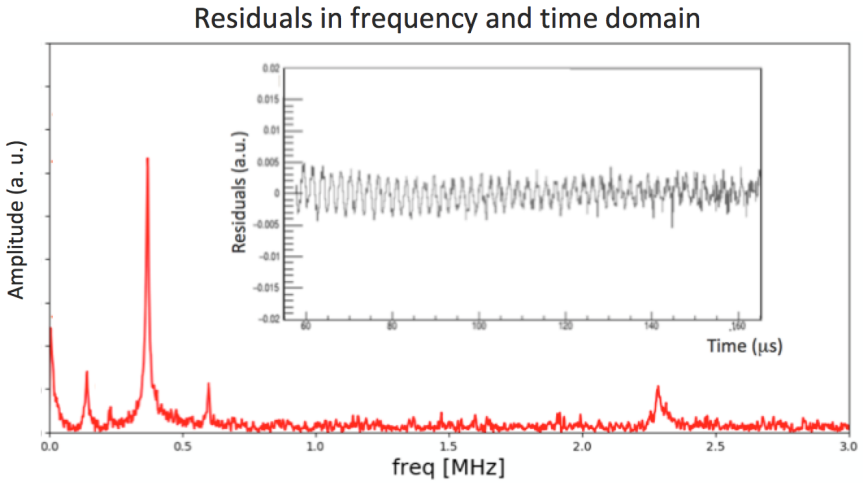

Figure 2: Residuals between function and data in the preliminary fit shown in the previous figure in the frequency and in the time domain. It is evident a residual fluctuation mostly due to Coherent Betatron Oscillations. Other minor peaks are visibles due to additional beam effects (see text).

The fit shows a very good qualitative agreement with data, given the statistics. However in fig.2 the residuals (data–fit) are plotted, both in the time and in the frequency domain. It is evident an oscillation which peaks at

$\simeq$ 370 kHz. This is due to beam Coherent Betatron Oscillations. The CBO modulation is physically caused by a mismatch between the emittance of the inflector and the acceptance of the storage ring. It causes the beam to oscillate radially with a frequency, as seen by a fixed detector, close to twice the $g-2$ one. It must be included in the fit, by adding extra-parameters, but it will also be studied independently with the tracking system, able to follow the beam profile, and the muon directions, in different locations around the ring.

5 Conclusion

The Muon $g-2$ experiment E989 at Fermilab started to collect data with the aim of improving by a factor 4 the precision of the previous BNL experiment.

A statistics larger than the one integratd at BNL has already been collected in Run 1 (April-July 2018).

The present muon storage rate is below that projected in the TDR by almost a factor of 2; several improvements are foreseen to be installed in Summer 2018, both in the accelerator complex and in the storage ring, which will allow to recover the design rate. In particular the interface between the two systems, the inflector, will be replaced with a new one, currently under test, which will be installed before the start of Run 2 (Oct, 1st 2018).

A preliminary analysis of the first collected data shows that the new systems installed in E989 (new segmented calorimeter, laser calibration system, straw tracker,...) are working as expected and they seem to be able to keep the systematic error at or below their budget.

If the E989 will confirm the previously measured value, then this could provide a 7σ discrepancy from the Standard Model, which would be a strong indication for new, as yet undiscovered, particles in loops which contribute to the muon anomaly.

6 Acknowledgments

This work was supported by Istituto Nazionale di Fisica Nucleare, the US DOE, Fermilab, and the EU Horizon 2020 Research and Innovation Program under the Marie Sklodowska-Curie Grant Agreement No.690385 and No.734303.

References

1. H. N. Brown et al. [Muon g-2 Collaboration], Phys. Rev. Lett. 86 (2001) 2227
2. J. Schwinger, Phys. Rev. 74 (1948) 416
3. P. Kusch, H. M. Foley, Phys. Rev. 74 (1948) 421
4. D. Hanneke *et al*, Phys. Rev. A. 83 (5): 052122
5. T. Aoyama *et al*, arXiv:1712:06060
6. C. Gnendiger *et al*, Phys. Rev. D88 (2013) 053005
7. F Jegerlehner, EPJ Web Conf 118 (2016) 01016
8. G. Colangelo *et al*, Phys. Lett. B735 (2014) 90
9. A. Keshavarzi *et al*, Phys. Rev. D 97, 114025
10. A. Kurz *et al*, Phys. Lett. B 734 (2014) 144
11. J. Kaspar, *et al*, JINST 12 (2017) no.01, P01009
12. J. D. Jackson, "Classical electrodynamics"

Frascati Physics Series Vol. 66 (2018)
Frontier Objects in Astrophysics and Particle Physics
May 20-26, 2018

The PADME experiment

M. Raggi
on behalf of the PADME collaboration *
Dipartimento di Fisica Sapienza Università di Roma,
Piazzale Aldo Moro 5 Roma Italy

Abstract

While accelerator particle physicists have traditionally focused on exploring dark matter through high energy machines, inspired by the WIMP paradigm, testing dark-sectors hypothesis requires innovative low energy and high intensity beams. This scenario offers attractive opportunities to low energy accelerators and small size experiments with high sensitivity detectors. In this paper we will focus our attention on the Dark Photon (DP) scenario, reviewing the current status of searches and new opportunities, with particular attention to the PADME experiment at Laboratori Nazionali di Frascati.

*P. Albicocco, J. Alexander, F. Bossi, B. Buonomo, A P. Caricato, C. Cesarotti, G. Chiodini, R. De Sangro, D. Domenici, F. Ferrarotto, G. Finocchiaro, S. Fiore, L. G. Foggetta, A. Frankenthal, G. Georgiev, A. Ghigo, P. Gianotti, F. Gontad, V. Kozhuharov, E. Leonardi, B Liberti, M. Martino, I. Oceano, F. Oliva, G. C. Organtini, G. Piperno, M. Raggi, F. Safai Tehrani, I. Sarra, B. Sciascia, T. Spadaro, S. Spagnolo, E. Spiriti, C. Taruggi, L. Tsankov, P. Valente, E. Vilucchi

1 Introduction

Strong limits recently imposed on the high mass dark matter particle by the LHC experiments, combined with null results from direct dark matter searches strengthen the believe that dark matter could be light and weakly coupled with the Standard Model (SM). Several models, commonly referred as "dark sectors" models, have been developed according to this hypothesis. Building a dark sector model requires to introduce at least a new interaction an a new mediator, a particle connecting the dark sectors to the SM sector. Several solutions are available depending on the interaction and mediator choice, scalar, pseudo-scalar or vector, and it's not excluded that more than one dark sector coexist in the dark matter world. No particular indication on the new particle mass are produced by the models, and the allowed parameter space in most cases spans several decades in mass and coupling strength. In the present document we will focus our attention on the vector portal dark sector [1)], introducing new $\mathrm{U}(1)_D$ interaction whose mediator is called Dark Photon (DP), or A' for its similarity with ordinary photons.

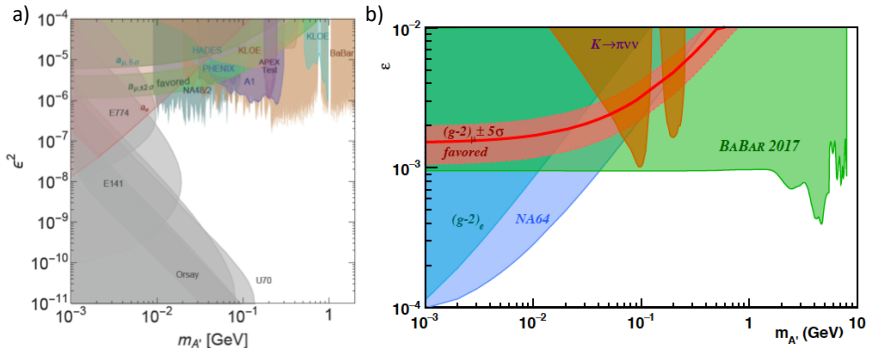

Figure 1: a) Constraints on dark photon "visible decays" [3)], b) Constraints on dark photon "invisible decays" [2)].

2 Status of the Dark Photon Searches

In the most common realisation of this model, the dark photon is able to mix with ordinary photon, giving rise to a reach phenomenology, and a large number of existing experiments are able to constrain the A' mass versus coupling parameter space. In this case the coupling of the dark photon to all fermions is just proportional to their electric charge, and it's therefore universal. Depending on the structure of the dark sector associated to the dark photon, two different dominating A' decay mode are identified. If the DP is the lightest particle in the dark sector it is forced to decay in pairs of SM particles, mostly lepton pairs (e^+e^-, $\mu^+\mu^-$), producing the so called "visible decays". Current experimental limits in this scenario are shown in Fig.1 a). A second and more intriguing possibility, is that the dark sector contains particles with masses smaller than half of the DP mass. In this case the dark photon will dominantly decay into dark matter particles, the so called "invisible decays" scenario, evading experimental detection. Few constrains are available in the decay into dark matter scenario summarised in Fig.1 b).

3 The PADME experiment at LNF

The PADME experiment [4) 5)] at the DAΦNE LINAC of the INFN Laboratori Nazionali di Frascati (LNF), has been designed to search for the dark photon by using a positron beam hitting a low Z target. The A' can be observed by searching for a narrow unexpected peak in the spectrum of the missing mass measured in single photon final states produced in association with a dark photon. The measurement requires the precise determination of the 4-momentum of the recoil photon and of the impinging positron.

The collaboration aims to complete the construction of the experiment in summer 2018 and to collect $\sim 10^{13}$ positrons on target by the end of 2018. The data taking is scheduled to start by September 2018. The PADME experiment at LNF-INFN, shown in Fig.2 will use 550 MeV positron impinging on 100μm thick active target made of polycrystalline diamond. The recoil photons from $e^+e^- \to \gamma A'$ annihilation process will be detected by a quasi-cylindrical BGO crystal calorimeter made of 616 20x20x230 mm^3 crystals, located 3.3 m downstream the target, providing very precise energy and position measurements. The non-interacted beam positrons, will be deflected outside the acceptance of

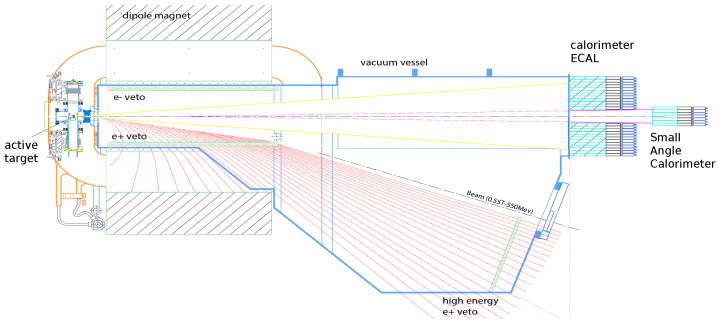

Figure 2: Layout of the PADME detector.

the calorimeter by a 1 m long dipole magnet. Three different sets of plastic scintillator bars, two of which located inside the magnet gap, will serve to detect the charged particles, thus providing an efficient veto for for the positron Bremsstrahlung background. In addition, a very fast small angle calorimeter, based of Cherenkov emission from PbF_2 crystals, will be placed along the beam axis downstream with respect to the main calorimeter, to help with the suppression of the three photon annihilation background. The target end the veto system are located in vacuum to minimise the possible beam-residual gas interactions

3.1 The PADME detector status

The construction of the PADME experiment has be completed in summer 2018 and the commissioning of the different detectors proceeds according to the schedule. In Fig.3 some pictures of the prototypes used to asses the detector performance are collected.

A the 100 μm active diamond target with graphite strips readout was one of the most challenging parts of the PADME experiment. After several test on the BTF beam line in Frascati [6] the detector construction has been successfully completed and operation in vacuum validated.

The PADME dipole magnet, an MBP-S dipole of the SPS transfer lines, providing 0.55 T magnetic field over a large (200x500x1000 mm^3) gap, has been characterised at Laboratori Nazionali di Frascati after the required modification of the gap height was performed at CERN.

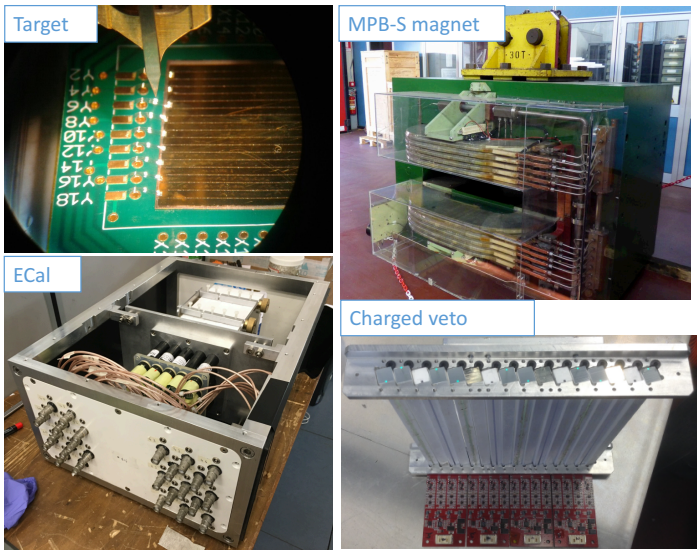

Figure 3: Prototypes of the PADME detector.

The prototypes of the charged veto detector systems have been finalised and tested using electrons and positrons from the LNF Beam Test Facility [7]. The full detector and associated electronics have been tested in vacuum before starting the commissioning inside the PADME vacuum system. Encouraging performance, in agreement with L3 experiment calorimeter performance, have been achieved with the PADME calorimeter prototype [8] during test at the Frascati Beam Test Facility. All the 616 BGO crystals scintillation units have been individually calibrated with 511KeV photons from a ^{22}Na radioactive source, before starting the assembly in the calorimeter mechanical structure.

The PADME experiment readout is based on the CAEN V1742 digitiser board (1-5 Gs/s and 12bit ADC) with optical link readout [?]. About 1000 channels including the readout of the electromagnetic calorimeter, SAC, and charged particle veto sub-detectors have been tested using the prototype data acquisition software. The Level 0 trigger distribution system has been successfully tested achieving the required synchronisation performance. The running of the experiment will start in September 2018 with the commissioning of the PADME beam line.

4 The PADME experiment sensitivity

The PADME experiment sensitivity estimate is based on a GEANT4 simulation extrapolated to 10^{13} positrons on target (POT) [5]. After recent upgrade of the DAΦNE LINAC the possibility to extend the bunch length duration to more than 250 ns, when the LINAC is operated in dedicated mode, was proved in early PADME run. In this conditions a data sample of 1×10^{13} POT can be obtained in 6 month while in 2 years a sample of 4×10^{13} POT is within reach. The bounds obtained for A' decaying into invisible particles, shown in Fig. 4, are obtained after a detailed background evaluation including positron Bremsstrahlung, two and three gamma annihilation. Signal events for different values of the A' mass, obtained using the CalcHep simulation tool, have been used to evaluate signal acceptance.

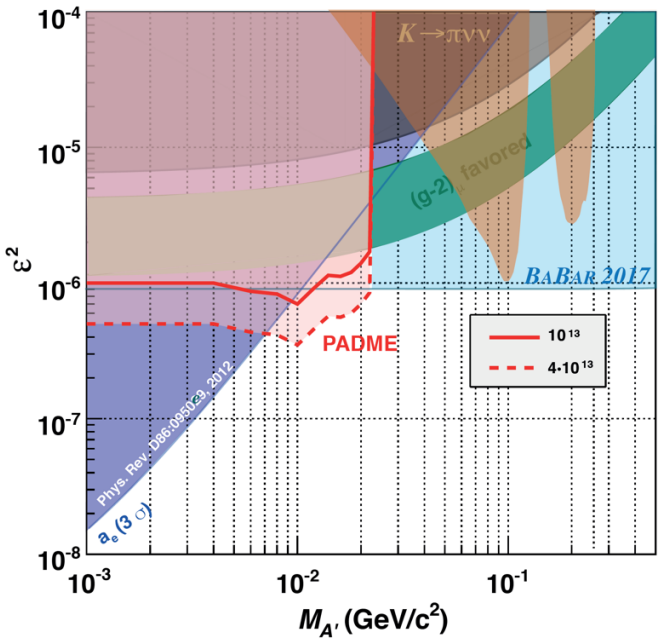

Figure 4: PADME estimated sensitivity for A' decaying into invisible particles for different values of the integrated luminosity.

4.1 Dark sector physics at LNF

Recently the possibility of extending the dark sector physics program at LNF has been explored, testing scenarios beyond the present PADME physics program. Several hypothesis have been put forward. The possibility of improving the luminosity of PADME using the DAΦNE ring as beam stretcher [9] can potentially overcome present 50Hz bunches limitation by providing to PADME a quasi-continuous ∼500 MeV positron beam allowing to collect a luminosity ∼1000 higher with respect to the present BTF beam. Another interesting scenario points to use the PADME experiment in dump mode to test the so called ^{8}Be anomaly [10]. The unique possibility of exploiting the resonant production of the 17 MeV X-Boson [11] by using a ∼ 282MeV positron beam on fixed target [12] offers to the Frascati laboratory an advantage over competitors that should not be underestimated.

5 Conclusions

Probing dark sector paradigm is a challenging and exciting perspective in the present panorama of dark matter searches. A wide effort in many laboratories in Europe and USA is already ongoing. The PADME experiment is starting its first data taking period in September with the aim of collecting a sample of 1E13 positrons on target during 2018.

References

1. B. Holdom, Phys. Lett. B **166**, 196 (1986)
2. J. P. Lees *et al.* [BaBar Collaboration], Phys. Rev. Lett. **119**, no. 13, 131804 (2017)
3. M. Battaglieri *et al.*, arXiv:1707.04591 [hep-ph].
4. M. Raggi and V. Kozhuharov, Adv. High Energy Phys. **2014**, 959802 (2014)
5. M. Raggi, V. Kozhuharov and P. Valente, EPJ Web Conf. **96**, 01025 (2015)
6. R. Assiro *et al.*, Nucl. Instrum. Meth. A **898**, 105 (2018)

7. A. Ghigo, G. Mazzitelli, F. Sannibale, P. Valente and G. Vignola, Nucl. Instrum. Meth. A **515**, 524 (2003).

8. M. Raggi *et al.*, Nucl. Instrum. Meth. A **862**, 31 (2017)

9. P. Valente, arXiv:1711.06877 [physics.acc-ph].

10. A. J. Krasznahorkay *et al.*, Phys. Rev. Lett. **116**, no. 4, 042501 (2016)

11. J. L. Feng, B. Fornal, I. Galon, S. Gardner, J. Smolinsky, T. M. P. Tait and P. Tanedo, Phys. Rev. D **95**, no. 3, 035017 (2017)

12. E. Nardi, C. D. R. Carvajal, A. Ghoshal, D. Meloni and M. Raggi, Phys. Rev. D **97**, no. 9, 095004 (2018)

Frascati Physics Series Vol. 66 (2018)
Frontier Objects in Astrophysics and Particle Physics
May 20-26, 2018

$K^+ \to \pi^+\nu\bar{\nu}$: First results from the NA62 experiment at CERN

Giuseppe Ruggiero
University of Lancaster, UK

Abstract

The decay $K^+ \to \pi^+\nu\bar{\nu}$, with a very precisely predicted branching ratio of less than 10^{-10}, is one of the best candidates to reveal indirect effects of new physics at the highest mass scales. The NA62 experiment at CERN SPS is designed to measure the branching ratio of the $K^+ \to \pi^+\nu\bar{\nu}$ with a decay-in-flight technique, novel for this channel. NA62 took data in 2016, 2017 and 2018. Statistics collected in 2016 allows NA62 to reach the Standard Model sensitivity for $K^+ \to \pi^+\nu\bar{\nu}$, entering the domain of 10^{-10} single event sensitivity and showing the proof of principle of the experiment. The preliminary result on $K^+ \to \pi^+\nu\bar{\nu}$ from the analysis of the 2016 data set is described.[1]

[1]The NA62 Collaboration: R. Aliberti, F. Ambrosino, R. Ammendola, B. Angelucci, A. Antonelli, G. Anzivino, R. Arcidiacono, M. Barbanera, A. Biagioni, L. Bician, C. Biino, A. Bizzeti, T. Blazek, B. Bloch-Devaux, V. Bonaiuto, M. Boretto, M. Bragadireanu, D. Britton, F. Brizioli, M.B. Brunetti, D. Bryman, F. Bucci, T. Capussela, A. Ceccucci, P. Cenci, V. Cerny, C. Cerri, B.

1 Introduction

The $K^+ \to \pi^+ \nu\bar{\nu}$ ($\pi\nu\nu$) is a flavour changing neutral current decay proceeding through box and electroweak penguin diagrams. A quadratic GIM mechanism and the transition of the quark top into the quark down make this process extremely rare. The Standard Model (SM) predicts [2] the branching ratio (BR) to be $(8.4 \pm 1.0) \times 10^{-11}$, where the precision on the external inputs dominates the uncertainty. The theoretical accuracy, instead, is at the level of 2%, as the SM BR includes NLO (NNLO) QCD corrections to the top (charm) quark contribution [3, 4] and NLO electroweak corrections [5]. Moreover the hadronic matrix element largely cancels when normalized to the precisely measured BR

Checcucci, A. Conovaloff, P. Cooper, E. Cortina Gil, M. Corvino, F. Costantini, A. Cotta Ramusino, D. Coward, G. D'Agostini, J. Dainton, P. Dalpiaz, H. Danielsson, N. De Simone, D. Di Filippo, L. Di Lella, N. Doble, B. Dobrich, F. Duval, V. Duk, J. Engelfried, T. Enik, N. Estrada-Tristan, V. Falaleev, R. Fantechi, V. Fascianelli, L. Federici, S. Fedotov, A. Filippi, M. Fiorini, J. Fry, J. Fu, A. Fucci, L. Fulton, E. Gamberini, L. Gatignon, G. Georgiev, S. Ghinescu, A. Gianoli, M. Giorgi, S. Giudici, F. Gonnella, E. Goudzovski, C. Graham, R. Guida, E. Gushchin, F. Hahn, H. Heath, T. Husek, O. Hutanu, D. Hutchcroft, L. Iacobuzio, E. Iacopini, E. Imbergamo, B. Jenninger, K. Kampf, V. Kekelidze, S. Kholodenko, G. Khoriauli, A. Khotyantsev, A. Kleimenova, A. Korotkova, M. Koval, V. Kozhuharov, Z. Kucerova, Y. Kudenko, J. Kunze, V. Kurochka, V.Kurshetsov, G. Lanfranchi, G. Lamanna, G. Latino, P. Laycock, C. Lazzeroni, M. Lenti, G. Lehmann Miotto, E. Leonardi, P. Lichard, L. Litov, R. Lollini, D. Lomidze, A. Lonardo, P. Lubrano, M. Lupi, N. Lurkin, D. Madigozhin, I. Mannelli, G. Mannocchi, A. Mapelli, F. Marchetto, R. Marchevski, S. Martellotti, P. Massarotti, K. Massri, E. Maurice, M. Medvedeva, A. Mefodev, E. Menichetti, E. Migliore, E. Minucci, M. Mirra, M. Misheva, N. Molokanova, M. Moulson, S. Movchan, M. Napolitano, I. Neri, F. Newson, A. Norton, M. Noy, T. Numao, V. Obraztsov, A. Ostankov, S. Padolski, R. Page, V. Palladino, C. Parkinson, E. Pedreschi, M. Pepe, M. Perrin-Terrin, L. Peruzzo, P. Petrov, F. Petrucci, R. Piandani, M. Piccini, J. Pinzino, I. Polenkevich, L. Pontisso, Yu. Potrebenikov, D. Protopopescu, M. Raggi, A. Romano, P. Rubin, G. Ruggiero, V. Ryjov, A. Salamon, C. Santoni, G. Saracino, F. Sargeni, V. Semenov, A. Sergi, A. Shaikhiev, S. Shkarovskiy, D. Soldi, V. Sougonyaev, M. Sozzi, T. Spadaro, F. Spinella, A. Sturgess, J. Swallow, S. Trilov, P. Valente, B. Velghe, S. Venditti, P. Vicini, R. Volpe, M. Vormstein, H. Wahl, R. Wanke, B. Wrona, O. Yushchenko, M. Zamkovsky, A. Zinchenko.

of the $K^+ \to \pi^0 e^+ \nu$ decay, with isospin breaking and non–perturbative effects calculated in detail [5, 6].

The $K^+ \to \pi^+ \nu\bar{\nu}$ decay is extremely sensitive to physics beyond the SM, probing the highest mass scales among the rare meson decays. The largest deviations from SM are expected in models with new sources of flavour violation, owing to weaker constraints from B physics [8, 9]. The experimental value of of the CP violating quantity ε_K limits the range of variation expected for $K^+ \to \pi^+ \nu\bar{\nu}$ BR within models with currents of defined chirality, producing also typical correlation patterns between the $K^+ \to \pi^+ \nu\bar{\nu}$ and $K_L \to \pi^0 \nu\bar{\nu}$ decay modes [10]. Present experimental constraints limit the range of variation within supersymmetric models [11, 12, 13]. The $K^+ \to \pi^+ \nu\bar{\nu}$ decay can also be sensitive to effects of lepton flavour non–universality [14] or can constrain leptoquark models [15] aiming to explain the measured CP violating ratio ϵ'/ϵ [16].

The experiments E787 and E949 at BNL [17, 18] studied the $K^+ \to \pi^+ \nu\bar{\nu}$ decay using a kaon decay–at–rest technique and measured a BR of $(17.3^{+11.5}_{-10.5}) \times 10^{-11}$. The NA62 experiment at CERN aims to measure precisely the BR of the $K^+ \to \pi^+ \nu\bar{\nu}$ decay with a novel kaon decay–in–flight technique. Here the first result of NA62 from the analysis of data collected in a data taking period in 2016 is reported, corresponding to about 5% fraction of the statistics collected by NA62 during a full–year data taking period in 2017.

2 The NA62 Experiment

The NA62 experiment is a fixed target experiment located at CERN. Fig. 1 shows a schematic view of the apparatus. NA62 adopts a kaon decay-in-flight technique. Primary SPS protons strike a target from which a secondary charged hadron beam of 75 GeV/c and 1% momentum bite is selected and transported to the decay region. The detailed descriptions of the apparatus can be found in [19]. The incoming kaon is positively identified by a differential Cerenkov counter (KTAG) and its momentum and direction are measured by three stations of Si pixel detectors (GTK). About 6% of beam particles are K^+. A guard ring detector (CHANTI) vetoes beam inelastic interactions occurring in GTK. A decay tank, holding a 10^{-6} mbar vacuum, is surrounded by lead-glass annular calorimeters (LAV) designed to catch photons up to 50 mrad. Four stations of straw chambers (STRAW) in vacuum trace downstream charged particles, with a dipole magnet providing a 270 MeV/c transverse kick for

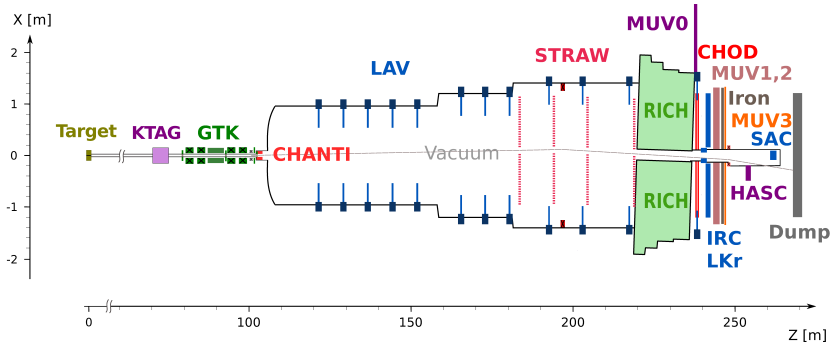

Figure 1: *Schematic layout of the NA62 experiment in the yz plane.*

momentum analysis. A RICH counter time-stamps and identifies charged particles; plastic scintillators (CHOD) are used for triggering and timing. Photon rejection in the forward region is provided by: an electromagnetic calorimeter of liquid krypton (LKr); small angle calorimeters (IRC and SAC). Hadron calorimeters (MUV1,2) and a plastic scintillator detector (MUV3) are used to suppress muons. The SPS delivers 3.3×10^{12} protons per pulse at full intensity to NA62, corresponding to 750 MHz particle rate in GTK. Information from CHOD, RICH, MUV3 and LKr are built up online to issue level zero trigger conditions. Software-based variables from KTAG, CHOD, LAV and STRAW provide higher level trigger requirements. $\pi\nu\nu$-triggered data are taken concurrently with downscaled samples of data for rare kaon decays studies and minimum bias.

The NA62 apparatus has been commissioned in 2015 and 2016. In 2016 NA62 has collected about 4.5×10^{11} kaon decays for $\pi\nu\nu$ at 20-40% of nominal intensity.

3 Principle of the Measurement

The signature of a $K^+ \to \pi^+\nu\overline{\nu}$ decay is one K^+ in the initial state and one π^+ with missing energy in the final state. The main kinematic variable is the squared missing mass $m^2_{miss} \equiv (p_K - p_\pi)^2$, where p_K and p_π are the 4-momenta of the K^+ and π^+, respectively. The two neutrinos carry away

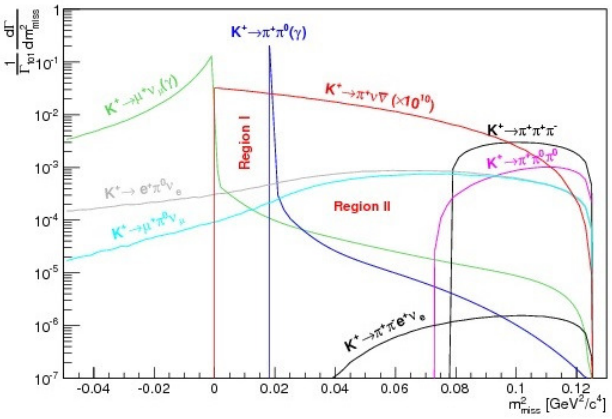

Figure 2: m^2_{miss} *of* K^+ *decays relevant to the* $K^+ \to \pi^+\nu\bar{\nu}$ *measurement. The* m^2_{miss} *is computed under the hypothesis that the charged particle in the final state is a* π^+*. Signal (red) is multiplied by* 10^{10} *for visibility. Two regions where to search for signal are also indicated.*

a large fraction of the momentum resulting in a broadly distributed missing mass, as shown in Fig. 2. Search for signal occurs in two regions of the m^2_{miss} spectrum across the $K^+ \to \pi^+\pi^0$ peak. Possible backgrounds are: the main K^+ decay modes $K^+ \to \pi^+\pi^0$ and $K^+ \to \mu^+\nu$ entering signal regions through non gaussian resolution and radiative tails of the m^2_{miss}; $K^+ \to \pi^+\pi^+\pi^-$ through non gaussian resolution tails; $K^+ \to l^+\pi^0\nu_l$ decays and more rare processes like $K^+ \to \pi^+\pi^- e^+\nu$ broadly distributed across the signal regions because of the neutrinos in the final state; events mimicking $K^+ \to \pi^+\nu\bar{\nu}$ originating along the beam line via inelastic interactions of beam particles with the material; K^+s that decay before entering the fiducial volume downstream to the last station of the GTK (GTK3). Each source of background requires different rejection procedures, depending on the kinematics and on the type of charged particle in the final state. The estimation of the expected background remaining after selection is done separately for each process.

A blind procedure was adopted for the 2016 $\pi\nu\nu$ analysis, with signal and control regions kept masked as long as the evaluation of expected signal and background was not complete. The analysis makes use of data acquired with

the dedicated $\pi\nu\nu$ trigger (*PNN*) and with a minimum bias trigger (*control*).

4 Selection

The $\pi\nu\nu$ selection proceeds through: definition of a K^+ decay with a charged particle in the final state; π^+ identification; rejection of events with γ or any other activity in final state; kinematic selection and definition of the signal regions.

Signals in RICH, LKr and CHOD detectors are spatially associated to tracks reconstructed in the STRAW to identify and timestamp the π^+'s. A K^+ is identified in KTAG and traced in GTK. The K^+ is matched to the candidate π^+ exploiting the $\mathcal{O}(100$ ps) time coincidence resolution between KTAG, GTK and RICH and the $\mathcal{O}$(mm) resolution of the closest distance of approach between the STRAW and GTK tracks. An about 50 m long fiducial decay region for $K^+ \to \pi^+\nu\bar{\nu}$ is chosen, starting from about 10 m downstream of the last GTK station. The selection of K^+ decays in this region makes use of criteria based on: reconstructed decay vertex, π^+ position extrapolated back at the entrance of the fiducial region, π^+ emission angle, extra-activity in CHANTI and GTK.

The $\pi\nu\nu$ analysis is restricted to $15 < P_{\pi^+} < 35$ GeV/c. This cut costs half of the signal acceptance, but improves significantly the π^0 detection and exploits the optimal range for π^+ identification and $K^+ \to \mu^+\nu$ rejection.

Calorimeters and RICH provide π^+ identification against μ^+ and positrons. A multi-variate classifier combines calorimetric information. RICH variables are used to build: a STRAW track-based likelihood discriminant; the mass of the particle using the momentum measured by the STRAW; the momentum of the particle assuming the π^+ mass. Achieved performances for π^+ momentum between 15 and 35 GeV/c are: 0.6×10^{-5} (78%) μ^+ (π^+) efficiency with calorimeters, 2.1×10^{-3} (82%) μ^+ (π^+) efficiency with RICH.

The LAV, LKr, IRC and SAC ensure rejection of photons with direction from 0 up to 50 mrad with respect to the beam axis. The time coincidence between extra energy in these detectors and π^+ is the main veto condition and typical veto time windows range from ± 3 to ± 10 ns. Further selection criteria based on extra activity in CHOD's and STRAW, called multiplicity rejection, are employed against photons interacting with material upstream of photon vetoes and losing energy either in the beam pipe or through hadron production.

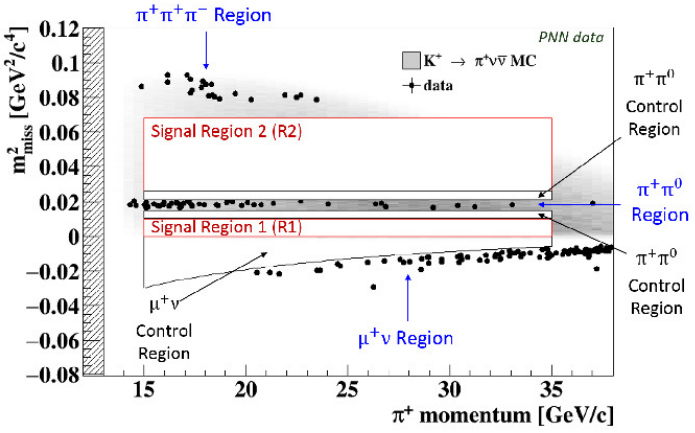

Figure 3: *m^2_{miss} as a function of P_{π^+} for PNN trigger data events (dots) passing the $\pi\nu\nu$ selection, but the cuts on m^2_{miss} and P_{π^+}. Grey area corresponds to the distribution of $\pi\nu\nu$ MC events, with darker (lighter) grey indicating more (less) populated regions. Red (black) lines define the signal (control) regions and are masked. Three background regions are also shown.*

Multiplicity rejection is also effective against decays like $K^+ \to \pi^+\pi^+\pi^-$ and $K^+ \to \pi^+\pi^- e^+\nu$. The achieved π^0 detection inefficiency is about 2.5×10^{-8}, measured on data.

The invariant $m^2_{miss} \equiv (p_{K^+} - p_{\pi^+})^2$ is used to discriminate between the signal and background kinematics, where p_{K^+} (p_{π^+}) is the K^+ (π^+) 4-momenta measured by the GTK (STRAW) under the hypothesis of the K^+ (π^+) mass. Fig. 3 shows the distribution of the remaining events in the ($m^2_{miss} - P_{\pi^+}$) plane, with P_{π^+} the magnitude of the π^+ 3-momentum. This plane defines three background regions mostly populated by $K^+ \to \pi^+\pi^0$, $K^+ \to \mu^+\nu$ and $K^+ \to \pi^+\pi^+\pi^-$ decays; signal regions below and above the $K^+ \to \pi^+\pi^0$ called *Region 1* and *2*, respectively; three control regions between the signal and the $K^+ \to \pi^+\pi^0$ and $K^+ \to \mu^+\nu$ regions. The 10^{-3} GeV^2/c^4 m^2_{miss} resolution of the $K^+ \to \pi^+\pi^0$ peak drives the choice of the boundaries of these regions. The same m^2_{miss} is also computed taking P_{π^+} measured with the RICH instead of the STRAW or assuming the nominal K^+ momentum and direction instead of the GTK measurements. Constraints on these variables are also applied

to define signal regions, providing additional power to suppress background coming from tracks mis-reconstructed in STRAW or GTK.

5 Single Event Sensitivity

The single event sensitivity SES is defined as $1/(N_K \cdot \varepsilon_{\pi\nu\nu})$, where N_K is the number of K^+ decays and $\varepsilon_{\pi\nu\nu}$ is the signal efficiency for the $K^+ \to \pi^+\nu\bar{\nu}$ selection. The number N_K is $(1.21 \pm 0.02_{syst}) \times 10^{11}$, measured using a sample of $K^+ \to \pi^+\pi^0$ and computed as $(N_{\pi\pi} \cdot D)/(A_{\pi\pi} \cdot BR_{\pi\pi})$. Here $N_{\pi\pi}$ is the number of $K^+ \to \pi^+\pi^0$ decays selected on control data using the same $K^+ \to \pi^+\nu\bar{\nu}$ criteria, except the γ, the multiplicity rejection and the cut on m^2_{miss}; $A_{\pi\pi}$ their selection acceptance estimated to be about 10% using a MC simulation; $BR_{\pi\pi}$ and $D = 400$ are the branching ratio of the $K^+ \to \pi^+\pi^0$ decay and the downscaling factor of the control trigger, respectively. Discrepancies in data/MC agreement and variation of the measured K^+ flux as a function of P_{π^+} are the main sources of systematic uncertainty to N_K.

The signal efficiency is computed separately in four bins of P_{π^+}, 5 GeV/c wide, as the product of three terms, $(A_{\pi\nu\nu} \cdot \epsilon_{RV} \cdot \epsilon_{trig})$. $A_{\pi\nu\nu}$ is the $K^+ \to \pi^+\nu\bar{\nu}$ selection acceptance extracted from MC; ϵ_{RV} the signal efficiency due to losses resulting from γ and multiplicity rejection induced by the random activity in the detectors; ϵ_{trig} the PNN trigger efficiency. Additional sources of event loss common both to $K^+ \to \pi^+\nu\bar{\nu}$ and $K^+ \to \pi^+\pi^0$ are not accounted for as they cancel in the signal to normalisation ratio entering SES.

The selection acceptance $A_{\pi\nu\nu}$ is about 4% overall (Fig. 4, a). Trigger efficiency is measured using control data and $K^+ \to \pi^+\pi^0$ control samples and is about 88%, weakly dependent on P_{π^+}, with losses due mainly to the LKr and MUV3 veto conditions. Random veto efficiency ϵ_{RV} is estimated on data using a sample of $K^+ \to \mu^+\nu$ candidates and corresponds to $\epsilon_{RV} = 0.76 \pm 0.04$, where the uncertainty comes from the estimation of the losses induced by the π^+ interactions. The random veto efficiency is flat as a function of P_{π^+}, but depends on the intensity (Fig, 4, b).

The final measured SES and the corresponding number of SM $K^+ \to \pi^+\nu\bar{\nu}$ expected in signal regions 1 and 2 are:

$$SES = (3.15 \pm 0.01_{stat} \pm 0.24_{syst}) \times 10^{-10}, \quad (1)$$

$$N^{exp}_{\pi\nu\nu}(SM) = 0.267 \pm 0.001_{stat} \pm 0.020_{syst} \pm 0.032_{ext}. \quad (2)$$

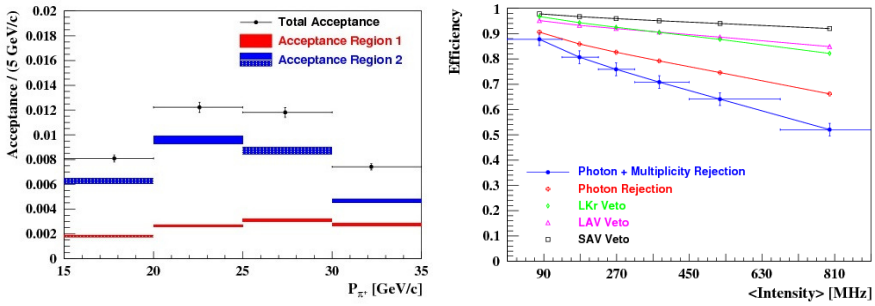

Figure 4: *a) $A_{\pi\nu\nu}$ per bins of P_{π^+} in regions 1+2 (dots) with total uncertainty and in regions 1, 2 (red, blue boxes) separately with total uncertainty (vertical box size). b) signal efficiency in bins of beam intensity after photon and multiplicity rejection due to the random activity with total uncertainty (blue dots), after photon rejection (red crosses), after IRC and SAC veto only (black square), after LAV veto only (pink triangle), after LKr only (green diamond). Lines are for eye guidance. Out–of–time activity in GTK is used to estimate the event–by–event intensity.*

The external error to $N_{exp}^{\pi\nu\nu}(SM)$ comes from the uncertainty on the SM $K^+ \to \pi^+\nu\bar{\nu}$ branching ratio. The systematic uncertainty on SES mostly comes from ϵ_{RV} and $A_{\pi\pi}$ and is propagated to $N_{\pi\nu\nu}^{exp}$.

6 Background estimation

Background from K^+ decaying in the fiducial region comes primarily from $K^+ \to \pi^+\pi^0$, $K^+ \to \mu^+\nu$, $K^+ \to \pi^+\pi^+\pi^-$ and $K^+ \to \pi^+\pi^- e^+\nu$.

Kineatic thresholds limit the m^2_{miss} spectrum of $K^+ \to \pi^+\pi^0$, $K^+ \to \mu^+\nu$ and $K^+ \to \pi^+\pi^+\pi^-$. To estimate the fraction of these decays remaining in signal regions, the assumption is made that π^0 rejection for $K^+ \to \pi^+\pi^0$, particle identification for $K^+ \to \mu^+\nu$ and multiplicity rejection for $K^+ \to \pi^+\pi^+\pi^-$ are independent from the m^2_{miss} cuts defining the signal regions. The number of expected events in signal regions from these processes, $N^{exp}_{background}$, is computed as $N(background) \cdot f^{kin}$; here $N(background)$ is the number of remaining PNN triggered events in the corresponding background region after the $\pi\nu\nu$ selection, but the cut on m^2_{miss}; f^{kin} is the fraction of background

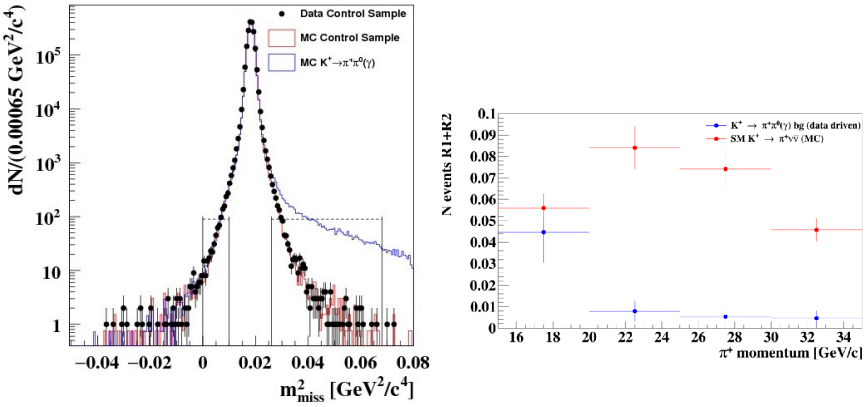

Figure 5: *a)* m^2_{miss} *distribution of the* $K^+ \to \pi^+\pi^0(\gamma)$ *control events selected on data tagging the* π^0 *(dots). Two* $K^+ \to \pi^+\pi^0(\gamma)$ *MC samples are superimposed: one selected as in data (red line), the other selected as* $\pi\nu\nu$ *(blue line, referred as MC* $K^+ \to \pi^+\pi^0(\gamma)$ *in the legend). The region between the two vertical lines joined by the dotted horizontal line at* m^2_{miss} *lower (higher) than the* $m^2_{\pi^0}$ *peak indicates region 1 (2). b) expected* $K^+ \to \pi^+\pi^0(\gamma)$ *background in bins of* P_{π^+} *compared to the expected number of SM* $K^+ \to \pi^+\nu\bar{\nu}$ *events.*

events entering signal regions through the reconstructed tails of the corresponding m^2_{miss} peak. The fraction f^{kin}, called *tails*, is modeled on control samples selected on data and eventually corrected for biases induced by the selection criteria using MC simulations. The above procedure is applied separately in four bins of P_{π^+} for $K^+ \to \pi^+\pi^0$ and $K^+ \to \mu^+\nu$. Expected background in control regions is derived similarly.

The reconstruction tails of the $K^+ \to \pi^+\pi^0$ m^2_{miss} distribution are studied from a $K^+ \to \pi^+\pi^0$ control sample selected tagging the π^0 with two γ's in LKr. Simulations accurately reproduces the tails over 4–5 orders of magnitudes (Fig, 5, a). The π^0 tagging does not bias the resolution tails of $K^+ \to \pi^+\pi^0$, but suppresses almost completely the radiative part coming from $K^+ \to \pi^+\pi^0\gamma$ decays. This radiative contribution is estimated using MC simulation and the measured single photon detection efficiency of the different photon vetoes. The background from $K^+ \to \pi^+\pi^0$ and from its radiative process integrated over bins of P_{π^+} is summarised in Tab. 1. The background depends on P_{π^+} as

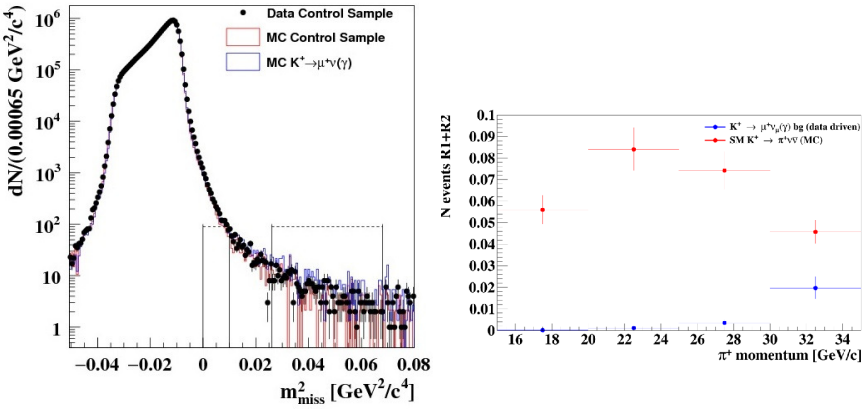

Figure 6: *a) m^2_{miss} distribution of the $K^+ \to \mu^+\nu(\gamma)$ control events selected on data (dots) with two MC $K^+ \to \mu^+\nu(\gamma)$ samples superimposed: one selected as in data (red line), the other selected as $\pi\nu\nu$ without particle identification (blue line, referred as MC $K^+ \to \mu^+\nu(\gamma)$ in the legend). The two regions between the two vertical lines joined by the dotted horizontal line correspond to region 1 and 2 (lower and higher m^2_{miss}, respectively). b) expected $K^+ \to \mu^+\nu(\gamma)$ background in bins of P_{π^+} compared to the expected number of SM $K^+ \to \pi^+\nu\bar{\nu}$ events.*

residual PNN trigger events in $\pi^+\pi^0$ region gather at low P_{π^+} (Fig. 5, b). After un-blinding the $K^+ \to \pi^+\pi^0$ control regions, one event is observed while $1.46 \pm 0.16_{stat} \pm 0.06_{syst}$ are expected.

Reconstruction tails of $K^+ \to \mu^+\nu$ are modeled by a control sample selected identifying the μ^+. Comparisons between data and MC suggest that tails are accurately simulated over 5 orders of magnitude (Fig. 6, a). The bias induced by the μ^+ identification is assigned as systematic uncertainty. The radiative contribution is included in the measured tails. Effects of possible correlation between the RICH π^+ identification and the m^2_{miss} are studied on data and a corresponding systematic uncertainty assigned to the expected $K^+ \to \mu^+\nu$ background. The final expectation integrated over P_{π^+} is summarised in Tab. 1. The background depends on P_{π^+} as both tails and particle identification increase at higher momenta as a consequence of $K^+ \to \mu^+\nu$ kinematics and RICH performances, respectively (Fig. 6, b). After un-blinding the $K^+ \to \mu^+\nu$ control region, two events are observed while $1.02 \pm 0.16_{stat}$ are

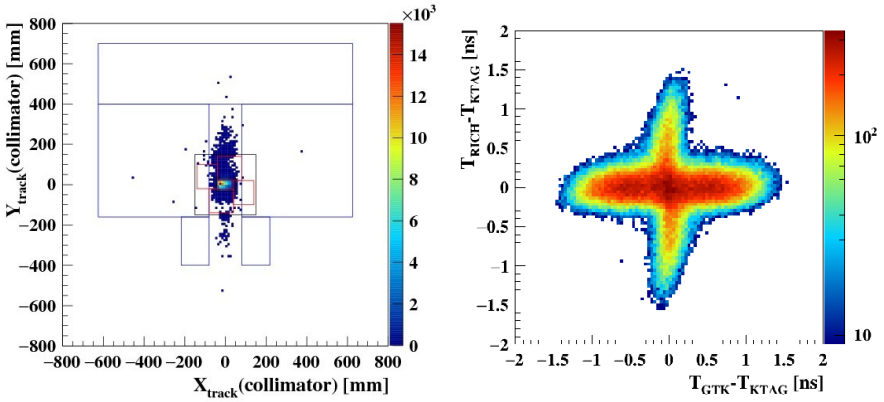

Figure 7: *a) position at the entrance of the fiducial region of π^+'s from a data sample enriched for upstream events. Blue lines correspond to the contour of the dipole before GTK3; red lines show the contour of the final collimator; black line indicate the acceptance region covered by CHANTI. b) time difference between RICH and KTAG versus GTK and KTAG for the same π^+'s of plot a).*

expected.

The $K^+ \to \pi^+\pi^+\pi^-$ decays could enter primarily region 2. The expected background is evaluated similarly to $K^+ \to \pi^+\pi^0$ and $K^+ \to \mu^+\nu$. Multiplicity rejection and kinematic cuts turn out to be very effective against $K^+ \to \pi^+\pi^+\pi^-$ decays and the expected background is found to be almost negligible (Tab. 1).

Background from $K^+ \to \pi^+\pi^-e^+\nu$ (K_{e4}) is expected in signal region 2. It is suppressed by multiplicity rejection, particle identification, kinematics and by the branching ratio [16] of 4.25×10^{-5}. As the K_{e4} kinematics is strongly correlated to the topology, the corresponding background (Tab. 1) is estimated using a MC sample of $4{\times}10^8$ simulated decays, validated on data using different K_{e4} enriched selections, orthogonal to $\pi\nu\nu$.

Considerations based on selection performances (Section 4) show that background from $K^+ \to e^+\pi^0\nu$, $K^+ \to \mu^+\pi^0\nu$ and $K^+ \to \pi^+\gamma\gamma$ decays is negligible.

Process	Expected events in signal regions
$K^+ \to \pi^+\pi^0(\gamma)$	$0.064 \pm 0.007_{stat} \pm 0.006_{syst}$
$K^+ \to \mu^+\nu(\gamma)$	$0.020 \pm 0.003_{stat} \pm 0.003_{syst}$
$K^+ \to \pi^+\pi^- e^+\nu$	$0.018^{+0.024}_{-0.017}\vert_{stat} \pm 0.009_{syst}$
$K^+ \to \pi^+\pi^+\pi^-$	$0.002 \pm 0.001_{stat} \pm 0.002_{syst}$
Upstream Background	$0.050^{+0.090}_{-0.030}\vert_{stat}$
Total Background	$0.15 \pm 0.09_{stat} \pm 0.01_{syst}$

Table 1: *Summary of the background estimation from the $\pi\nu\nu$ analysis of 2016 data. Here $K^+ \to \pi^+\pi^0(\gamma)$ ($K^+ \to \mu^+\nu(\gamma)$) stays for $K^+ \to \pi^+\pi^0$ ($K^+ \to \mu^+\nu$) plus $K^+ \to \pi^+\pi^0\gamma$ ($K^+ \to \mu^+\nu\gamma$) decays.*

In addition to K^+ decays in the fiducial region, backgrounds can originate from upstream events classified as π^+ from:

1. K^+ decays upstream of the decay region, most notably between GTK stations 2 and 3, matched to a pileup beam particle;

2. interactions of a beam π^+ mostly with GTK station 3, but also with station 2, matched to a pileup K^+;

3. interactions of a K^+ with material in the beam, produced either as prompt particle originating from the interaction or as a decay product of a neutral kaon.

The interpretation of the upstream events in terms of the above topologies is supported by a closer look to a $\pi\nu\nu$-like data sample enriched for upstream events. The position of the π^+ mesons at the entrance of the fiducial region (Fig. 7, a) indicates their origin upstream or via interactions in GTK stations and drives the choice of a geometrical cut covering the central aperture of the dipole (box cut defined by $|X_{track}| < 100$ mm and $|Y_{track}| < 500$ mm); the distribution of the time coincidence between KTAG-RICH and GTK-KTAG suggests an accidental source for these events (Fig. 7, b). The estimation of the upstream background is made on data using a purely data–driven method and is shown in Tab. 1, where The statistics of the data samples limits the accuracy of the final value.

Summing up the various the contributions, the overall final expected background in region 1 and 2 is $0.15 \pm 0.09_{stat} \pm 0.01_{syst}$ (Tab. 1).

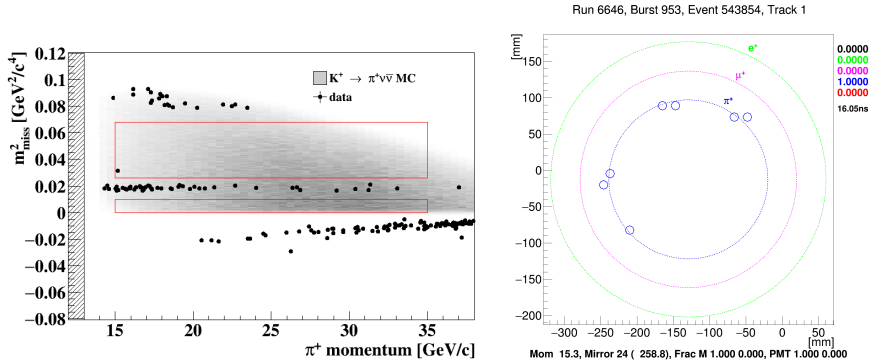

Figure 8: *a) m^2_{miss} as a function of P_{π^+} for PNN trigger data events (dots) passing the $\pi\nu\nu$ selection, but the cuts on m^2_{miss} and P_{π^+}. The grey area corresponds to the distribution of $\pi\nu\nu$ MC events. Red lines define the signal regions. The event observed in region 2 is shown. b) position of the hits in the RICH forming the ring associated to the π^+ of the observed event in region 2, as given by the RICH event display. The circles illustrate the positron, muon and pion hypothesis, showing a perfect agreement of the observed event with the pion hypothesis.*

7 Result

After un-blinding the signal regions, one event is found in region 2, as shown in Fig. 8 (a). The corresponding π^+ has a momentum of 15.3 GeV/c. The RICH clearly indicates that it is a pion (Fig. 8, b).

The statistical model is that of a counting experiment with the expected signal in Sec. 5 and the expected background in Tab. 1. The hybrid frequentistic–bayesian prescription described in [20] is applied to account for the uncertainty on the expected background. Using the CL_s method [21], the observed upper limit on the $K^+ \to \pi^+\nu\bar{\nu}$ branching ratio is

$$BR(K^+ \to \pi^+\nu\bar{\nu}) < 14 \times 10^{-10} \text{ @ } 95\% \text{ CL}, \tag{3}$$

where expected limits is $BR(K^+ \to \pi^+\nu\bar{\nu}) < 10 \times 10^{-10}$.

8 Conclusions

The first search for the decay $K^+ \to \pi^+\nu\bar{\nu}$ with kaon decays in-flight is reported. The data collected in 2016 amount to about 1% of the total exposure of the NA62 experiment in 2016-2018. The SES is found to be 3×10^{-10}. The analysis has revealed one candidate event compatible with the SM expectation (0.27) and with the background expectation (0.15). Interpreting the candidate as background leads to the upper limit 14×10^{-10} at 95% CL on the $K^+ \to \pi^+\nu\bar{\nu}$ branching ratio. The NA62 experiment has already collected more than 20 times the statistics presented here and the analysis of this larger data sample is in progress.

References

1. J.H. Christenson *et al*, Phys. Rev. Lett. **13**, 138 (1964).
2. A. J. Buras, D. Buttazzo, J. Girrbach–Noe and R. Knegjens, JHEP 1511 (2015) 33.
3. G. Buchalla and A. J. Buras, Nucl. Phys. B 548 (1999) 309.
4. A. J. Buras, M. Gorbhan, U. Haisch and U. Nierste, JHEP 11 (2006) 002.
5. J. Brod, M. Gorbahn and E. Stamou, Phys. Review D 83 (2011) 034030.
6. G. Isidori, F. Mescia and C. Smith, Nucl. Phys. B 718 (2005), 319.
7. F. Mescia and C. Smith, Phys. Review D 76 (2007), 034017.
8. M. Blanke, A.J. Buras and S. Recksiegel, Eur. Phys. J. C 76 (2016) no.4, 182.
9. M. Blanke, A. J. Buras, B. Duling, K. Gemmler and S. Gori, JHEP 0903 (2009) 108.
10. A.J. Buras, D. Buttazzo and R. Knegjens, JHEP 1511 (2015) 166.
11. G. Isidori, F. Mescia, P. Paradisi, C. Smith and S. Trine, JHEP 0608 (2006) 064.
12. T. Blazek and P. Matak, Nucl. Phys. Proc. Suppl. 198 (2010) 216.

13. M. Tanimoto and K. Yamamoto, PTEP 2016 (2016) no.12 123B02.

14. M. Bordone, D. Buttazzo, G. Isidori and J. Monnard, Eur. Phys. J. C 77 (2017) no.9 618.

15. C. Bobeth and A. J. Buras, JHEP 1802 (2018) 101.

16. C. Patrignani *et al*, Particle Data Group, Chin. Phys. C 40 (2016) 100001.

17. A.V. Artamonov *et al*, Phys. Rev. Lett. 101 (2008) 191802.

18. A.V. Artamonov *et al*, Phys. Rev. D 79 (2008) 092004.

19. E. Cortina Gil *et al*, J. Instrum. 12 (2017) P05025.

20. R.D. Cousins, et al., Nucl. Instrum. Methods A 529 (2008) 480.

21. A.L. Read, J. Phys. G 28 (2002) 2693.

Frascati Physics Series Vol. 66 (2018)
Frontier Objects in Astrophysics and Particle Physics
May 20-26, 2018

ASI programs in astronomy, astrophysics and fundamental physics

Elisabetta Cavazzuti
Agenzia Spaziale Italiana, Via del Politecnico snc, 00133 Roma

Abstract

ASI funds and leads scientific space-based projects in several science topics, among which astronomy, astrophysics and fundamental physics. Here I will review the main on-going programs and the near-future projects.

1 Introduction

Italian Space Agency funds and leads scientific space programs, since Phase 0/A studies, i.e. from paperwork only, to final delivery of the payloads and disposal of the mission (when is led by ASI). The department appointed to lead the astrophysics, cosmology and solar exploration programs is named Exploration and Observation of the Universe (hereafter EOS). Synergic with EOS is the Space Science Data Center (http://www.ssdc.asi.it/, hereafter SSDC, former ASDC). Data from all scientific missions funded by ASI end up being archived

at and distributed by the SSDC. Recently it has been created a so-called Research group, which is also (but not only) synergic with EOS and SSDC. ASI is part of the European Space Agency and cooperates as well in bilateral or multilateral programs with other space agencies (NASA, JAXA, Roscosmos, CNSA etc). Finally ASI owns and leads an equatorial ground base in Malindi (Kenya), involved in many space programs. Currently it is supporting among other programs AGILE, Swift and NuSTAR and it is foreseen to be involved in many future EOS missions. Last but not least, synergic with the EOS group is the italian scientific community (INAF, INFN, CNR, Universities, etc).

All these entities work together to define the road maps for the space-based scientific missions and experiments.

2 ASI science programs

EOS department involves programs from different scientific areas: cosmology, IR, optical and UV astronomy, high energy astrophysics, cosmic rays experiments, fundamental physics, solar system exploration and exoplanets. In this proceeding all but solar system and exoplanets programs will be considered.

Currently operating scientific missions supported by ASI are Newton-XMM (ESA), INTEGRAL (ESA), Swift (NASA), AGILE (ASI), Fermi (NASA), AMS-02 (DoE), NuSTAR (NASA), GAIA (ESA) and CALET (JAXA). For these missions, ASI funds the scientific teams in charge of on-orbit support and data analysis.

2.1 Programs in the development phase

The near future missions already approved to be launched and in the development phase are:

LARES–2 (ASI) – An experiment approved and led by ASI and planned for a launch in 2019. The main objectives of the LARES–2 experiment are gravitational and fundamental physics, including accurate measurements of General Relativity, in particular a test of frame-dragging aimed at achieving an accuracy of a few parts in a thousand, i.e., aimed at improving by about an order of magnitude the present state-of-the-art and forthcoming tests of this general relativistic phenomenon. LARES–2 will also achieve determinations in space geodesy (Ciufolini et al (2017) **?)**).

EUCLID (ESA) – Euclid is an ESA Medium Class mission in the Cosmic Visions program (see https://www.euclid-ec.org/ for details) foreseen to be launched in 2021. Euclid is primarily a cosmology and fundamental physics mission. Its main scientific objective is to understand the source of the accelerating expansion of the Universe and discover its very nature that physicists refer to as dark energy. Euclid will then address to the following questions: is dark energy merely a cosmological constant, as first discussed by Einstein, or is it a new kind of field that evolves dynamically with the expansion of the universe? Alternatively, is dark energy instead a manifestation of a breakdown of General Relativity and deviations from the law of gravity? What are the nature and properties of dark matter? What are the initial conditions which seed the formation of cosmic structure? What will be the future of the Universe over the next ten billion years?

Contribution from Italy are: for NISP infrared instrument, the Detector Processing Unit (DPU) / Detector Control Unit (DCU) with on-board data processing software, the high-level software for instrument control, the Grism Wheel Assembly (GWA) Unit and the EEWS of warm electronics and instrument; for the VIS visible instrument, the Command and Data Processing Unit (CDPU) and related on-board software. Also within the consortium, Italy is responsible for the Euclid Consortium Science Ground Segment (EC-SGS) of the mission, which will receive and analyze the data produced on board. Italian scientists also hold key roles in several Science Working Groups (SWG) of the consortium and in the various mission and consortium boards.

IXPE (NASA) – The Imaging X-ray Polarimetry Explorer (IXPE) is a NASA mission to which Italy contributes with the whole focal plane providing X-ray polarimeters (see http://ixpe.msfc.nasa.gov for details). Its launch is foreseen on April 2021. IXPE exploits the polarization state of light from astrophysical sources to provide insight into our understanding of X-ray production in objects such as neutron stars and pulsar wind nebulae, as well as stellar and supermassive black holes. Technical and science objectives include: improving polarization sensitivity by two orders of magnitude over the X-ray polarimeter aboard the Orbiting Solar Observatory OSO-8, providing simultaneous spectral, spatial, and temporal measurements, determining the geometry and the emission mechanism of Active Galactic Nuclei and microquasars, finding the magnetic field configuration in magnetars and determining the magnitude of

the field, finding the mechanism for X ray production in pulsars (both isolated and accreting) and the geometry, determining how particles are accelerated in Pulsar Wind Nebulae.

Italy holds the Co-PIship of the mission and contributes with the whole focal plane, i.e. 3 detector Units and the Detector Service Unit, along with the related software. Italy contributes also to the Ground Segment with the development of part of the instrument software and the involvement of the SSDC as possible mirror archive.

H.E.R.M.E.S. (ASI) – High Energy Rapid Modular Ensemble of Satellites (H.E.R.M.E.S.) is a swarm of LEO nanosatellites equipped with keV-Mev scintillators, with sub μs time resolution. It is a fully italian project led by University of Cagliari (see http://hermes.dsf.unica.it/). The aim is Fast and precise measure of the position of bright, transient HE events & fine temporal structure [GRBs, GW events, FRB HE counterparts, magnetar fares].

Characteristics of the project are: scintillator Crystals: CsI (classic) or LaBr3 or CeBr3 (rise-decay: 0.5 - 20 ns); Photo-detector: Silicon Photo Multiplier (SiPM) or Silicon Drift Detector (SDD); Effective area: 10 $\times$ 10 cm; Energy band: 3 keV - 50 MeV; Energy resolution: 15% at 30 keV; Temporal resolution: $\leq$ 10 nanoseconds

Athena (ESA) – Advanced Telescope for High-ENergy Astrophysics – will be an X-ray telescope designed to address the Cosmic Vision science theme 'The Hot and Energetic Universe'. The theme poses two key astrophysical questions: how does ordinary matter assemble into the large-scale structures we see today? and how do black holes grow and shape the Universe?

To address the first question, it will be necessary to map hot gas structures in the Universe – specifically the gas in clusters and groups of galaxies, and the intergalactic medium – determine their physical properties and track their evolution through cosmic time.

To answer the second question, supermassive black holes (SMBH) must be revealed, even in obscured environments, out into the early Universe, and both the inflows and outflows of matter and energy as the black holes grow must be understood.

Because most of the baryonic component of the Universe is locked up in hot gas at temperatures of millions of degrees, and because of the extreme ener-

getics of the processes close to the event horizon of black holes, understanding the Hot and Energetic Universe requires space-based observations in the X-ray portion of the electromagnetic spectrum.

By combining a large X-ray telescope with state-of-the-art scientific instruments, Athena will be able to make an important contribution to answering these questions.

Contribution from Italy: XIFU CoPI-ship; contribution to XIFU with anticoncidence TES microcalorimeter & background, Instrument Control Unit, Filters, Science Innovation Center; contribution to WFI: contribution synergical with XIFU. The italian team is also involved in the ESA Study Team and co-chairs 9 of the Mission & Science Worging Groups.

Lisa (ESA) – The Laser Interferometer Space Antenna (LISA) will be the first space-based gravitational wave observatory. Selected to be ESA's third large-class mission, with a launch in 2034, it will address the science theme of the Gravitational Universe. LISA will consist of three spacecraft separated by 2.5 million km in a triangular formation, following Earth in its orbit around the Sun.

The contribution from Italy will be the Gravitational Reference Sensor (GRS) on board LISA PF which needs to be optimized for LISA.

LSPE (ASI) – The LSPE is a project aimed at measuring the polarization of the Cosmic Microwave Background (CMB) at large angular scales, and in particular to constrain the curl component of CMB polarization (B-modes) produced by tensor perturbations generated during cosmic inflation, in the very early universe. A second target is to produce wide maps of foreground polarization generated in our Galaxy by synchrotron emission and interstellar dust emission. These will be important to map Galactic magnetic fields and to study the properties of ionized gas and of diffuse interstellar dust in our Galaxy. The mission is optimized for large angular scales, with coarse angular resolution (around 1.5 degrees FWHM), and wide sky coverage (25% of the sky). The project is splitted in two experiments: STRIP (STRatospheric Italian Polarimeter, Bersanelli et al.(2012) [?]) – an array of coherent polarimeters using cryogenic HEMT amplifiers – will survey the sky at 43 and 90 GHz. SWIPE (Short Wavelength Instrument for the Polarization Explorer, de Bernardis et al.(2012) [?]) – an array of bolometric polarimeters, using large

throughput multi-mode bolometers and rotating Half Wave Plates (HWP) – will survey the same sky region in three bands at 95, 145 and 245 GHz. The wide frequency coverage will allow optimal control of the polarized foregrounds, with comparable angular resolution at all frequencies. SWIPE will be put on a stratospheric balloon and will fly in a circumpolar long duration mission during the polar night. Using the Earth as a giant solar shield, the instrument will spin in azimuth, observing a large fraction of the northern sky. The payload will host two instruments. STRIP will be ground based and synergic with SWIPE observations.

2.2 Programs in Phase A with pending approval

There are projects still in the approval phase for which ASI funds the study activity and these are:

eXTP (CNSA, CAS) – The enhanced X-ray Timing and Polarimetry mission (eXTP) (Zhang et al.(2016) **?**)) is a Chinese-led science mission designed to study the state of matter under extreme conditions of density, gravity and magnetism. Primary goals are the determination of the equation of state of matter at supra-nuclear density, the measurement of QED effects in highly magnetized star, and the study of accretion in the strong-field regime of gravity. Primary targets include isolated and binary neutron stars, strong magnetic field systems like magnetars, and stellar-mass and supermassive black holes.

The mission carries a unique and unprecedented suite of state-of-the-art scientific instruments enabling for the first time ever the simultaneous spectral-timing-polarimetry studies of cosmic sources in the energy range from 0.5-30 keV (and beyond). Key elements of the payload are: the Spectroscopic Focusing Array (SFA); the Large Area Detector (LAD); the Polarimetry Focusing Array (PFA); the Wide Field Monitor (WFM).

The eXTP international consortium includes major institutions of the Chinese Academy of Sciences and Universities in China, as well as major institutions in several European countries and other International partners. Two of the four instruments will be under responsibility of China and two under responsibility of Europe.

The perspective Italian contributions to the eXTP mission include: Coordination of the European Consortium; Contribution to the science case and

mission definition; PI-ship of the LAD instrument; Large-area Silicon Drift Detectors for the LAD; AIVT of the LAD 1; Physical calibrations of the LAD; Large-area Silicon Drift Detectors for the WFM; Front-End Electronics board and AIV for the WFM; Physical calibrations of the WFM Detection Plane (i.e., at the detectors level); SFA and PFA optical design; PFA GPD and Back-End Electronics; Malindi ground station; Support to scientific software and archive.

THESEUS (ESA) – is a mission concept proposed in response to the ESA call for medium-size mission (M5) within the Cosmic Vision Programme and selected by ESA on 2018 May 7 to enter an assessment phase study (see https://www.isdc.unige.ch/theseus/ for details). The mission is designed to vastly increase the discovery space of the high energy transient phenomena over the entirety of cosmic history. Its primary scientific goals will address the Early Universe ESA Cosmic Vision themes "How did the Universe originate and what is made of?" (4.1, 4.2 and 4.3) and will also impact on "The gravitational wave Universe" (3.2) and "The hot and energetic Universe" themes. This is achieved via a unique payload providing an unprecedented combination of: 1) wide and deep sky monitoring in a broad energy band (0.3keV – 20 MeV); 2) focusing capabilities in the soft X-ray band providing large grasp and high angular resolution; and 3) on board near-IR capabilities for immediate transient identification and redshift determination.

Italy has the PI-ship (Lorenzo Amati, University of Ferrara) and would provide the X-Gamma rays Imaging Spectrometer (XGIS): 3 coded-mask X-gamma ray cameras using bars of Silicon diodes coupled with CsI crystal scintillators observing in 2 keV – 10 MeV band, a FOV of $\sim$2 sr, overlapping the SXI, with $\sim$ 5' source location accuracy.

LiteBird (JAXA) – is a satellite led by JAXA (see http://litebird.jp/eng/ and http://www.litebird-europe.eu/ for details) that will search for primordial gravitational waves emitted during the cosmic inflation era (around $10^{-}38$ sec after the beginning of the Universe). Its goal is to test representative inflationary models (single–field slow-role models with large field variation) by performing an all-sky CMB polarization survey.

Primordial gravitational waves are expected to be imprinted in the CMB polarization map as special patterns, called the "B-mode". If we succeed to detect them, it will provide entirely new and profound knowledge on how our

Universe began.

From the viewpoint of high-energy physics or elementary particle physics, the observation of the CMB B-mode is very important because it will allow us to search for physics in ultra high-energy scales, which are not accessible with man-made accelerators. Measurements of CMB polarization will open a new era of testing theoretical predictions of quantum gravity, including those by the superstring theory.

LiteBIRD was recently nominated one of the 7 large-scale projects in the MEXT 2017 roadmap. Support from NASA has funded detector and cryogenic readout system development in the USA for Phase A, and is now supporting risk-mitigation R&D.

With the LiteBIRD baseline design still under discussion, Europe has an opportunity to provide significant impact on the final payload by delivering the High-Frequency Telescope (HFT) unit.

2.3 R&D and Data Analysis activities

ASI is funding also two main stream activities on cosmology and high energy astrophysics. Under these activities, research and development are funded. ASI issues calls for R&D relying on international peer reviews to select submitted proposals, and participates to MIUR calls (Progetti Premiali) . Thanks to past R&D calls the polarimeter has been funded leading to the selection of IXPE mission by NASA. This indicates, if still necessary to be understood, that R&D is mandatory for healthy scientific communities.

In the last call the following projects have been funded:

- 3D-CZT Module (3DCaTM) for spectroscopic imaging, timing and polarimetry in hard X-/soft γ rays satellite mission (E. Caroli, INAF)
- FluChe - Fluorescence and Cherenkov light detection with SiPM for space applications (O. Catalano, INAF)
- Increase of the Technological Readiness Level for the realization of hard X-/soft Gamma-ray Laue optics (E. Virgili, Uni Ferrara)
- STAR-X: the next generation of X-ray imaging surveys (R. Gilli, INAF)
- POX (Pangu [sub-GeV γ ray telescope] Optimization and eXperimental verification) (D. D?Urso, Uni Sassari)

Data analysis as well is funded for both on orbit missions with ASI contribution and proposals approved by Time Allocation Committees of other missions (Chandra, HST etc). In the last call 20 proposals for 18-month long projects have been funded.

3 Acknowledgements

This proceeding has been possible thanks to the whole italian scientific community.

References

1. I. Ciufolini *et al*, A new laser-ranged satellite for General Relativity and space geodesy: I. An introduction to the LARES2 space experiment, The European Physical Journal Plus, 2017, doi = 10.1140/epjp/i2017-11635-1.
2. Bersanelli, M., Mennella, A., Morgante, G., et al. 2012, SPIE, 8446, 84467C
3. de Bernardis, P., Aiola, S., Amico, G., et al. 2012, SPIE, 8452, 84523F
4. Zhang, S. N., Feroci, M., Santangelo, A., et al. 2016, SPIE, 9905, 99051Q

Frascati Physics Series Vol. 66 (2018)
Frontier Objects in Astrophysics and Particle Physics
May 20-26, 2018

POEMMA and EUSO-SPB: Space Probes of the Highest Energy Particles

Angela V. Olinto,
The University of Chicago, Chicago, IL, USA
for the JEM-EUSO [1)] and POEMMA [2)] collaborations

Abstract

Space probes enable the monitoring of colossal volumes of the Earth's atmosphere to study extensive airshowers (EASs) produced by ultra-high energy cosmic rays (UHECRs) and cosmic neutrinos (CNs). We discuss two leading projects designed to monitor the atmosphere from above to detect EASs through fluorescence and Cherenkov signals. The Probe Of Extreme Multi-Messenger Astrophysics (POEMMA) mission is designed to observe UHECRs and CNs from space with the goals of a significant increase in statistics of observed UHECRs at the highest energies and the target of opportunity search for CNs from extremely energetic transient astrophysical events. The Extreme Universe Space Observatory on a Super Pressure Balloon-2 (EUSO-SPB2) is being built to open the new era of space observations of fluorescence and Cherenkov from UHECRs. Both missions will provide new windows onto the most energetic environments and events in the universe and onto particle interactions well beyond accelerator energies.

Figure 1: Missions to study UHECRs and cosmic neutrinos (CNs) from space. POEMMA (Probe Of Extreme Multi-Messenger Astrophysics) to observe EASs from lower Earth orbit, and EUSO-SPB2 (Extreme Universe Space Observatory on a Super Pressure Balloon 2) from about 33 km. From space the volume of atmosphere monitored can be many orders of magnitude larger than on the ground.

1 Introduction

The origin of the highest energy cosmic particles, the ultra-high energy cosmic rays (UHECRs) is still unknown, after over half a century since their discovery [3]. The observation that cosmic rays can exceed 10^{20} eV poses some interesting and challenging questions: Where do they come from? How are they accelerated to such high energies? What do they tell us about these extreme cosmic accelerators? How strong are the magnetic fields that they traverse on their way to Earth? How do they interact in the source, in extragalactic and galactic space, and in the atmosphere of the Earth? What can we learn about particle interactions at these extreme energies? The discovery of their sources will reveal the workings of the most energetic astrophysical accelerators in the universe and enable the study of particle interactions at these otherwise inaccessible energies.

Candidate sources range from the birth of compact objects to explosions related to gamma-ray bursts or to events in active galaxies (see, e.g.,

Figure 2: EUSO-SPB1 was launched April 24th 23:51 UTC 2017 from Wanaka, New Zealand as a mission of opportunity on a NASA super pressure balloon test flight planned to circle the southern hemisphere.

reviews [4, 5]). Current observations show a spectrum and sky distribution consistent with an origin in extragalactic astrophysical sources. Questions arise from an unexpected evolution of composition indicators and hints of correlations and anisotropies in the sky distribution.

As UHECRs propagate from distant extragalactic sources they interact with cosmic background radiation losing energy through the Greisen-Zatsepin-Kuzmin (GZK) effect [6] and producing cosmogenic neutrinos [7]. Observations from the leading UHECR observatories, the Pierre Auger Observatory [8] in Mendoza, Argentina, and the Telescope Array (TA) [9] in Utah, USA, show a spectral shape consistent with the GZK effect, but also explainable by the maximum energy of the unidentified astrophysical accelerators, $E_{\max}$. Higher statistics measurements of both the flux and the composition of UHECRs above 10 EeV (1 EeV = 10^{18} eV) together with the detection of the flux of cosmogenic neutrinos can settle this long-standing mystery (see e.g., [4, 5] for more details).

Observations by POEMMA and EUSO-SPB2 (see Figure 1) aim at reaching the necessary sensitivity at the highest energies to achieve charged particle astronomy and to observe high energy cosmic neutrinos (CNs), which will further illuminate the workings of the universe at these extreme energies. In addition to fostering a new understanding of high-energy astrophysical phenomena, the study of ultra-high energy cosmic rays and neutrinos can constrain the

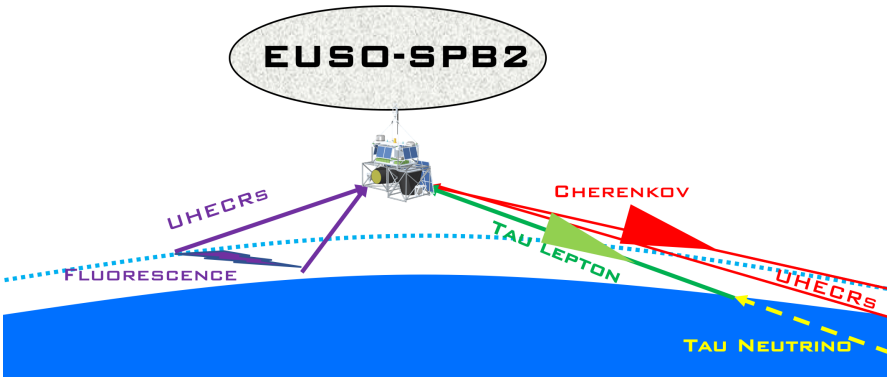

Figure 3: EUSO-SPB2 detection modes: fluorescence from below the balloon altitude and Cherenkov from above and below the limb of the Earth.

structure of the Galactic and extragalactic magnetic fields as well as probe particle interactions at energies orders of magnitude higher than achieved in terrestrial accelerators.

POEMMA, the Probe Of Extreme Multi-Messenger Astrophysics, [10] was selected by NASA for an Astrophysics Probe Mission Concept Study (under ROSES-2016) in early 2017. The comprehensive 18-month POEMMA study involves instrument and mission definition at the Integrated Design Center (IDC) of the Goddard Space Flight Center (GSFC) and an independent cost assessment in preparation for the 2020 Astronomy and Astrophysics Decadal Survey [11] in the United States. Here we report on the preliminary concept for POEMMA ahead of the POEMMA Study Report to be submitted to NASA.

EUSO-SPB2 is the second generation of the Extreme Universe Space Observatory on a Super Pressure Balloon, which is being built under the JEM-EUSO [1] program [12]. EUSO-SPB1 [13] was launched April 24th 23:51 UTC 2017 from Wanaka, New Zealand as a mission of opportunity on a NASA super pressure balloon test flight planned to circle the southern hemisphere (see Figure 2). After 12 days 4 hours aloft, the flight was terminated prematurely in the Pacific Ocean about 300 km SE of Easter Island. EUSO-SPB2 [14] is designed to be more sensitive than EUSO-SPB1 and to test both the fluorescence and the Cherenkov techniques for observing UHECRs and CNs from above.

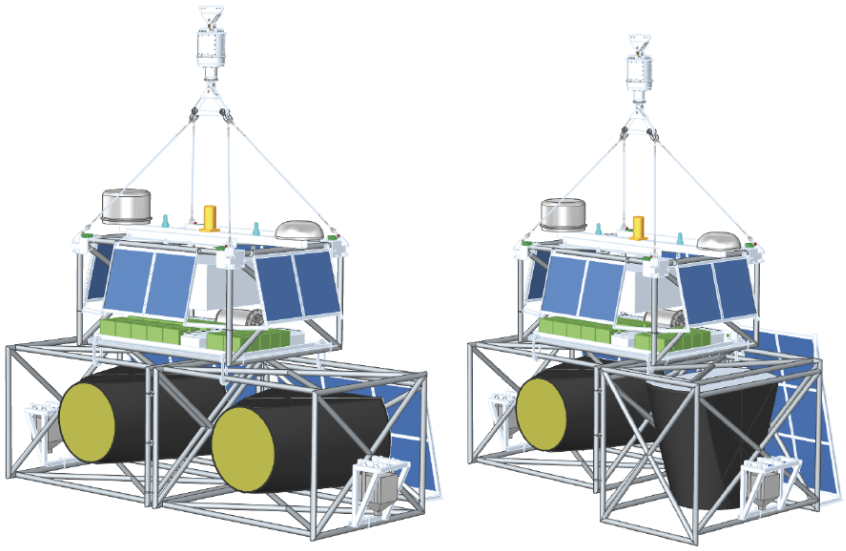

Figure 4: EUSO-SPB2 design with two telescopes: a Fluorescence telescope and a Cherenkov telescope. The fluorescence telescope can observe at nadir, while the Cherenkov telescope is aimed at the limb of the Earth.

EUSO-SPB2 will fly two different cameras serving also as a pathfinder for the POEMMA hybrid camera design.

2 EUSO-SPB2

The second generation Extreme Universe Space Observatory on a Super-Pressure Balloon (EUSO-SPB2) is under construction to fly from Wanaka, NZ by 2022. The primary scientific goal of EUSO-SPB2 [14] is to make the first observations of UHECR extensive air showers via two complementary techniques. EUSO-SPB2 will look down on the atmosphere with an optical fluorescence detector from the near space altitude of 33 km and will look towards the limb of the Earth to observe Cherenkov signal of UHECRs from above the limb and CNs showers generated just below the limb (see Figure 3).

EUSO-SPB2 is composed of two telescopes: a fluorescence telescope and

a Cherenkov telescope. The fluorescence telescope can observe from nadir to the limb, while the Cherenkov telescope is aimed at the limb of the Earth (see Figure 4). (Simulations to obtain the optimal pointing angle for fluorescence are underway.)

Both telescopes are based on a Schmidt optical design of spherical mirrors with large fields of view (FoVs). The mirrors are designed to be $\sim$ 2m by 1m, with a larger FoV in the horizontal direction (between 36^o and 45^o) and shorter FoV in the vertical direction (between 11^o and 5^o) to maximize observations along the horizon for both limb (in Cherenkov) and tilted from nadir (fluorescence) modes. The optical system collection area will be about 0.8 m^2. The Cherenkov telescope will have a bifocal design to ensure two measurements of the same Cherenkov event with the same telescope projected into two areas of the focal surface. The bifocal technique will constrain the rate of false positives from background, such as cosmic rays hitting a pixel of the focal surface.

The fluorescence camera is based on the JEM-EUSO design of photodetector modules (PDM) built of multi-anode photomultiplier tubes (MAPMTs) as flown in sub-orbital space in EUSO-Balloon [15] and EUSO-SPB1 [13] and soon to be deployed in the International Space Station (ISS) as mini-EUSO [16]. (1 PDM = 36 MAPMTs = 2,304 pixels.) The EUSO-SPB2 fluorescence camera will be composed of 3 PDMs (6,912 pixels), or three times the area of EUSO-SPB1, and a faster time resolution of 1μs compared to 2.5μs for EUSO-SPB1. The new design lowers the energy threshold of EUSO-SPB2 to allow for larger number of detected events per flight day. The focal surface of the Cherenkov telescope has an innovative design based on SiPMT sensors and a dedicated ultrafast electronics to detect the fast Cherenkov emission of EASs from UHECRs above the Earth's limb and to search for EASs produced by τ-lepton decays leaving from the ground just below the limb. The τ-lepton decay induced showers are the signature of tau CNs skimming the Earth.

EUSO-SPB2 will be a pioneering mission to first detect fluorescence and Cherenkov from EASs from above. The mission will develop the innovative techniques leading the way towards a space-based program of UHECR and CN observatories.

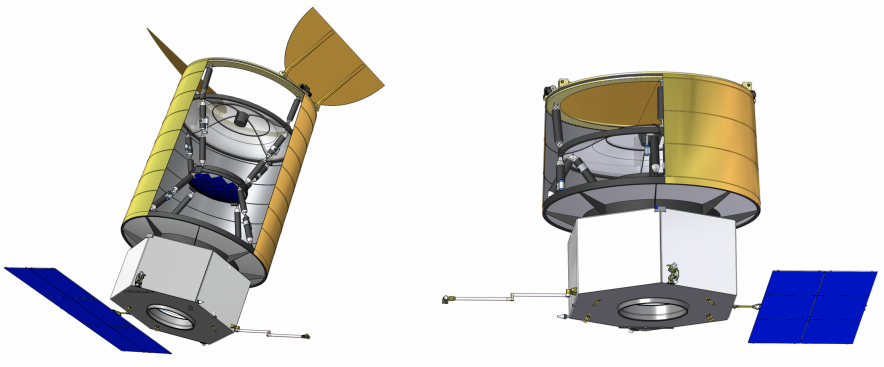

Figure 5: POEMMA deployed with open shutter doors (left) and in stowed position for launch (right). Openings on the light shield display the internal structure of corrector plate and focal surface in the middle of the telescope (blue). Spacecraft bus shown with solar panel (blue) and communications antenna deployed in both images.

3 POEMMA

POEMMA is being designed to enable charged particle astronomy with a significant increase in exposure to the highest energy particles ever observed, UHECRs, and the capability to observe cosmic neutrinos (CNs) through the observations of fluorescence at extreme energies and Cherenkov radiation at lower energies produced by upward-going τ-lepton decays (see Figures 5 to 7). POEMMA will provide an all-sky survey of UHECRs (Figure 9) with an order of magnitude larger exposure compared to ground array measurements (Figure 8) and two orders of magnitude higher exposure in fluorescence mode when compared to ground fluorescence observations (significantly improving the determination of composition above 10s of EeVs). The increase in exposure combined with the full-sky coverage should reveal the sources of these extremely energetic particles that are known to reach Earth from extragalactic sources and that are yet to be identified. These unidentified sources achieve extreme acceleration through mechanisms that are not presently understood.

In addition to the significant increase in UHECR statistics though the

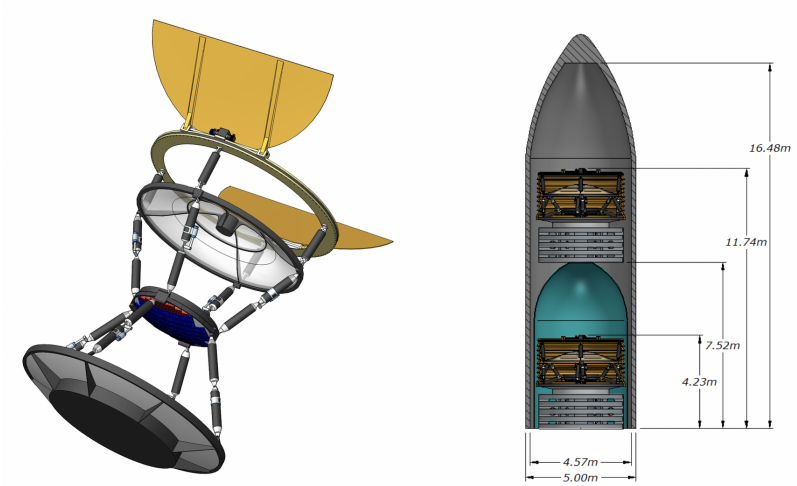

Figure 6: Left: POEMMA structure in deployed observing mode. POEMMA 4m diameter Schmidt optics mirror (grey at the bottom) with 45^o field of view (FoV), focal surface with blue (MAPMT) and red (SiPM) sensors, corrector plate on top (with infra-red camera at its center); and open shutter doors. Right: Atlas V accommodation of both satellites in stowed position for launch. Lower unit in a capsule for structural safety during launch.

fluorescence observations, POEMMA is being designed to detect Cherenkov radiation of upward EASs initiated by τ-lepton decay, where the τ-lepton is the product of ν_τ interacting in the Earth with energies above about 30 PeV. POEMMA also has sensitivity to neutrinos with energy above 30 EeV via the observation of (mainly) electron neutrinos in the atmosphere using EAS fluorescence measurements. The observation of cosmic neutrinos (both astrophysical and cosmogenic) will help solve the puzzle of the origin of UHECRs. It will also begin a new field of astroparticle physics with the study of neutrino properties at energies orders of magnitude above those reached by human-made accelerators.

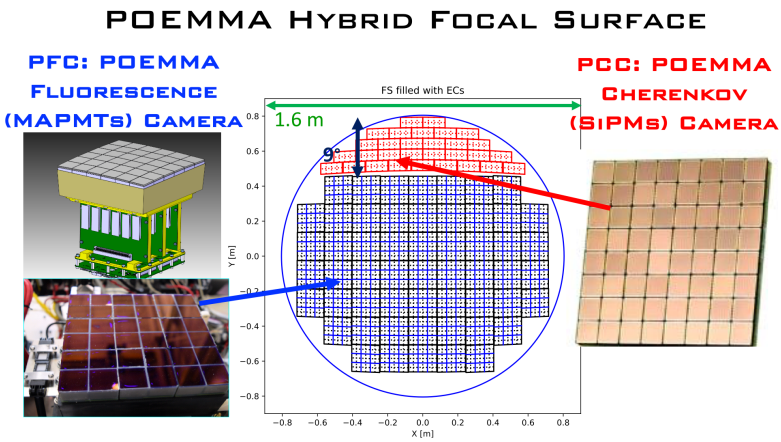

Figure 7: POEMMA Hybrid Focal Surface of 1.6m diameter. PFC (POEMMA Fluorescence Camera) composed of 55 PDMs (total 126,720 MAPMT pixels) with 1μs time gates; and PCC (POEMMA Cherenkov Camera) with 28 SiPM focal surface units (FSU) (total 14,336 pixels; 1 FSU = 64x4x2 = 512 pixels). PCC observes solid angle of 9^o by 30^o to monitor the Earth's limb for up-going EASs.

3.1 POEMMA Design

The POEMMA design combines the concept developed for the Orbiting Wide-field Light-collectors (OWL) [17, 18] mission, the experience of the Extreme Universe Space Observatory (EUSO) on the Japanese Experiment Module (JEM-EUSO) [12, 19] fluorescence detection camera, with the recently proposed CHerenkov from Astrophysical Neutrinos Telescope (CHANT) [20] concept to form a multi-messenger probe of the most extreme environments in the universe.

Building on the OWL concept, POEMMA is composed of two identical satellites flying in formation with the ability to observe overlapping regions during moonless nights at angles ranging from Nadir to just above the limb of the Earth. The satellites will fly at an altitude of about 525 km with separations ranging from 300km for stereo fluorescence UHECR observations to 25km when pointing at the Earth's limb for both fluorescence and Cherenkov observations

of UHECRs and CNs (see Figure 10).

POEMMA satellites detect UHECRs through the observation of particle cascades (or EASs) produced by the interaction of UHECRs or tau-decays with the Earth's atmosphere. Particles in EASs excite nitrogen molecules in the atmosphere, which fluoresce in the ultraviolet (UV) and can be observed by fast UV cameras (1μs). The fluorescence technique has been perfected by the leading ground-based UHECR observatories, Auger [8] and TA [9], while EUSO-Balloon [15] and EUSO-SPB1 [13] recently pioneered the fluorescence technique from suborbital space.

POEMMA specifications (see Figures 5,6, and 7).
Two 4 meter F/0.64 Schmidt telescopes: 45 ^{o} FoV
Hybrid focal surface (MAPMTs and SiPM); 3mm pixels
Instrument Mass: 1,550 kg
Primary Mirror: 4 meter diameter
Corrector Lens: 3.3 meter diameter
Focal Surface: 1.6 meter diameter
Optical Effective Area: from 6 to 2 m^2
Power: 590 W
Data: 1 GB/day

Each POEMMA satellite consists of a 4-meter diameter Schmidt telescope with a fast optical design. The optical effective area ranges from 6 to 2 m^2 depending on the angle of incidence. Each POEMMA telescope monitors a massive 45^o field of view (FoV) with a refractive aspheric aberration corrector plate. A lens-cap lid (or shutter door) and a cylindrical light shield shroud protect the mirror of stray light and micrometeoroid. The mirrors act as large light collectors with modest imaging requirements.

The POEMMA focal surface is composed of a hybrid of two types of cameras (see Figures 6 and 7): over 85% of the focal surface is dedicated to the POEMMA fluorescence camera (PFC), while POEMMA Cherenkov camera (PCC) occupies the crescent moon shaped edge of the focal surface, which images the limb of the Earth. The PFC is composed of the EUSO designed Photo Detector Modules (PDM) based on multi-anode photomultiplier tubes (MAPMTs) as flown in sub-orbital space in EUSO-Balloon [15] and EUSO-SPB1 [13]. The typical time between images for the PFC is 1μsec. The

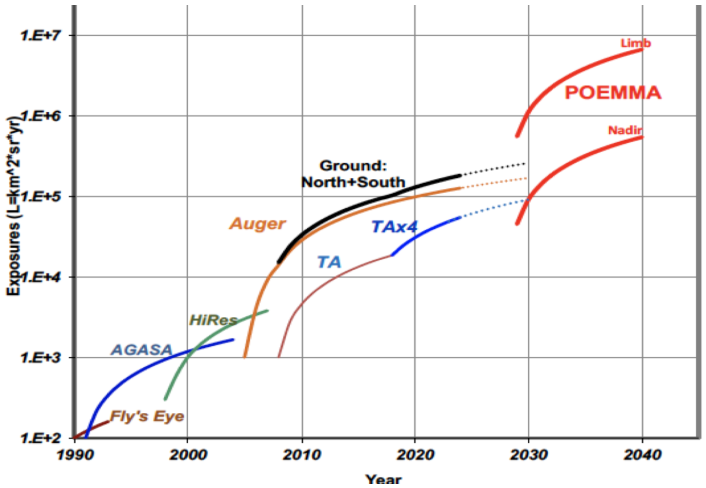

Figure 8: POEMMA exposure as a function of time as compared to current ground-based UHECR experiments and future plans for the decade. POEMMA exposure grows from observing Nadir to the direction of the Earth's limb.

much faster POEMMA Cherenkov camera (PCC) is composed of Silicon photomultipliers (SiPMs) designed to detect the 10ns to 100ns Cherenkov flashes. The PFC registers UHECR tracks from Nadir to just below the Earth's limb, while the PCC registers light within the Cherenkov emission cone of up-going showers around the limb of the Earth and also from UHECRs above the limb of the Earth (see Figure 10).

3.2 POEMMA Science Goals

POEMMA will provide a new window onto the universe's most energetic environments and events. The instrument is designed to help answer the following science questions.

What objects can accelerate particles to ultra-high energies? To discover the sources of UHECRs, POEMMA will survey from space orders of magnitude larger volumes of the atmosphere when compared to ground observatories over the full sky with nearly uniform exposure (see Figure 8 and 9). The related questions of *how are the sources distributed in the sky?* will be addressed with

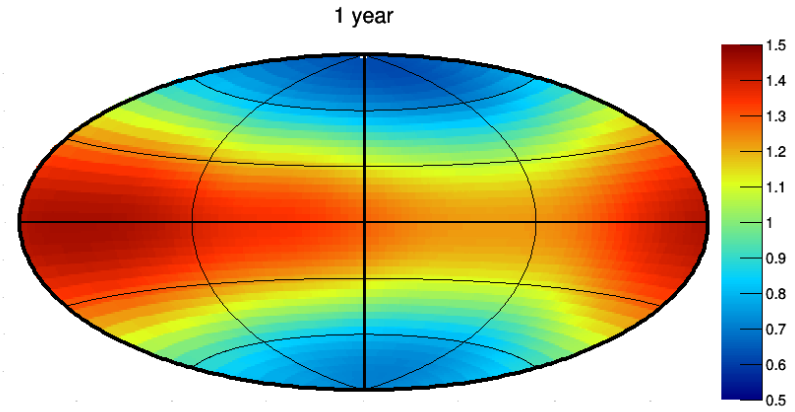

Figure 9: POEMMA's UHECR sky exposure, in declination versus right ascension for one year with the color scale denoting the exposure variations in terms of the mean response.

a full sky map of UHECRs with significantly higher statistics at the highest energies, where pointing to the sources becomes feasible (above ∼10 EeV). POEMMA is designed to reach unprecedented geometrical apertures $> 10^6$ km^2 sr yr, which, after duty cycle corrections, correspond to annual exposures of more than 10^5 km sr yr at the highest energies. POEMMA will also have high angular resolution ($\sim 1^o$).

POEMMA will enable more sensitive sky maps leading to the discovery of the brightest sources of UHECRs in the sky, which are likely to be relatively nearby (within ∼100 Mpc). The appearance of nearby sources in the sky is regulated by the GZK effect, which suppress the contribution from very distant accelerators at energies above about 60 of EeV. The 10 EeV UHECR sky is isotropic because sources throughout the observable universe contribute without any damping, while the 100 EeV UHECR sky should only show the nearby sources as the GZK effect obfuscates sources further then 100 Mpc moving closer to 10 Mpc at 100 EeV. A clear source distribution will become apparent when a high statistics map above 60 EeV is produced by POEMMA. In addition, observations above 10s of EeV avoid large deviations (compared to

the few degrees angular resolution) from source to arrival directions on Earth due to cosmic magnetic fields. The angular size of the nearby sources in the sky will probe the magnitude and structure of extragalactic and galactic magnetic fields. Above 10s of EeV, *Charged Particle Astronomy* is finally attainable.

POEMMA will also address *what is the composition of the UHECRs above 10 EeV and how does it evolve as energies reach 100 EeV?* POEMMA stereo observations of UHECRs will yield significant increase in measurements of the maximum of extensive airshowers, $X_{\rm max}$, with rms resolution below ~ 30 g/cm^2 at the highest energies. A large sample of well reconstructed events with better $X_{\rm max}$ separation will be used to distinguish light and heavier nuclei above 10s EeV. These composition measurements together with spectrum and sky distribution of anisotropies will determine the source class of UHECRs.

What are the sources of cosmic neutrinos? By observing the Cherenkov signal from τ decays from the limb of the Earth, POEMMA will search for cosmic neutrinos for a wide range of energetic transient event models. POEMMA can observe tau neutrinos at energies above 30 PeV to discover neutrinos from transient events. POEMMA can search for cosmic neutrinos with two techniques. With the same system designed to observe UHECRs, the PFC can detect deeply penetrating horizontal showers initiated by all flavors of EeV neutrinos in the atmosphere. In addition, the PCC based on the CHANT concept can observe the signal produced from tau neutrinos from above about 30 PeV (where astrophysical IceCube neutrinos are expected) to 10 EeV (where cosmogenic neutrinos can be discovered). The observations of neutrinos from energetic astrophysical transients will establish new astroparticle studies of neutrino properties energies well above those accessible in human-made laboratories.

Additional science themes include the study of *how strong are magnetic fields in the extragalactic medium?* Cosmic magnetic fields are traditionally challenging to measure and very little is known about magnetic fields outside galaxies and clusters of galaxies. The pointing pattern to UHECR sources will constrain these extragalactic fields directly. POEMMA will also study atmospheric phenomena in the optical and the UV such as transient luminous events in the upper atmosphere, will observe meteors arriving on Earth, and will search for meteorite (see, e.g., similar studies for JEM-EUSO in [21, 22]).

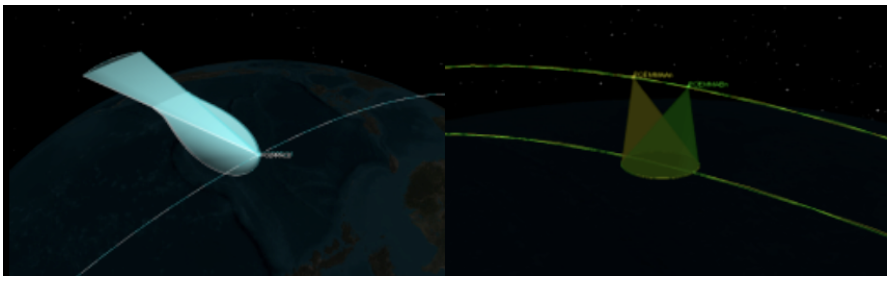

Figure 10: Illustration of two modes of observations by POEMMA: stereo fluorescence mode (right) for precision UHECR observations; and large geometry Cherenkov and Fluorescence observation mode towards the limb for both UHECRs and CNs (left). The two spacecraft are separated by 300 km in stereo mode (right), while for the limb observing mode their separation is only 23 km (left).

3.3 POEMMA Mission Overview

The POEMMA mission involves two satellites flying in formation in a relatively low-altitude (525 km), near-equatorial orbit (28.5^o). Each satellite is independent. Satellites will be launched stowed. Once on orbit, the telescopes will be deployed along with the solar array, light shield, and the communications antenna. The mirror and data module are attached to the satellite bus.

Both satellites can be launched as a dual-manifest on the same launch vehicle in an Atlas V using the long payload fairing as shown in Figure 6. The satellites will be inserted into a circular orbit at an inclination of about $28.5^{\rm o}$ and an initial altitude of 525 km and a separation of 300 km. The most common flight configuration will be the UHECR stereo observation mode, shown in (Figure 10 right). The target-of-opportunity (TOO) observing mode will require a maneuver to closer distance such that both satellites observe the same Cherenkov signal from Earth-skimming neutrinos from the transient source. Once extreme transient event alerts are received, for example, from the gravitational wave signature of a binary neutron-star merger, the satellites will maneuver to a closer separation distance of about 25km and an appropriate attitude to follow the target-of-opportunity (TOO) of the transient source as it rises and sets in the Earth's limb (Figure 10 left). While the PCC is searching for neutrinos from the TOO, the PFC continues to observe UHECRs with a

monocular view of EASs. A sequence of observing formation stages, varying between stereo and TOO modes, will be planned to address each science goal for the minimum 3 year mission with a 5 year mission goal.

4 Acknowledgement

The POEMMA concept study is funded by NASA Award NNX17AJ82 at the University of Chicago. EUSO-SPB2 is funded at the University of Chicago by NASA Award 80NSSC18K0246.

References

1. EUSO-SPB is part of the JEM-EUSO collaboration; http://jem-euso.roma2.infn.it

2. The POEMMA collaboration includes J. H. Adams[2], R. Aloisio[3], L. A. Anchordoqui[4], D. R. Bergman[5], M. E. Bertaina[6], P. Bertone[7], M. J. Christl[7], J. Eser[8], F. Fenu[6], E. A. Hays[9], E. Judd[10], J. Krizmanic[9], E. Kuznetsov[2], J. McEnery[9], J. W. Mitchell[9], A. Neronov[11], A. N. Otte[12], J. S. Perkins[9], P. Reardon[2], M. H. Reno[13], F. Sarazin[8], K. Shinozaki[6], L. Wiencke[8], R. M. Young[7], [2] *University of Alabama, Huntsville, AL, USA;* [3] *Gran Sasso Science Institute, L'Aquila, Italy;* [4] *City University of New York, Lehman College, NY, USA;* [5] *University of Utah, Salt Lake City, Utah, USA;* [6] *Universita di Torino, Torino, Italy;* [7] *NASA Marshall Space Flight Center, Huntsville, AL, USA;* [8] *Colorado School of Mines, Golden, CO, USA;* [9] *NASA Goddard Space Flight Center, Greenbelt, MD, USA;* [10] *Space Sciences Laboratory, University of California, Berkeley, CA, USA;* [11] *University of Geneva, Geneva, Switzerland;* [12] *Georgia Institute of Technology, Atlanta, GA, USA;* [13] *University of Iowa, Iowa City, IA, USA.*

3. J. Linsley, 1963, Phys. Rev. Lett., 10, 146.

4. K. Kotera and A. V. Olinto, Ann. Rev. Astron. Astrophys. **49**, 119 (2011) [arXiv:1101.4256 [astro-ph.HE]].

5. L. A. Anchordoqui, Physics Reports, arXiv:1807.09645 [astro-ph.HE].

6. K. Greisen, Phys. Rev. Lett. 16, 748 (1966). G. T. Zatsepin and V. A. Kuzmin, JETP Lett. 4, 78 (1966).

7. V. S. Berezinsky and G. T. Zatsepin, Physics Letters B 28, 423-424 (1969).

8. A. Aab et al., (Pierre Auger Collaboration), Nucl. Instr. and Methods in Phys. Res. **A** (798) 172-213 (2015).

9. T. Abu-Zayyad, et al. (Telescope Array Collaboration), Nucl. Instr. and Methods in Phys. Res. **A** (689) 87-97 (2012).

10. A. Olinto et al (POEMMA Coll.), PoS(ICRC2017) 542 (2017).

11. http://sites.nationalacademies.org/SSB/CurrentProjects/SSB_185159

12. M. Bertaina for the JEM-EUSO collaboration, Search for UHECRs from Space, the JEM-EUSO program *These Proceedings.*.

13. L. Wiencke and A. Olinto for the JEM-EUSO Coll., PoS(ICRC2017), 1097 (2017).

14. J.H. Adams et al, ArXiv e-prints [[arXiv]1703.04513 (2017).

15. J.H. Adams *et al* (JEM-EUSO Coll.), Experimental Astronomy **40** 281 (2015).

16. F. Capel *et al*, Advances in Space Research 10.1016/j.asr.2017.08.030 (2017).

17. F.W. Stecker et al., Nucl. Phys. B 136C, 433-438 (2004).

18. J. F. Krizmanic et. al., 33rd- Int. Cosmic Ray Conference, Rio De Janeiro, 2013.

19. J. H. Adams Jr. et al., (JEM-EUSO Collaboration), Experimental Astronomy **40** 3-17 (2015).

20. A. Neronov, D. V. Semikoz, L. A. Anchordoqui, J. H. Adams, A. V. Olinto, Phys. Rev. D 95, 023004 (2017), arXiv:1606.03629.

21. J.H. Adams Jr et al, (JEM-EUSO Collaboration), Experimental Astronomy **40** 239-251 (2015).

22. M. Bertaina et al, (JEM-EUSO Collaboration), Experimental Astronomy **40** 253-279 (2015).